UNIVERSITY OF GLASGOW

The Rotor Wake in Ground Effect and its Investigation in a Wind Tunnel

Nita Darshini Nathan

A thesis submitted in fulfilment of the requirements for the degree of Doctor of Philosophy

Department of Aerospace Engineering
Faculty of Engineering

May 2010

I, Nita Darshini Nathan, hereby declare that this work has not been submitted for any other degrees at this University or any other institution and that, except where reference is made to the work of other authors, the material presented is original.

Abstract

Rotorcraft operating in ground effect have been known to experience beneficial performance effects as well as operational difficulties during low speed forward flight. While these have been attributed to the formation of the ground induced wake, limited experimental investigations of the wake have been conducted. Difficulties in re-creating representative forward flight ground boundary conditions in wind tunnels have meant a lack of quantitative information on the ground effect wake. This research is based on experimentally investigating the ground effect wakes of rotors in forward flight, to detail the fluid mechanics associated with the ground effect wake and to identify the influence of rotor parameters and ground boundary conditions on the formation of the ground effect wake. Particle Image Velocimetry (PIV) tests were conducted on wide regions of the ground effect wake produced by a rotor model in a wind tunnel fitted with a moving ground.

Results from this research showed the ground effect wake to consist of a flow separation boundary and a region of recirculation, formed by the rotor tip vortex system trailing along the ground plane. Unsteadiness of the wake was seen to result in a constantly evolving wake, and this was observed to affect the classification of the ground effect flow regimes. Flow visualisation experiments conducted on the brownout phenomenon showed the ground effect wake features to influence the dust pick-up and transport mechanisms involved in the dust cloud formation. Experimental testing showed rotor parameters such as collective angles, rotor trim settings, rotor ground distance and root cut-out ratios to cause insignificant changes to the fluid mechanics of the ground effect wake, affecting only the location of the wake features. Effects of ground boundary conditions on the ground effect wake fluid mechanics were observed to be most significant, affecting both the location and detailed structure of the wake features. Results from this research show that ground effect experimental testing can be conducted in the wind tunnel environment and highlight the importance of accurately representing the ground boundary conditions during ground effect experimental testing.

Acknowledgements

This dissertation was completed with the support, guidance and assistance of many people in my life, to whom I am forever indebted to.

Firstly, I would like to sincerely thank my supervisor, Dr. Richard Green, for providing me with this opportunity to pursue a research in rotorcraft aerodynamics. I am ever grateful to him for his invaluable guidance, advice and assistance during the course of my research.

I would also like to thank Prof. Richard Brown and Dr. Emmanuel Bernard for providing me valuable comments and assistance during the course of my research. I would also like to extend my thanks to Mr. Tony Smedley, Mr. Robert Gilmour, Mr. Neil Owen and all the other technical support staff involved in this research.

Special thanks to my mother, brother and aunt, who have supported and tolerated my prolonged absence from home throughout this research period. Their unwavering belief in me was a pillar of strength during difficult times.

Finally, I would like to thank my friends, Mr. Alex Newton Alexander and Mr. Hasan Musfique, for their constant presence during my research and life in Glasgow, making it fun and enjoyable.

Publications

1. N.D. Nathan and R.B. Green, "Wind tunnel investigation of flow around a rotor in ground effect", AHS Specialists' Conference on Aeromechanics, San Francisco, USA, January 2010.

2. N.D. Nathan and R.B. Green, "Flow Visualisation of the helicopter brown-out phenomenon", The Aeronautical Journal, Volume 113, No. 1145, July 2009.

3. N.D. Nathan and R.B. Green,, "Measurements of a rotor flow in ground effect and visualisation of the brown-out phenomenon", 64^{th} Annual Forum of the American Helicopter Society, Montréal, Canada, May 2008.

4. N.D. Nathan and R.B. Green, "A rotor rig design for ground effect wake analysis", Post-graduate Conference, University of Glasgow, Scotland, Glasgow, UK, April 2006.

Technical Reports

1. R.B. Green, N.D. Nathan and R.E. Brown, "Report on the enhancements to the model rotor testing capabilities for improved visualisation experiments of helicopter brown-out phenomenon", Glasgow University Aero Report, No. 0705, July 2007. *(Technical Report submitted to QinetiQ. Ltd, under PO number CDAIR-04619)*

Contents

List of Figures

List of Tables

Nomenclature

Acronyms

CFD	Computational fluid dynamics
DPIV	Digital Particle Image Velocimetry
FDA	U.S. Food and Drug Administrations
FFT	Fast Fourier Transform
GE	Ground effect
Q-switch	Quality switch
RANS	Reynolds Averaged Navier-Stokes
RMS	Root-mean-square
RPM	Revolutions per minute
V/STOL	Vertical and/or Short Take-off and Landing
VTM	Vorticity Transport Model

Greek symbols

Δt	Inter-pulse time delay, s
Γ	Circulation, $= 2\pi r_v V_\theta$, $m^2 s^{-1}$
Γ_{TV}	rotor blade tip vortex circulation, $m^2 s^{-1}$
θ_{1c}	lateral cyclic pitch, ^{o}
θ_{1s}	longitudinal cyclic pitch, ^{o}
μ	Advance ratio, $V_\infty / \Omega R$
μ^*	Normalised advance ratio, $= \mu / \sqrt{C_T/2}$
ν	Kinematic viscosity, $= \zeta / \rho$, $m^2 s^{-1}$
Ω	Rotational Speed, $rads^{-1}$

ρ	Density, kgm^{-3}
θ_0	Blade collective pitch, ^{o}
ζ	Dynamic viscosity, $kgm^{-1}s^{-1}$

Variables

c	Blade chord length, m
C_T	Rotor thrust coefficient, $T/\rho A(\Omega R)^2$
D	Rotor diameter, m
D_p	Pixel particle displacement, $pixels$
d_p	Physical particle displacement, m
$\mathbf{x}_{EN}$	enstrophy centroid, $\frac{1}{EN}\int \mathbf{x}\omega^2 dA$, m
EN	total enstrophy, $\int \omega^2 dA$, s^{-2}
EN_t	enstrophy threshold
$\mathbf{F}$	PIV calibration function
$\mathrm{f}_{\#}$	f-number (focal ratio)
$\frac{y}{R}$	Normalised distance above the rotor hub
h	Height of rotor above the ground, m
K_∞	Power induced out of ground effect
K	Power induced in ground effect
θ	Camera perspective angle, ^{o}
ε_x	Perspective error, ^{o}
(r, y, z)	PIV co-ordinate system
(u, v, z)	Longitudinal, vertical and lateral velocity components along the (r, y, z) plane
R	Rotor radius, m
r	Spanwise location, m
Re_c	Chord based Reynolds number $= \Omega rc/\nu$
Re_Γ	Circulation Reynolds number $= \frac{\Gamma_{TV}}{\nu}$
$\bar{r}_{EN}$	mean enstrophy dispersion radius, m

r_v	Radial distance, m
r_{vor}	radius of a circular vortex, m
$\frac{r}{R}$	Normalised spanwise location
T	Rotor thrust, N
u	Longitudinal velocity component along the r-axis, ms^{-1}
w	Lateral velocity component along z-axis, ms^{-1}
v	Vertical velocity component along y-axis, ms^{-1}
V_{ff}	Forward flight speed, ms^{-1}
V_g	Ground velocity, ms^{-1}
V_h	Hover induced velocity, $= \Omega R\sqrt{C_T/2}$, ms^{-1}
V_∞	Wind tunnel/flight velocity, ms^{-1}
ω	Vorticity, $= \partial v/\partial x - \partial u/\partial y$, s^{-1}
V_θ	Swirl velocity of a vortex, ms^{-1}
V_{tip}	Rotor blade tip velocity, $= \Omega R$, ms^{-1}
y	Height above the ground, m

Abbreviations

CCD	Charge coupled device
C.G	Centre of Gravity
CW	Continuous Wave
GE	Ground Effect
DAQ	Data Acquisition
IGE	In Ground Effect
LDV	Laser Doppler Velocimetry
L.E	Leading Edge
LLS	Laser Light Sheet
NACA	National Advisory Committee for Aeronautics
Nd:YAG	Neodymium doped Yttrium Aluminum Garnet
NI	National Instruments

OGE	Out of Ground Effect
PCIe	Peripheral Component Interconnect Express
PC	Personal Computer
PIV	Particle Image Velocimetry
2D2C PIV	Two-dimensional two-component PIV
ROI	Region of Interest
VRS	Vortex ring state

Chapter 1

Introduction

When a helicopter is operating close to the ground, it is said to be in ground effect (IGE). Ground effect operations may include takeoff and landing routines, operations in forward flight and even hover near the ground. The presence of the ground near the vicinity of the rotor has been known to alter its aerodynamics from that commonly experienced out of ground effect (OGE). Most significantly, ground effect operations have been seen to enhance the performance of rotors, with the power required to produce identical levels of thrust significantly lower compared to OGE flight.

Ground effect operations have also been known to cause handling and operational difficulties. Pilots' accounts of experiencing particular periods of handling difficulties, especially during slow transition flights from hover in ground effect, reflect US military reports which show significant damage to helicopters and fatalities because of ground effect related operations [1]. Ground effect operations have also affected civilian helicopter operations, with statistics from the UK attributing 20% of all light helicopter accidents to handling issues during hover or low speed forward flight operations in ground effect [2]. Some of the ground effect related difficulties highlighted in these documents include handling difficulties due to cyclic trim adjustments required during ground effect transition flights, hot gas re-ingestions (especially in the case of VTOL aircraft) resulting in the loss of engine performance [3], and loss of pilot visibility during specific ground effect operations. Helicopter operations in desert terrains is one example of ground effect operations resulting in the loss of visibility. Commonly referred to as the brownout condition,

it results in the loss of situational awareness due to the formation of huge clouds of dust ahead of the helicopter, obstructing the pilot's view [4]. These dust clouds have sometimes been observed to be large enough to engulf helicopters, causing collisions and fatalities.

Research on rotors in ground effect has been conducted for many decades now, with a wide range of experimental, numerical and computational studies undertaken to understand the performance implications of helicopter ground effect operations. While it has been understood through these studies that the performance benefits experienced are a result of changes induced by the ground on the rotor wake, lesser focus has been placed on the attempt to understand the evolution and formation of the wake itself. Experimentally, ground effect wake research has been further hindered by the ability in successfully re-creating accurate ground effect conditions during the experiments. Limitations of experimental techniques that have been employed to investigate the rotor wake thus far have also contributed to the situation. Such issues have meant that experimental information available on the ground effect wake of rotors are incomplete. Where available, they are mostly focused on specific features or regions of the wake. Difficulties in measuring accurate flow information from the highly three-dimensional and unsteady wake in ground effect have made numerical and computational ground effect research the most abundant source of information on the ground effect wake.

While simulation based research provides the best option to a complete, three-dimensional analysis of the ground effect wake, most of these results still need to be verified. Current verifications have been based on limited flight test data and even more limited accurate experimental data. Most of the available experimental data have additionally been focused on the salient features in the flow-field and their influence on the rotor performance. Quantitative data on the formation of these salient features, their evolution and impact on the surrounding flow-field and near the ground have been limited, or in most cases, qualitatively inferred from simple experimental visualisations in the past, restricting verification of the ground effect wake formation and dynamics. The lack of understanding of the ground effect wake and its surrounding flow-field have in general meant little understanding of other ground effect based phenomena; an example of this is the brownout situation, mentioned previously. Little knowledge is thus far available

on the dust pick-up and transport mechanisms resulting in the formation of large dust clouds in these conditions.

Advances that have been made in technology and computing in recent times, have meant that more advanced and accurate experimental techniques can now be employed for the measurements of highly complex flow-fields. Non-invasive optical experimental techniques such as Laser Doppler Velocimetry (LDV), Particle Image Velocimetry (PIV) and Laser Light Sheet (LLS) techniques can now be exploited to more accurately investigate highly unsteady flows. Accessibility to these techniques means that the ground effect wake of a rotor can now be experimentally investigated to greater detail.

1.1 Scope of the Dissertation

One of the biggest challenge of rotor wakes in ground effect experimentation has always been the ability to accurately simulate ground effect operations in a wind tunnel environment. Unlike conventional rotorcraft experiments involving a model and the freestream wind source (in the case of hover, even this is not required), ground effect testing involves a third and important factor; the ground. The necessity of accurately re-creating ground conditions within the experimental environment means that experiments of ground effect cannot be as simple as using a conventional wind tunnel. Experiments done with just a rotor model fitted in a wind tunnel with a static ground plane do not satisfy the conditions of simulating a real helicopter moving over a stationary ground with a flight velocity. In fact, investigations of this nature are analogous to a hovering rotor over a stationary ground plane, encountering a strong head wind. While the difference between the two experimental scenarios is known, rectifying this in experimental situations is not easily done.

Work carried out in this research attempts to contribute to the above-mentioned limitations in rotor ground effect wake research through a set of well-conditioned experiments. One of the primary goals of this research was to conduct experimental investigations on a rotor model to quantitatively investigate the ground effect

wake. Besides the salient features of the wake, information on the formation, structure and evolution of the flow-field was sought. With numerous research activities already conducted on the performance implication of ground effect, this research was constructed to focus solely on the fluid mechanics of the wake and its influence on wide regions of the flow surrounding the rotor. The need to investigate wide regions of the flow-field meant that a suitable experimental technique needed to be employed in this research. Both flow visualisation and Particle Image Velocimetry were chosen to provide quantitative and qualitative information of the flow-field.

Another objective of this research was to re-create, more accurately, ground effect forward flight conditions in a wind tunnel environment. To achieve this, a model rotor with trim capabilities had to be designed. More importantly, a realistic representation of the ground boundary conditions was required for this to be achieved. A wind tunnel fitted with a moving ground plane (rolling road) was used to represent the ground conditions in forward flight operations in ground effect. Quantitative investigations of the wake were then conducted to establish any differences between the resulting wake for the moving and fixed ground plane configurations.

In addition to these, the re-creation of the brownout phenomenon was also to be attempted in a wind tunnel facility. This was to be performed to qualitatively identify mechanisms which contribute to the formation of the dust cloud, a characteristic feature of the helicopter ground effect wake during operations near erodible ground surfaces.

1.2 Contributions of the Dissertation

Based on the above-mentioned objectives, this research on the ground effect wake of rotors has made the following contributions:

1. The brownout phenomenon was re-created in an experimental facility with the use of talcum powder to simulate ground debris. Flow visualisation experiments conducted allowed for the identification of flow structures and

dust transport mechanisms resulting in the formation of the dust cloud that may lead to the so-called brownout phenomenon.

2. Quantitative investigations of wide areas of the ground effect wake of a rotor were conducted in a wind tunnel using Particle Image Velocimetry. Three-dimensional velocity information from the flow-field were used to identify the ground effect wake features, their influence on the surrounding flow-field, and was used in the definition and classification of the ground effect flow regimes.

3. Effects of rotor parameters on the formation of the wake were characterised. Factors such as rotor collective angles, rotor ground distances and blade root cut-out ratios were seen to have little effect on the ground effect wake structures. Rotor trim conditions defined for this research was seen to cause small changes to the location of the wake and the classification of the ground effect flow regimes.

4. The most prominent modification to the ground effect wake caused by wind tunnel interference effects was a change in the flow separation location, and this was observed to occur most significantly at the low forward flight speeds, where the wake spread was seen to be the greatest.

5. Ground boundary conditions were seen to have the most significant effect on the fluid mechanics of the ground effect wake, with modifications to both the flow separation point locations and detailed wake structures observed. These have implications on ground effect testing in a wind tunnel.

1.3 Structure of this Dissertation

This dissertation presents the research conducted in relation to rotor wakes in ground effect and its investigation in a wind tunnel facility.

The current chapter continues by introducing the aerodynamic concept of a rotor flow in ground effect. A review of the most significant research conducted on rotors in ground effect is presented. The motivations of this research are presented, and this chapter also highlights the methodology that was adopted during the course

of this research.

Chapter 2 provides details of the experimental methodology used in this research. It provides a systematic breakdown of the different sets of experiments conducted, providing information on the experimental facilities, rotor models and experimental techniques used. It also introduces the model rotor designed specifically for this research. This rotor was used for a wide range of experiments conducted to investigate the effects of the wind tunnel ground boundary conditions and rotor parameters on the ground effect wake.

Results obtained from the different experiments conducted during this research are presented in Chapters 3 - 5 of this dissertation.

Chapter 3 presents results from the flow visualisation experiments conducted on a small-scale rotor model in a wind tunnel. This investigation formed part of the preliminary investigations of the ground effect flow-field and provided useful qualitative descriptions of the salient flow features of the ground effect wake. It also allowed for wind tunnel simulation of the brownout phenomenon. Insights into the mechanisms involved in particle pick-up and transport are also discussed in this chapter, with the aid of flow visualisation images of the flow-field.

Chapter 4 presents quantitative information obtained from Particle Image Velocimetry (PIV) experiments conducted with the rotor model used in the flow visualisation experiments . Experiments using this rotor served as a preparatory exercise to the main set of experiments that were to be conducted with the larger rotor designed for this research. Useful information obtained from these experiments regarding the ground effect flow-field are detailed in this chapter and used to quantitatively explain some of the observations made from the flow visualisation experiments, discussed in Chapter 3.

Chapter 5 presents results from the main set of PIV experiments conducted with a rotor model designed to work in a wind tunnel fitted with the moving ground. Variations in the wake caused by differing rotor trim configurations and ground

boundary configurations are analysed to identify the configuration best representative of the ground effect flow-field of a helicopter in forward flight. Based on this, flow structures observed in the ground effect flow-field are identified through a series of flow pathlines, vorticity and velocity fluctuation plots derived from the PIV results. Measurements conducted to determine the out-of-plane velocity components in the flow-field are also presented to characterise the three-dimensional nature of the wake. Additionally, the effects of varying rotor parameters on the ground effect wake structures are also presented in this chapter.

An analysis of the PIV results is presented in Chapter 6. Validation of these experimental results is conducted in this chapter, and is used to highlight the influence of wind tunnel interference effects on the ground effect wake. Additionally, the physics of formation of the ground effect wake is described based on the results gathered from the flow visualisation and PIV experiments. The PIV results were also used to classify the ground effect wake into different ground effect flow regimes and to identify the effects of rotor parameters and ground boundary conditions on the fluid dynamics of the wake. Analyses of the importance of these parameters in wind tunnel experimentation on ground effect is also presented in this chapter.

The dissertation is concluded in Chapter 7, which summarises the main contributions and results from this research. Recommendations for future work, which can be conducted to further this research are also outlined in this chapter.

1.4 Overview of Ground Effect

When a helicopter is operated close to the ground, it is said to be operating in ground effect (IGE). The presence of the ground plane close to the vicinity of the rotor disk has been seen to significantly alter its aerodynamics compared to when it is operated out of ground effect (OGE). Numerous experimental, numerical and computational analyses have been carried out to accurately predict and understand rotor behaviour in ground effect. Most have concentrated on the performance aspects of rotor operations in ground effect; in analysing and predicting changes to the handling and control of helicopters during ground effect operations. One shortcoming of these past research has been the lack of investigations on the

fluid dynamics associated with the wake formed during ground effect operations. This has been made evident by the lack of quantitative information available on the formation and evolution of the ground effect wake. Most of the information currently available on the fluid dynamics of the wake has been qualitatively obtained through flow visualisations or analysis of specific points in the ground effect flow-field.

The following sections provide an overview of ground effect research that has been conducted to date. Significant research findings regarding the impact of ground effect operations on the performance, handling qualities and resulting wake are detailed, and make evident the lack of quantitative data available on the fluid dynamics of the ground effect wake. Additionally, the need for a better understanding of the ground effect wake fluid mechanics is highlighted through discussion of a situation where the ground effect wake has been seen to cause operational difficulties. Based on these, the motivations and methodology adopted for this research are briefly highlighted at the end of the section.

1.4.1 Hover in Ground Effect

Analysis of available literature suggests that the ground has the most influential effect on the rotor in two flight regimes; in hover, where the most significant performance gains are experienced, and in low speed forward flight.

Most ground effect analyses have identified the beneficial effects of ground effect operations on rotor power and thrust. Flight testing on helicopters and experimental testing on isolated rotor models have shown that the power required to hover in ground effect is significantly less than out of ground effect, at a given rotor thrust [5–10]. Experimental studies have shown these performance benefits to be affected by parameters such as blade loading [9], number of rotor blades, blade shape, blade twist and aspect ratio [11]. The inclination of the ground over which the rotor is hovering is also seen to change hover performance in ground effect [5]. Most substantially, the rotor height, h, above the ground is seen to have the greatest influence on the rotor hover performance in ground effect. Mathematical analysis conducted by Küssner [6] and Betz [7], have shown most of the

performance advantages in ground effect hover to be experienced at heights up to one rotor radius above the ground. Performance related research has also shown the rotor to lose most of its performance benefits obtained in ground effect hover as it reaches a distance of one rotor diameter above the ground [8, 10, 11], after which it is considered to be out of ground effect.

Beneficial performance effects experienced by rotors in ground effect hover piqued numerous research activities in mathematical and computational modelling of ground effect hover [7, 8, 10, 12–18]. The earliest numerical analysis was carried out by Betz [7] and Cheeseman and Bennett [12], who used a source and image to model the influence of the ground on the rotor, while Knight and Hefner [8] and Rossow [19] made used of a vortex cylinder method to analyse this effect. More recently, Hayden derived an empirical method of predicting power induced in ground effect hover by analysing a range of flight tests conducted in ground effect hover and by employing methods suggested by Betz and Cheeseman and Bennett [10]. Based on this, the induced power variation with rotor ground distance, $\frac{h}{R}$, was derived to vary according to the equation,

$$\frac{K}{K_\infty} = \frac{1}{0.9926 + 0.3794(\frac{2R}{h})^2} \tag{1.1}$$

where K represents the power induced in ground effect, K_∞, the power induced out of ground effect and R, the rotor radius. More recently, computational simulations of ground effect hover have also been attempted. Numerous free-wake models have been created with varying degrees of success. Most of these models utilise an image wake system to simulate the ground plane [13, 15]. Other computational methods have employed a surface singularity method to represent the ground plane [18] or a grid of vortex panels to represent inclined ground surfaces [17]. A finite inflow model, representing the ground and rotor as disturbances in a flow-field, with the ground represented using the image rotor method, has also been employed to simulate ground effect hover [16].

The most obvious difference in the wake of a hovering rotor in ground effect is the expansion of the wake instead of the normal contraction experienced out of

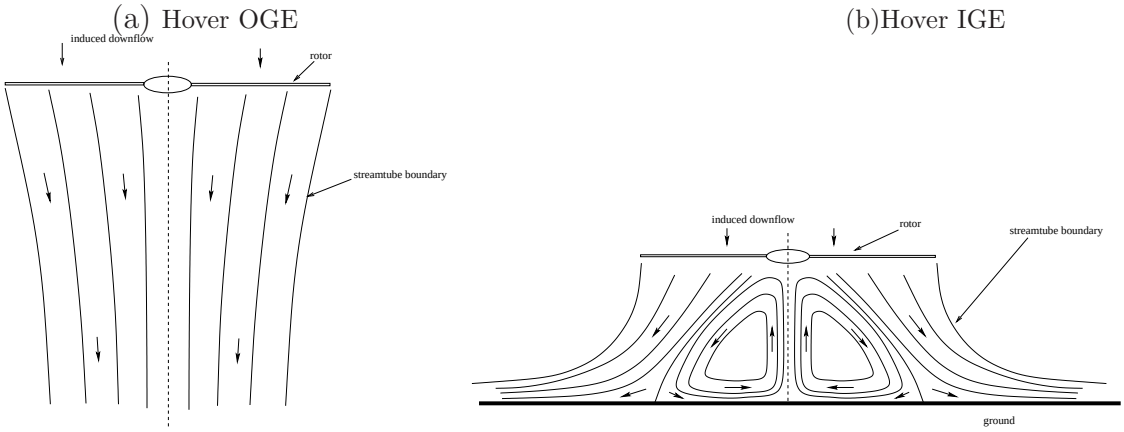

FIGURE 1.1: Comparison between the out of ground effect (OGE) and in ground effect (IGE) wake of a hovering rotor. The figure shows schematic diagrams of mean flow streamlines. [5]

ground effect. Smoke flow visualisation experiments conducted by Fradenburgh showed this expansion [5], and a schematic of this is presented in Figure 1.1. Velocity measurements conducted during this research identified the presence of a 'dead-air' region in the central region of the expanding rotor wake, possessing low magnitude negative velocity associated with an upwash through the rotor disk (in contrast to the positive velocities associated with the rotor downwash). Analogous to the fountain effect commonly associated with hot exhaust gas jets on VTOL aircraft [3], this 'dead-air' region represents the induced velocity profile altered by the presence of the ground near the vicinity of the rotor. Observations from these experiments suggest that part of the root vortex system leaving the rotor blades will flow along the ground towards the centre of the rotor disk and result in vorticity to be transported vertically upward through the centre of the rotor disk [5].

It is conceptually easy to observe that the presence of the ground plane near the vicinity of the rotor alters the trailing rotor wake, affecting both the slipstream and inflow velocities, which in turn, has an effect on the thrust and power characteristics of the rotor [11]. Evidence for this is seen from experiments where the presence of the ground plane within the vicinity of the rotor was seen to alter the axial and radial locations of the tip vortices shed by the rotor [20]. More recent particle image velocimetry (PIV) experiments conducted with a ground plane and rotor model, have traced the variation in the tip vortex trajectories caused by varying rotor ground distances [21]. More in-depth analysis of the tip vortex

system of the wake of a rotor in ground effect hover was conducted by Lee *et. al*, using flow visualisation and phase-resolved PIV [22].

1.4.2 Ground Effect in Low Speed Forward Flight

Ground effect has also been seen to have substantial effects on the performance of a rotor in low speed forward flight. Experiments conducted by Sheridan and Weisner showed changes in the power required in ground effect forward flight compared to hover in ground effect [23]. Power measurements at low speed forward flight showed an initial increase in the power required from hover. At a particular flight speed, the power required peaks at a value close to that required by the rotor out of ground effect. Beyond this, an increase in the flight speed is seen to reduce the overall power required. A re-creation of the power variation in ground effect, measured by Sheridan and Weisner, is presented in Figure 1.2 [23]. Performance measurements conducted by Curtiss *et. al* showed similar trends, and it was observed that the performance variations in forward flight were influenced by the rotor ground distance, $\frac{h}{R}$, disk loading and collective angles [24]. Both studies attribute changes in the power required in ground effect to changes in the inflow through the rotor disk, caused by flow features formed in the ground effect wake.

Experimental evidence suggests that as the rotor moves from hover into forward flight, the downwash through the rotor expands over the ground plane and interacts with the oncoming freestream. The location of this flow interaction was seen to be affected by the advance ratio, $\mu = \frac{V_{ff}}{V_{tip}}$, the non-dimensional forward flight speed, where V_{ff} represents the flight speed and V_{tip} represents the rotor tip speed. Interaction between the opposing flows results in flow separation along the ground; the rotorwash expanding along the ground is seen to roll up to form a vortex as a result of this separation. Flow visualisation experiments conducted by Sheridan and Weisner showed the wake roll up to form a horse-shoe shaped vortex in the flow-field [23], and this is shown in Figure 1.3, which presents a three-dimensional view of the ground effect wake obtained from computational simulations of a helicopter in ground effect [25]. At low advance ratios, a weak horse-shoe vortex was seen to form in the flow-field ahead of the rotor disk. As the forward flight speed of the rotor was increased, this roll up was seen to occur nearer the rotor disk; the horse-shoe vortex was seen to become more prominent

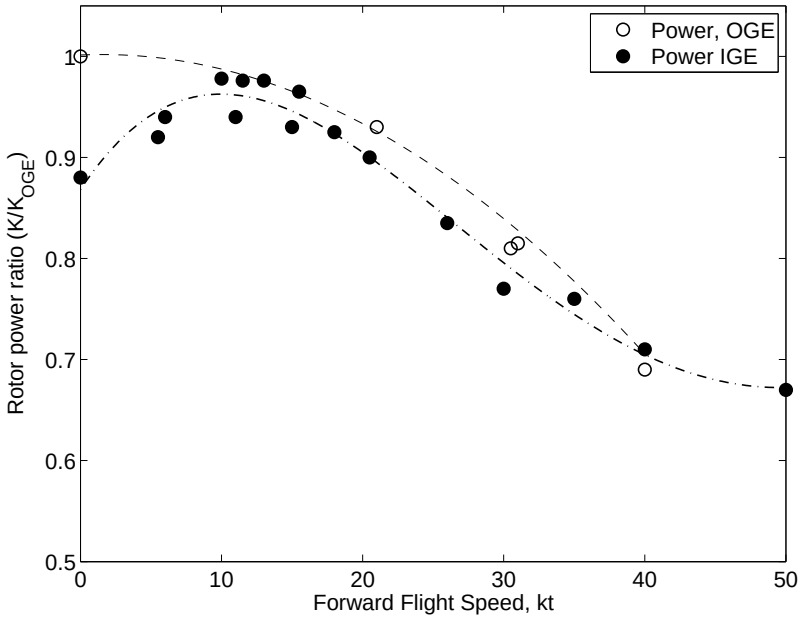

FIGURE 1.2: Comparison of the power required in ground effect and out of ground effect [11].

and was observed to be the strongest when it formed under the leading edge of the rotor disk [23]. Further increments in the forward flight speed resulted in the vortex to form downstream of the leading edge of the rotor disk, where it was seen to grow progressively smaller and weaker with increasing flight speed, until it eventually disappeared from the flow-field [23]. Presence of the ground induced vortex in the wake has been documented to exist up to a forward flight speed equivalent to an advance ratio of $\mu \approx 0.1$, beyond which it is not visible in the flow-field [11]. A set of schematic diagrams, shown in Figure 1.4, was produced by Sheridan and Weisner to illustrate their observations from the flow visualisation tests and to explain the effect of the wake on the power required by the rotor at the different flight speeds [23].

Schematic diagrams presented in Figure 1.4 show the changes to the inflow through the rotor disk brought about by the changing topology of the ground effect wake. As the ground induced vortex forms close to the rotor disk, as seen in Figure 1.4 (b) and (c), additional inflow is induced through the rotor disk. Some of the freestream is seen to flow around the forming vortex and as the vortex approaches the rotor at higher flight speeds (advance ratios), greater inflow is induced through the rotor disk. At the point of maximum induced inflow through the rotor, the power required was observed to be the highest. This corresponds to the peak in

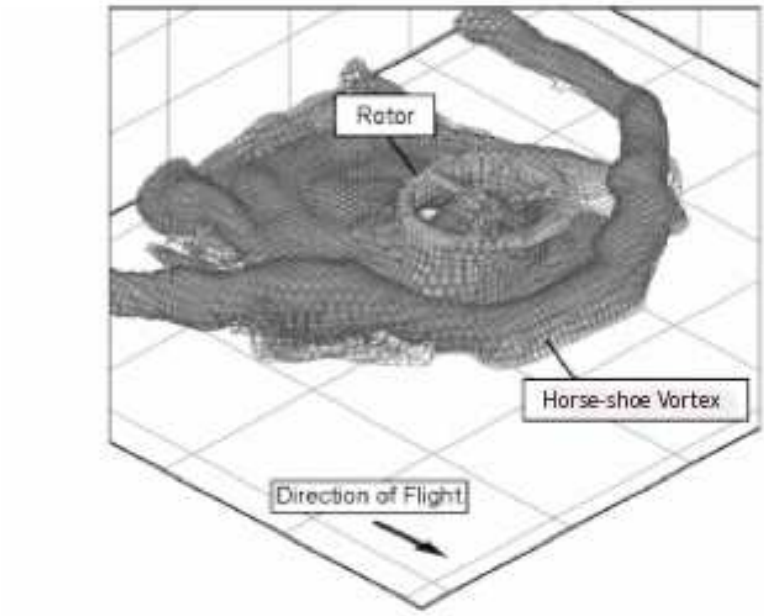

FIGURE 1.3: Representation of the ground effect wake obtained from computational simulations conducted by Brown and Whitehouse [25].

the in-ground-effect (IGE) power curve observed in Figure 1.2, with the power required almost equivalent to that required by the rotor operating out of ground effect (OGE). Increasing the advance ratio further was seen to cause the vortex to form further downstream beyond the leading edge of the rotor disk, contributing both inflow and upflow (positive inflow) through the disk, as shown in Figure 1.4 (d). The power required by the rotor at this point is lower, and is seen to fall significantly lower than that required OGE, as shown in Figure 1.2.

Besides changes to the performance characteristics of the helicopter, changes in the location of the ground effect flow features were also seen to affect its trim characteristics and fuselage forces and moments [23]. Flight operations in ground effect have been known to significantly alter the lateral cyclic inputs required to trim the rotor during ground effect low speed forward flight [26]. Experimental tests conducted using a model helicopter showed this change in lateral cyclic input to be related to the location of the ground induced vortex. Figure 1.5, a re-creation of the results presented by Sheridan and Weisner, shows the alterations in the lateral cyclic angles required to compensate for the changes in inflow caused by

(a) Wake roll-up occurs upstream, far ahead of the rotor disk

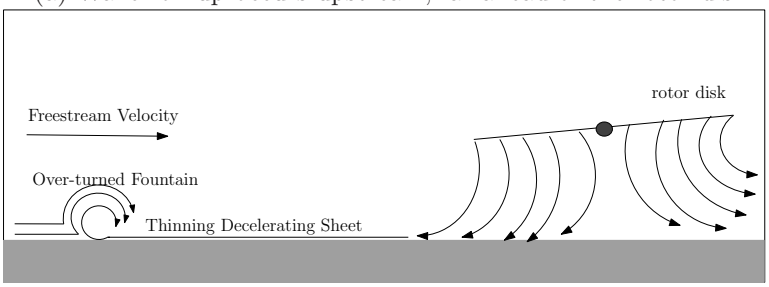

(b) Vortex forms closer to the rotor at higher forward flight speed

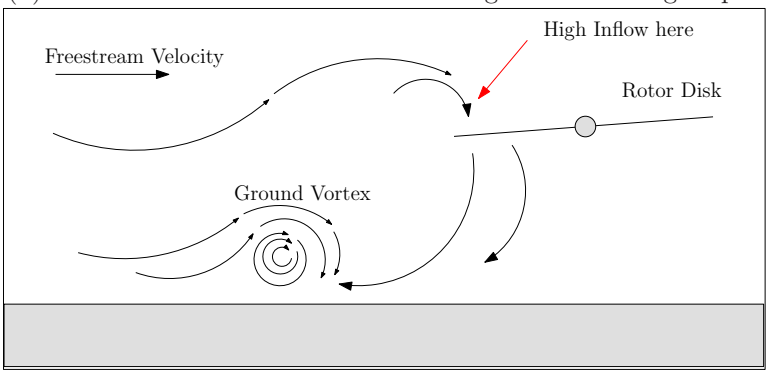

(c) Vortex strongest when it is just ahead of the rotor disk

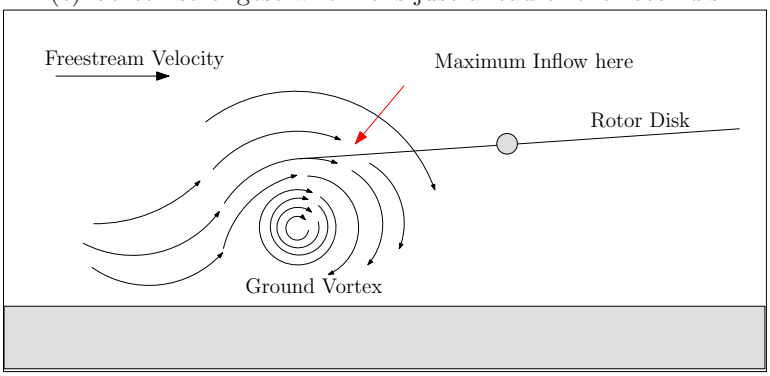

(d) Vortex loses strength and becomes smaller when speed is increased further

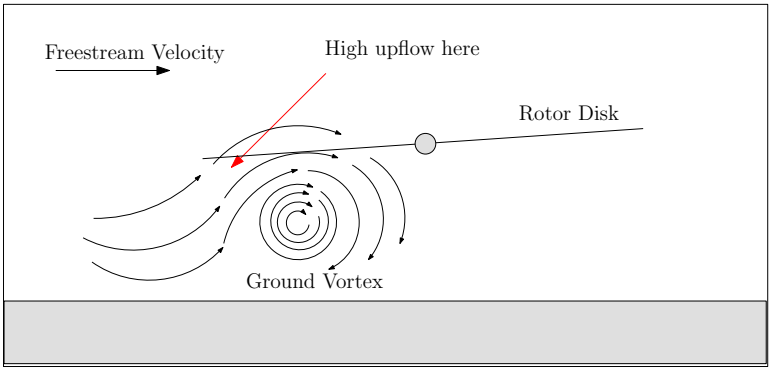

FIGURE 1.4: Schematic diagrams of the evolution of the ground effect wake at low speed forward flight [23].

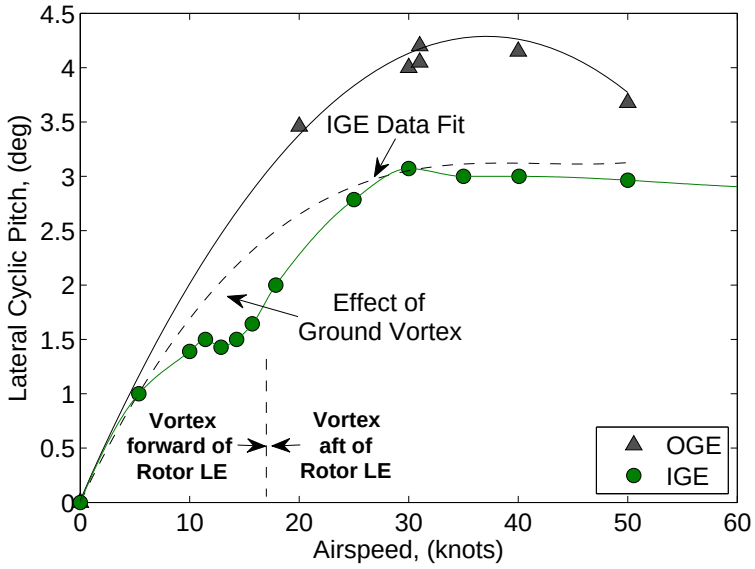

FIGURE 1.5: Variation in the lateral cyclic pitch angle required during ground effect operations [23]. Location of the ground vortex with respect to the leading edge (LE) of the rotor disk is presented.

the ground vortex located aft of the leading edge of the rotor disk [23]. Known as over-running the ground vortex, this step-like change in lateral cyclic input has been especially noticeable in helicopter flight data during transition from hover to forward flight in ground effect.

Additional measurements conducted during these studies have also shown the ground vortex position to have prominent effects on the fuselage moments and forces, although these were observed to be less significant compared to the aerodynamic effects of the ground on the main rotor [23]. Measurements conducted on a model rotor showed the fuselage pitching moments to become more negative as the ground vortex formed closer to the rotor. This effect is then reversed and the pitching moments seen to increase and become more positive as the ground vortex forms under the rotor disk [23]. Measurements of the fuselage lift were seen to fall linearly from hover values as the ground vortex formed in the flow-field and approached the rotor, but this was seen to increase as the ground vortex passed under the rotor leading edge [23].

Most ground effect literature has shown the ground effect flow-field to be similar to that represented in Figure 1.4, where the wake roll-up begins as a small vortex

far upstream of the rotor disk and builds in size and prominence as the flight speed is increased. Benchmark ground effect research conducted by Curtiss *et. al* [24, 27], using an isolated rotor towed along a flat track in a towing shed, showed similar results. Measurements conducted during these experiments also reflected the influence of the ground induced vortex on the rotor hub moments. Data from these tests indicated a distortion of the trailing wake caused by the ground vortex to result in changes to the inflow around the leading edge of the rotor disk, subsequently resulting in nose up pitching and rolling moments to be measured at the rotor hub [27]. Additionally, results from experiments conducted with different rotor disk tilt angles showed this to have little influence on the rotor wake, thrust and hub moments during ground effect [24].

Regarded as one of the most substantial research efforts conducted in ground effect to date, this research also established that the majority of the ground effect wake can be categorised into two flow regimes. Known as the recirculation regime and the ground vortex regime, these flow regimes were used to characterise the ground effect flow for a variety of ground distances ($\frac{h}{R}$) and collective pitch angles [24, 27]. Classifications of the ground effect wake into the different flow regimes were conducted using the thrust normalised advance ratio, μ^*, given by the equation,

$$\mu^* = \frac{\mu}{\sqrt{C_T/2}} \tag{1.2}$$

where μ is the representative advance ratio of the flow and C_T is the rotor thrust coefficient. Essentially the forward flight speed scaled with respect to the hover induced velocity, considerations of this thrust normalised advance ratio, μ^*, ensured that same wake deflection angles were maintained for the different ground distances and collective settings [23, 24]. This then allowed for the comparison of similarly formed wake at different rotor ground distances or thrust settings. Based on data obtained from their flow visualisation experiments conducted at different normalised advance ratios, Curtiss *et. al* categorised the ground effect wake into the different flow regimes [27]. A re-creation of their experimental results is shown in Figure 1.6.

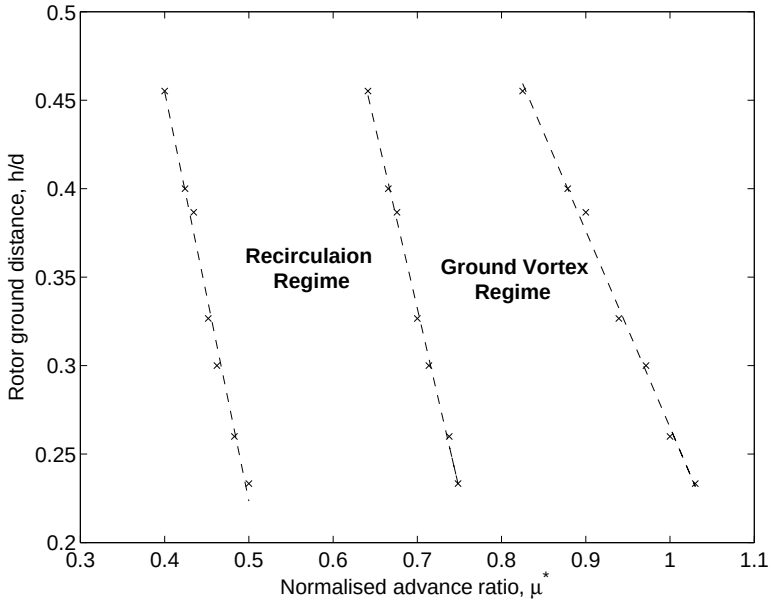

FIGURE 1.6: Classification of the ground effect wake into the different flow regimes at a range of ground distances. Diagram adapted from research conducted by Curtiss *et. al* [24, 27].

According to Curtiss *et. al*, the ground effect wake was considered to be in the recirculation flow regime when a portion of the trailing rotor wake expanding radially upstream away from the rotor, separates from the ground and is recirculated through the rotor [27]. Flow visualisation studies conducted during their research showed the recirculation of the rotor wake to be less obvious near hover and more prominent at higher normalised advance ratios [27]. The lower boundary of the recirculation regime, as defined in Figure 1.6 was thus defined at normalised advance ratios where the recirculatory pattern through the rotor disk was well-defined in the flow with the wake at advance ratios lower than the recirculation regime, exhibiting lesser tendencies of wake recirculation through the disk. At these low advance ratios, the wake was seen to show trends similar to hover in ground effect cases, where the trailing rotor wake was seen to expand far upstream from the rotor. The ground vortex flow regime was classified by Curtiss *et.al* as the advance ratios at which the recirculation through the rotor disk is replaced by a well-defined vortex, formed under the leading edge of the rotor disk, with the upper boundary of the ground vortex regime signifying the disapperence of the ground vortex under the rotor disk, as the trailing rotor wake is swept downstream by the freestream [27].

Interactions between the oncoming freestream and the rotorwash expanding along the ground plane have been seen to result in the formation of a horse-shoe shaped boundary on the ground plane, some distance upstream from the rotor disk. The location of this interaction boundary is determined by the advance ratio of the flow and was visualised by a surface flow visualisation experiment conducted by Boyd *et. al* [28] using smoke/tufts on a static ground plane. With increasing freestream velocity, this interaction boundary was seen to form closer to the rotor. Surface flow visualisations also established that the symmetry of the interaction boundary on the ground depended upon the rotor system used. With a rigid rotor, the inability of the rotor to compensate for the differential in lift produced at the advancing and retreating sides meant that an asymmetric interaction boundary resulted on the ground. According to Kusmarwanto, this boundary would otherwise be symmetric and parabolic in shape, if the rotor is allowed to trim, although no evidence was presented to illustrate this claim [29]. The presence of this horse-shoe shaped interaction boundary around the front end of the rotor disk however highlights the three-dimensional nature of the ground effect wake.

1.4.2.1 Recirculation Regime

As the rotor moves into forward flight, the rotor wake becomes skewed backwards. In ground effect forward flight, the skewed wake undergoes a contraction up to a distance of 25% below the rotor, after which the presence of the ground was seen to result in the expansion of the wake [29]. The expanding rotor wake encounters the freestream, which then causes a roll up of the wake. The recirculation regime occurs when this wake roll up occurs near the rotor disk, causing a recirculation of part of the wake through the rotor. This re-ingestion of the wake was observed by Curtiss *et. al* to become more prominent as the advance ratio increased and the wake roll-up occurred nearer the vicinity of the rotor disk [27]. It was also noticed that the resulting ground effect wake in the recirculation regime affected large proportions of the ground effect flow-field upstream of the rotor disk [27]. Flow visualisation experiments conducted by Ganesh *et. al*, using an isolated rotor model in a wind tunnel fitted with a static ground plane, identified the ground effect wake in the recirculation regime to feature a recirculation loop [30–32]. A schematic of this recirculation loop is presented in Figure 1.7, and through the experiments, it was identified that this recirculation loop was characterised by 7-8

tip vortices re-directed back towards the rotor and re-ingested through it [30]. Hot-wire anemometry studies conducted by Curtiss *et. al* reported large fluctuations in the wake during the recirculation regime, although little lateral flow was observed in the flow-field [24]. Similar hot-wire measurements conducted by Ganesh *et. al* near the rotor disk plane during the recirculation regime, also showed the presence of fluctuations in the inflow near the rotor, which was measured to be 5-10% higher than that experienced OGE, and these fluctuations have been attributed to the ingestion of the tip vortices from the recirculation loop [31, 32].

Interactions of the rotor wake with the oncoming freestream flow demands the presence of a separation line along the ground plane, which determines the spatial width of the ground effect wake. At low advance ratios, flow separation occurs far upstream of the rotor resulting in a wide wake. Increments of the advance ratio was seen to result in this separation line to form nearer the rotor, reducing the spatial width of the wake. Hot-wire experiments conducted by Saijo *et. al* measured the fluctuations of the flow separation position in the plane along the rotor longitudinal axis [30]. It was observed through these tests that in the recirculation regime, the separation point along the ground oscillated about a mean ground position with a low frequency, between 2-4 Hz [30]. Fluctuations of this separation point were seen to be consistent throughout the advance ratios within the recirculation regime, although the fluctuation amplitudes were seen to reduce as the advance ratio was increased. At a high enough advance ratio, the recirculation loop disappeared from the flow-field. A vortex was seen in its place, just under the leading edge of the rotor disk, with the flow separation point forming on the ground just ahead of

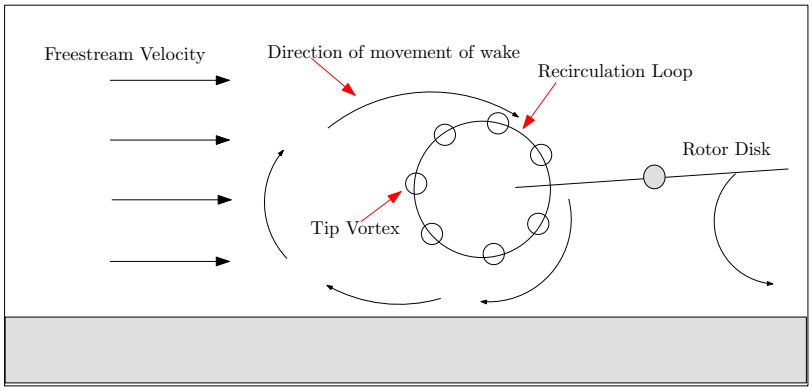

FIGURE 1.7: Formation of the recirculation loop [30].

the rotor disk. Measurements showed lesser fluctuations in the separation point during the ground vortex regime, suggesting a steadier flow-field [30].

1.4.2.2 Ground Vortex Regime

The formation of a well-defined vortex, just under the rotor disk has been defined as the start of the ground vortex regime, and a schematic of this can be seen in Figure 1.4 (d). The corresponding range of advance ratios where the vortex forms under the rotor disk is known as the ground vortex regime. The formation of this ground vortex is generally noted to be a function of advance ratio, blade collective pitch and rotor ground distance [27]. Qualitative analysis in the ground vortex regime, with the rotor ground distance at $0.9R$, has shown the ground vortex to be of comparable height, although it is unclear from these results if this size of the ground vortex is dependent upon the rotor ground distance [24]. These experiments were also used to derive the locations of the centre of the ground vortex, for a variety of normalised advance ratios and rotor ground distances [33].

While Saijo *et. al* identified the ground vortex regime to be steadier than the recirculation regime in terms of separation point fluctuations [30], Curtiss *et. al* observed from their smoke flow visualisation experiments significant lateral motion of the smoke streams during the ground vortex regime [24]. This was less apparent during the recirculation flow regime, where the smoke streams were seen to remain in the vertical plane in which they were first injected. It was thus contended that the distinction between the two ground effect flow regimes could be made through consideration of the degree of lateral flow present in the ground effect wake [24]. Additional experiments on the effect of translational acceleration/deceleration on the ground vortex regime were also conducted and showed this to affect the onset of the ground vortex regime [27].

Other hot-film investigations along a vertical plane extending from the ground to the height of the rotor disk, just ahead of the leading edge of a model helicopter's rotor disk have shown a highly unsteady flow-field [34]. Like Curtiss *et. al*, these investigations also made use of flow visualisation images to classify the ground effect wake into the different ground effect flow regimes. Additionally, the effect of the ground vortex on the empennage lift, tail rotor power and fin side force

were measured for right sideward flight conditions. It was determined from these experiments that the interactions of the ground vortex with the tail rotor and the fin was a function of the main rotor disk loading, and that an increase in this would result in significant alterations to the tail rotor effectiveness and the fin loads, causing additional handling difficulties for pilots [34].

More recent experiments on the ground vortex regime, were conducted using more advanced optical experimental techniques like Particle Image Velocimetry (PIV) [35, 36]. Laser Light Sheet (LLS) and PIV experiments conducted by Boer *et. al* were concentrated on a $0.7R \times 0.6R$ region of the flow-field to investigate the ground vortex formed under the rotor disk, and were used to identify changes to the location of the ground vortex cores for changing rotor ground distances and flight speeds [35]. While detailed information on the ground vortex was established through these experiments, details about the structure, size and strength of the ground vortex were not provided. PIV measurements of the ground vortex conducted by Ganesh *et. al* showed the ground vortex to form with vorticity ingested from the tip vortices trailed by the rotor blades, and showed the ground vortex strength to be more than four times that of the tip vortices [26, 36]. These PIV experiments were primarily conducted to investigate the flow-field under the rotor disk leading edge, with the wake examined up to 1.45 radii (1.45R) ahead of the rotor hub. Two-dimensional velocity information from the ground vortex were obtained from the field-of-view ($0.66R \times 1.45R$, with the origin from the rotor hub), with the PIV employing oil particles generated by an oil atomizer, with nominal diameters of 0.19mm. While quantitative investigations of the ground vortex regime have been conducted, only small regions of the flow-field have been imaged in an attempt to investigate the ground vortex characteristics.

1.4.2.3 Computational and Numerical Simulations of Ground effect in low speed forward flight

Most of the quantitative experimental data available on the rotor wake in ground effect were obtained from a two-dimensional slice of the wake, with some qualitative insights into the three-dimensional nature of the wake obtained from the flow visualisation experiments. While these results have hinted at the unsteady and three-dimensional nature of the wake, more detailed insights into the unsteadiness

associated with the ground effect wake have mainly been provided by numerical and computational analyses of ground effect.

In addition to the numerous theoretical and computational models used to simulate ground effect hover, some models have also been created to simulate ground effect forward flight. These include free vortex/wake models, including those created by Saberi and Maisel [13], Lee and He [37] and Griffiths and Leishman [18]. A free wake analysis was also conducted by Sun [33], by only considering the rotor tip vortices, with the ground plane modelled using the method of images. These simulations were primarily conducted to investigate the location and strengths of the ground vortex. Results from these investigations suggested the ground vortex to possess a vortex strength at least three times that of the tip vortices shed by the rotor [33]. Additionally, it was contended that the formation of the ground effect wake features were similar to that presented in Figure 1.4, where a wake roll up, occurring far upstream was seen to form closer to the rotor disk as the flight speed was increased [33]. A mathematical analysis of the performance of a rotor in ground effect forward flight was conducted by Heyson using a nested-doublet distribution and an image rotor for the ground simulation. Results from this analysis showed ground effect to affect rotors lesser as the ground distance and forward flight speed increased, a result similar to those measured from experimental analyses of ground effect [38, 39].

A recently proposed computational fluid dynamics (CFD) tool by Moulton *et. al* makes use of the Reynolds Averaged Navier-Stokes (RANS) concept to predict the rotorwash velocities in the ground effect wake of a rotor [40]. Comparisons of the velocity predictions with flight test data showed good correlation, proving the success of this method. More recently, Brown and Whitehouse made use of the Vorticity Transport Model (VTM) together with a ground plane modelled with the method of images to predict the ground effect wake of a helicopter in hover and forward flight [25, 41]. The VTM showed good prediction of the rotor performance characteristics in ground effect and also identified the presence of vortical ring-like structures in the far wake of the rotor hovering in ground effect. Additionally, the VTM also predicted plumes of vorticity accumulating above the rotor hub, during the hover regime [25]. Mathematical modelling of ground effect, conducted by Conlisk *et. al*, predicted similar vortical structures in the hover ground effect wake

of rotors, with verification of the model showing good correlation to experimental performance data in hover. Resulting wake geometries in ground effect operations could also be predicted from these models [42, 43].

One important conclusion that can be drawn from this review of the literature available on rotors in ground effect is that, while numerous research have been conducted on the condition, most have focused on the resulting impact of these operations on the rotor performance. Information on the actual flow structures in the ground effect wake are still lacking, and this has affected the understanding of the evolution and unsteadiness of the wake, and the influence of the ground on the wider flow-field around the rotor. Limited information available in these areas make operational difficulties encountered in ground effect difficult to understand. An example of such a problem is the brownout phenomenon, described in the next section.

1.4.3 The Brownout Phenomenon

Ground effect operations of helicopters, while seen to provide performance benefits, have also in some instances been seen to hinder helicopter operations. This is specifically the case if the ground surface contains loose particles that can be entrained into the ground effect wake during flights close to the ground [44]. Operations in these scenarios have seen particle entrained wakes forming huge clouds of debris ahead of helicopters, often obscuring the pilot's view and causing disorientation. Normally affecting helicopter operations in desert terrains, this situation is commonly referred to as "brownout", although operations near sand, dry snow (whiteout in this case) and even water can result in this loss of situational awareness. Brownout is normally defined as the situation where pilots lose situational awareness because of debris clouds formed during ground effect operations in dusty conditions, and an example of this is shown in Figure 1.8. Brownout has been seen to affect most V/STOL aircraft, although some have been seen to cope with the situation better than others. With the mechanics and causes of this condition relatively unexplored, pilots have usually been left to deal with this problem using their experience and expertise. Brownout conditions have thus been known to have caused many mishaps leading to both the lost of lives and helicopters.

FIGURE 1.8: Sand and dust cloud below an MV-22, possibly in a landing manoeuvre (source: `www.defenseindustrydaily.com`)

Recent military reports approximate three out of four helicopter accidents in military operations in Iraq and Afghanistan to be a result of brownout [45]. Another source quotes brownout related accidents to have claimed 50 lives and the loss of more than 20 helicopters since 2001 [46]. Additionally, operations in brownout conditions, especially in arid terrain have been seen to cause extensive damage to exposed helicopter components such as engines and rotor blades, with sources quoting this to be a $100-million-a-year problem for the U.S. military [47].

The brownout condition may occur during landing, take-off, hover and low speed forward flight operations near erodible ground surfaces. Formation of the dust cloud occurs when the recirculatory wake associated with ground effect entrains the loose ground material. It has been contended that the intensity of the dust cloud is affected by the composition of the soil (particle size, shape, density and compactness), while the amount of dust uplifted from the ground is dependent on aerodynamic parameters such as disk-loading, number and arrangement of the main rotors [44].

Considerably few studies on the brownout phenomenon have been conducted and a majority of them have been focused on the general formation, location and spread of the dust cloud. While several numerical models have been proposed, most research on brownout has concentrated on the development of simulation tools for pilot training programs. Very little experimental study on the fluid dynamics of brownout are available, and those that have been done have been concentrated on

hovering helicopters. Quantitative flight data from brownout field studies using a H-21 tandem rotor helicopter was conducted by Rodgers in an attempt to quantify dust cloud concentrations around the helicopter in brownout [48]. Flight testing on different soil surfaces were conducted with results showing a dust distribution trend around the helicopter, with the greatest concentrations of dust seen to be located around the rotor overlap locations and between 1/3 - 2/3 radii ahead of the front rotor [48].

Where experimental brownout data is limited, greater attention to this phenomenon has been placed by the Computational Fluid Dynamics (CFD) community. Attempts have been made to correlate the brownout phenomenon with visualisations made from simulated ground effect [49]. Several mathematical models incorporated with dust/debris transport models have been developed in an attempt to re-create brownout conditions computationally. Most of these simulations adapt particle and dust transport models that have been developed in sedimentology studies to suit the dynamics and time frames of the clouds created by a rotorcraft's wake. Some of these simulation models worth mentioning include attempts made using time-averaged Navier-Stokes analysis to predict rotor outwash in the far wake of helicopters and the incorporation of particle entrainment models to simulate particle pick-up along the ground [50]. Work described by Leishman [44] and Keller *et. al* [51] incorporate a Lagrangian based dust transport model with a free wake model of ground effect. In these studies, a number of dust particles are modelled to represent the particles constituting the dust clouds. The dynamics of these particles are tracked as they are entrained into the wake, with the formation and properties of the resulting dust clouds inferred from these representative particles. Such models have been proven to be useful in allowing for better understanding of interactions of the wake with the surrounding ambient conditions and topologies, and some have been integrated with pilot training aids to expose pilots to brownout conditions [52].

Another branch of CFD based simulation of brownout is modelled in the Eulerian frame of reference. These studies concentrate on the modelling of the dust density distribution in the flow around the helicopter without considering the dynamics of the individual particulate matter. Mass and transport equations are used in the simulations to evaluate the dust cloud evolution in the vicinity of the helicopter.

Models developed by Ryerson *et. al* [50] and Phillips and Brown [53] adopt this Eulerian approach to brownout modelling. Both models employ a two phase transport equation to represent the behaviour of the fluid and the particles suspended within it. In Ryerson *et. al*, a transport equation, assuming the convection of particles with the fluid velocity and a particle fall-out model, incorporated to include gravitational effects on particles, is proposed [50]. Phillips and Brown propose a similar transport equation, with a particle entrainment model for a 'sub-layer' - the small region of fluid just above the ground, developed [53]. This entrainment model is based on a simple semi-empirical model that is based on the saltation process [54] described in wind and water erosion processes. This particle transport model is integrated with Brown's Vorticity Transport Model (VTM) [55] to simulate debris distributions within dust clouds during helicopter brownout operations.

Recent military operations in arid terrains have meant that solutions to the brownout phenomenon have been energetically pursued. Most solutions that have been thus far suggested relate to altering brownout operational conditions. Solutions of this nature include chemically treating soil to compact it, installing helipads and polymer matting at landing sites [56] and more famously, installing pilot cueing systems to help augment visual signals through dust clouds [57, 58]. While these remedies make brownout manageable, it is worth considering brownout from an aerodynamic perspective to identify the mechanisms at work during the formation of these dust clouds. While it is appreciated that a complete aerodynamic solution to this problem is unlikely and cannot be made without compromise to other performance capabilities of helicopters, some design modifications can possibly reduce problems associated with it. Evidence of some helicopters handling brownout better than others exists [44], and further justifies the need to understand the underlying ground effect physics behind the brownout phenomenon.

1.5 Research Motivation

While extensive experimental research into ground effect operations of rotors have been conducted, a review of the literature available have shown most to have concentrated on the effect of the ground on the performance of the rotor. This includes

research that was aimed at identifying alterations to helicopter handling and control in ground effect. While it was identified that the formation of the ground effect wake features played a crucial role in influencing the flow-field surrounding the rotor, little quantitative analyses of these wakes have been performed. Such detailed investigations mainly lack in areas associated with the unsteadiness and influence of the ground on the broad flow-field surrounding the rotor. Fluid flow interactions leading up to the formation of the ground effect wake have also attracted limited attention. Experimental investigations into the three-dimensional nature of the ground effect wake have also been seen to be severely lacking. Limited understanding of the ground effect wake have meant limited knowledge of the interactions and causes of flow-based operational difficulties encountered by helicopters in ground effect operations, such as the brownout condition.

Although some aspects of the ground effect wake have been substantially investigated, most of the experimental studies that have been conducted have underlying assumptions or limitations, which raise concern over the accuracy of the results. One major concern regarding experimental ground effect research has been the choice of conducting experiments in wind tunnels. Issues relating to the interference effects contributed by the wind tunnel walls particularly hinder ground effect experimentation. More importantly, the usage of a static ground plane during ground effect tests, especially in forward flight conditions, have raised concern over the accuracy of the derived experimental results. A review of the available literature has shown that with the exception of experiments conducted by Curtiss *et. al* [24, 27, 33], all other experimental testing of ground effect of rotors involve a stationary ground plane. While most of these studies acknowledge the importance and need of incorporating more accurate ground boundary conditions during testing, none have done so. As such, no information of the impact of the ground boundary conditions on experimental ground effect data is currently available.

Another limitation of the available experimental ground effect data is associated with the spatial resolution of the results. With the ground effect wake known to affect substantial portions of the flow-field around the rotor and possess a highly three-dimensional and unsteady nature, very little of the extended flow-field has actually been investigated experimentally. Similar limitations exist in terms of the knowledge of the cross-flow velocities affecting the wake. Most existing ground

effect data were obtained through probe based experimental techniques or qualitative experiments, limiting the spatial resolution of the data to specific points in the flow-field. Where more advanced, high spatial resolution techniques such as PIV have been used, the chosen regions of investigations have been limited to small regions particularly concentrating around the rotor disk leading edge.

These limitations in experimental ground effect data served as a motivation for this research. It was realised that availability of such data, obtained using high spatial resolution experimental techniques, would provide high quality flow-field data, useful for validating CFD codes and helpful in understanding the flow physics relating to ground effect. Based on this, quantitative investigations of wide regions of the ground effect wake of rotors in forward flight were conducted to identify effects of the ground on broad regions of flow around the rotor. Additionally, information such as the unsteadiness and cross-flow velocities associated with the flow-field were also derived from the results. More importantly, to investigate the effect of wind tunnel experimental testing on the ground effect wake, a wind tunnel facility fitted with a moving ground plane was chosen. This allowed for a comparison of data between experiments conducted in a "conventional" wind tunnel environment with a stationary ground, and in a tunnel which could better re-create ground conditions of ground effect operations in forward flight. Data comparison between the two cases will allow for the effect of the ground to be quantified. Together with this, the effect of rotor parameters such as trim, ground distance and blade root cut-out ratios were sought, to allow for a better quantitative insight of the ground effect flow-field.

To quantitatively investigate the ground effect flow-field, a suitable experimental technique had to be chosen. The most important factor that had to be considered in this process was the spatial resolution of the technique. As wide regions of the flow-field were to be investigated, it was also important to choose a technique that would allow for such measurements in a time-efficient manner. Based on this, Particle Image Velocimetry was chosen as the main experimental technique to be used for this research. Particle Image Velocimetry (PIV) is a mature, well developed experimental technique that can be used to measure three-dimensional velocity information from wide regions of a flow. Its non-invasive, instantaneous measurements of a flow allow for accurate measurements of unsteady flow and meant that

PIV was the most suitable technique to be used for the quantitative analysis of the ground effect wake. To allow for three-component velocity measurements of the ground effect flow-field, Stereoscopic Particle Image Velocimetry was used in this research. Fundamental concepts of the PIV experimental technique and details of the Stereoscopic PIV method are provided in Appendix A for the interested reader.

Chapter 2

Experimental Methodology

2.1 Introduction

Based on the objectives set out at the onset of the research, a series of experiments, aimed at gathering qualitative and quantitative information of the ground effect flow-field of a rotor in forward flight, was performed. These experiments were designed to study wide areas of the ground effect flow-field and to determine the significance of the ground boundary conditions on the fluid dynamics of the ground effect wake. The experiments conducted produced both qualitative images, visualising the influence of ground effect on the rotor flow-field, and three-dimensional velocity data from wide regions of the wake surrounding the rotor. Rotor trim conditions, rotor ground distances, collective angles, root cut-out ratios, flight speed (advance ratio) and ground configurations were varied during these experiments to determine their influence on the resulting rotor wake. The following sections of this chapter describe the various experiments that were conducted during the course of this research and provide details on the experimental facilities, rotor models, experimental techniques and apparatus used during each experiment.

2.2 Ground Effect Experimentation

Two different experimental techniques were used in this research to investigate the ground effect wake of rotors in forward flight. Flow visualisation techniques were first used to identify and visualise salient flow features in the ground effect

flow-field. In addition, the technique provided a simple way to simulate the fluid dynamics leading to the brownout phenomenon and visualise the dust transport mechanisms that lead to the formation of the brownout causing dust clouds. Quantitative measurements of the ground effect flow-field were performed using Particle Image Velocimetry (PIV). Most of the experiments conducted during this research made use of PIV, as this technique enabled the ground effect wake structures to be examined in great detail. All the experiments conducted during the course of this research have been divided into three sections in this chapter:

1. Flow Visualisation
2. Preliminary Ground Effect Flow Investigations
3. Ground Effect Experimentation with varying ground boundary conditions

Both the Flow Visualisation and Preliminary Ground Effect Investigations were conducted with a view of providing useful guidelines and experience for the main set of ground effect experiments that were to be conducted later. Results from these tests were used in the design of the rotor and set-up of the main PIV experiments.

2.3 Flow Visualisation of the ground effect wake of a rotor

Flow Visualisation is a qualitative experimental technique that can often be performed with relative ease to gain a basic idea about the general features in a flow-field. These experiments are frequently conducted as a prelude to further experimental measurements and provide a visual representation of the flow to be investigated. Such experiments may be simple to do and can be performed in any fluid medium, with the use of suitable seeding particles to make the fluid flow visible. With adequate illumination, the flow around the required experimental model can be visualised in a short period of time. Images recorded from these experiments can be used to identify salient flow features and establish general observations about the flow-field.

The flow visualisation experiments described herein provide qualitative information of the ground effect flow-field. These tests were also used to provide a representation of ground effect conditions that may lead to the brownout condition, and to identify the wake features resulting in the formation of the huge dust clouds observed during this phenomenon.

2.3.1 Wind Tunnel Facility

The flow visualisation experiments were conducted in the so-called Smoke Tunnel, a closed section, non-return type wind tunnel especially used for flow visualisation. The Smoke Tunnel has a 0.91m $\times$ 0.91m square, 4m long working section, with a settling chamber and 9:1 contraction at the upstream end and a fan at the downstream end of the working section. The maximum speed of the tunnel is some 2.5ms^{-1}. Flow visualisation is achieved by injecting smoke or some other seeding medium into the air flow at a desired location in the test section. Filters downstream of the fan remove the seeding medium from the air before discharge into the atmosphere. A suitably placed flood lamp, flash lamp or 5W, continuous wave (CW) laser are available to illuminate the desired portion of the flow-field for investigation. For ground effect testing in this tunnel, the rotor assembly used was simply placed on the floor of the tunnel.

2.3.2 Rotor Model

The physical size of the rotor models used for these ground effect tests was limited by the sizes of the wind tunnels used to conduct the experiments. Literature has suggested that for experimental testing of fixed wing models, the model-span-to-tunnel-width ratio should typically be between 0.3-0.5 to minimise wall constraint effects on the flow [59]. While this guideline applies to fixed wing models, very little information is available for rotor model testing in wind tunnels. Some literature suggest model-span-to-tunnel-width ratios lesser than 0.5 for OGE performance testing of rotor models, with the tests conducted at advance ratios in excess of 0.1 to ensure minimal wind tunnel effects [11]. Other literature have suggested fixed wing tunnel wall corrections to be applicable to rotor performance tests conducted at advance ratios above 0.1 [60], although questions have been raised regarding the validity of rotor data corrected using these methods [11]. As such, no exact

guidelines have been made available for rotor testing in wind tunnels with information even more limited for ground effect testing and wake related experiments. Beyond suggestions of using small rotors in large wind tunnels or open jet tunnels to minimise interference effects [11], and suggestions of using a ground board length in excess of 2.5 rotor diameters for ground effect testing [61], information to size rotor models for ground effect wind tunnel testing were largely unavailable.

With this research primarily concentrated on the investigation of the wake of a rotor in ground effect, the extent and size of the resultant wake generated by the rotor in ground effect during the tests had to be taken into account to ensure that the wind tunnel working section was long and wide enough for the wake to form without significant obstructions. Data from past ground effect experiments, mostly qualitatively derived, could not be used to clearly establish the spread of the wake during ground effect forward flight testing. Moreover, this was seen to be influenced by a range of rotor parameters [24]. A review of the model-span-to-tunnel-width ratios of rotor models used in past ground effect experiments showed the rotor model sizes to comply with the 0.3-0.5 model-span-to-tunnel-width ratio limits stated by Barlow *et. al* [59]. Wind tunnel experiments conducted by Boyd and Kusmarwanto made used of a rotor with a span-to-width ratio of 0.22 [28, 29], while Ganesh *et. al* made use of a rotor with a 0.43 span-to-width ratio for all their ground effect experiments [30–32].

Since very little guideline have been made available for rotor in ground effect experimental testing, it was decided that for the purposes of this research, a reasonably sized rotor model, capable of producing a clearly defined helical wake, similar to that produced by a helicopter, would be used. As in the case of past ground effect related experiments, the models used for this research will have a model-span-to-tunnel-width ratio of 0.3-0.5. Based on these, a $0.15m$ diameter rotor was used for the flow visualisation experiments. This model rotor has been successfully used for past vortex ring state (VRS) experiments conducted in a similarly sized wind tunnel [62] and has a model-span-to-tunnel-width ratio of 0.16. Based on readily available propellers designed for model aircraft, it produced a useful vortex wake that was representative of a helicopter rotor wake in that, it consisted of inter-twined, helical vortices. Although these propellers were highly

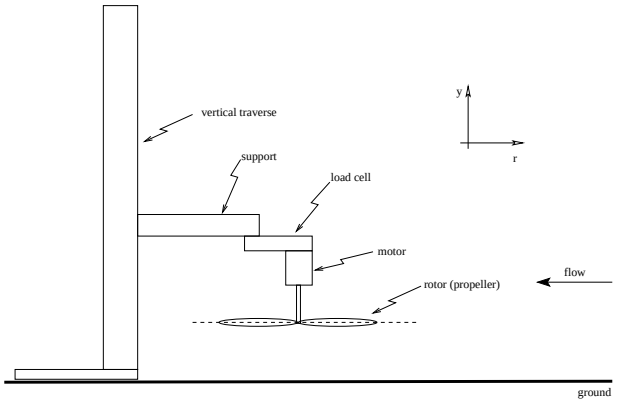

FIGURE 2.1: Schematic diagram of rotor system, motor, load-cell and vertical traverse. The sense of the (r, y) coordinate system is shown, but its origin is at the centre of the rotor.

twisted, some modern helicopter main rotors do have large amounts of twist.

The model propeller used for this rotor rig was manufactured by Graupner and had a diameter of $148mm$. These propellers have a $15mm$ diameter hub, a root chord of $10.5mm$, a square-cut tip with a chord of $8mm$, and a maximum chord of $14.6mm$ at around the 50% outboard position, where the thickness ratio was measured to be 16.4%. It is not clear what aerofoil section(s) are used for these propellers, although they are cambered, and had a twist of about 10^o. The propellers were fixed onto the shaft of a small electric motor capable of spinning the rotor at a rate of 120Hz ($7200RPM$) (speed controlled simply by increasing the supply voltage). The rotor speed was monitored using a Unilux Highlighter Stroboscope, and the thrust was measured by mounting the motor on a $0.6kg$ load-cell. This assembly was fixed to the end of a long sting, attached to a hand-cranked vertical traverse unit, which was placed on the floor of the wind tunnel so that the rotor disk was nominally in the horizontal plane with the motor above the disk. The rotor had a fixed pitch of $75mm$ with no pitch adjustments possible. The rotor hub was rigid and no blade flapping degree-of-freedom was present, therefore all the tests performed using this model were for an untrimmed rotor state. A schematic of the rotor model is shown in Figure 2.1. This rotor system will be referred to as Rotor A for simplicity, and a summary of the important rotor dimensions are given in Table 2.1.

Rotor A	**Dimensions**
Blades	2
Rotor radius	$75mm$
Pitch	$75mm$
Twist	10^o
Hub diameter	$15mm$
Blade tip	Square-cut tip
Root Chord	$10.5mm$
Tip Chord	$8mm$
Max Chord	$14.6mm$ at 50% outboard of root
Max Thickness Ratio	16.4% at 50% outboard of root

TABLE 2.1: Rotor A Dimensions

2.3.3 Flow Visualisation of the brownout phenomenon

During the brownout phenomenon, debris on the ground is picked up by the ground effect wake to form a dust cloud ahead of the helicopter. To reflect this, a suitable seeding medium was required to simulate the properties of the ground dust. Talcum powder was chosen as the seeding medium for these brownout flow visualisation tests conducted, because of its ability to readily represent 'dust' along the ground. Additionally, the talcum powder particles provided the flow-field images with good contrast, allowing the evolution of the ground effect flow-field to be better illustrated. These reasons, including issues relating to safety of both the wind tunnel and experimentalists, made this choice of seeding the most appropriate. The talcum powder used during the tests was Body Powder Talc and conforms to the U.S. Food and Drug Administrations (FDA) regulations, who limit the sizes of the talc particles used in cosmetic body powders between a range of $8\mu m - 12\mu m$ [63].

The seeding particles were introduced into the flow by simply spreading the talcum powder along the floor of the wind tunnel, just below and ahead of the rotor. This ensured that the rotor wake could pick up the particles from the ground as the wake trailed along it. At the rotor speed and wind tunnel speed settings used, it was observed that the talcum powder was lifted off the ground by only the action of the rotor induced flow. The wind tunnel speed alone could not achieve this;

and this was important given that the forward flight of the rotor was simulated by the wind tunnel flow. Before the start of each test, the talcum powder was replenished so as to ensure that the particles could easily be picked up by the flow. As the talcum powder layer on the ground depleted during the course of the experiment, it was essential that the camera photography was done as soon as possible after the rotor was switched on, subject to the decay of the start-up transient.

The major difficulty with the flow visualisation was brought about by the high rotational speeds of the rotor and consequently the high frequency of passage of the trailed vortices over the ground; while still photographs or standard video rates are useful, time-resolved video using a high speed camera would allow more information from the flow visualisation to be gained. This was recognised, and a Mikrotron MotionBlitz high-speed digital video camera was used for these experiments. This camera was capable of recording at a frame rate of 500Hz at a full-frame resolution of 1k $\times$ 1k pixels, and was fitted with a range of Nikon lenses to suit the field-of-view and the amount of illumination available. Illumination for this investigation was provided by a Laser Quantum Elite-532 $5W$ continuous wave (CW) laser, with a wavelength of $532nm$. The laser beam was expanded into a light sheet of approximately $2mm$ thickness, and was aligned to illuminate a plane along the longitudinal axis of the rotor, along the symmetry plane of the flow. The brownout visualisations were conducted at flight speeds corresponding to normalised advanced ratios of $\mu^* = 0.37$ and $\mu^* = 0.65$, at rotor ground distances of half (0.5R) and one (1.0R) radius. The rotor was operated at a rotational speed of $94Hz$ ($5640RPM$) with the rotor thrust coefficient, C_T, held constant at $C_T = 0.015$ for all the tests. The normalised advance ratio (μ^*) values that were required during the tests were obtained by varying the wind tunnel freestream velocity. The wind tunnel speed was measured using a pitot-static probe placed at the tunnel working section entry, and this ensured that the rotor operation did not have any effect on the wind tunnel calibration. A summary of the different tests conducted for flow visualisation of the brownout phenomenon is shown in Table 2.2.

2.4 Preliminary ground effect flow investigations

Preliminary ground effect flow investigations were conducted using a home-built PIV system. These experiments were conducted using the same rotor model used in the Flow Visualisation tests discussed in Section 2.3.2. Quantitative analysis of the wake of the rotor in ground effect forward flight was conducted using two-dimensional two-component (2D2C) digital PIV. 2D2C PIV allows for the measurement of the *(u,v)* velocity components from a two-dimensional slice of the flow-field. These experiments allowed for the flow associated with Rotor A to be quantified and provided a useful insight into the ground effect flow-field.

2.4.1 Wind Tunnel Facility for preliminary flow investigations

The wind tunnel used for these PIV measurements was the so-called Anatomy Wind tunnel, another small scale wind tunnel owned by the University of Glasgow. The tunnel has a 1.15m $\times$ 0.85m octagonal working section, with a contraction ratio of 9:1 and a turbulence level of 0.3%. It is a closed return tunnel, capable of a top speed of some 30ms^{-1}. For ground effect testing, a raised ground board had to be placed into the wind tunnel working section due to its limited optical access. This allowed for the PIV cameras to be set level with the ground plane to capture the wake as close to the ground plane as possible.

2.4.2 Rotor Model

The rotor model used for the preliminary PIV investigations was the same as that used during the flow visualisation experiments. With both the Smoke and Anatomy tunnels having similar cross-sectional dimensions, their wake constraints (model-span-to-tunnel-width ratios) were similar. Measured to be 0.13 for the Anatomy tunnel, this was significantly lower than the requirements stated by Barlow *et. al* [59], an ensured minimal wind tunnel blockage effects on the development of the ground effect wake.

To test the effect of rotor blade root cut-out on the rotor wake in ground effect, cut-outs were made at the roots of the propellers used in Rotor A. For this analysis, an identical propeller to Rotor A was used, with a 40% span cut-out made at the root. This propeller was used only for the PIV experiments, to identify any differences in the wake influenced by the root cut-outs. A variety of ground distances, $\frac{h}{R} = 0.5, 1.0, 1.5$ and 2.0, were tested for a range of normalised advance ratios between $0.3 < \mu^{\star} < 1.3$. As in the case of the flow visualisation tests, all the PIV testing done using this rotor model was for an untrimmed rotor state, as this rotor had no pitch, lead-lag or flapping degrees-of-freedom. For each ground distance, the rotor was operated with a constant thrust coefficient of $C_T \approx 0.015$ for Rotor A (and $C_T \approx 0.013$ for Rotor A with the blade root cut-out) , with the rotor power allowed to vary according to the influence of the ground. The normalised advance ratio for the various test cases were achieved by maintaining the rotational speed of the rotor at $94Hz$ ($5640RPM$) and varying the wind tunnel freestream velocity accordingly. A pitot-static probe placed at the entry of the tunnel working section was used to measure the freestream speed, and this ensured that the rotor operation did not affect the calibration of the wind tunnel. Details of the tests conducted at the different ground distances and normalised advance ratios are summarised in Table 2.2.

2.4.3 Rotor in ground effect experiments using PIV

Particle Image Velocimetry (PIV) is an optical experimental technique used to quantitatively measure fluid flows. It utilises light reflecting properties of tracer particles suspended in a fluid to measure its velocity. This methods relies on the fundamental assumption that the tracer particles suspended in the flow faithfully follows the fluid motion. In this technique, tracer particles of nominal diameters between $1 - 2\mu m$ are used to seed the flow. A powerful light source, usually a pulsed laser, is used to illuminate the required region of interest of the flow-field. The laser beam is normally expanded into a thin light sheet of $2 - 3mm$ thickness, and the laser is pulsed to produce short, powerful bursts of light. In the case of two-dimensional two-component (2D2C) PIV, the method employed for this preliminary investigation of the ground effect flow-field, an imaging system is placed normal to the flow region of interest. Two successive images of the particle seeded flow-field, separated by a known time delay, referred to as the inter-pulse time

delay, Δt, is recorded. Particle displacements between the two recorded images are derived through correlation analysis. Images recorded during the PIV are sub-divided into smaller interrogation areas, and corresponding interrogation areas are usually cross-correlated to derive the particle pixel displacement information. A calibration of the PIV system is done to relate the pixel and physical coordinates of the flow-field and provide transfer functions necessary to convert the derived pixel displacements to physical particle displacements. With the inter-pulse time delay known, the velocity of the flow-field is then derived from the images. (*A more detailed description of the principles of PIV can be obtained from Appendix A*).

The home-built PIV system used for these ground effect tests has been employed in a range of rotor flow tests in the past [62, 64, 65]. It is based on a Spectra-Physics Lab130-10 Nd:YAG single cavity, double pulsed, frequency doubled laser, with a wavelength of $532nm$, operating at a repetition rate of $10Hz$. The laser was Q-switched, to produce short, high energy laser pulses [66], with pulse duration of $8ns$. The laser beam was expanded into a light sheet that was aligned with the symmetry plane of the rotor, along the wind tunnel longitudinal axis. Different regions of the flow, upstream of the rotor hub were investigated by traversing the light sheet along this plane. For the 2D2C PIV, a Kodak MegaPlus ES1.0 digital video camera, with a 1008×1018 pixel CCD chip, fitted with a 50mm focal length Nikon lens set to f-number, $f_{\#} = 2.4$, was used to capture images of the flow. The camera has a 9 micron pixel size and a bit-depth of 8. The camera was placed normal to the object plane illuminated by the laser light sheet of approximately $2mm$ thickness. Seeding was produced using a Concept Systems ViCount Smoke Generator that heats smoke oil to produce a fine oil mist; the manufacturer claims a nominal smoke particle diameter of 0.2μm. Image capture was done using a National Instrument (NI) PCI-1424 digital frame grabber operated using LABVIEW. The laser, camera control and image capture systems were all synchronised using a NI PCI-TI0-10 counter timer card and controlled by a single computer.

A photograph of the experimental set-up of the 2D2C PIV is shown in Figure 2.2 (a). Its corresponding schematic, in Figure 2.2 (b), better illustrates the set-up and shows the positions of the laser light sheet, the rotor and the camera with respect to one another. For this PIV set-up, two regions of the flow-field were

(a) Experimental Set-up in wind tunnel

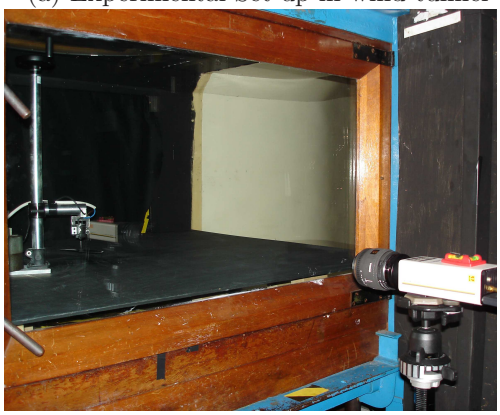

(b)Schematic of Experimental Set-up

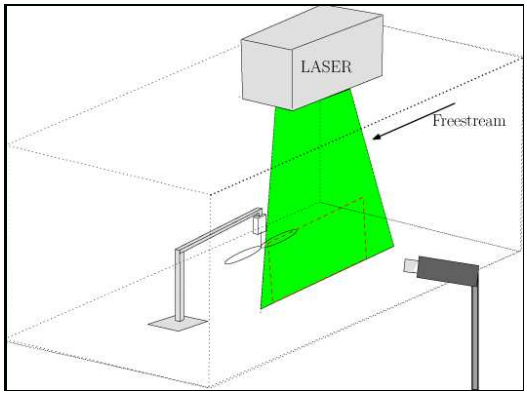

(c) ROI just ahead of the rotor hub

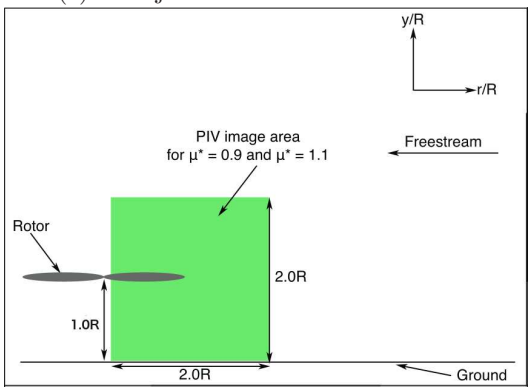

(d) ROI ahead of the rotor disk L.E

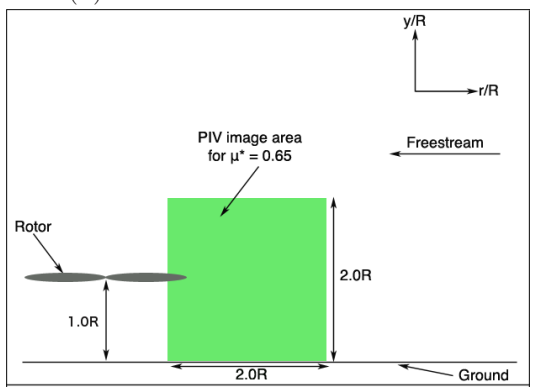

FIGURE 2.2: 2D2C PIV set-up for preliminary investigation of the ground effect flow-field. Frame (a) shows the experimental set-up, with Frame (b) showing the plane of illumination of the light sheet. Frames (c) and (d) show the regions considered for the 2D2C PIV using the Kodak MegaPlus ES1.0 digital video camera.

primarily of interest. Figure 2.2 (c) and Figure 2.2 (d) illustrate these regions of interests (ROI), with the first concentrating on a region under the rotor disk, ahead of the rotor hub, and the latter figure illustrating the region of interest ahead of the leading edge (L.E) of the rotor disk. These areas of the flow-field were considered due to evidence from literature suggesting the presence of most of the ground effect flow features in these areas [27]. The plots also indicate the range of normalised advance ratios tested at each camera view and this was determined during the course of the experiments. The optical arrangement for both the PIV set-ups, allowed for a 15cm $\times$ 15cm square field-of-view of the flow to be recorded. Scaled in terms of the rotor radius, this amounts to a two radii (one diameter) square field-of-view. Spatial resolution of the measurements are usually dictated by the field-of-view, and for the current experimental set-up, the effective measurement area per point was around 0.036R $\times$ 0.036R.

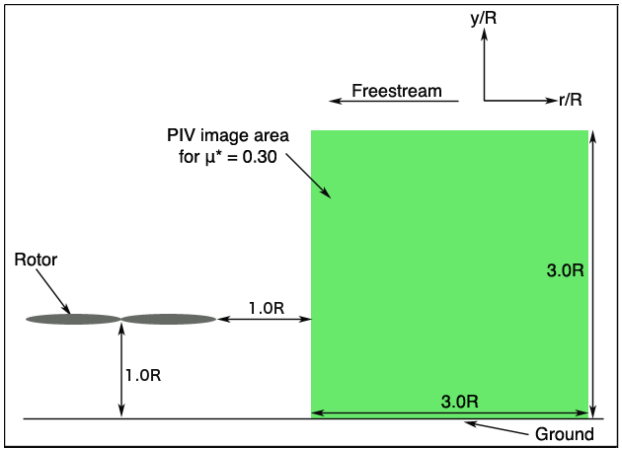

FIGURE 2.3: 2D2C PIV region of interest using the Redlake MegaPlus MP4 camera. A larger field-of-view was obtained from this camera.

In cases where the ground effect wake was seen to extend further upstream than one rotor diameter, a higher resolution Redlake MegaPlus MP4 digital video camera, with a 2048 × 2048 pixel CCD chip, was used. This camera has a 7.2 micron pixel size and a bit-depth of 10. It allowed for wider fields-of-view to be captured with no compromise to the resolution of the velocity vector maps derived from the images. For these tests, the effective measurement area per point was around 0.044R × 0.044R. This camera was used especially for the lower normalised advance ratio cases, where the wake was seen to spread upstream, far ahead of the rotor. Figure 2.3 illustrates the region of the flow-field investigated with the higher resolution Redlake MegaPlus MP4 camera, with the experimental set-up similar to that shown in Figure 2.2 (a) and (b). The camera was fitted with a $50mm$ Nikon lens set to $f_{\#} = 2.4$ and was used to image a three radii square field-of-view of the ground effect flow-field. Image capture in this case was done using a National Instruments (NI) PXI-1033 chassis, housing a camera link NI PXI-1428 digital frame grabber and a NI PXI-6602 counter timer unit. A NI TB-2715 Terminal Block was integrated with the counter timer unit to allow synchronisation of the laser, camera controls and imaging system. This system was connected via a PCIe interface card to a PC, where LABVIEW was used to control the camera and laser systems. A Concept Systems ViCount Smoke Generator was again used to create the tracer particles used to seed the flow.

Double frame, double exposure PIV was used to record images of the flow-field, where two images, separated by a known inter-pulse time delay, Δt, are taken.

For each test case, 300 image pairs were recorded, with the laser inter-pulse time delay set at $\Delta t = 90\mu s$. Analysis of the images, by successive cross-correlation and Lagrangian tile-shifting algorithms were conducted and produced high-resolution velocity vector maps [64].

Rotor	**Ground boundary condition**	**Trim**	**Ground distance**	**Wind tunnel**	**Measurements**	C_T	μ^*
A	stationary	Untrimmed	1R & 0.5R	Smoke Tunnel	Flow Visualisations (brownout)	0.015	0.37 & 0.65 (max)
A	stationary	Untrimmed	2R, 1.5R, 1R & 0.5R	Anatomy Tunnel	2D2C PIV	0.015	0.3 - 1.3
A (Root cut-out)	stationary	Untrimmed	2R, 1.5R, 1R & 0.5R	Anatomy Tunnel	2D2C PIV	0.013	0.3 - 1.3
Large	stationary & moving	Untrimmed & Quasi-Trimmed	1R & 2R	Argyll Tunnel	2D2C PIV	0.010 & 0.015	0.3 - 1.0
Large	stationary & moving	Untrimmed & Quasi-Trimmed	1R & 2R	Argyll Tunnel	Stereo PIV	0.010 & 0.015	0.3 - 1.0
Small	stationary & moving	Untrimmed	1R	Argyll Tunnel	2D2C PIV	0.010	0.3 - 1.0

TABLE 2.2: Summary of Ground Effect Experiments

2.5 Ground effect experimentation with varying ground boundary conditions

A major aim of this research was to investigate the influence and importance of ground boundary conditions on the wake produced by a rotor in ground effect. A wind tunnel fitted with a rolling road was used to vary the ground boundary conditions during these tests. To investigate the effect of the rotor on the ground effect wake, the states of the rotor had to be controllable. Using data and set-up experiences gained from the preliminary tests, a suitable rotor model was manufactured.

PIV was the experimental method used in these tests to obtain three-dimensional flow data for wide areas of the ground effect wake. The tests were done for a range of ground distances, rotor trim conditions, normalised advance ratios and ground boundary conditions. The following subsections provide details of the wind tunnel facility, rotor models and experimental equipment used to conduct these experiments.

2.5.1 Wind Tunnel and Rolling Road Facility

The wind tunnel used for these experiments is the so-called Argyll wind tunnel. It is a closed return tunnel with an octagonal cross-sectional working section, measured to have a width of $2.7m$ and a height of $2.0m$, and a maximum flow velocity of some $72ms^{-1}$. A rolling road, of $1.9m$ width and a length of $3.9m$ makes up the floor of the working section, with the rolling road belt having a width of $1.63m$. The rolling road is claimed to reach speeds comparable to the speeds of the tunnel, although the tunnel can be used independently from the rolling road as required. A diagrammatic representation of the wind tunnel working section and the rolling road is shown in Figure 2.4.

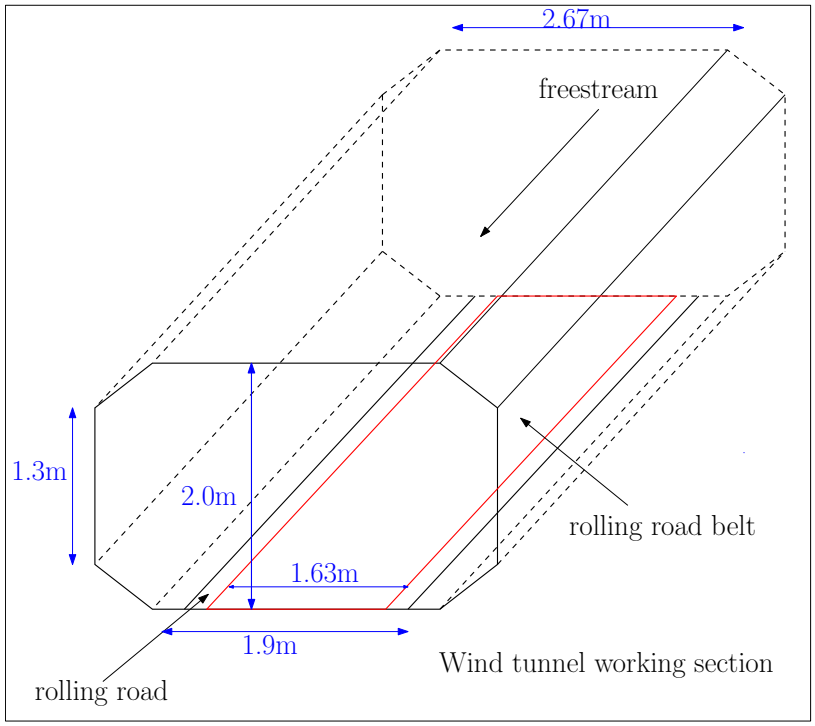

FIGURE 2.4: Cross-section of the working section of the Argyll Wind Tunnel and rolling road.

2.5.2 Rotor Rig

2.5.2.1 Requirements and Constraints

A suitable rotor model had to be manufactured for these experiments to meet the objectives of this research. The rig had to be designed to satisfy the research objectives, while complying to the constraints imposed by the experimental facility. Factors such as the interference effects of the wind tunnel walls on the rotor wake, the spread of the rotor ground effect wake, and set-up difficulties had to be considered during the design process.

A fully controllable rotor model had to be manufactured to ensure that identical rotor configurations could be maintained during investigations of the ground effect wake. This was particularly important when comparisons were made with other ground effect data or different tests cases. Previous research have also identified rotor trim to have an effect on the symmetry of the ground interaction boundary [29] and affect the inflow through the rotor disk [23]. In addition to this, the designed rotor model also had to be able to operate in an untrimmed configuration

to allow for data verification and comparisons between results derived from fixed pitch rotor models. This thus meant that the rotor model had to be designed to allow for blade pitch adjustments. Incorporating a pitching mechanism which will allow for collective and cyclic adjustments of the blade pitch angles during rotor operations, will ensure that the trim status of the rotor model is easily controlled.

To facilitate testing at different ground distances, an appropriate mechanism allowing for rotor height adjustments above the ground plane also had to be designed. The rig also had to be designed to be compact, while housing all the required instrumentation that would be used to define the rotor state. This would ensure minimal interference from the rotor on the developing ground effect wake.

Investigations of the ground boundary effect on the rotor wake meant that the Argyll wind tunnel, with its rolling road facility would be used to vary the ground boundary conditions. A suitable mounting mechanism for the rotor had to be additionally considered to ensure that the rolling road could be operated without obstruction from the rotor.

The rotor model also had to be sized appropriately based on the physical dimensions of the wind tunnel. Factors such as wall constraints and wake blockage had to be considered to ensure that the developing wake from the rotor model was unaffected. For the PIV, camera access locations and the moving ground conditions also had to be considered to ensure that the experiments are conducted efficiently and valid data from the flow-field is obtained.

2.5.2.2 Rotor Sizing

Initial rotor sizing to determine the amount of power required to operate the rotor was performed before detailed design of the rig was considered. Basic design parameters, such as the rotor hub design, number of rotor blades and disk diameter had to be considered before a power estimate could be derived. Initial design considerations favoured the use of a teetering rotor hub for the rig due to its simplicity of design and ease of manufacture. Although a teetering hub would have also simplified the trimming process, the need to be able to control the rotor trim

status meant that pitch adjustment capabilities needed to be implemented with the teetering hub. This would also have required the implementation of fly-bars with the teetering hub [67]. Since this would have further complicated the aerodynamics of the rotor wake, this idea was abandoned for a rigid hub with direct cyclic control inputs.

A four-bladed rotor design was identified instead with the rotor hub controlled by a conventional swashplate. Based on this four-bladed rotor, the power required for operation was estimated using momentum theory calculations [11]. Calculations for a range of rotational speeds and rotor diameters (considering the size limitations of the wind tunnel) were performed to estimate the power required for a range of flight speeds. Results from these calculations were used to identify a suitable motor unit to power the rotor rig. A diameter of $1.0m$ was selected for the rotor rig, and mean that the model-span-to-tunnel-width ratio (based on the Argyll Wind tunnel dimensions) would be 0.37. Although this was within the range stated by Barlow *et. al* [59], a smaller rotor diameter could have been used to ensure minimal wall effects on the wake. This choice of rotor diameter was made primarily to obtain better definition of the ground effect wake features and the tip vortex cores structures with the cameras available with the PIV system. The dimension of the rotor model was also influenced by the need to build a rig capable of withstanding high loading and vibrations expected to be experienced by the model during the testing. With the lateral spread of the ground effect wake at different normalised advance ratios measured during the preliminary brownout flow visualisation tests, it was identified that the wake produced by this rotor may be subjected to interference effects from the wind tunnel walls. To identify any effects of the wind tunnel walls on the wake structures, data obtained from this rotor model was verified with PIV results from tests performed using a smaller rotor model installed and tested in the same wind tunnel. (Refer to section 2.5.2.7).

2.5.2.3 Rotor design

Design of the rotor model was based on components used in radio-controlled helicopter models. Main rotor components of helicopter models, such as the swashplate, rotor hub and blades were utilised in the construction of the rotor rig as these

would have been complex, costly and time-consuming to manufacture. Commercial availability also meant that these parts could readily be replaceable if damaged during experimental testing.

Schematics of the designed rotor rig are shown in Figures 2.5 - 2.7. The rotor hub, shaft, swashplate, swashplate driver and rotor blades used for this model were sourced from Vario Helicopter[1]. The rotor hub is rigid, capable of pitch alterations, with no lead-lag and flapping degrees-of-freedom. Blade flapping, due to the flexibility of the rotor blades was observed to result in a flap/cyclic phase lag close to 90^o. An aluminium swashplate is connected to the rotor hub via pitch linkages, and the rotor shaft is a circular steel shaft of $10mm$ diameter. A swashplate driver, connected to the inner ring of the swashplate and attached to the shaft was used to ensure that the blade cyclic pitch angles varied correctly around the azimuth. A Panasonic A-series (MSMA - 082A1C) servo motor and controller unit, capable of $750W$ power and a rated speed of $3000RPM$, were used to drive the rotor through a pulley and belt system, that connected the motor shaft to the rotor shaft (Figure 2.5). A belt-drive was chosen for the rig to isolate the motor vibrations from the rotor system. Load-cells, used to measure the thrust produced by this rotor system, was attached under the base plate of the rotor.

The rotor pitching mechanism is based on the concept used in the Thunder Tiger Raptor 60 radio-controlled helicopter model [68]. Components of this are shown in Figures 2.5 and 2.6. The pitching mechanism consists of a top plate, rocker arm and two RS-42DBL10 series digital linear actuators (stepper motors), capable of withstanding $100N$ of load. Both the rocker arm and the stepper motors sit on the top plate and are connected to the swashplate via connecting arms (see Figure 2.6) . A displacement transducer was connected to each stepper motor to measure the cyclic pitch inputs transmitted to the rotor blades during rotor operations. This set-up allows for automatic cyclic pitch control of the blades during rotor operation, but only manual adjustments for collective blade pitch angles. Automatic collective blade pitch angle alteration was considered unnecessary to incorporate in the model as it would contribute to additional complexity and bulk of the overall system.

[1]Vario Helicopter UK Sales, 229 Church Lane, Lowton, Warrington, Cheshire WA3 2RZ

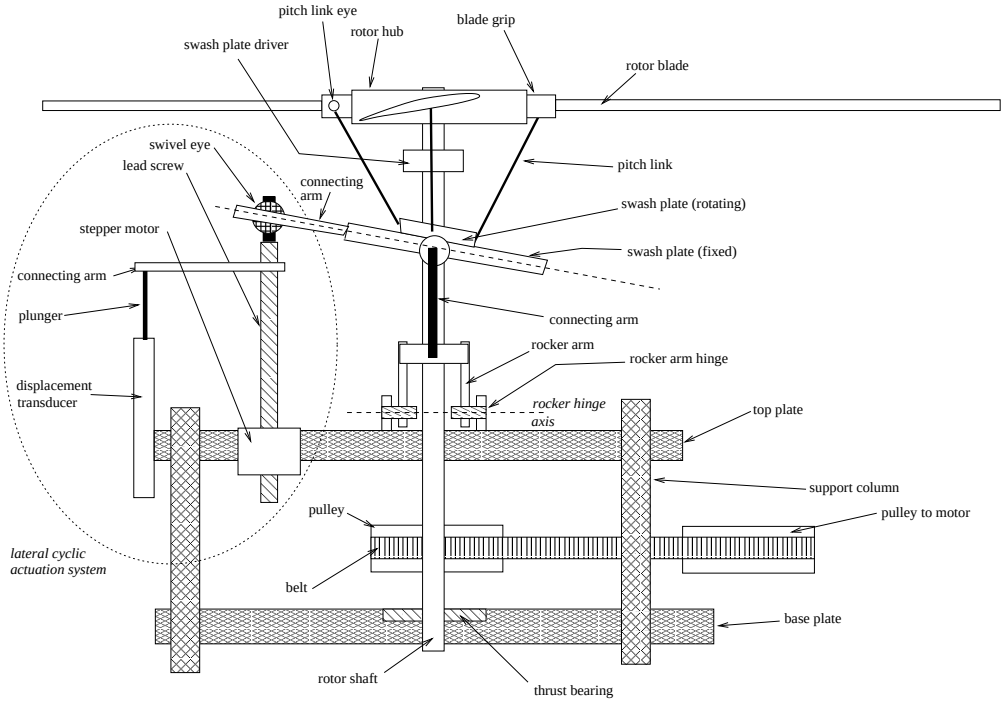

FIGURE 2.5: Schematic of designed rotor rig - SideView

Manual adjustments of the blade collective angles (θ_0), can be made by adjusting the height of the top plate, seen in Figure 2.5, along the support columns. As the top plate is adjusted, the rocker arm and stepper motors, attached to the top plate, move together with it, adjusting the height of the swashplate along the rotor shaft accordingly. This swashplate height adjustment is in-turn transmitted to the rotor hub via the pitch linkages, connecting the swashplate and rotor blades. This process could have been automated by simply including an additional stepper motor to adjust the height of the top-plate, although manual adjustment was maintained to keep the rotor design simple and compact.

Blade cyclic angles are implemented by the lateral and longitudinal cyclic actuation systems shown in Figures 2.5 and 2.6, respectively. Both the actuators work independently of one another, with a voltage change raising or lowering the stepper motor lead screw. For the lateral cyclic actuation system, shown in Figure 2.5, a stepper motor actuation alters the height of the lead screw. The swivel eye, holding the connecting arm, moves accordingly, tilting the swashplate along the longitudinal cyclic swivel axis, as shown in the figure. This is transmitted to the rotor hub and results in a change in the lateral cyclic blade pitch angles, θ_{1c}. The longitudinal cyclic actuation system is shown in Figure 2.6. The presence of

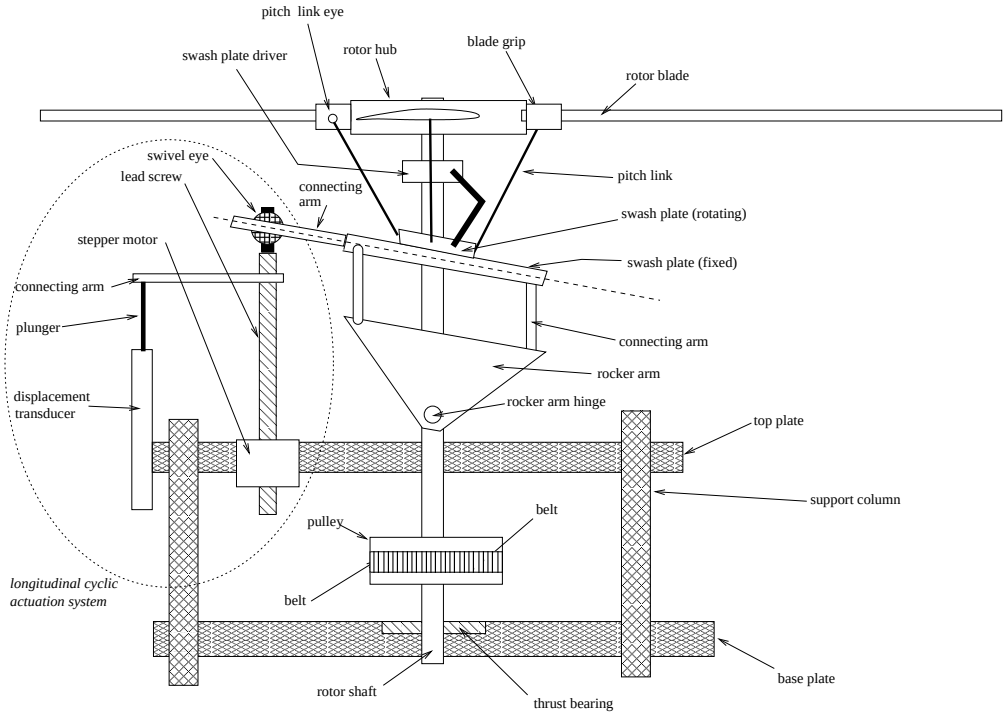

FIGURE 2.6: Schematic of designed rotor rig - Front View

the lateral cyclic pitch mechanism ahead of the rocker arm is omitted from this figure to illustrate the longitudinal cyclic actuation mechanism. As in the case of the lateral cyclic actuation system, an actuation of the longitudinal cyclic stepper motor alters the height of the swivel eye on the lead screw. This in-turn alters the tilt of the swashplate along the lateral cyclic swivel axis. The rocker arm, connected to the same end of the swashplate rotates about its hinge, according to the orientation of the swashplate. The rocker arm also helps hold the orientation of the swashplate to ensure that the cyclic inputs are maintained around the rotor azimuth. This lateral tilt in swashplate is transmitted to the rotor blades via the pitch links and results in a change in the longitudinal cyclic blade pitch angles, θ_{1s}.

Locations of the different rotor components and cyclic pitch actuation assemblies with respect to the rotor hub are illustrated in Figure 2.7. The top view of the rotor system presented in this figure also shows the rotor model having an anti-clockwise rotation. The rotor blades used for this model are reflex cambered, with a span of $675mm$ and a blade chord of $53mm$. Since suitable sized blades could not be purchased, and would have been costly to manufacture, these blades were eventually cut down to the $1.0m$ diameter required for the rig. The blades, made of glass reinforced plastic, have a profile thickness of $6.8mm$. The blade aerofoil

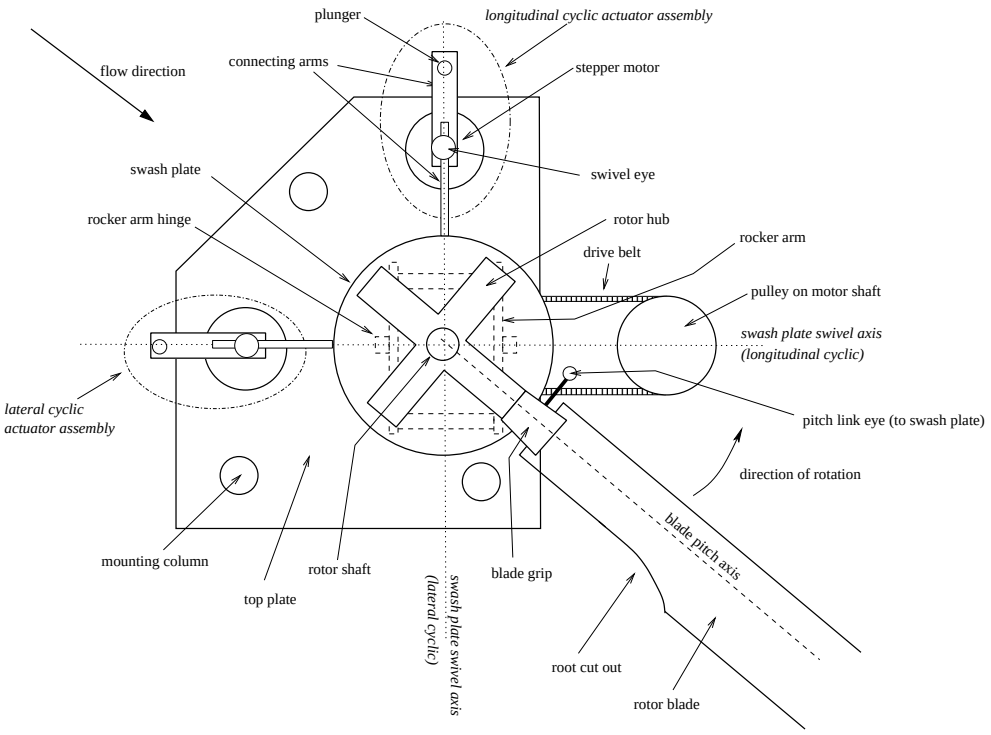

FIGURE 2.7: Schematic of designed rotor rig - Top View

Large Rotor	**Dimensions**
Blades	4
Rotor radius	$500mm$
Pitch	Collective and Cyclic Variable
Blade tip	Square-cut tip
Blade Chord	$53mm$
Root Cut-out Radius	$15cm$
Max Thickness Ratio	12% at 50% outboard of root ($6.8mm$)

TABLE 2.3: Large Rotor Dimensions

section is thought to be a NACA - 2412 section [69], although this is not confirmed by the manufacturer. A summary of the rotor model is given in Table 2.3 and for simplicity, this rotor is referred to as the Large Rotor throughout the rest of this dissertation.

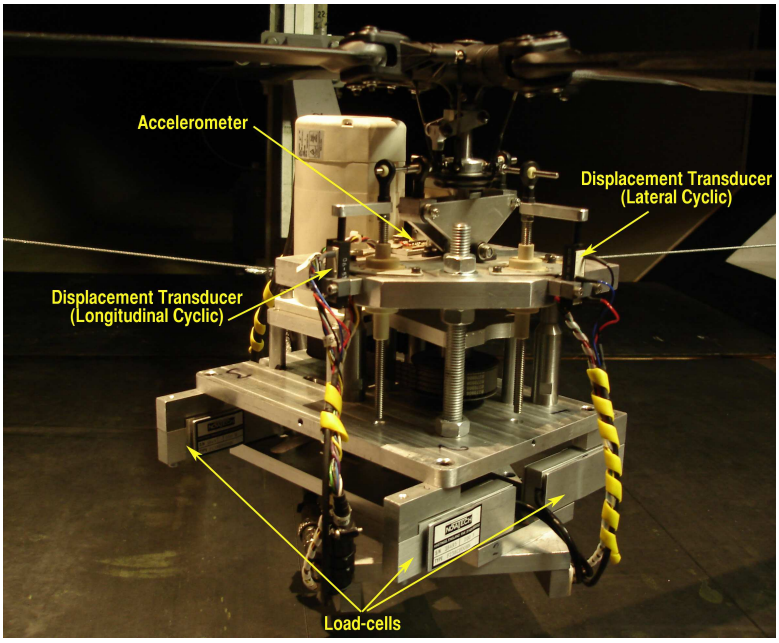

FIGURE 2.8: Instrumentation on the rotor rig

2.5.2.4 Rotor Instrumentation

Figure 2.8 shows a photograph of the manufactured rotor rig. All the different components of the rotor model can be seen in the picture, which also highlights the instrumentation installed on the rig, used to quantify the rotor status during the experiments.

Cyclic blade pitch angle inputs applied by the stepper motors to the rotor blades were measured by two Bei Duncan Electronics 9600 Series displacement transducers. These displacement transducers were attached to the lead screws of the stepper motors via connecting arms (details of which are presented in Figure 2.5) and recorded a change in voltage for a change in the height of the lead screw (blade cyclic pitch). Together with these transducers, the height of the top plate with respect to the base plate was calibrated to quantify the collective and cyclic pitch input to the rotor blades. Calibration curves of the displacement transducers and the top plate can be found in Appendix B, with the calibration done to a precision of $\pm 0.3^o$.

Thrust from the rotor was measured using four Novatech F238 load-cells, capable of measuring loads up to $100N$. The load-cells were attached at the corners of

the base plate of the rotor system, as seen from Figure 2.8. While these load-cells were used to measure the vertical forces acting on the rotor system, they could still transmit horizontal forces. The total thrust produced by the rotor rig was obtained by a simple addition of the vertical forces measured by each individual load-cell. With the distance between the positions of the load-cells known, trimming of the rotor was accomplished by calculating the pitching and rolling moments associated with the vertical forces measured by each load-cell, with reference to the position of the rotor hub.

Signals from the displacement transducers, load-cells (connected to load-cell amplifiers) and motor system were monitored through a National Instruments NI-USB-6229 DAQ (Data Acquisition) box and a computer. A LABVIEW program running on the computer was used to calculate the rotor thrust and cyclic blade pitch angles set during the experiments. Speed, power and torque information measured by the motor controller unit were also displayed to provide a comprehensive idea of the state of the rotor during the testing. The LABVIEW program also provided a live display of the location of the vertical thrust centroid of the rotor system, calculated from the vertical force information provided by the load-cells. The display was used to show the location of the vertical centroid with respect to the rotor hub and was used to trim the rotor. For experiments where a trimmed rotor configuration was required, the longitudinal and lateral cyclic angles were adjusted manually to an accuracy of $\pm 0.5cm$, to align the vertical force centroid of the system with the rotor hub, such that the moments associated with the vertical forces about the rotor hub, were zero. With only the vertical forces and moments considered in this process, the Large Rotor only maintained a quasi-trim state in these experiments. (*Further details are provided in Section 5.1.2.*) For the untrimmed rotor state, both the lateral and longitudinal cyclic blade pitch angles were set to zero, with an accuracy of $\pm 0.01^o$.

2.5.2.5 Installation in the Argyll Wind Tunnel

The rotor model was installed in the Argyll Wind Tunnel using an existing sting support system, originally designed for a different research project [70]. This sting was modified by including an additional support arm on which the rotor rig was attached, and is shown in Figure 2.9. This sting support had an added advantage

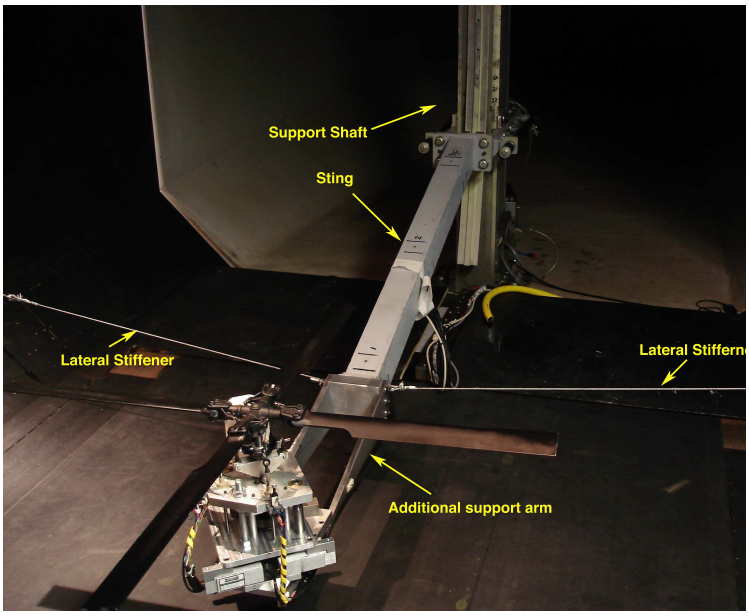

FIGURE 2.9: Wind Tunnel installation of the Large Rotor

of being attached to the support shaft by rollers, which allowed for the height of the rotor rig to be altered easily. The different rotor ground distances that were required during the ground effect experiments were thus easily achieved. Also, the arrangement of the sting support system ensured that the rolling road could be operated for the moving ground configuration tests without any hindrance from the rotor system. Lateral stiffeners were additionally attached from the side walls of the tunnel to the rotor support system to reduce lateral vibrations during operations and add to the rigidity of the system during prolonged testing.

2.5.2.6 Performance Testing

Extensive performance testing of the Large Rotor at $1100RPM$ $(16Hz)$ in the wind tunnel showed consistent and smooth rotor operations with low vibrations. At this speed, excessive vibrations were only observed at the extreme cyclic pitch angle settings ($\approx 16^o$) and during resonance, observed to occur when the rotor was operated at a rotational speed of $780RPM$ $(13Hz)$. Blade tracking was checked to ensure that there was no significant rotor balance issues. An upstream looking view of the rotor set-up in the wind tunnel is shown in Figure 2.10. The rotor was oriented and positioned in the manner shown in the figure to ensure that the cyclic pitch changes of the blades occurred at the right azimuthal locations. No

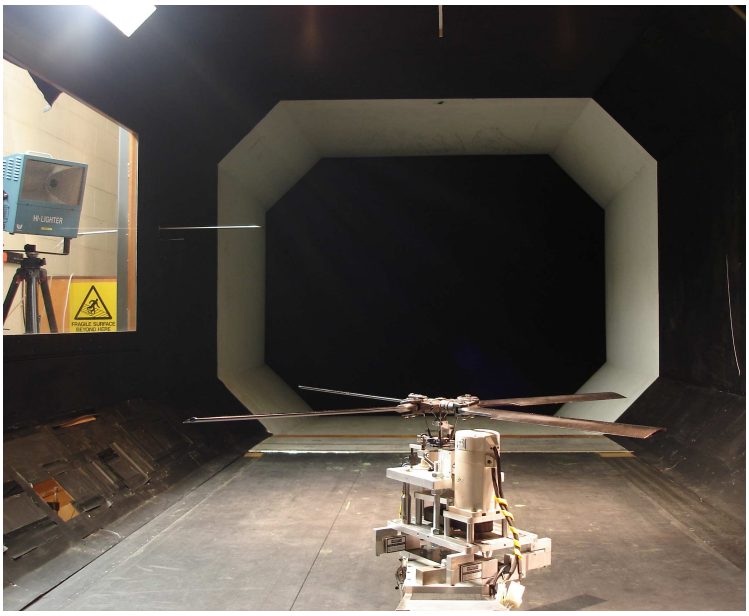

FIGURE 2.10: Large Rotor set-up in the wind tunnel

disk tilt was incorporated in the model as this has been seen to have a minimal effect on the ground effect wake [24].

2.5.2.7 Small Rotor Model

To investigate the effect of wind tunnel wall constraints on the experimental results from the Large Rotor, further PIV experiments were conducted using a smaller rotor in the wind tunnel. A two-bladed rotor model with a rotor diameter of $310mm$ was used for these experiments. The rotor blades had a symmetrical aerofoil section with a $31.7mm$ chord, were 10.7% thick, were un-tapered, untwisted and had a fixed pitch of 10^o. The blades were purchased ready-made and the aerofoil section was similar to that of the NACA 4-digit section with the same thickness.

A $400W$ Panasonic AC digital servo motor, capable of a rated speed of $5000RPM$ $(83Hz)$, was used to power the Small Rotor model. An accompanying Panasonic motor control unit was used to provide torque and speed information during the experimentation. Both the rotor and servo motor were attached to a $20kg$ Novatech F-310 load-cell and this was connected to a PC via a NI-USB-6629 DAQ interface to provide the thrust information of the rotor. Only untrimmed ground effect tests were performed with this rotor system due to its fixed pitch. The rotor

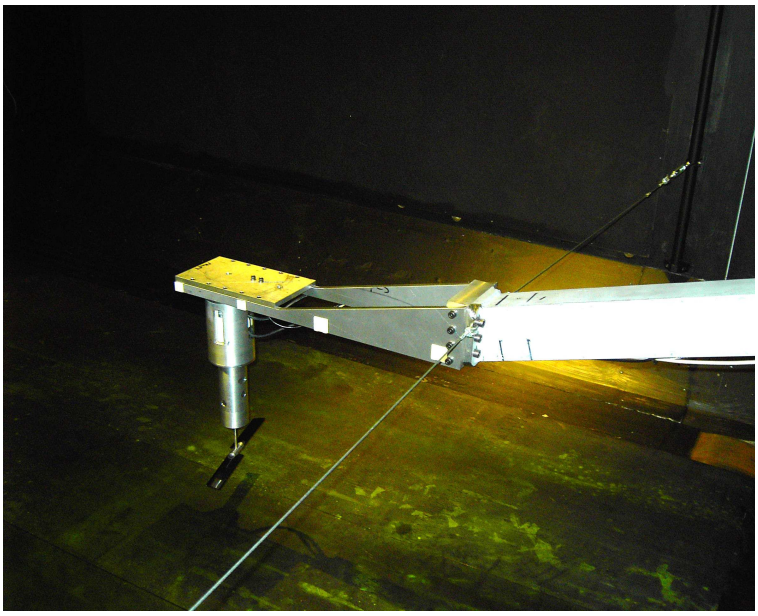

FIGURE 2.11: Small Rotor set-up in the wind tunnel

Small Rotor	Dimensions
Blades	2
Rotor radius	155mm
Pitch	10^o
Blade tip	Square-cut tip
Blade Chord	31.7mm
Max Thickness Ratio	10.7% at 50% outboard of root

TABLE 2.4: Small Rotor Dimensions

system was installed in the wind tunnel using a base-plate attached to the sting and support system used for the Large Rotor tests. The set-up of this system in the wind tunnel is shown in Figure 2.11. Details of this rotor system is provided in Table 2.4 and for simplicity, this rotor is referred to as the Small Rotor.

2.5.3 Experimental Testing in the Argyll Wind Tunnel

Extensive PIV tests were conducted with the Large Rotor during the course of this research to investigate the ground effect wake. A summary of the tests performed with this rotor is presented in Table 2.2. To fully quantify the ground effect wake formed by this rotor, a series of 2D2C and Stereoscopic PIV tests were performed for a range of rotor ground distances, collective blade pitch angles and normalised

advance ratios. Stereoscopic Particle Image Velocity (PIV) employs the same fundamental concepts of 2D2C PIV to derive three-component velocity information from a two-dimensional slice of the flow-field. This method employs two imaging systems, placed off-axis, by a known perspective angle, θ, to the plane of interest in the flow-field. Images of the same region of the flow, recorded by the two imaging systems are then analysed to derive in-plane (u, v) velocity components associated with the flow. With the perspective angles between the imaging system and the plane of the flow known, the cross-flow velocity component, w, from the imaged region can also be derived. Stereoscopic (Stereo) PIV is known to produce more accurate measurements of the in-plane velocity components in the flow-field and a more detailed description of this method is provided in Appendix A.

A commercial PIV system (LaVision) was used for wide area PIV testing performed with the Large Rotor. The LaVision system consists of a Litron double cavity, Nd:YAG laser, which is Q-switched to produce $0.5J$ pulses of $8ns$ pulse duration. The laser is frequency doubled with a $532nm$ wavelength. Two Imager pro X, 11 Megapixel cameras (4008×2672 pixel CCD chip), with $9\mu m$ pixel size and a bit depth of 14, were used together with the laser to obtain PIV data of flow areas in excess of $1m^2$. Correct focus for Stereo PIV could be achieved using manual focus and scheimpflug adapters or, alternatively, using remote control focus and scheimpflug mounts. DaVis 7.2, the software accompanying the LaVision system, was used to control a computer installed with a Maxtrox Solios CameraLink frame-grabber and a software controlled Programmable Timing Unit (PTU) (Version 9) [71]. These were used to synchronise the laser, camera control and imaging system. The cameras were focused on a laser light sheet of approximately $4mm$ thickness, aligned with the symmetry plane of the rotor along the wind tunnel longitudinal axis for most of the tests conducted. Seeding particles used in the PIV was produced by a PivTech 40 Seeding Generator, which uses pressurised air and olive oil to generate an oil mist with mean particle diameters of approximately $1\mu m$.

The main challenge faced during the set-up of the PIV system in the Argyll wind tunnel, was the alignment of the cameras with the regions of interest in the ground effect flow-field. To record the wake close to the ground, the cameras were required to be aligned level with the ground of the wind tunnel. Poor optical access of the

Argyll wind tunnel meant that the cameras had to be mounted to rails which were attached to beams making up the frame of the wind tunnel working section. Slots had to be cut out along the side walls of the working section, close to the level of the ground, to allow optical access for the cameras to view the required region of interest. A photograph of the PIV camera set-up for the Stereoscopic PIV experiment is shown in Figure 2.12. Focusing of the PIV cameras on the required region of interest was performed manually using manual focus lenses and for the stereo PIV, manual scheimpflug adaptors were used. For the stereo PIV set-up, the cameras were arranged in the angular displacement stereo PIV arrangement, to allow for greater measurement accuracy of the velocity components (refer to Appendix A). In this case, scheimpflug adaptors were used to ensure uniform magnification gradients across the image. Camera perspective angles were determined by the DaVis 7.2 software during the calibration procedure.

A range of Nikon fit camera lenses ($50mm$ and $105mm$ focal lengths with $f_{\#} = 2.8$ and $200mm$ focal length with $f_{\#} = 4.0$), were used to obtain the required fields-of-view during the tests, and these are schematically illustrated in Figure 2.13. Most of the regions of interests (ROI) were of the flow-field near the ground and were mainly taken to capture the development of the ground effect wake features. As in the case of the preliminary PIV tests, two regions of the flow-field were concentrated on; upstream of the rotor disk and under the leading edge of the rotor disk, as shown in Figures 2.13 (a) and (b). For these cases, the $50mm$ lenses with $f_{\#} = 2.8$ were fitted to the cameras to obtain a $1.0m \times 0.7m$ field-of-view . The effective measurement area per point in these tests was around 0.013R $\times$ 0.013R.

Specific regions of the ground effect wake were imaged using a Sigma $105mm$ lens with $f_{\#} = 2.8$, and these tests were mainly concentrated in the region near the ground plane coincident with the leading edge of the rotor tip, as shown in Figure 2.13 (c). In this case, the PIV field-of-view was $0.4m \times 0.25m$ and the effective measurement area per point was around 0.0062R $\times$ 0.0062R. PIV tests of the developing tip vortex system was also conducted, as shown in Figure 2.13 (d) and this was used primarily to measure the circulation strength of the tip vortex system, to characterise the rotor flow. A Nikon $200mm$ lens was used for these tests and provided a $0.25m \times 0.2m$ field-of-view, with the effective measurement area per point around 0.004R $\times$ 0.004R. The fields-of-view presented in Figure

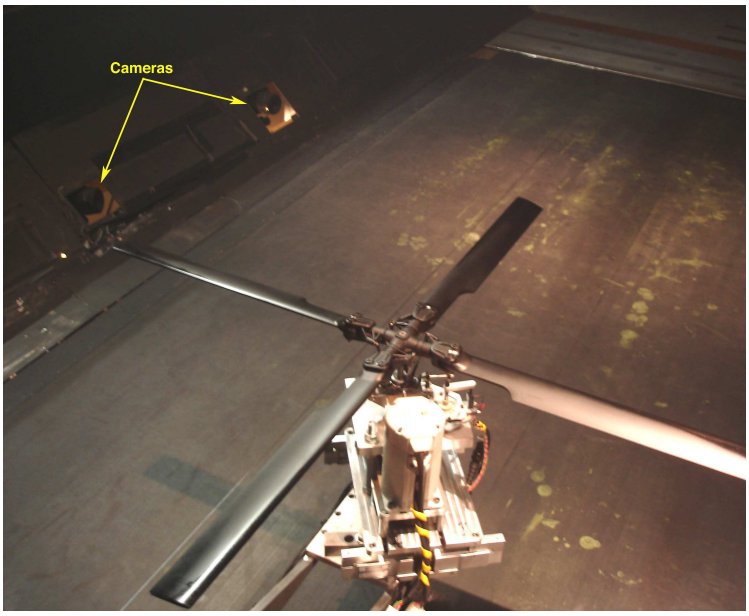

FIGURE 2.12: Camera Access in the Argyll wind tunnel. The picture shows the Stereo PIV arrangement of the cameras during one of the tests.

2.13 were tested for both the 2D2C PIV and Stereoscopic PIV cases. In the case of the Small Rotor, the Sigma $105mm$ lens with $f_{\#} = 2.8$, was used to image the rotor wake at two locations, as shown in Figure 2.14. Only 2D2C PIV was performed with the Small Rotor for a $0.4m \times 0.25m$ field-of-view, and the effective measurement area per point was around 0.0062R $\times$ 0.0062R.

The PIV tests for the Large Rotor were performed for 4 different experimental configurations; (i) Ground stationary with an untrimmed rotor, (ii) Ground moving with an untrimmed rotor, (iii) Ground stationary with a quasi-trimmed rotor and (iv) Ground moving with a quasi-trimmed rotor. These configurations allowed for the influence of rotor trim and more importantly the effect of the ground boundary conditions on the ground effect wake of the rotor to be investigated. The tests were carried out at two different collective pitch settings of $\theta_0 = 8.8^o$ and $\theta_0 = 12.8^o$. At $\theta_0 = 8.8^o$, the rotor thrust coefficient was $C_T = 0.010$, while at $\theta_0 = 12.8^o$, the thrust coefficient was $C_T = 0.015$. Both thrust coefficients quoted are for IGE hover conditions, for a rotor ground distance of $\frac{h}{R} = 1.0$, and this C_T was constant throughout the range of normalised advance ratios tested. The rotor was operated at a rotational speed of $16Hz$ $(960RPM)$, with a rotor tip speed of $V_{tip} = 50.3ms^{-1}$. The rotational speed of the rotor was kept constant and the wind tunnel speed changed appropriately to vary the advance ratio of the

flow. As in the case of the preliminary tests, the wind tunnel speed for these PIV experiments was measured using a pitot-static probe placed at the entrance of the tunnel working section to avoid any alteration to the wind tunnel calibration by the rotor operation. For the cases where the rolling road was moving, the speed of the rolling road was matched to the speed of the wind tunnel freestream, V_∞, with an accuracy of $\pm 0.1 ms^{-1}$. Two rotor ground distances of $\frac{h}{R} = 1.0$ and $\frac{h}{R} = 2.0$ were tested for a range of normalised advance ratios between $0.3 < \mu^* < 1.0$.

Double frame, double exposure PIV was used for both the 2D2C and Stereo PIV tests, and 120 image pairs were recorded for each test case. With the $50mm$ lenses, the time delay was set to $\Delta t = 300\mu s$, and for the $105mm$ and $200mm$ focal length lenses, the time delays were set to $\Delta t = 200\mu s$ and $\Delta t = 100\mu s$ respectively. For the PIV test cases conducted in the flow regions ahead of the rotor disk (Figure 2.13, View 1), the laser was unsynchronised with the rotor. For all the other fields-of-view tested near/under the rotor disk, shown in Figure 2.13, the PIV sampling was synchronised with the rotor azimuth, with a phase angle of 45^o. This was done to ensure that the area under the rotor disk was unaffected by shadow during blade passage through the lightsheet and also to avoid camera damage due to laser reflection. The images were post-processed with the DaVis 7.2 software using an initial interrogation window size of 64×64 pixels, with a 50% overlap. An iterative scheme was employed with the final interrogation window size of 32×32 pixels [71].

PIV tests with the Small Rotor were performed for two experimental configurations; (i) Ground stationary with an untrimmed rotor and (ii) Ground moving with an untrimmed rotor. The tests were carried out at the fixed rotor pitch of $\theta_0 = 10.0^o$, with the rotor operated at a rotational speed of $60Hz$ $(3600RPM)$ and a rotor tip speed of $V_{tip} = 56.5 ms^{-1}$. The rotor had an OGE hover thrust coefficient of $C_T = 0.010$ and the advance ratio for the tests were set by varying the tunnel velocity. The tests were carried out at normalised advance ratios between $0.3 < \mu^* < 1.0$ and at a ground distance of $\frac{h}{R} = 1.0$. For all the PIV tests conducted, 120 image samples were taken with a $\Delta t = 200\mu s$. For these experiments, the rotor was unsynchronised with the laser. With the Small Rotor's model-span-to-tunnel-width ratio around 0.10, the results from these experiments were used to identify any wind tunnel interference effects affecting the experimental results obtained from the Large Rotor.

2.6 Summary

This chapter describes the flow visualisation and PIV experiments that were conducted to investigate the rotor wake in ground effect. These experimental methods were used to gather both qualitative and quantitative information of wide areas of the ground effect flow-field. The experiments were aimed at identifying the effects of rotor parameters and ground boundary conditions on the ground effect wake of the rotor. Data from the flow visualisation experiments was compared with PIV results obtained using the same rotor model, to identify the mechanisms at work within the brownout flow-field. These tests were also used as a preliminary investigation of ground effect and results obtained from these tests were used in the design and set-up of the main experiments on ground effect. The main set of ground effect experiments were conducted in a wind tunnel installed with a moving ground, to analyse the effect of ground boundary conditions on the ground effect wakes of rotors. A rotor rig was designed especially for these tests and was used to investigate the influence of other factors such as rotor ground distances, collective angles and trim configuration on the ground effect wake. The following chapters present the results from the flow visualisation and PIV experiments conducted on ground effect.

(a) View 1: PIV field-of-view ahead of the rotor disk

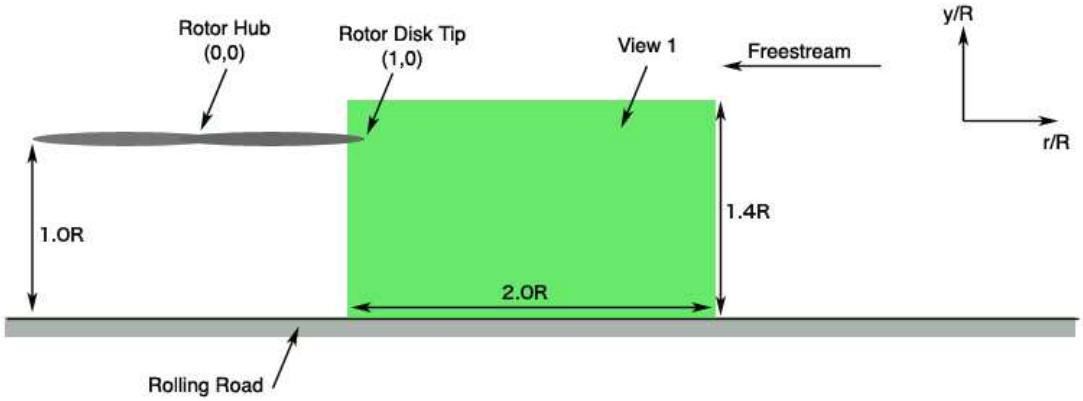

(b) View 2: PIV field-of-view under the rotor disk leading edge

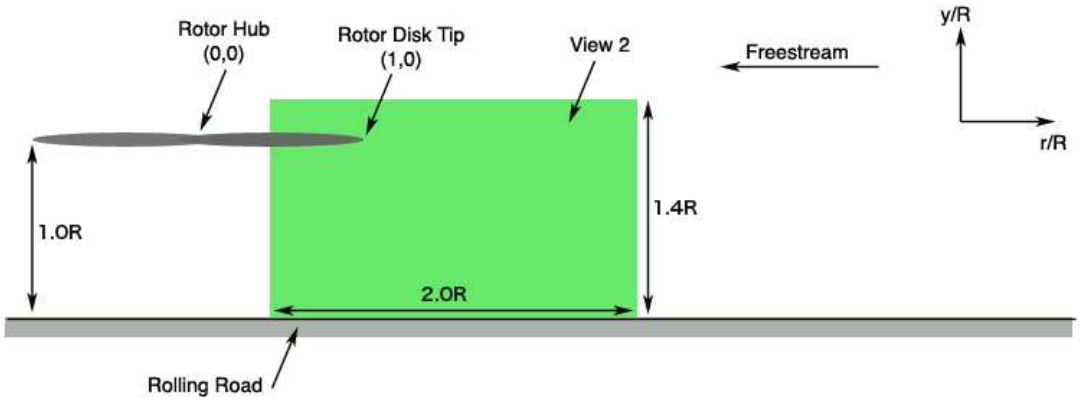

(c) View 3: PIV field-of-view at the ground, under the rotor disk leading edge

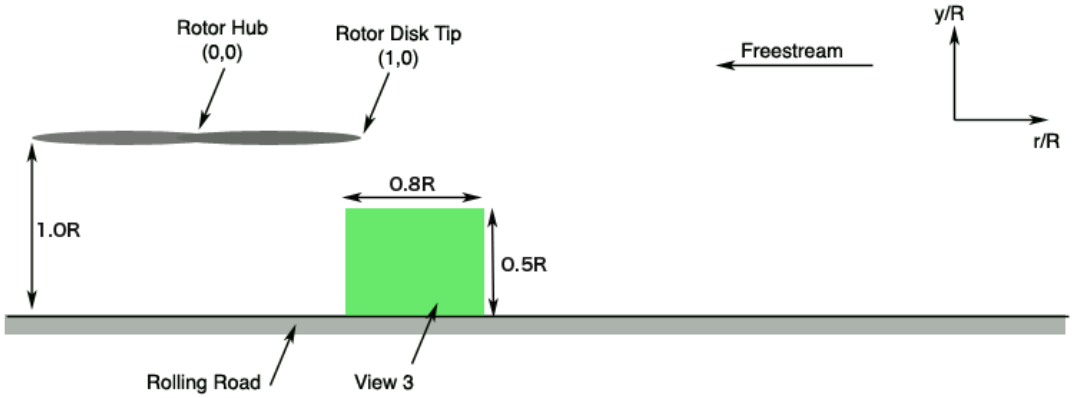

(d) View 4: PIV field-of-view at the rotor blade tip

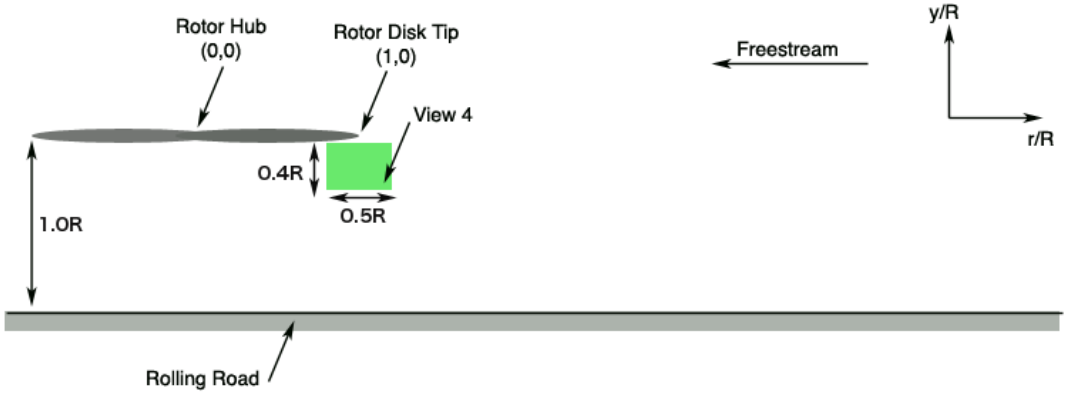

FIGURE 2.13: Ground effect fields-of-view of the Large Rotor.

(a) View 5: PIV field-of-view ahead of the rotor disk

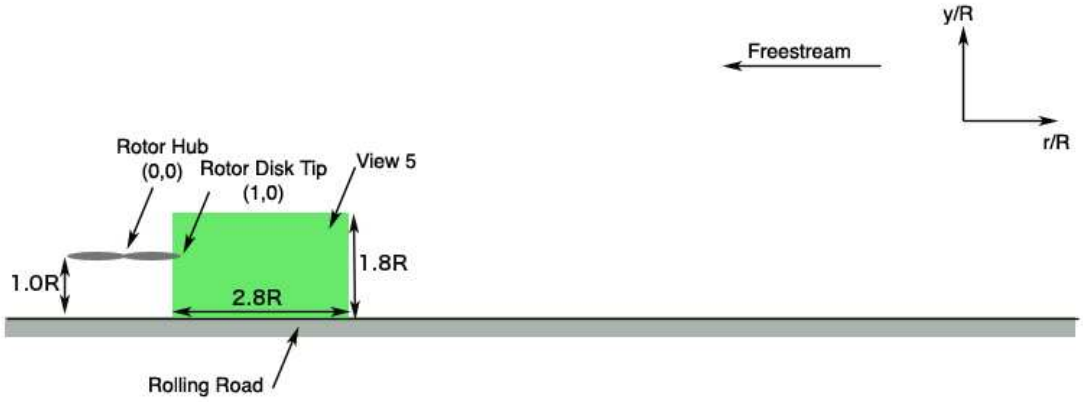

(b) View 6: PIV field-of-view further ahead of the rotor disk

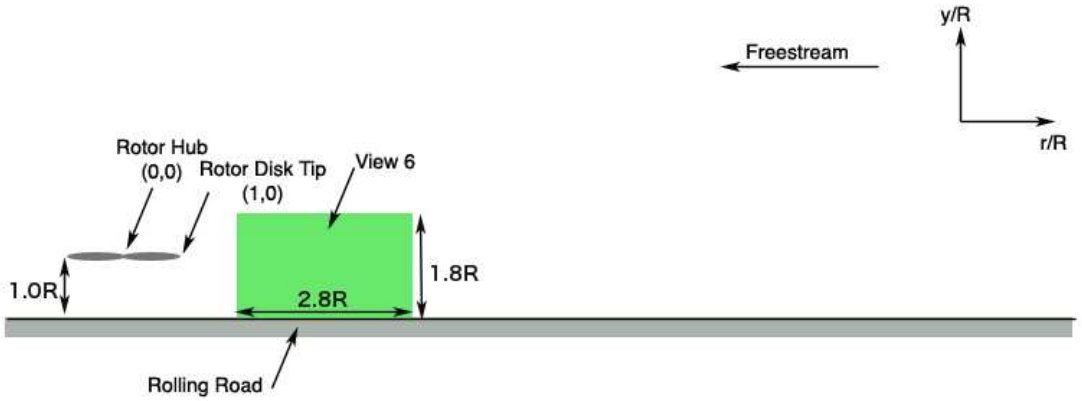

FIGURE 2.14: Ground effect fields-of-view of the Small Rotor.

Chapter 3

Brownout Dust Cloud Flow Visualisations

3.1 Introduction

Flow visualisation experiments were conducted as part of preliminary investigations of the wake of a rotor in ground effect. Primarily conducted in view of simulating helicopter brownout, a phenomenon experienced by helicopter pilots during ground effect operations near erodible surfaces, these experiments also provide visualisations of the ground effect wake of rotors, the underlying fluid dynamics leading to the brownout condition. In other words, the flow visualisation experiments conducted provided information about both the brownout condition and the ground effect wake features causing it. These experiments also act as a prelude to the quantitative experiments that were to be conducted for rotor operations in ground effect.

Still images extracted from movie sequences recorded by a high speed video camera are presented in the following sections, to help in the description of the flow features identified during the tests. The movies were recorded with a camera frame rate of $300Hz$ and a shutter speed of $750\mu s$. In each image presented, the wind tunnel flow is from right to left and the rotor is visible at the left edge of the field-of-view. A summary of the rotor parameters are presented in Table 3.1 with in-depth details of the experiment provided in Section 2.3. While the brownout phenomenon is

Experimental Parameters	**Values**
Rotor Model	Rotor A
Radius (R)	$0.075m$
μ^* tested	0.37 & 0.65 (max)
Ground distances tested	$0.5R$ & $1.0R$
Rotor C_T (OGE)	0.015
Rotational Speed	$5640RPM$ $(94Hz)$

TABLE 3.1: Rotor and experimental parameters for the flow visualisation tests conducted to simulate the helicopter brownout phenomenon.

known to affect all the ground effect flow regimes, normalised advance ratios tested in these experiments mainly fell within the recirculation flow regime ($\mu^* <= 0.65$) described by Curtiss *et. al* [24]. This was limited by the maximum speed of the wind tunnel; with the flow advance ratios achieved by maintaining a constant rotor rotational speed and adjusting the freestream velocity, the maximum speed of the wind tunnel limited the maximum advance ratio that could be achieved for the tests.

3.2 Flow visualisation of the helicopter brownout phenomenon

Flow visualisations of the simulated brownout phenomenon showed the rotor wake to be dominated by the tip vortex system leaving the rotor disk and a cloud of powder present ahead of and around the rotor. As the tip vortices left the rotor disk and encountered the ground, they were seen to trail along it. At a particular upstream position, governed by the relative velocities of the trailing tip vortices and the opposing freestream, the trailed vortices moved up and away from the ground. A separation zone was seen to occur at the ground around this location and the vortices were seen to move upwards, away from the ground, picked up by the wind tunnel freestream and re-directed back towards the rotor. Figure 3.1, a snapshot taken with the rotor at a ground distance of 1.0R and a normalised advance ratio of $\mu^* = 0.65$, show the identified flow structures in the wake. Talcum powder seeding, representing debris spread along the ground ahead of the rotor,

was picked up and entrained by the vortices as they trailed along the ground towards the separation zone, indicated by the bright white region on the ground in the image. As the tip vortices left the ground at the separation zone, entrained seeding particles were seen to follow the tip vortices' trajectories towards the rotor. Most of the particles were eventually seen to cluster in the region between the rotor and the separation zone, forming a cloud of dust. It is the formation and presence of this dust cloud ahead of the helicopter during landing that results in pilots losing visual and situational awareness, the so-called brownout.

Comparisons of this with a representative image from a lower normalised advance ratio case, $\mu^* = 0.37$, presented in Figure 3.2, show the separation zone to be less prominent but further upstream in the flow-field (to the right of the rotor). A wider camera field-of-view was required in this case to capture the whole wake and the powder was seen to rise higher into the flow-field than during the tests at the higher normalised advance ratio, presented in Figure 3.1. Contamination of the air by the action of the rotor in the lower normalised advance ratio case was greater in coverage and showed the severity of the situation at the lower flight speeds. The apparent wavy effect noticed along the ground in these images is a feature in all the stills and is a result of the seeding being picked off the ground

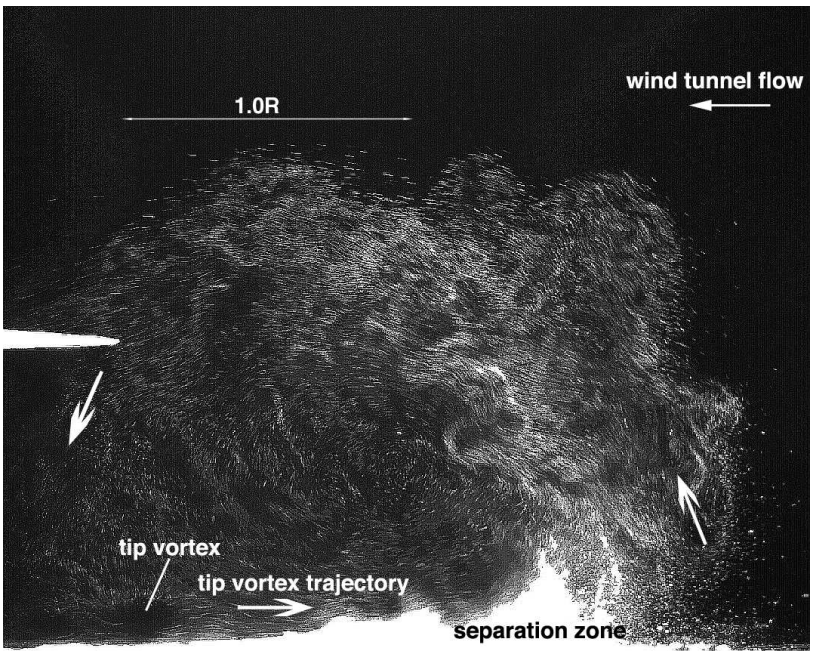

FIGURE 3.1: A still from high speed video sequences of simulated brownout using talcum powder spread over the tunnel floor. The rotor was at a ground distance of 1.0R and operated at a normalised advance ratio of $\mu^* = 0.65$.

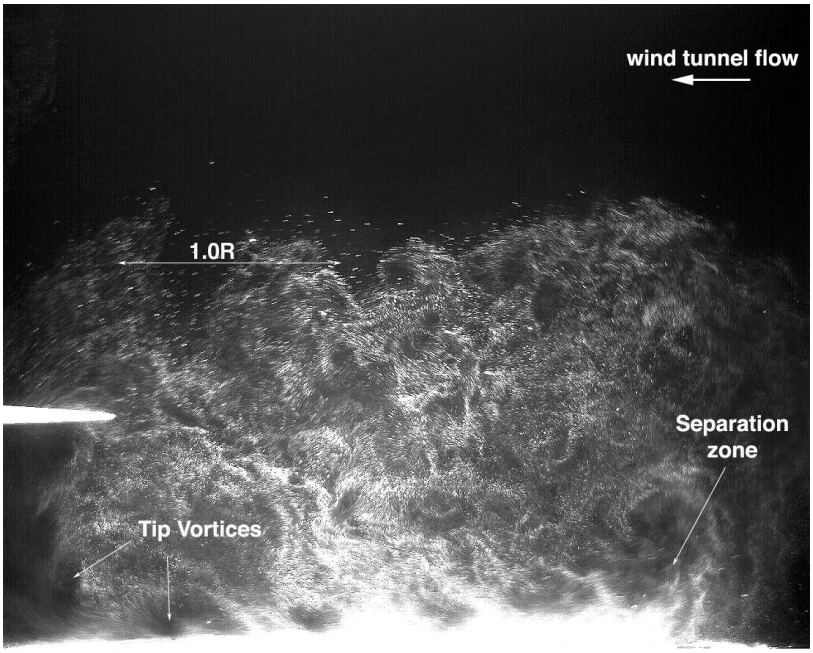

FIGURE 3.2: A still from high speed video sequences of simulated brownout using talcum powder spread over the tunnel floor. The rotor was at a ground distance of 1.0R and operated at a normalised advance ratio of $\mu^* = 0.37$.

by the tip vortices as they moved along the ground from left to right.

Flow structures identified in the wake at this rotor ground distance were also present when the rotor was operated closer to the ground plane, confirming them to be features of the ground effect wake. Tests conducted with the rotor at a ground distance of 0.5R, showed the tip vortex system expanding along the ground plane and a separation point formed upstream of the rotor. For comparable normalised advance ratios, the estimated location of the separation zone at the lower ground distance was seen to be further ahead of the rotor, although the extent of coverage of the dust cloud was seen to be similar to that produced when the rotor was higher above the ground. Representative snap-shots of the wake at the normalised advance ratio of $\mu^* = 0.65$, at the different ground distances, are shown in Figure 3.3 and highlight the differences in the wake between the cases.

Video sequences from the flow visualisation also displayed the unsteady nature of the flow-field with fluctuations of the separation zone observed at both normalised advance ratios tested. In both test cases, the separation zone was seen to follow an oscillatory motion, moving back and forth around a mean ground

(a) $\mu^* = 0.65$ at $h/R = 0.5$ (b) $\mu^* = 0.65$ at $h/R = 1.0$

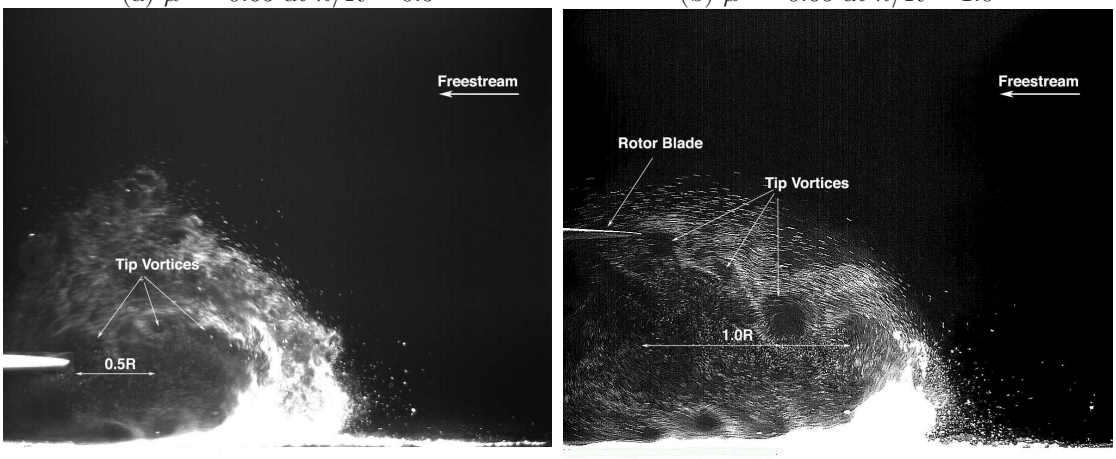

FIGURE 3.3: Stills comparing the wake at different rotor ground distances. In both cases, the rotor was operated at $\mu^* = 0.65$. In frame (a), the rotor was at a ground distance of 0.5R while in frame (b), the rotor was at a distance of 1.0R above the ground.

location. Movement of the separation zone was seen to be more pronounced and frequent at the lower normalised advance ratio, suggesting greater unsteadiness at this speed. The dust clouds formed at both normalised advance ratios tested also showed unsteady variations in size; in some instances reaching regions of the flow-field as high as (or even higher than) the rotor distance off the ground. Strong three-dimensionality of the flow was also exhibited in the tests, where the movie sequences showed small clusters of powder appearing (and disappearing) from the plane of observation. Dust not originating from anywhere within the plane of view was frequently seen appearing, while particles in the plane of illumination were constantly seen to swirl out of the plane of view. These observations suggest the presence of cross-flow components in the flow-field and warrant further investigations.

3.2.1 Tip Vortex Track

Images from the flow visualisation, while displaying the nature of the wake, revealed some of the more persistent flow structures present in the ground effect flow-field. The wake was seen to be dominated by the tip vortex system trailed from the rotor. These tip vortices are clearly visible in Figure 3.2, beneath the rotor disk and appear as small circular regions with dark cores devoid of seeding.

In these experiments, the tip vortices were observed to have large cores at relatively young wake ages (i.e. near the rotor disk) because of the choice of seeding particles used for this visualisation. Large diameters and the relative density of the talcum powder particles meant that they were unable to accelerate with the air flow, thus portraying the tip vortices to have large cores. Visualisations of the wake showed the vortices to expand out along the ground ahead of the rotor disk; tests conducted at different longitudinal planes parallel to the longitudinal axis of the rotor disk provide evidence for the expansion to be a three-dimensional process, occurring around the front end of the rotor disk. Additionally, the side walls of the wind tunnel were noticeably sprayed with powder after the experiments, suggesting a radial expansion of the wake as was visualised by Kusmarwanto [29].

At the flow separation zone, the trailing vortices were seen moving away from the ground and picked up by the tunnel flow and re-directed back towards the rotor. The well-defined track, maintained by the vortices along the ground, was seen to disappear once these vortices reached the separation zone. The dark cores of the vortices, visible along the ground plane, were seen to lose definition after this point, most probably due to vortex dissipation [72], which can explain the difficulty in tracking the vortices after the separation zone. Analysis of the images at a high normalised advance ratio, where the tip vortices leaving the separation zone were more defined, however, showed the vortices following different paths after leaving the ground. Observations showed some vortices directed back to the rotor to be re-ingested, an example of which is shown in Figure 3.3 (b). This re-ingestion path taken by the vortices was similar to observations seen in the recirculation regime, where the trailing rotor wake was seen to be recirculated through the rotor disk [24]. Re-ingestion of the tip vortices however, was not commonly observed in the flow visualisation movie sequences, and was even less frequently observed at the lower normalised advance ratio test.

Instead of re-ingestion, the movies showed most of the vortices leaving the ground at the separation zone to accumulate in the region of the flow between the rotor and the separation zone, coincident with where the dust cloud was seen to form. An example of this is shown in Figure 3.4; in this image, a vortex that has left the ground is seen accumulating within the dust cloud, just above the ground, to the left of the separation zone. The presence of this accumulating vortex was seen to

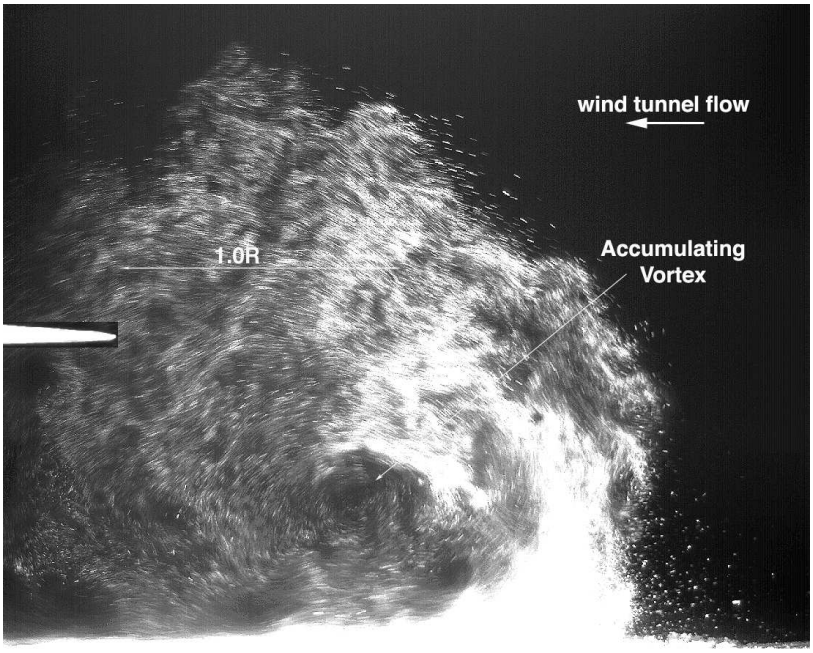

FIGURE 3.4: Image showing a vortex accumulating within the dust cloud, just after leaving the flow separation zone. The rotor was at a ground distance of 1.0R and operating at a normalised advance ratio of $\mu^* = 0.65$.

recirculate dust entering the cloud before the vortex was eventually convected back towards the rotor by the wind tunnel freestream. The accumulation of vortices in the zone of the dust cloud appeared to be a more salient feature of the wake at the lower normalised advance ratio than the recirculation and re-ingestion of the tip vortices. At the higher normalised advance ratio, this accumulation process was also seen to occur, although in this case, clearly defined tip vortices were also seen to be circulated back towards the rotor plane and re-ingested through it.

The presence of vortices in the dust cloud region imply the presence of vorticity; this is reflected by observations of the dust particles present in this region following a swirling motion similar to the rotational sense of the tip vortices. This swirling motion of the dust particles were more visible along the ground plane, when the dust particles were entrained by the tip vortices. It was also observed that some regions of the flow near the ground plane showed dust particles to rotate in a sense opposite to the rotation of the tip vortices. An example of this is shown in Figure 3.5; in this image vortices rotating opposite to the rotational sense of the tip vortices were observed around the flow separation region. The appearance of these oppositely rotating vortices, especially near the ground plane and flow separation

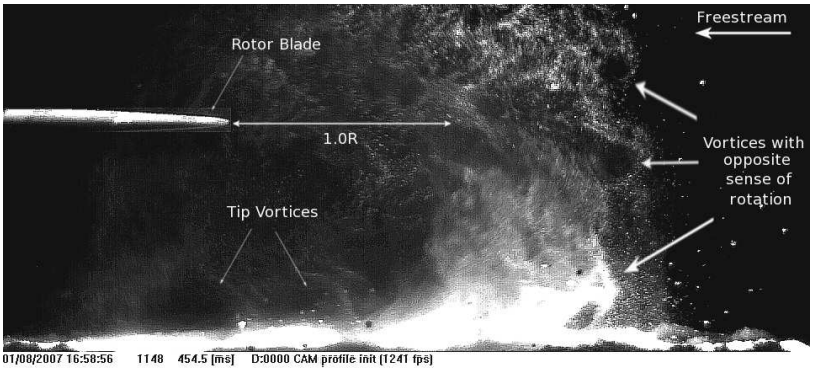

FIGURE 3.5: Image showing a series of vortices in the flow-field, seen to rotate in a sense opposite to the tip vortices trailed from the rotor blades. The rotor was at a ground distance of 1.0R and operating at a normalised advance ratio of $\mu^* = 0.37$.

zone imply secondary separation caused by the trailing tip vortices. Quantitative data of the flow-field is however required before these observations can be substantiated. It however could be established through the flow visualisations that the different paths taken by the tip vortices as they moved back towards the rotor was one of the contributing factors influencing the unsteady nature of the wake.

3.3 Dust Transport Mechanism

Video sequences of the simulated brownout phenomenon revealed the trailing tip vortex system as the sole contributor to the formation of the dust cloud. Recordings of the rotor wake trailing along the ground were obtained using a higher camera frame rate of $1241Hz$ at a frame resolution of 960×456 pixels, and showed the tip vortex system involved in the transport and uplifting of loose dust particles from the ground. Vortices trailed along the ground after the rotor start-up transient were seen to pick up particles from the ground all along the trail, with the most uplifting occurring at the lower right of each vortex as shown in Figure 3.6. As the vortices moved along the ground, the lightest of these surface particles were quickly suspended in the flow just above the ground. These suspended particles were seen to be entrained into the vortices and followed their path as they progressed along the ground plane. Heavier particles however, once dislodged from the ground by the tip vortices, were seen to be projected away from the ground and initially followed the mean direction of the flow. The heavier mass and size of these particles were seen to prevent them from following the tip vortex trajectories

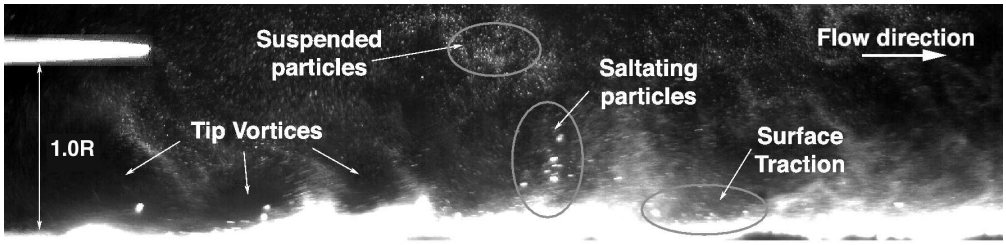

FIGURE 3.6: Still from video sequence showing particles uplifted from the ground. Most of the dust were seen to be picked up from the lower right corner of the vortices. The rotor was at a ground distance of 1.0R and operating at $\mu^* = 0.37$.

and resulted in them eventually returning to the ground some distance away from where they were initially dislodged. Other more heavier particles were observed to move along the ground plane, guided by the general flow direction of the tip vortices until the separation zone where they were seen to accumulate, resulting in the separation zone to collect most of the dust. This accumulation of particulate matter around the separation zone was also observed in brownout simulations carried out by Leishman *et. al*, where it was observed that 'dunes' were formed due to the tip vortex track along the ground [44].

The movement of the dust particles visualised at the ground plane showed similarities to those identified in sedimentology research. In these studies, soil transport by wind are classified into three broad categories, namely surface traction, saltation and suspension. Surface traction refers to a process where soil particles move (roll) along the surfaces in the direction of the wind [73]. Saltation refers to a process whereby particles are ejected from the ground due to pressure differences or impulse forces acting near the surfaces [54]. Particles uplifted in this manner are usually seen returning to the ground surface a small distance away [74]. Suspension refers to the process where particles uplifted by the wind are not seen to return to the ground within the immediate vicinity. The initiation of particle movement in these processes has been related to a surface shear stress and threshold velocity, and has been proven to be directly dependent on the nature of the particles (i.e. particle density, composition, diameter) [54]. Dust transport processes observed in the flow visualisations showed all three soil transport processes at work in the flow-field, and show the presence of the fast moving tip vortices

along the ground to provide the velocity required to transport these particles. Observations from these movie sequences suggest that these complex dust transport models are required to be implemented in simulation models of brownout that wish to accurately capture the dust distribution patterns around helicopters.

While the trailing tip vortices affect the particle pick-up mechanisms at the ground, the presence of the ground plane near the trailing vortices from a rotor has been known to affect the dynamics of the tip vortices. Literature provides information of hover in ground effect experiments showing significant vortex merging to occur as trailed rotor tip vortices encounter the ground plane [22]. Additionally, these experiments also show quantitatively that the tip vortices undergo vortex stretching, a process known to delay the onset of viscous diffusion by reducing the vortex core sizes [75]. While it was not possible to visualise vortex stretching from the visualisation experiments conducted for this research, significant vortex merger was observed to occur in the flow-field. Figure 3.7 shows a sequence of images which track two tip vortices as they trail from the rotor disk. In this case, the rotor was at a ground distance of 1.0R and operating at a normalised advance ratio of $\mu^* = 0.37$.

Figure 3.7 (a) shows two individual tip vortices leaving the rotor plane and trailing beneath the rotor disk. The vortices were seen to maintain their separation distances as they were convected towards the ground plane, as shown in Figure 3.7 (b). As the vortices encountered the ground, the first vortex was seen to decelerate, while the second vortex, maintaining its descent rate, was seen to catch up with the first. Eventually, the two vortices were seen to merge, with the preceding tip vortex seen to tuck under the vortex in front of it. Between the time frames of Figures 3.7 (c) - (d), the two vortices merged to form a single vortex, which was seen to travel along the ground, causing additional dust to be dislodged along its path. Figure 3.7 (e) illustrates this, with the image also showing the trajectories taken by larger particles uplifted by earlier vortices trailing along the ground plane. These particles, first seen uplifted from the ground in Figure 3.7 (d), were seen to carry on with their trajectories as they followed the general flow direction set by the vortices along the ground. These particles were eventually seen to fall to the ground, some distance away from their original positions. Figure 3.7 (f) shows the merged vortex, continuing in its path along the ground further uplifting

more particles along its way until it reaches the separation zone. Figure 3.7 (f) also shows a younger pair of tip vortices just reaching the ground and starting the merger process.

(a) Start of sequence

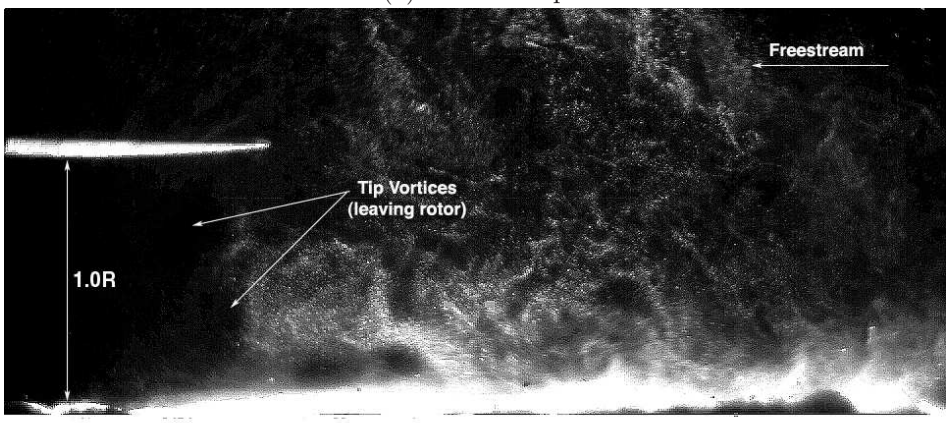

(b) 6.7 revolutions after frame (a)

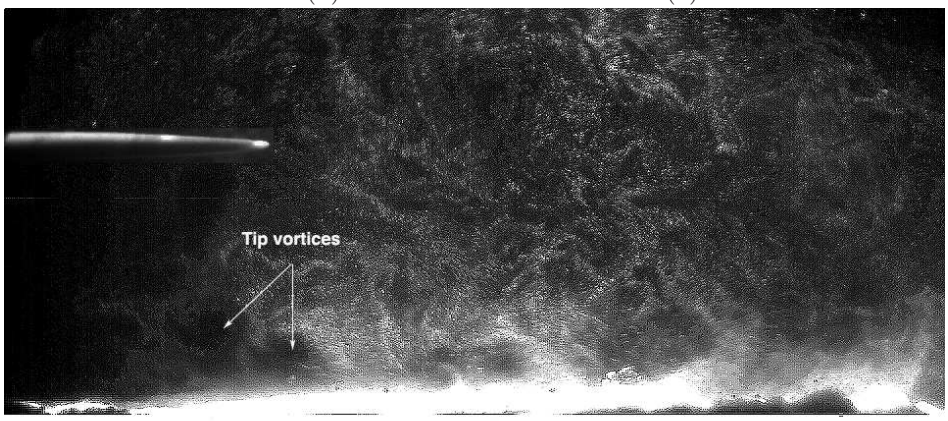

(c) 15.7 revolutions after frame (a)

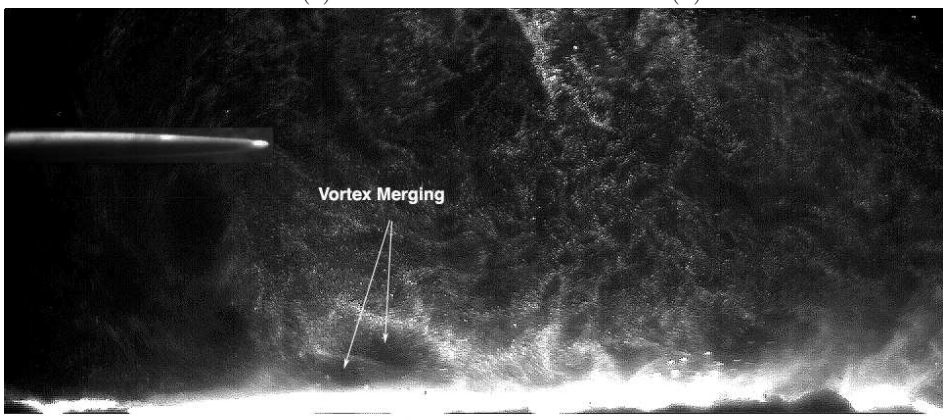

Figure continued on the next page

(d) 18.5 revolutions after frame (a)

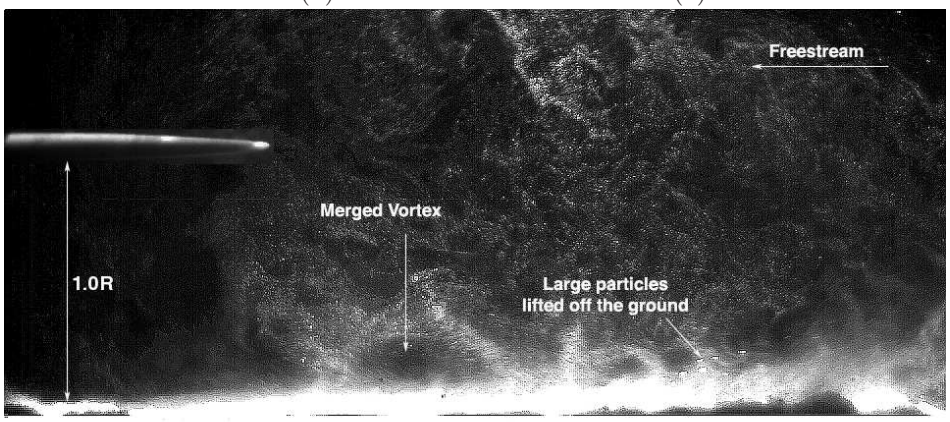

(e) 26.9 revolutions after frame (a)

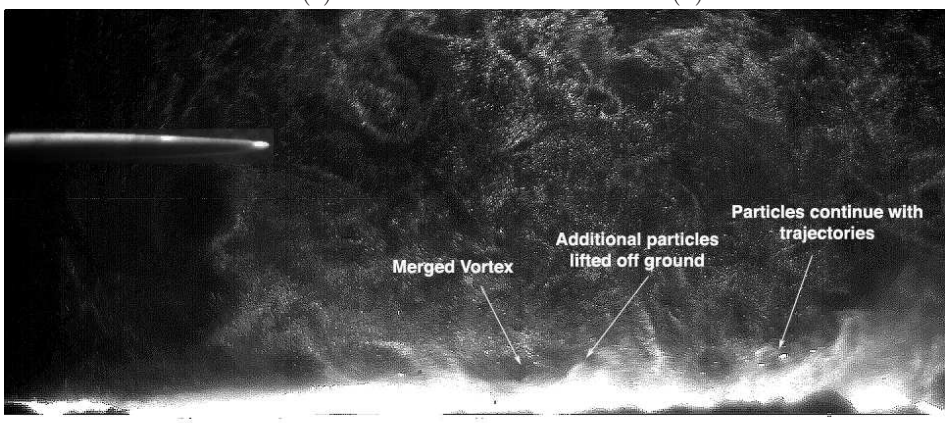

(f) 38.7 revolutions after frame (a)

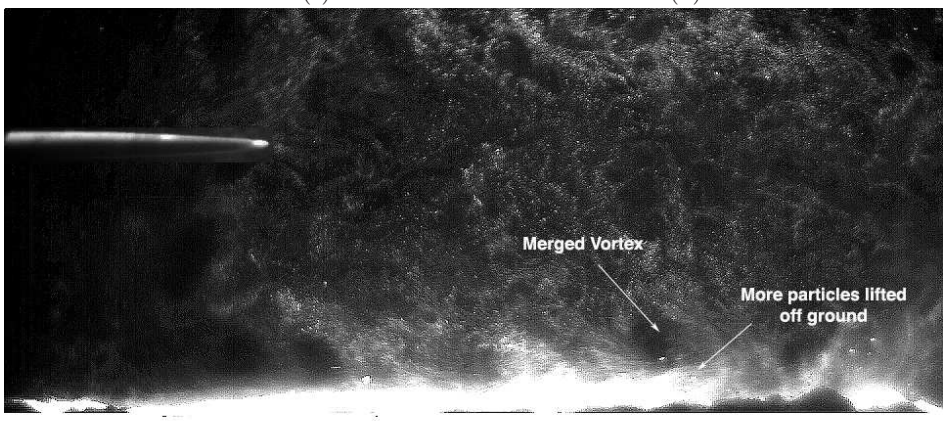

FIGURE 3.7: Sequence of stills showing vortex merger taking place near the ground plane. The rotor was at a ground distance of 1.0R and was operated at a normalised advance ratio of $\mu^* = 0.37$.

(a) Start of sequence

(b) 2.8 revolutions after frame (a)

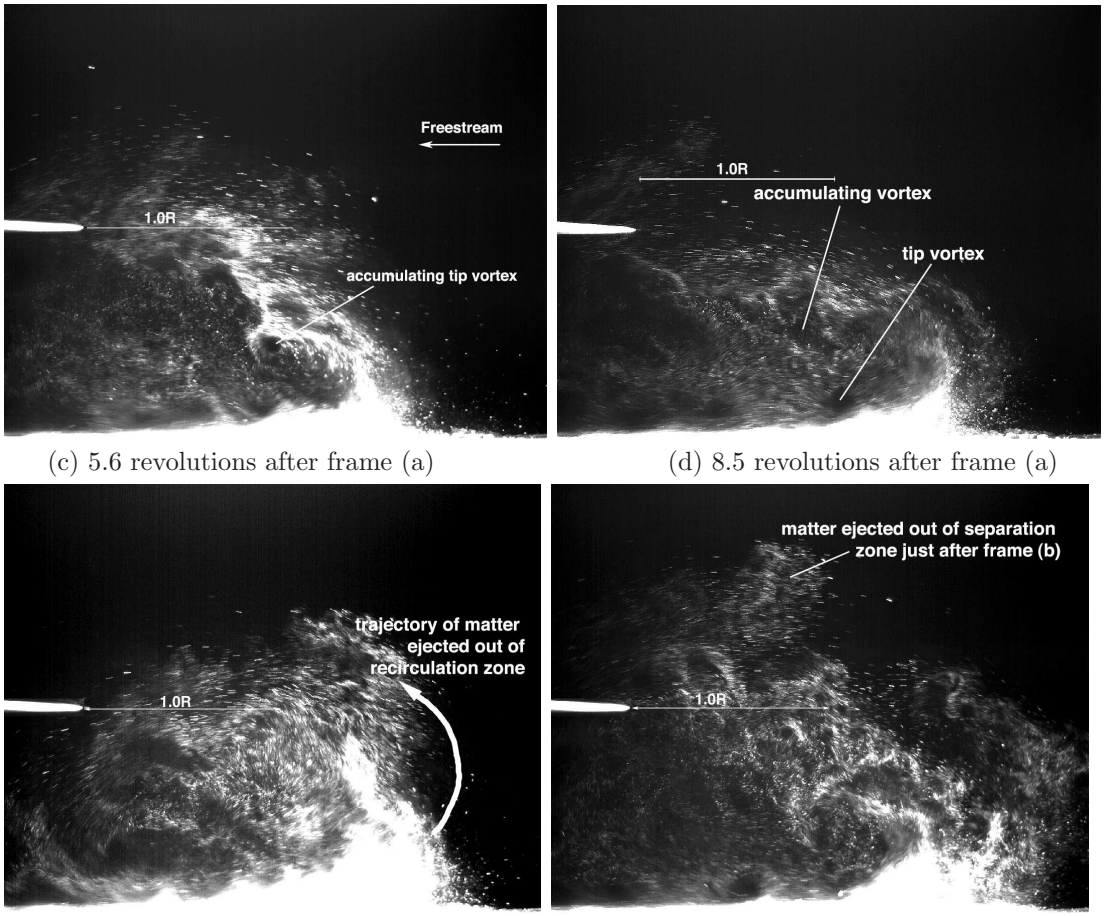

(c) 5.6 revolutions after frame (a)

(d) 8.5 revolutions after frame (a)

FIGURE 3.8: Stills from high speed video sequences of simulated brownout using talcum powder spread over the tunnel floor with the rotor at a ground distance of 1.0R and operating at a normalised advance ratio of $\mu^* = 0.65$.

Observations from the flow visualisation, suggest the vortex merging process to occur more frequently at the lower normalised advance ratio. This, coupled with the greater distances trailed by the vortices before reaching the separation zone, resulted in a larger quantity of dust particles to be uplifted from the ground at the lower normalised advance ratio as compared to the higher test speed. As the vortices reached the separation zone, more particles were uplifted and most followed the trajectories of the tip vortices back towards the rotor. Some particles however, were seen to be ejected through the separation zone after they were dislodged from the ground by the tip vortices. The heavier of these particles were seen falling back to the ground some distance to the right of the separation zone, while the lighter particles were directed back towards the separation zone by the freestream.

The flow visualisation movie sequences showed the quantity of dust uplifted from the ground to be strongly dependent upon the trajectories of the tip vortices as they leave the ground. Depending upon the distances of the separation zone from the rotor, which was governed by the normalised advance ratio of the flow, the vortices were either re-ingested through the rotor, or accumulated within the dust clouds before they were eventually directed back towards the rotor by the freestream. Often, the accumulating vortices were seen to influence the quantity of dust picked up at the ground, in addition to recirculating particulate matter as they left the ground at the separation zone. This was seen to occur indirectly, with these accumulating vortices accelerating the tip vortices below them along the ground plane.

An example of this is shown in a series of snapshots in Figure 3.8. The figure traces the path of the trailed tip vortices along the ground at a ground distance of 1.0R, and a normalised advance ratio of $\mu^* = 0.65$. Due to high velocities associated with the trailing tip vortices, regions of the flow, especially near the ground where the vortices trail, appeared as streaks, blurred due to camera exposure times. Figure 3.8 (a) shows a vortex that has left the ground at the separation point, moved up into the dust cloud, and starting to approach the rotor. The dust cloud already present in the image is the accumulated effect of thousands of rotor revolutions prior to this instant. As this vortex moved back towards the rotor, it was seen to accelerate tip vortices below it, which were seen moving rapidly to the right along the ground in the images. The accumulating vortex can be seen in Figure 3.8 (b), and below it, just to its right, another vortex next to the ground is indicated. As this vortex was 'accelerated' towards the separation zone, the higher velocities associated with it resulted in a large amount of powder to be ejected out into the flow to the right of the separation zone, as is shown in Figure 3.8 (c). While the particles entrained by the vortex followed its trajectory towards the rotor, some of the ejected material was seen to be pushed through the separation zone to its right, as is indicated in Figure 3.8 (c). The heavier of these particles were eventually seen to fall to the ground to the right of the separation zone, while the lighter particles were seen to be transported by the freestream along the path indicated in Figure 3.8 (c). This was seen to result in the eventual increase in size of the dust cloud as can be seen in Figure 3.8 (d). As in the case of the vortex merger, the accumulation of vortices in the wake between the rotor and the separation

zone was more noticeable at the lower normalised advance ratio case as compared to the higher normalised advance ratio case, and can be the cause of the bigger dust cloud noticed at the lower test speed.

3.3.1 Dust Distribution

Differences in the interactions of the tip vortices in the wake have been seen to affect the distribution of particles within the dust cloud. In the flow visualisation images, distribution of the particles within the cloud is inferred from the variation of illumination intensity across the wake region. Figure 3.9 shows instantaneous images of the flow-field from the two normalised advance ratio cases tested. At the higher normalised advance ratio, Figure 3.9 (a) shows the greatest concentration of the dust near the ground around the flow separation zone, which appear to be the brightest region in the flow-field. At the lower normalised advance ratio, Figure 3.9 (b) shows the dust to be more distributed throughout the extent of the dust cloud, with the concentration of dust particles around the separation zone less intense than at the higher advance ratio. The chosen images in Figure 3.9 are crude representations of the average trend observed in the flow-field at the two normalised advance ratios. There were instances when the dust cloud was seen to build up and reach heights far above the rotor ground distance. This was eventually convected downstream by the wind tunnel flow and usually resulted in the rotor model to be engulfed by the dust cloud. These severe changes in the spread of the dust cloud were more frequent at the lower normalised advance ratio tested, and additionally showed the higher reaching particles to display no preferred sense of rotation, unlike the dust particles closer to the ground, which showed a rotational sense complimentary to the rotation of the tip vortices. While processes like those previously described account for the uplifting of particles from the ground, the presence of dust so high above the rotor cannot be explained from the flow visualisation. More quantitative research is required to be carried out before the presence of these high reaching dust clouds and variations in size of the clouds can be convincingly explained.

Comparisons of the flow visualisation results with simulation studies of brownout show good correlation in terms of dust distribution differences at varying normalised advance ratios. One such brownout simulation study was conducted by

Phillips and Brown using the vorticity transport model (VTM) integrated with a particle transport model [76]. Figure 3.10 presents average dust distribution plots obtained from this simulation, for a tandem rotor helicopter performing a landing manoeuvre at a ground distance of 0.88R. Simulation results from flight conditions resulting in flow separation to occur in locations similar with those obtained in the flow visualisation experiments were considered in this figure, as this was observed from the flow visualisation to have an effect on the distribution of particles within the dust clouds. A comparison of Figure 3.9 and 3.10 show good correlation, with results from the simulations indicating the dust concentration at the flow separation region to be less intense at the lower normalised advance ratio case compared to the results from the higher flight speed. Similar results were seen from the flow visualisation images, although the extent of coverage of the dust cloud at the lower normalised advance ratio appears to be marginally bigger than that seen in the simulation data. With the simulation results presenting the mean flow data from the time-averaged flow-field and the flow visualisation presenting instantaneous flow data, this may be a reason for the observed difference between the two sets of results.

While the flow visualisation experiments show features of the ground effect wake and provide insights into the interactions of the tip vortices with the ground, the lack of quantitative information of the wake hinders understanding of the dust cloud formation. Observations concerning the sporadic expansion of the dust clouds, the expulsion of particles through the separation zone and the fluctuations of the separation zone cannot be quantified through these visualisations alone. Quantitative information of the flow-field is required if explanations for these wake features are to be obtained.

3.4 Summary

Flow visualisation experiments were conducted to qualitatively investigate the brownout phenomenon experienced by helicopters when operating close to surfaces covered with debris or erodible material. These experiments also provided insights into the ground effect wake, which is the primary factor behind this brownout phenomenon. From the flow visualisation movie sequences, it was identified that the

(a) $\mu^* = 0.65$ at 1.0R (b) $\mu^* = 0.37$ at 1.0R

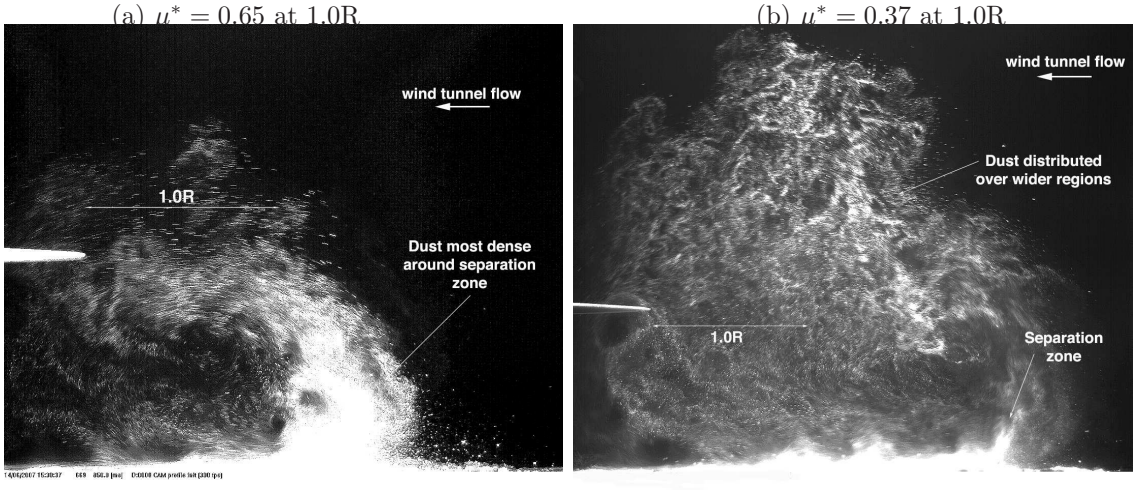

FIGURE 3.9: Instantaneous images comparing particle distributions within the dust cloud. In both frames, the rotor was operated at a ground distance of 1.0R. In frame (a), $\mu^* = 0.65$ and in frame (b), $\mu^* = 0.37$.

(a) $\mu^* = 0.29$ at 0.88R (b) $\mu^* = 0.12$ at 0.88R

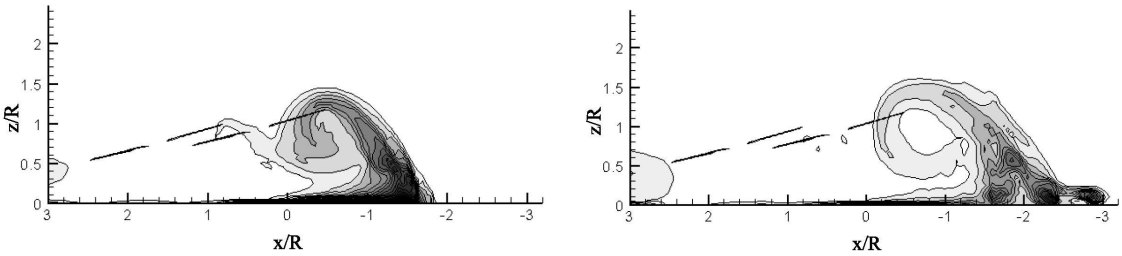

FIGURE 3.10: Mean dust distributions around a tandem rotor helicopter performing a landing manoeuvre at a ground distance of 0.88R. Images obtained from VTM simulations of brownout. In frame (a), $\mu^* = 0.29$ and in frame (b), $\mu^* = 0.12$ [76]. (Images courtesy of C. Philips, University of Glasgow.)

ground effect wake primarily consisted of the rotor tip vortex system, seen to expand along the ground upstream of the rotor. A flow separation zone is formed in the flow-field as a result of the rotor wake and freestream interactions and causes the trailing vortices to leave the ground and to be directed back towards the rotor by the freestream. While some of these vortices appeared to be re-ingested through the rotor, tests at both normalised advance ratios showed most of the vortices to accumulate in the flow region between the rotor and the separation zone. With the tested normalised advance ratios corresponding to the recirculation flow regime, results from these experiments were in contrast with observations from previous flow visualisation studies conducted by Curtiss *et. al* [24] and Ganesh *at. al* [31], which suggest the re-ingestion of tip vortices during the recirculation regime to be a well-defined process.

Visualisations of the brownout flow-field also revealed particle transport mechanisms at work in the wake. Dust particles at the ground were seen to be transported by traction, saltation and suspension; processes associated with particle transport by wind identified in sedimentology studies. Depending on the sizes of the particles, some were seen to be entrained by the vortices and follow their trajectories, while some were seen to be uplifted from the ground before they returned back to the ground some distance away. Some of the heavier particles were seen to roll along the ground in the direction of the tip vortex trail along the ground. Observations of the particle transport mechanisms at work in the ground effect flow-field proved the need for complex transport models to be incorporated in simulation models of brownout to accurately predict dust cloud formations.

Comparisons of the flow visualisations performed at two different normalised advance ratios also showed important differences in the flow-field, which may influence the formation of the dust cloud. The lower normalised advance ratio case showed significant vortex mergers occurring near the ground plane, a feature less prominent at the higher normalised advance ratio test. Vortices leaving the ground plane were also seen to accumulate ahead of the rotor more frequently at the lower normalised advance ratio, while the re-ingestion process was seen to be more common at the higher normalised advance ratio. This accumulation process was seen to induce further dust pick up from the ground, as the vortices along the ground were seen to be accelerated by the accumulating vortices, causing large quantities of dust to be uplifted from the ground as these accelerated vortices leave the separation zone. While these explain the larger size of the dust cloud at the lower normalised advance ratio, they fail to explain the instances when the dust clouds reach regions of the flow-field further than the rotor height above the ground. Such sporadic expansion of the dust clouds were clearly visible at both normalised advance ratios, and highlight the unsteady nature of the wake. Further quantitative insights into the ground effect wake of rotors are required before these unsteady features, and the dust cloud evolution during the brownout phenomenon can be better understood. Based on this, quantitative velocity measurements of the ground effect wake were conducted using Particle Image Velocimetry. Wide areas of the flow-field close to the rotor were investigated to provide further insights into the formation of the brownout dust clouds. Results from these tests are described in the following chapter.

Chapter 4

Preliminary Ground Effect Investigations

4.1 Introduction

As a continuation of the preliminary investigations of rotors in ground effect, PIV was used to investigate the salient flow structures present in the ground effect wake. Results from these experiments were used as guidelines for the set-up of the larger scale ground effect experiments that were to be conducted. Flow characteristics identified from the PIV could also be used to explain features of the dust cloud evolution observed from the brownout flow visualisation experiments.

PIV results from experiments conducted using the rotor model that was used in the flow visualisations experiments are presented in this chapter. Additionally, the effect of blade root cut-out ratio on the fluid dynamics of the ground effect wake was analysed by using the same rotor model with a different root cut-out ratio. Details of the PIV experiments conducted were discussed in Section 2.4 and some of the important rotor and experimental parameters are listed in Table 4.1.

Results presented in the following sections mainly cover a $2.0R \times 2.0R$ field-of-view of the rotor ground effect wake, as was represented schematically in Figures 2.2 (c) - (d). Wide areas of the ground effect flow-field, particularly regions immediately upstream and under the rotor disk were measured to track the evolution of the

Experimental Parameters	**Values**
Rotor Model	Rotor A (including root cut-out)
Radius (R)	$0.075m$
μ^* tested	0.3 - 1.3 (max)
Ground distances tested	0.5R, 1.0R, 1.5R & 2.0R
Rotor C_T (OGE)	0.015
Rotational Speed	$5640RPM$ $(94Hz)$

TABLE 4.1: Rotor parameters for the preliminary PIV investigations using model Rotor A.

ground effect wake. Double frame, double pulse PIV was conducted and 300 image pairs recorded for each test case, with the inter-pulse time delay, Δt, between the successive images set at $\Delta t = 90\mu s$. This inter-pulse time delay was appropriate for experiments that were conducted between a freestream velocity range of $1.2ms^{-1} < V_\infty < 4.75ms^{-1}$.

4.2 PIV Data presentation and validity

PIV is a non-intrusive technique used for measuring velocity over a wide area of the flow-field in a near instant. It is particularly advantageous for the investigation of unsteady flows since the vorticity is readily obtained from a single snap-shot of the velocity field. Statistics of the unsteady flow can also be calculated if a sufficiently large number of velocity fields are captured. Turbulent investigations of the wake produced by a small hovering rotor, conducted by Ramasamy *et. al* using PIV, showed that a sample of 100-200 velocity fields were required to capture the first-order velocity fluctuations within the wake [77]. In these preliminary investigations, the selected PIV field-of-view, choice of time delay, seeding density and the thickness of the light sheet were seen to combine to produce a high resolution velocity map of excellent fidelity. The chosen PIV sample size additionally allowed for velocity fluctuation information to be derived from the velocity maps.

For this preliminary analysis, PIV was used to obtain the (u, v) velocity field in the (r, y) plane. In the forthcoming sections, PIV data will be presented in a series

of velocity, vorticity or flow pathline plots, and are scaled with respect to the rotor radius, R, with $\frac{r}{R}$ representing the normalised spanwise location in the flow-field and $\frac{y}{R}$, the normalised distance above the rotor disk. In these plots, the rotor hub is at the origin of the co-ordinate system used, $(\frac{r}{R}, \frac{y}{R}) = (0, 0)$, and the leading edge blade tip at the ordinate $(\frac{r}{R}, \frac{y}{R}) = (1, 0)$. If present within the field-of-view, the rotor disk is represented by a black line in the velocity and vorticity plots (or by a red line in the flow pathline plots). The ground plane is represented in these plots by a black line along $\frac{y}{R} = -1$. The u and v velocity components presented in these plot represent the longitudinal and vertical velocity components along the (r, y) directions. Velocity, where presented, has been scaled with V_h, where $V_h = V_{tip}\sqrt{\frac{C_T}{2}} = 3.84ms^{-1}$, is the hover induced velocity ($V_{tip} = \Omega R = 44.3ms^{-1}$ is the rotor tip speed) and vorticity has been scaled with $\frac{V_h}{R}$.

4.2.1 Data Validity

PIV data can be subjected to a variety of errors affecting the accuracies of the results. Systematic bias errors are most common in PIV data and can be revealed using velocity histograms [78]. The most common error affecting digital PIV is peak-locking, a situation where the computed velocity fields have results biased toward discrete values, resulting in the velocity vector maps to have block-like appearances. The velocity histograms for a peak-locked velocity field will appear distorted and contain peaks. This situation occurs primarily due to the small size of the seeding particles producing a sub-pixel particle image on the camera chip [78]. In these preliminary experiments, the only velocity clustering tended to occur around the imposed wind tunnel speed and around zero velocity (corresponding to masked out-of-bounds areas and low magnitude u and v velocity components). The absence of peak-locking around other values of velocity indicates a well-conditioned experiment and analysis for PIV, notwithstanding loss of detail associated with the low spatial resolution of the PIV in the vortex cores.

4.2.2 Experimental Validity

Limitations imposed by the size of the wind tunnel facility and the huge spatial extent of the ground effect wake meant constraints on rotor size. Smaller rotors had to be used to allow the ground effect wake to develop to its full extent without any

interference from the wind tunnel walls. This implies low chord based Reynolds number, $Re_c < 1,000,000$ for the experiments. The main issue however, regarding the fluid dynamics of the wake is the circulation Reynolds number, $Re_\Gamma = \frac{\Gamma_{TV}}{\nu}$, where Γ_{TV} is the tip vortex circulation, and ν, the kinematic viscosity of air. Literature states that if this Re_Γ is above a moderate value of at least 10,000, the vortex wake dynamics will be inertia dominated [79] and can be considered to be representative of those of much larger rotor systems.

For the preliminary experiments conducted using Rotor A, the representative chord based Reynolds number was 26,000. With the rotor in hover, the out of ground effect thrust coefficient was measured to be $C_T = 0.015$. A range of advance ratios was investigated by varying the wind tunnel speed accordingly, with the rotor rotational speed maintained at $5640RPM$ $(94Hz)$. The thrust coefficient was observed to remain constant over the range of advance ratios tested. In hover, the PIV data indicated a tip vortex circulation Reynolds number of $Re_\Gamma = 15,000$ close to the rotor disk plane.

4.3 PIV Analysis of the ground effect flow-field

PIV analysis of a flow produces velocity vector maps for the flow region under investigation. When averaged, these are helpful in identifying gross structures present in the flow-field. Figure 4.1 shows the average velocity plot of the ground effect wake, derived from 300 instantaneous samples of the flow-field, with the rotor at a distance of half a diameter from the ground plane ($\frac{h}{R} = 1.0$) and operated at a normalised advance ratio of $\mu^* = 0.65$. The direction of the flow is indicated by the vector directions while the velocity magnitudes are represented by the contours in the plot. From the figure, it can be seen that the flow along the ground plane comprised of high magnitude velocity, which is seen to reduce to zero at a particular point along the ground. With reference to the flow visualisation images of the ground effect flow-field, this point is identified as the flow separation point. In the case of the PIV, the flow separation location is topological [80] and identified through analysis of the u-velocity component close to the ground plane. The location along the ground where the u-velocity component changes sign is identified as the point where the freestream flow encounters the rotor wake

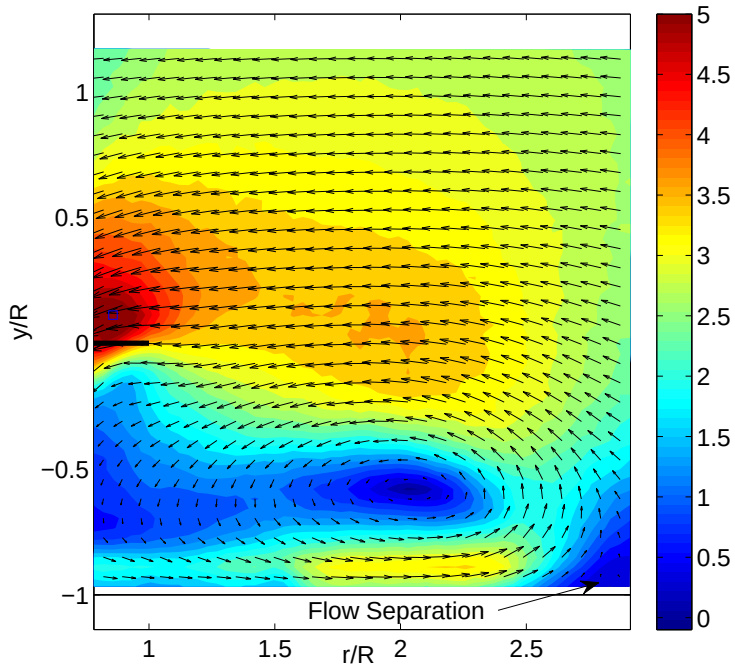

FIGURE 4.1: Mean velocity vector map, showing the velocity magnitude, flow separation location and recirculation region in the ground effect flow-field. The rotor was at a ground distance of 1.0R and operated at a normalised advance ratio of $\mu^* = 0.65$.

expanding along the ground upstream from the rotor. Interactions between the opposing flows result in the formation of a separation point, where the u-velocity component will be zero. A linear interpolation scheme is utilised to identify from the PIV velocity plot the location along the ground plane where the u-velocity component is zero. Figure 4.1 also shows the flow leaving the ground at the topological flow separation point location, being re-directed back towards the rotor and forming a recirculatory region just ahead of the rotor disk. Velocity information of the flow-field obtained from the PIV was used to identify the vorticity associated with this recirculatory flow region and its extent of influence in the ground effect flow-field.

Flow pathlines and vorticity ($\omega = \frac{\partial v}{\partial r} - \frac{\partial u}{\partial y}$) constructed from the mean velocity for $\mu^* = 0.3$, $\mu^* = 0.65$ and $\mu^* = 0.9$ with the rotor at a ground distance of half a diameter ($\frac{h}{R} = 1.0$) are presented in Figure 4.2. Mean flow pathlines are derived by placing seed points at selected locations in the velocity field, and the pathlines are formed by tracing a particle released from each seed point. These flow patterns are only cartoons; in reality, the flow is three-dimensional and unsteady, so

no pathline pattern like those presented would ever be observed, but they are a useful aid in interpreting the results.

Figure 4.2 presents data from different camera fields-of-view (as discussed in Section 2.4), depending upon the locations of the salient flow structures of the wake at the different normalised advance ratio settings. For the lowest setting of $\mu^* = 0.3$, the mean flow pathlines in Figure 4.2 (a) show a recirculation zone centered at around 3R, approximately one diameter ahead from the leading edge of the rotor disk. The mean topological flow separation point is to the far right, off the view of the image. Vorticity, corresponding to the flow-field at $\mu^* = 0.3$ is presented in Figure 4.2 (b), and shows a region of low positive vorticity extending to around 4R upstream of the rotor hub and to a height of around $\frac{y}{R} = 0.6$ above the rotor disk. Most of this vorticity is contained within the recirculation zone seen in Figure 4.2 (a), although significant vorticity levels are seen higher than this recirculation zone. A thin ribbon of high vorticity is seen at the left side of the image and this corresponds to the trailing rotor wake expanding along the ground. It is the separation of this expanding wake at the separation point that results in the formation of the recirculatory region and vorticity ahead of the rotor disk.

As the normalised advance ratio was increased, flow separation was seen to occur closer to the rotor disk. The vorticity region resulting from this separation was seen to be more compact and confined within a smaller area, carrying greater vorticity magnitudes. Figure 4.2 (c) shows the flow-field at $\mu^* = 0.65$, and the mean separation is seen at the right edge of the mean flow pathline plot. The corresponding mean vorticity, shown in Figure 4.2 (d), is stronger and confined within a smaller zone than the lower normalised advance ratio case, reaching heights of around $\frac{y}{R} = 0.2$ above the disk. Further increments in normalised advance ratio showed the resulting recirculation region to be tucked under the rotor disk and the topological flow separation to occur very close to the rotor disk. At $\mu^* = 0.9$, shown in Figure 4.2 (e), this is seen at $\frac{r}{R} = 1.1$, with the resulting recirculation zone confined under the rotor disk, and the vorticity seen from Figure 4.2 (f) to just reach to about $\frac{y}{R} = -0.3$. The high magnitude positive vorticity to the left of the recirculation zone, extending from the rotor disk plane, is the rotor tip vortex system. The negative vorticity trail seen at the left edge of the image is the root vortex system trailing from the rotor. The evolution of the ground effect wake

is evident from these plots, which show the main feature of the wake, the region of recirculation, to evolve from a wide-spread area of relatively low vorticity at low advance ratios, to a small concentrated vortex of high magnitudes at higher advance ratios.

Mean vorticity data obtained from the PIV tests show the presence of a region of recirculation and vorticity at every normalised advance ratio examined. It is evident from both the PIV and the flow visualisations that the tip vortex track along the ground feeds this region of recirculation and its resulting path is key in the size, location and formation of this feature. Information on the tip vortex trajectories can be obtained from the PIV through the instantaneous snap-shots of the flow-field. As an example, Figure 4.3 presents instantaneous vorticity data from the ground effect flow-field obtained at a normalised advance ratio of $\mu^* = 0.65$, and shows the typical paths taken by the tip vortices, the clusters of high magnitude positive vorticity in the flow-field. Corresponding velocity data from the PIV showed the tip vortices leaving the ground around the topological flow separation point and initially heading back towards the rotor. As these vortices were seen to move back towards the rotor, they were seen to either accumulate and merge ahead of the rotor disk, as in Figure 4.3 (a) or were seen to be directed back towards the rotor disk, as in Figure 4.3 (b).

Curtiss *et.al* described the ground effect wake in the recirulation regime to show recirculation of the trailing rotor wake through the rotor disk [24, 27]. Based on this, Ganesh *et. al* identified re-ingestion of a loop of tip vortices through the rotor disk (see Figure 1.7) as indicative of the recirculation regime [30, 31]. Extensive testing at a ground distance of $\frac{h}{R} = 1.0$ during this preliminary ground effect investigation showed flow features similar to that used to define the recirculation regime to exist at normalised advance ratios between $0.3 < \mu^* < 0.9$. In this advance ratio range, some instantaneous vorticity plots showed part of the trailing rotor wake to be re-directed back towards the rotor disk leading edge, implying re-ingestion, and an example of this is shown in Figure 4.3 (b). However, this was not consistently observed in all the instantaneous plots, with some of the instantanous vorticity plots showing vorticity to be accumulated close to the ground plane, ahead of the rotor disk, in a manner similar to that shown in Figure 4.3 (a). Similar observations were made from the movie sequences obtained from the

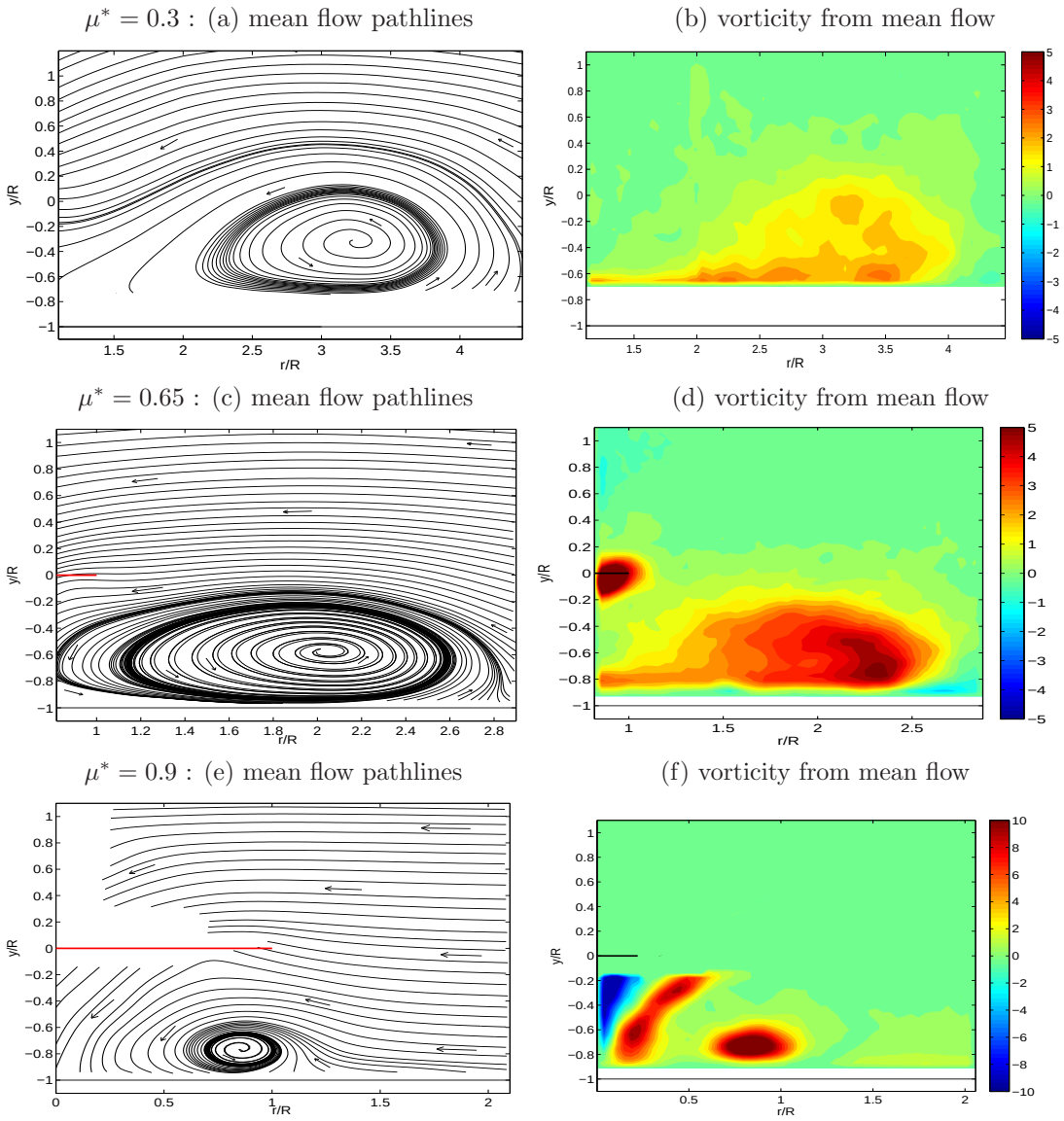

FIGURE 4.2: Mean flow pathlines and mean non-dimensional vorticity from PIV for the rotor at 1.0R above the ground for $\mu^* = 0.3$ (frames (a) and (b)), $\mu^* = 0.65$ (frames (c) and (d)) and $\mu^* = 0.9$ (frames (e) and (f)). For (a) and (b) the field-of-view is from 1R to 4.5R upstream of the rotor hub, while for the higher normalised advance ratios, the field-of-view is smaller and includes some of the flow below the disk. The images in frames (a) and (b) are obtained using a higher resolution camera to capture the spread of the wake at this low μ^*. In frame (f), the vorticity scale has been changed to account for the higher magnitude vorticity in the more concentrated ground vortex tucked under the rotor.

brownout flow visualisation. Although this normalised advance ratio range falls within the recirculation flow regime defined by Curtiss *et. al*, the PIV data did not show the consistent recirculation/re-ingestion of the wake used to define this flow regime [24, 27, 30, 31]. Instead, the PIV data implied that vorticity was occassionally re-ingested through the rotor disk, thus suggesting a complex flow-field in this advance ratio range.

The ground vortex regime, identified by Curtiss *et. al* [24, 27] to be characterised by the presence of a concentrated vortex under the rotor disk, was seen from these preliminary PIV investigations to exist between $0.9 < \mu^* < 1.2$ for this rotor ground distance. Instantaneous vorticity plots in this ground effect regime showed a tight vortex just under the rotor disk leading edge, showing little movement in its location. An example of this is shown in Figure 4.4, where a compact vortex, with vorticity strength comparable to the strength of the tip vortex system leaving the rotor disk, is seen to be the dominant feature of the flow-field. In this plot, the traces of positive vorticity seen around and above the rotor disk leading edge are processing artefacts, resulting from surface glare off the rotor rig components. As the normalised advance ratio was increased, this ground vortex was seen to become weaker, smaller and form more inboard of the disk leading edge. The ground vortex was eventually seen to disappear from the flow-field at around $\mu^* = 1.2$. Comparisons of the flow features in the ground vortex regime, identified through the PIV, were consistent with observations made by Curtiss *et. al* [24, 27] and Ganesh *et. al* [30, 31], unlike the case of the recirculation regime.

The instantaneous vorticity plots also revealed the presence of clumps of negative vorticity in the flow, not visibile in the mean vorticity data due to the averaging process. These negative vorticity concentrations were seen to be more prominent and stronger in magnitudes at the higher normalised advance ratios, $\mu^* > 0.65$. An example of this is shown in Figure 4.3 (a), where clumps of negative vorticity are seen close to the ground and higher up. The source of this negative vorticity is attributed to secondary separation induced by the rotor tip vortex system trailing along the ground plane. Evidence for this secondary separation was provided by the brownout flow visualisation movies, where talcum powder particles, especially along the ground plane, were seen to swirl in a rotational sense opposite to that of the tip vortices (see Figure 3.5). The PIV data presented by Ganesh *et. al* [32, 36]

(a) Accumulation of tip vortices (b) Tip vortices re-directed towards rotor

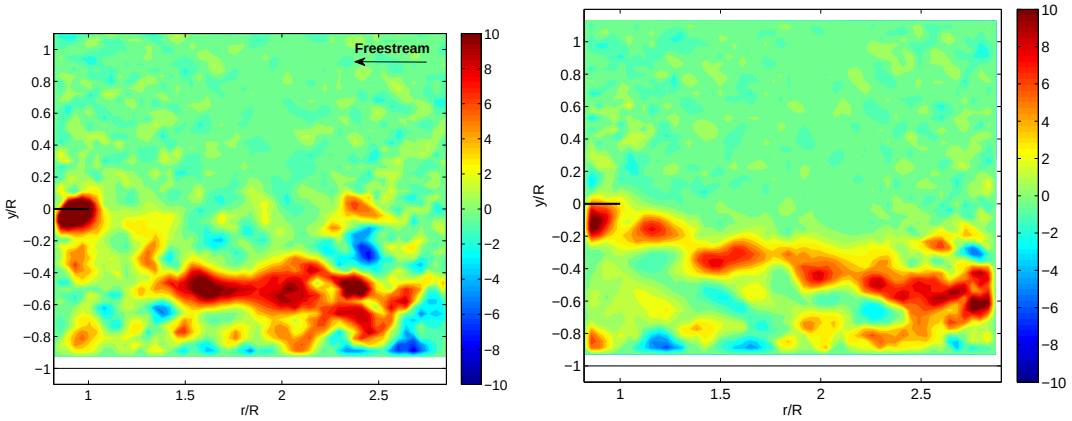

FIGURE 4.3: Instantaneous vorticity plots from PIV for the rotor at 1.0R above the ground for a normalised advance ratio of $\mu^* = 0.65$. Frame (a) shows the accumulation of the tip vortices ahead of the rotor while frame (b) shows the re-direction of the tip vortices towards the rotor disk leading edge.

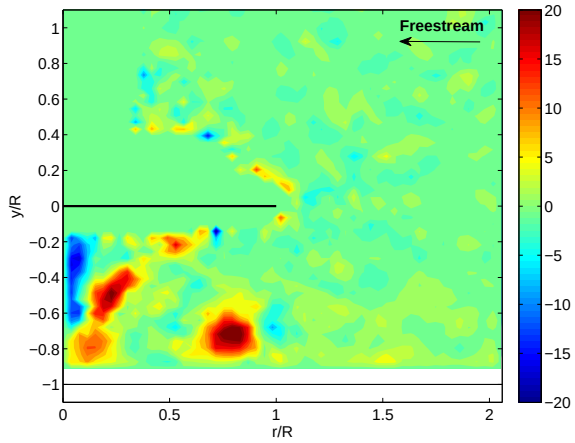

FIGURE 4.4: Instantaneous vorticity plot showing a ground vortex formed just under the leading edge of the rotor disk plane. The rotor was at a ground distance of 1.0R and operating at a normalised advance ratio of $\mu^* = 0.9$.

do not show any trace of this negative vorticity, although this may be due to the resolution of their PIV data. Their PIV experiments made use of particles with nominal diameters of 0.19mm, far larger than the particles used in this research. This will have an effect on the accuracy and spatial resolution of the PIV, making vortical features in the flow-field difficult to visualise.

(a) Mean vorticity at $h/R = 1.0$ (b) Mean vorticity at $h/R = 0.5$

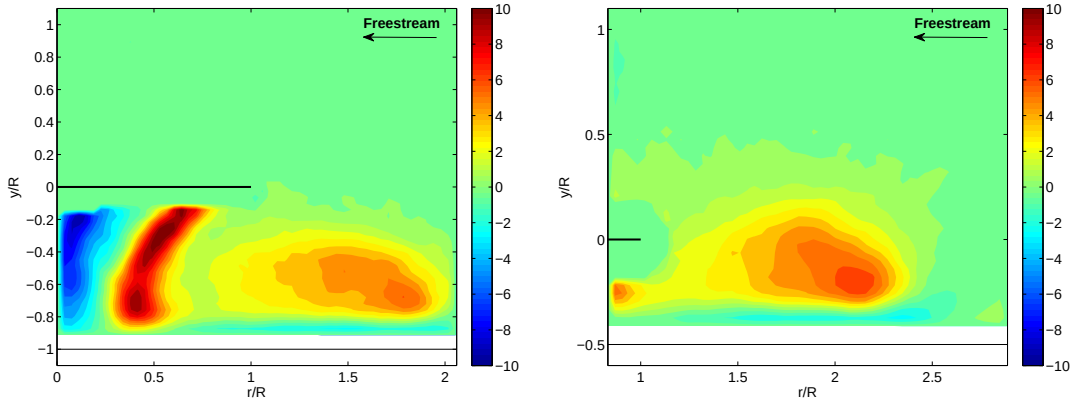

FIGURE 4.5: Mean vorticity plots from PIV for the rotor at 1.0R and 0.5R above the ground for $\mu^* = 0.7$. For frame (a), the field-of-view is under the rotor disk while the field-of-view is just ahead of the rotor disk for frame (b).

4.3.1 Investigation of rotor ground distance variations

Variations in the rotor ground distance was seen to displace the location of the region of positive vorticity for the range of forward flight speeds tested. A reduction in the rotor ground distance was seen to extend the wake further upstream, and cause the mean recirculation (vorticity) region to extend to greater heights above the rotor disk plane. Figure 4.5 compares the location of the region of vorticity for the same normalised advance ratio of $\mu^* = 0.7$, at rotor ground distances of half a diameter (1.0R) and a quarter of a diameter (0.5R). Figure 4.5 (a) shows the vorticity centroid located at $\frac{r}{R} \approx 1.6$, whereas this is located at $\frac{r}{R} \approx 2$ in Figure 4.5 (b). These shifts in the location of the recirculation zone were comparable to the observations made from the flow visualisation experiments conducted at similar ground distances. The vorticity strengths of these regions were observed to be comparable despite the differences in their locations.

Shifts in the mean flow separation location and recirculation zone at different rotor ground distances imply a change in the normalised advance ratios at which the different identified ground effect flow regimes occur. A reduction in ground distance, seen to move the separation zone further upstream, implies that both the recirculation and ground vortex regimes occur at higher advance ratios. At higher ground distances, the effect is opposite. These observations coincide well with observations established by Curtiss *et. al* [24, 27].

4.3.2 Investigation of blade root cut-out ratios

Influence of the rotor blade root cut-out ratio on the dynamics of the ground effect wake was also investigated in these preliminary PIV investigations. It is well known that during hover in ground effect, the presence of a root cut-out creates a gap in the middle of the disk, through which some of the rotorwash is allowed to escape. This "fountain-effect" allows parts of the rotor disk nearer the hub to be influenced by an upflow, thus reducing the overall thrust required by the rotor [81]. In forward flight, this effect is eliminated by the skewing of the wake, although the overall influence of ground effect has not been quantitatively investigated.

Rotor A was modified to incorporate a blade root cut-out ratio. Both the leading edge and trailing edge portions of the inner 40% of the rotor span were cut away so that little or no useful lift would be generated over the inboard section of the rotor disk. Root cut-outs have a direct influence over the effective spanwise distribution of lift [82] and hence the thrust coefficient, C_T. To facilitate comparisons at similar normalised advance ratios with the unmodified rotor, the physical thrust was maintained at the same value by changing the rotational speed of the rotor. For these experiments, the rotor was operated at $6180RPM$ $(103Hz)$, with a thrust coefficient of $C_T = 0.013$.

Figure 4.6 presents the mean vorticity plots at a normalised advance ratio of $\mu^* = 0.7$ for the rotor $1.0R$ off the ground, with Figure 4.6 (a) showing the flow-field from the basic configuration and Figure 4.6 (b) showing the flow-field from the root cut-out configuration. It was important here that the flow beneath the rotor was seen, so the laser sheet was positioned so that the in-board flow up to about $0.2R$ of the blade could be seen. The root cut-out ratio was observed to move the region of vorticity upstream and away from the rotor, and the resulting mean vorticity within the region was seen to be slightly reduced compared to the wake from the unmodified rotor. The lower vorticity levels were also observed to penetrate higher into the flow-field; this is a consequence of the mean flow separation occurring further from the rotor disk. In the case with the root cut-out, it was also observed that the magnitude of the tip vorticity was higher. Additionally, the root vorticity, the inboard region of negative vorticity immediately under the rotor disk, appeared to be more prominent. This is a consequence of the root cut-out on the rotor disk,

(a) no root cut-out (b) 40% root cut-out

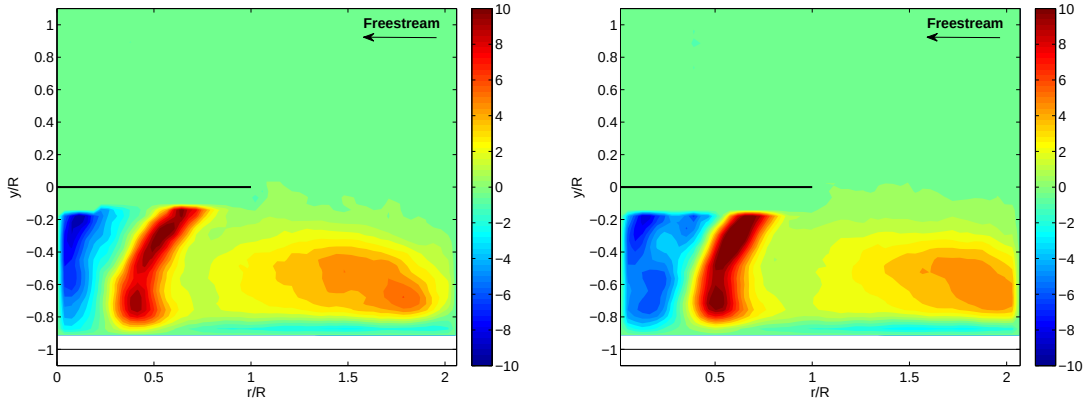

FIGURE 4.6: Effect of root cut-out on mean vorticity. In both cases the rotor ground distance was 1.0R, and operating at a normalised advance ratio of $\mu^* = 0.7$.

and may be due to the formation of a counter-rotating root vortex system inboard of the rotor disk. Similar observations were made at the other normalised advance ratios tested. The higher tip vorticity is expected, as the root cut-out reduces the rotor solidity, and for the same physical thrust the induced velocity at the disk must be higher. This in turn leads to a more upstream projection of the recirculation zone in the case of the root cut-out, due to the higher rotor induced velocity along the ground. This would explain the lower maximum vorticity within the recirculation zone, and the overall effect is similar to a slight reduction in normalised advance ratio.

4.4 Brownout Flow Visualisation and PIV Results Comparisons

Quantitative and qualitative measurements of the flow around a rotor in ground effect forward flight, were conducted as part of preliminary investigations of the ground effect flow-field. A simple, small scale rotor model was used for these tests with the rotor untrimmed in all the experiments, but this should not affect the basic phenomena under investigation. Trim could be achieved in real helicopters through the centre of gravity (c.g.) position or through the usage of cyclic pitch controls. In these experiments, the c.g. location and the trim state of the isolated rotor model is of little significance although this will become meaningful when

comparisons with other similar research on isolated rotors are conducted. Also in these experiments, the ground was stationary relative to the rotor hub. As it was established early through the flow visualisation and the PIV that the ground effect wake is a result of the rotor tip vortices tracking along the ground, the relative velocity effects at the ground plane plays a significant part in the wake development. These preliminary PIV experiments conducted are hence not a true kinematic representation of a rotor moving over a stationary ground, although they provide a useful platform for qualitative (and limited quantitative) analysis of the ground effect flow.

The brownout flow visualisation experiments have proven to be a highly effective way of visualising the dust cloud generated by the rotor near the ground. Dust pick-up processes and the ground effect flow features affecting these processes could be clearly seen from the flow visualisation movie sequences. PIV was used to measure the velocity in selected areas around the rotor, and the magnification used allowed the image processing algorithms to produce high fidelity velocity maps that were almost completely free of erroneous measurements [78]. Quantitative data from the PIV showed the ground effect flow-field to be characterised by a trail of tip vortices along the ground forming a mean flow separation zone and a region of mean recirculation containing positive vorticity ahead of the rotor. Varying normalised advance ratios were seen to affect the trailing tip vortex trajectories, and this was seen to influence the classification of the wake into the different ground effect flow regimes.

Based on the instantaneous flow-field data obtained from the preliminary PIV tests, the ground effect wake could be classified into the ground vortex flow regime defined by Curtiss *et. al* [24, 27]. At a particular advance ratio influenced by the rotor ground distance, flow separation was seen to occur very close to the rotor disk and the resulting region of vorticity was observed to form under the rotor. At these normalised advance ratios, the flow-field essentially consisted of a ground vortex, tightly packed and high in vortex strength; this was similar to the observations made by Curtiss *et. al* [24, 27] about the flow-field in the ground vortex regime. Extensive PIV testing using Rotor A at a ground distance of 1.0R, showed the ground vortex regime to exist between $0.9 < \mu^* < 1.2$, with the ground vortex disappearing from the field-of-view for the current PIV set-up at $\mu^* > 1.2$. At

lower normalised advance ratios between $0.3 < \mu^* < 0.9$, no ground vortex was observed in the flow-field, although a wide region of vorticity was seen to exist ahead of the rotor disk leading edge.

Analyses of the instantaneous flow data at these normalised advance ratios ($0.3 < \mu^* < 0.9$) showed the flow-field to be largely varying, with the vorticity associated with the trailed tip vortices located in continuously different regions of the imaged flow-field. PIV data from each normalised advance ratio within this range showed a mixture of images showing accumulation of vorticity near the ground ahead of the rotor leading edge, and a wider spread of vorticity throughout the imaged field-of-view, particularly close to and above the rotor disk, implying a re-ingestion of this vorticity. This was in contrast with observations made by Curtiss *et. al* [24, 27], who classified the ground effect wake at these normalised advance ratios to be the recirculation regime as it showed a well-defined recirculation of the trailing rotor wake through the rotor disk. The continuously evolving flow-field recorded by the PIV at these normalised advance ratios ($0.3 < \mu^* < 0.9$), showing only occasional re-ingestion of the vorticity, meant that the flow was more complicated than suggested, and could not be classified into the recirculation flow regime defined by Curtiss *et. al* [24, 27].

The distinct difference between observations made by Curtiss *et. al* [24, 27] and observations from the PIV, at normalised advance ratios between $0.3 < \mu^* < 0.9$, may be due to the differences in the experimental conditions between the two sets of tests. A towing facility, with an isolated rotor model moved over the ground was used by Curtiss *et. al* [24, 27], while these preliminary PIV experiments were conducted in a wind tunnel with a fixed stationary ground. This essentially makes the ground boundary conditions different between the two cases and may be the likely reason for the absence of consistent recirculation [24, 27] and the recirculation loop [30, 31] from the PIV data at these normalised advance ratios. In addition to this, the wind tunnel ground boundary layer will have an added effect on the ground effect wake in these PIV tests. Assuming that the ground board was a flat plate, the average wind tunnel boundary layer thickness at the rotor location on the ground board was calculated to be around 1cm for these preliminary tests; when scaled with respect to the rotor radius, this amounts to 0.15R. With both the PIV and the flow visualisations suggesting secondary flow

separation caused by the passage of the tip vortices along the ground plane, the presence of this ground boundary layer ahead of the rotor must have an effect on this process. Further investigations of the effect of the ground boundary conditions on the formation of the ground effect wake, are however required before an explanation can be provided for these observed differences in the ground effect flow-field.

Based on the current fixed ground plane test conditions, a comparison of the PIV results and brownout visualisations showed the dust cloud to extend at least as far forward as the mean vorticity region ahead of the rotor, identified from the PIV. This can be observed when comparing Figures 4.2 with Figures 3.1 and 3.2 from Chapter 3. In Figure 4.2 (d) the positive vorticity region is seen to extend as far forward as about $\frac{r}{R} = 2.6$, while in Figure 3.1 for the same normalised advance ratio of $\mu^* = 0.65$, the dust cloud was seen to extend by just under 2R forward of the tip of the disk, equivalent to just under 3R from the hub. The corresponding values for the normalised advance ratio case of $\mu^* = 0.3$ are 4.5R for the PIV vorticity (as shown in Figure 4.2(b)) and 3.8R for the brownout case (as shown in Figure 3.2), although the brownout test was conducted at a higher normalised advance ratio value of $\mu^* = 0.37$ where the dust cloud would have been smaller. Inspection of the brownout movie sequences showed that while dust particles suspended in the flow close to the ground showed rotation corresponding to positive vorticity, those forming parts of the dust cloud high up above the ground showed no preferred sense of rotation. PIV results showed only weak positive or negative vorticity extending far above the level of the rotor disk, but where the dust cloud was seen to extend the highest, the vorticity (or at least the lateral component resolvable in these experiments) was of low magnitude and no preferred sign.

Observations from the brownout visualisations showed the dust pick-up processes to be similar to the suspension, saltation and traction processes seen in wind-blown processes and sedimentology [54]. In general, these processes are related to a surface shear and a threshold velocity that initiates particle movement along the ground. The flow visualisation movie sequences showed the tip vortices to track rapidly along the ground plane and velocities relating to these cases were measured in the PIV experiments.

Figure 4.7 shows an instantaneous snap-shot of the normalised velocity field corresponding to the $\mu^* = 0.65$ case, also tested in the flow visualisation experiment. High velocity magnitudes are seen just above the ground and these occur along the track of the ground trailing tip vortices, identified from the PIV vorticity plots. With the flow visualisation movie sequences showing the ground dust particles becoming airbourne just ahead of the tip vortices as they trail along the ground plane, the high magnitude velocity zones observed in this velocity plot would appear to be broadly coincident with the locations where the dust is picked up off the ground plane. Presence of high velocity imply high shear in these zones, and the direction of the high velocity being away from the ground provides further evidence of particle uplift and transport towards the flow separation point.

Dust uplift near the ground thus occurs due to the high velocity bearing rotor-wash expanding along the ground plane. As the tip vortices from the rotor blade trailing edge are transported along with this downwash along the ground plane, vorticity associated with the tip vortices are also tagged along with the flow and the dust uplifted at the ground. Vortex lines move with the fluid, resulting in the location of the high velocities, vorticity and dust to coincide. The dust particles, once uplifted from the ground, will follow their own trajectories, depending upon their relative sizes and densities. Smaller particles will tend to follow the flow closely, resulting in the recirculation zone to be heavily contaminated by the dust. This forms a cloud ahead of the rotor disk, which results in the so-called brownout phenomenon. Larger particles uplifted from the ground by the trailing tip vortices will be ejected from regions of high spatial and temporal accelerations to contaminate the wider flow-field. Figure 4.8 shows a schematic diagram of the sequence resulting in the formation of the dust cloud in the ground effect flow-field.

With the location of dust particles coinciding with regions of high magnitude velocity zones and the flow visualisation images showing occasional bursts of dust particles present in regions of the flow-field higher than the rotor disk above the ground, a more sensitive indicator from the PIV data of the likely presence of ground dust in the flow would be the velocity fluctuations observed in the flow-field. Velocity fluctuation statistics from the PIV data are conveniently represented by the root-mean-square (RMS) velocity fluctuations about the mean and these also provide a good indication of the relative unsteadiness of the flow. Figure 4.9

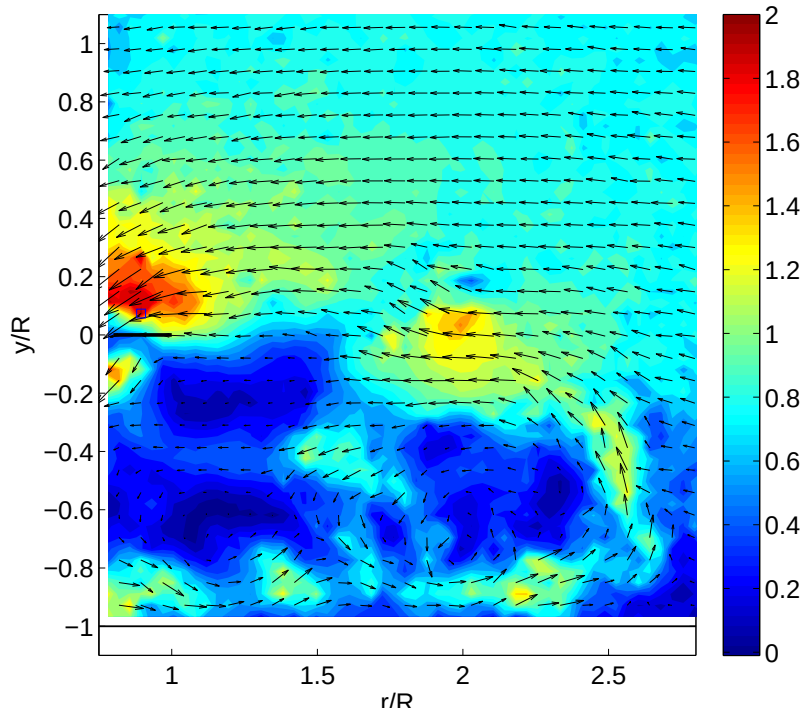

FIGURE 4.7: An instantaneous velocity plot from the ground effect flow-field, where the rotor ground distance was 1.0R and operating with a normalised advance ratio of $\mu^* = 0.65$. The contours show the normalised velocity distribution in the flow-field.

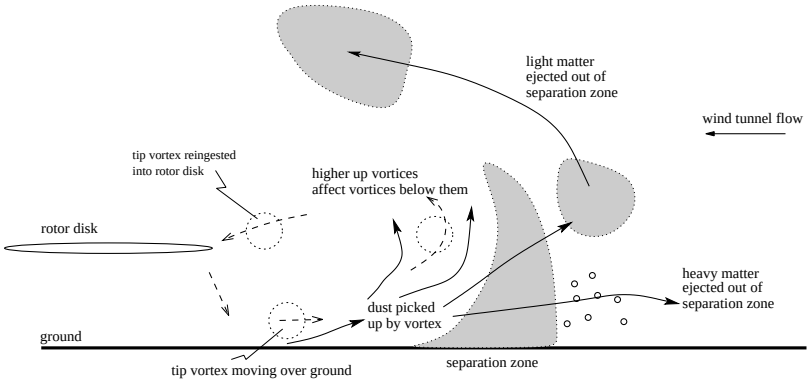

FIGURE 4.8: Schematic diagram of the dust cloud formation during the brownout phenomenon. Vortex and dust particle trajectories are indicated by the dashed and solid lines respectively, and selected areas of dust particle laden flow are highlighted.

shows the RMS velocity fluctuations of the ground effect wake at different normalised advance ratios for cases where the rotor ground distance was 1.0R. Frame (a) of Figure 4.9 features a much larger region of the wake compared to the other frames to allow for the RMS fluctuations associated with the majority of the mean recirculation region to be captured in the plot. Velocity fluctuations are observed to be smaller for the lower normalised advance ratio cases shown in Figures 4.9 (a) and (b), compared to those observed at the higher normalised advance ratio cases, seen in frames (c) and (d). The fluctuations, although lower in magnitude for the lower advance ratio cases, are seen to affect a greater proportion of the flow-field. In the ground vortex regime, represented by frames (c) and (d), the fluctuations are confined within the location of the ground vortex itself and hence are observed to affect smaller regions of the flow-field. These results imply greater unsteadiness in the wake at the lower normalised advance ratios as wider areas of the flow-field were observed to be affected by the velocity fluctuations. This is despite the lower magnitudes of fluctuations observed at these normalised advance ratios.

At the lower normalised advance ratios of $\mu^* = 0.3$ and $\mu^* = 0.65$, the RMS velocity plots show a distribution of the velocity fluctuations experienced within the flow-field, with the higher magnitude fluctuations seen to occur closer to the ground. In regions above the height of the rotor disk, the fluctuations show low magnitudes. Brownout flow visualisation observations at $\mu^* = 0.37$, show the flow-field high above the rotor disk to contain dust on occasion, although this is not reflected in the RMS plots. Examining the PIV velocity history at specific points in the flow, much like placing a hot-wire probe at a particular location, revealed a behaviour in the flow-field, unnoticeable from these RMS plots. Figure 4.10 shows both the u and v velocity component fluctuations experienced at a point $(\frac{r}{R}, \frac{y}{R})$=(2.0, 0.8) in the flow-field, with the rotor at a ground distance of 1.0R and operating at $\mu^* = 0.35$. As can be seen in the plot, there were instances in the flow-field where there was higher or lower velocities relative to the mean. Since the PIV conducted was not time-resolved, the periodicity of the velocity fluctuations could not be determined. Vorticity plots corresponding to a mean case and a high velocity deviation case were considered, as shown in Figure 4.11. The difference between the two frames is clear and at the stated location of $(\frac{r}{R}, \frac{y}{R})$=(2.0, 0.8); frame (a) shows the presence of moderate vorticity concentrations around that region, while frame (b) shows no vorticity around that point. The presence of

(a) $\mu^* = 0.3$: rms velocity

(b) $\mu^* = 0.65$: rms velocity

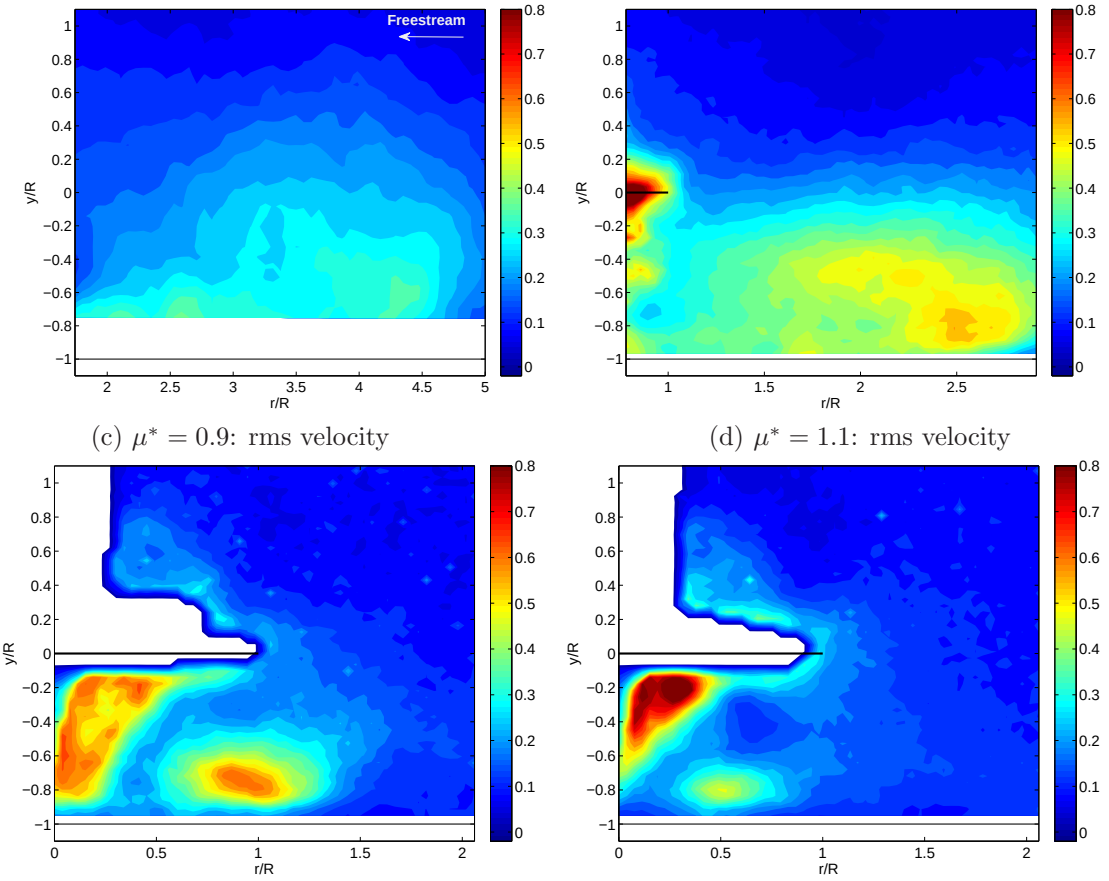

(c) $\mu^* = 0.9$: rms velocity

(d) $\mu^* = 1.1$: rms velocity

FIGURE 4.9: Root mean square velocity from PIV for the rotor at 1.0R above the ground for $\mu^* = 0.3$, $\mu^* = 0.65$, $\mu^* = 0.9$ and $\mu^* = 1.1$.

occasional vorticity concentrations high up in the flow-field, brought about by the velocity fluctuations can explain the occasional bursts in dust seen from the flow visualisations. When this occurs, the fluid, carrying both the vorticity from the tip vortices and the dust particles gets transported high up in the flow-field thus causing the tip vortices (and dust particles) to reach higher up into the flow-field than observed in the average cases. Further investigations are however required to determine the cause of these velocity fluctuations.

4.5 Summary

Preliminary investigations of the ground effect flow-field was conducted using a small rotor model, with fixed pitch. Flow visualisations and PIV investigations were performed to obtain qualitative and limited quantitative information of the

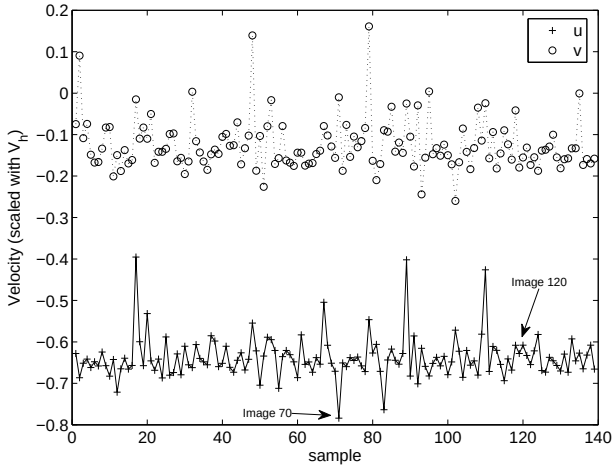

FIGURE 4.10: Velocity fluctuations at a point in the flow-field for the case where the rotor was 1.0R above the ground with the flow at a normalised advance ratio of $\mu^\star = 0.35$. The velocity fluctuations were measured at a point 2R from the rotor hub and at a height of $\frac{y}{R} \approx 0.8$.

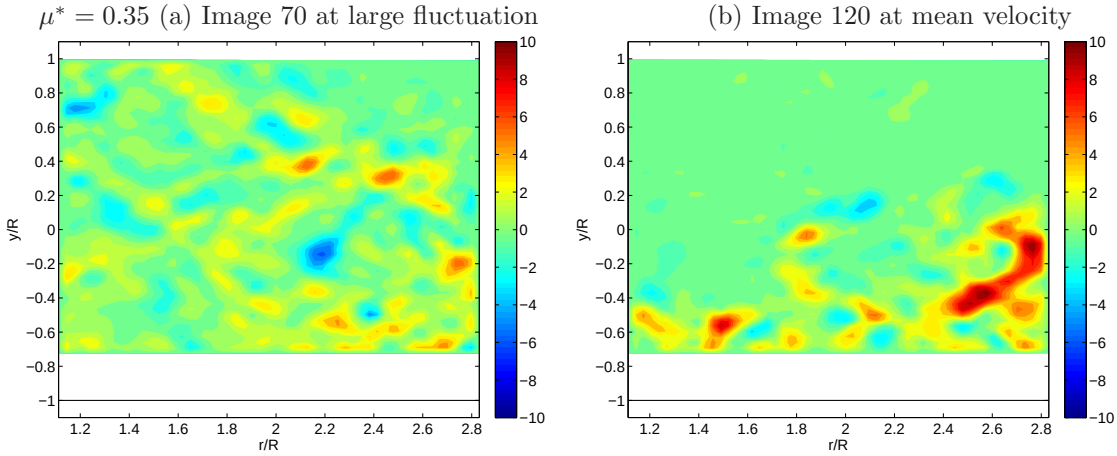

FIGURE 4.11: Individual PIV vorticity plots showing unsteadiness in the flow-field at $\mu^\star = 0.35$. The rotor was at ground height of 1.0R and Frame (a) shows a plot where the vorticity reaches the height of $\frac{y}{R} \approx 0.8$ while Frame (b) shows no vorticity at that height.

ground effect flow-field. The experiments also served as a basis of investigation of the brownout phenomenon, with the PIV data providing quantitative information that could be used to explain certain features observed from the dust cloud flow visualisation experiments.

To summarise the PIV results, it was observed that the ground effect flow-field was characterised by a trail of tip vortices along the ground forming a mean flow separation zone and a region of mean recirculation containing positive vorticity

ahead of the rotor. Both the location of the flow separation and recirculation zone were observed to be a function of the rotor ground distance and advance ratio. Increments in normalised advance ratio was seen to cause flow separation to occur nearer the rotor and the resulting recirculation zone to become more compact in size and contain higher vorticity magnitudes. A reduction in the rotor ground distance was seen to shift the wake further upstream for comparable normalised advance ratios, with the opposite effect observed at higher ground distances. Root cut-out was seen to cause a shift in the mean recirculation region further upstream from the rotor disk and was also seen to affect the mean vorticity magnitudes observed in the flow-field.

A stable ground vortex, formed under the leading edge of the rotor disk, was observed to dominate the ground effect flow-field at the high normalised advance ratios, and this was used to characterise the ground vortex flow regime. At lower normalised advance ratios where the recirculation region was seen to form ahead of the rotor disk leading edge, the instantaneous vorticity data from the PIV showed a constantly fluctuating flow-field. In these cases, the flow-field were seen to either consist of vorticity spread throughout the imaged field-of-view or accumulated close to the ground plane. With only a proportion of the PIV images at each of the lower advance ratios implying a re-ingestion of the tip vortices, the recirculation flow regime could not be characterised from these preliminary PIV investigations. Effect of the ground boundary configuration on wake development may be a cause of this and requires further investigations.

Comparisons of the brownout dust visualisations and the PIV showed the mean recirculation region and the dust cloud to be in comparable locations for similar normalised advance ratios. The PIV velocity maps showed the flow near the ground to contain high velocities, directed away from the ground plane as the rotorwash was seen to trail along the ground. This implies high shear at these locations and explain the uplifting and transport of loose particles from the ground surface. Since vorticity associated with the tip vortices are also carried in this flow, the locations of the vorticity, high velocity and the dust coincide. With the smaller dust particles following the flow closely, this explains the location of most of the dust particles within the recirculation zone as was observed from the flow visualisation. The occasional instances where the dust cloud was seen to penetrate

high above the rotor disk can be explained by velocity fluctuations observed to occur in the flow-field. The PIV tests provide evidence for the existence of these velocity deviations, and corresponding vorticity information show instances where the velocity fluctuations were seen to transport vorticity higher into the flow-field than that observed from the averaged data. This suggests instantaneous velocity fluctuations to be the cause of the intermittent variations in the dust cloud size observed in the flow visualisation movie sequences, although there is no way of validating this unless quantitative measurements are carried out in parallel with the flow visualisations. More sophisticated experimental set-ups with better seeding are however required if this is to be performed.

The preliminary investigations of the ground effect wake were conducted with a rotor model that was not trimmed in any way. Although trim effects will not affect the gross features of the flow-field, comparisons with other ground effect experiments can be difficult if the experiments were conducted with different rotor trim settings. More importantly, the preliminary investigations were conducted in a wind tunnel with a stationary ground surface. This makes the ground boundary conditions different from a helicopter moving over a stationary ground, and has an added effect of the ground boundary layer on the wake to be considered. While this may not have an effect on the gross flow features investigated in these experiments, more sophisticated experiments with a moving ground are necessary to completely investigate the ground effect of a rotor. For the purposes of this research, this was conducted using a moving ground plane installed in the wind tunnel. An isolated rotor model, capable of trim was used to allow for comparisons between the experiments conducted with the varying ground boundary configurations. PIV experimental results from these experiments are presented in the following chapter.

Chapter 5

Large Rotor Experimental Results

5.1 Introduction

This chapter discusses data obtained from PIV tests conducted using the Large Rotor in the Argyll wind tunnel. Both two-dimensional two-component (2D2C) and Stereoscopic PIV tests were performed to obtain quantitative information from wide regions of the ground effect flow-field. A range of rotor parameters (i.e. rotor trim conditions, ground distance and collective angles) and ground boundary conditions were tested to investigate the effects of these on the fluid mechanics of the ground effect wake. All the results presented in this chapter are obtained from PIV tests conducted with the Large Rotor collective angle at approximately $\theta_0 = 8.8^o$ and at a ground distance of $\frac{h}{R} = 1.0$, unless otherwise stated. A summary of the rotor and experimental parameters considered during the PIV tests are presented in Table 5.1 and a schematic of the rotor arrangement in the wind tunnel is presented in Figure 5.1. Further details concerning the experimental methodology can be obtained from Section 2.5.3.

5.1.1 Ground boundary configurations

Investigations of the effects of the ground boundary conditions on the ground effect wake of the rotor were conducted using the rolling road facility installed

Large Rotor	Parameters
Radius (R)	$0.5m$
μ^* tested	0.3 - 1.0
Rotational Speed	$960RPM$ $(16Hz)$
Rotor C_T (in hover)	0.010 at $\theta_0 = 8.8^o$ & 0.015 at $\theta_0 = 12.8^o$
Ground distances	$1.0R$ & $2.0R$
Rotor Configuration	Quasi-Trimmed & Untrimmed
Rolling Road	Stationary $(V_g/V_\infty = 0)$ & Moving $(V_g/V_\infty = 1)$

TABLE 5.1: Large Rotor and experimental parameters used for the PIV tests conducted in the Argyll wind tunnel.

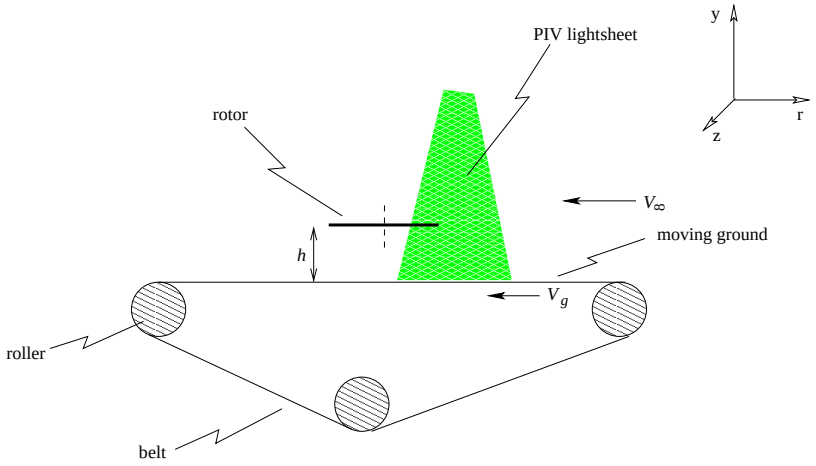

FIGURE 5.1: Schematic diagram of the arrangement of the Large Rotor model in the Argyll wind tunnel.

in the wind tunnel. Ground boundary conditions were varied by changing the rolling road (ground) speed, V_g, relative to the wind tunnel freestream speed, V_∞. Two ground boundary configurations were tested during this research; a stationary ground configuration represented by $V_g/V_\infty = 0$ and a moving ground configuration represented by $V_g/V_\infty = 1$, where the rolling road speed was set to within $\pm 0.1ms^{-1}$ of the wind tunnel speed.

5.1.2 Rotor trim conditions

The preliminary ground effect investigations, presented in Chapter 4, showed significant changes to the shape of the resulting wake as the normalised advance ratio was varied. With changes in the location of the ground effect features known to

affect the inflow through the rotor disk [23, 24, 27], the trim state of the rotor would be different for each advance ratio setting, if a fixed pitch rotor model was used for the investigations. This meant that for a comparison of the ground effect wake at different advance ratios, it was essential that the rotor model could be operated as close to the same trim condition as possible. To facilitate this as well as comparisons/verifications with untrimmed ground effect wake data from fixed pitch models, the Large Rotor rig used for these experiments was designed with trimming capabilities.

Trimming on the Large Rotor was conducted using the cyclic pitch actuation systems (refer to Figures 2.5 and 2.6). In this case, the cyclic pitch angles were adjusted to align the vertical force centroid with the rotor hub. Trimming of the Large Rotor in this manner only allowed for a quasi-trim state; while the load-cell arrangement on the rig allowed for the measurement of the vertical forces acting on the rotor rig, the side forces acting on the rotor system could not be measured, and was thus not accounted for during the trimming process. This means that the trimming method employed by the Large Rotor was not the same as zero rolling and pitching moments obtained during wind tunnel trim, where force equations are solved, or during free-flight trim, where the forces and moments contributed by all the components of the helicopter are considered to derive the rotor disk orientation and control settings [11]. For the purposes of this research, this trim condition is referred to as the quasi-trim state of the Large Rotor. In addition to experiments conducted with the quasi-trimmed Large Rotor, experiments with the Large Rotor in an untrimmed configuration, where the cyclic pitch angles on the rotor were set to zero, were also conducted.

5.1.3 PIV Data presentation and validity

PIV results presented in the following sections are categorised into the experimental configurations tested during the experiments. Four different experimental configurations were tested, and these were namely; (i) rotor untrimmed, rolling road stationary ($V_g/V_\infty = 0$), (ii) rotor quasi-trimmed, rolling road stationary ($V_g/V_\infty = 0$), (iii) rotor untrimmed, rolling road moving ($V_g/V_\infty = 1$) and (iv) rotor quasi-trimmed, rolling road moving ($V_g/V_\infty = 1$).

Most of the PIV plots presented cover a $2.0R \times 1.4R$ field-of-view of the rotor ground effect flow-field, as represented schematically in Figure 5.2. Wide regions of the ground effect wake, upstream of the rotor, was investigated using View 1, as shown in Figure 5.2 (a), while View 2, shown in Figure 5.2 (b), was used to investigate the development of the ground effect wake under the rotor disk by capturing data from about $0.2R$ inboard of the leading edge of the rotor. Double frame, double pulse PIV was conducted and 120 image pairs recorded for each test, with an inter-pulse time delay between successive images set at $\Delta t = 300\mu s$, appropriate for a freestream velocity range of $1.5ms^{-1} < V_\infty < 5.0ms^{-1}$. For View 1, the laser was un-synchronised with the rotor, while for View 2, the laser was phase-locked with rotor azimuth, with a phase angle of 45^o. Synchronisation of the PIV laser triggering with rotor azimuth was done for View 2 to avoid shadow, glare and beam reflections in the regions beneath the rotor disk plane so that valid flow data could be captured near and under the rotor disk.

The recorded PIV images were processed using the DaVis 7.2 software [71]; an iterative scheme with a 50% overlap was used, with a final PIV interrogation window size of 32×32 pixels [78]. Peak-locking effect in the derived PIV vector maps was calculated by DaVis 7.2 to have an average value of 0.0651, and was observed to be within the acceptable range of < 0.1 [83]. The choice of the PIV parameters combined to produce good quality velocity data, with the only source of erroneous data observed at the edges of the PIV vector maps. These were due to poor illumination quality at the edges of the images and inherent properties of the imaging system and were especially noticeable in the wide area field-of-view test results. To measure the cross-flow velocity component, w, observed within the wake, Stereoscopic (Stereo) PIV tests were performed on similar regions of the flow-field. Validation of the stereo PIV results was conducted using a uniform freestream in the wind tunnel. These tests were used to benchmark the PIV set-up, and revealed no velocity gradients across the imaged field-of-view.

PIV results from the Large Rotor experiments will be presented in a series of velocity, vorticity or mean flow pathline plots, in the forthcoming sections. The (r, y, z) co-ordinate system adopted in the PIV is shown in Figure 5.1, with the origin at the rotor hub. The (u, v, w) velocity components presented in the plots represent the longitudinal, vertical and lateral velocity components along the (r, y)

(a) PIV field-of-view ahead of the rotor disk

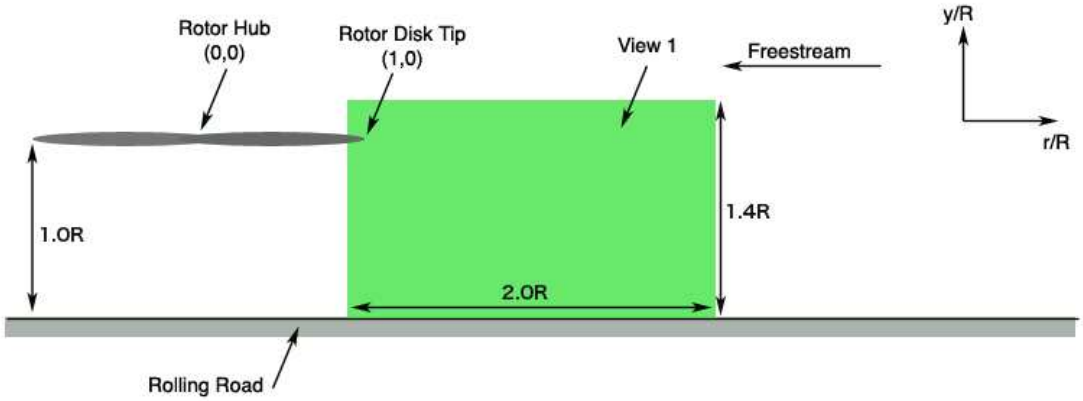

(b) PIV field-of-view under of the rotor disk leading edge

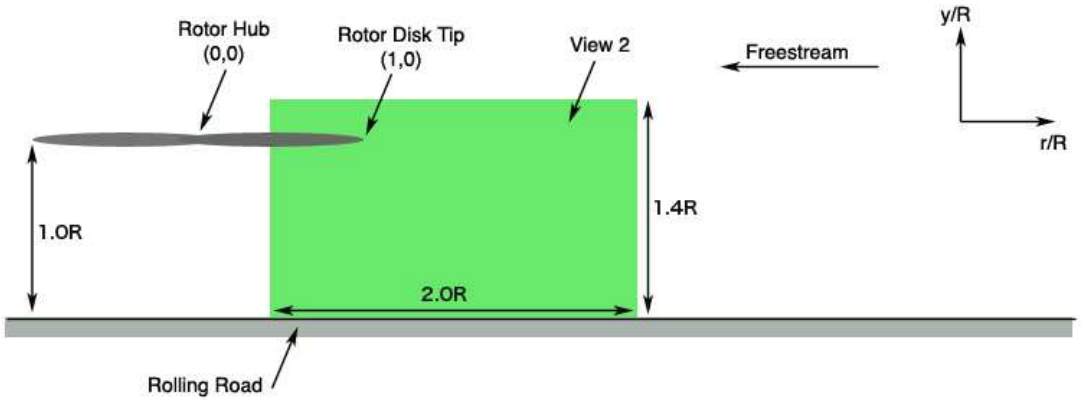

FIGURE 5.2: Ground effect field-of-views represented in PIV data presented in Chapter 5.

plane. All the plots presented in this chapter represent the flow in the (r, y) plane, and are scaled with respect to the rotor radius, R, with $\frac{r}{R}$ representing the normalised spanwise location in the flow-field and $\frac{y}{R}$, the normalised distance from the rotor hub. If present within the field-of-view, the rotor disk is represented by a black line in the plots (or by a red line in the mean flow pathline plots), with the rotor hub at the origin and the leading edge blade tip at the ordinate $(\frac{r}{R}, \frac{y}{R}) = (1, 0)$. For most of the PIV data presented, the rotor is at a ground distance of $\frac{h}{R} = 1.0$ and in these cases, the ground is represented on the PIV plots by a black line along $\frac{y}{R} = -1$. Velocity, where presented, has been scaled with V_h, where $V_h = V_{tip}\sqrt{\frac{C_T}{2}} = 3.55ms^{-1}$, is the hover induced velocity ($V_{tip} = \Omega R = 50.3ms^{-1}$ is the rotor tip speed), and vorticity has been scaled with $\frac{V_h}{R}$.

5.1.4 Experimental Validity

PIV conducted under the rotor disk allowed for the tip vortex system trailed by the rotor blades to be visualised. Based on the u and v velocity components, the circulation within the tip vortex was calculated [84], and was used to derive the circulation Reynolds number, Re_Γ, of the experiments. At the rotor collective angle of $\theta_0 = 8.8^o$, the mean circulation Reynolds number was calculated to be $Re_\Gamma = 60,000$, and at the higher rotor collective angle of $\theta_0 = 12.8^o$, this was calculated to be around $Re_\Gamma = 79,000$. A representative blade chord Reynolds number, at the rotor blade tip, was estimated to be at a moderate value of about $Re_c = 182,000$. The measured Re_Γ for all the test cases was well above the value suggested by Savaş *et. al* [79], and implies that the flow can be considered to be inertia dominated and representative of a larger rotor system.

Details of the tip vortices trailed by the rotor blades were obtained from the PIV measurements near the rotor disk plane using a $200mm$ focal length lens. The camera field-of-view (View 4) corresponding to these tests, shown in Figure 2.13 (d), allowed for improved spatial resolution of the tip vortex system. A snap-shot of the velocity field near the rotor disk plane at an instant of time is presented in Figure 5.3. The rotor leading edge is located at $(\frac{r}{R}, \frac{y}{R}) = (1, 0)$, and the rotor was quasi-trimmed in ground effect at a normalised advance ratio of $\mu^* = 0.51$, with a collective angle of $\theta_0 = 12.8^o$, and the ground stationary ($V_g/V_\infty = 0$). The velocity plot shows details of the tip vortices trailed beneath the rotor disk. Contour levels signify the physical velocity magnitudes observed across the imaged region, with the flow velocity reaching a maximum value of some $18.9ms^{-1}$. The corresponding vorticity plot presented in Figure 5.4, where the vorticity presented is scaled with $V_h = 4.35ms^{-1}$, clearly identifies the tip vortices imaged. From the vorticity plot, the diameter of the tip vortex trailed by the rotor blade was measured to be about $0.05R$ (or $2.5cm$). When scaled with respect to the rotor chord length, c, this amounts to $0.47c$.

Both the u and v velocities measured along a horizontal plane, $\frac{y}{R} = -0.2338$, through the centre of the vortex core, are plotted in Figure 5.5. The locations of the tip vortex boundaries and its measured centroid location are also indicated in this figure. Measurements of the v-velocity component across the vortex core,

corresponding to the swirl velocity component of the vortex, show the peak swirl velocity to be 20% of the blade tip velocity ($V_{tip} = 50.3ms^{-1}$). Velocity distributions observed across the vortex core, and the asymmetry of the peak swirl velocities on the opposite sides of the vortex show similarities to results from other previously conducted experiments [85]. 14 measurement points across the vortex core were obtained from the PIV and this was used to derive the circulation associated with the tip vortex of the rotor system, calculated in this case to be about $\Gamma_{TV} = 0.88m^2s^{-1}$. With the rotor in the said configuration, the PIV data indicated a tip vortex circulation Reynolds number of $RE_\Gamma = 61,000$.

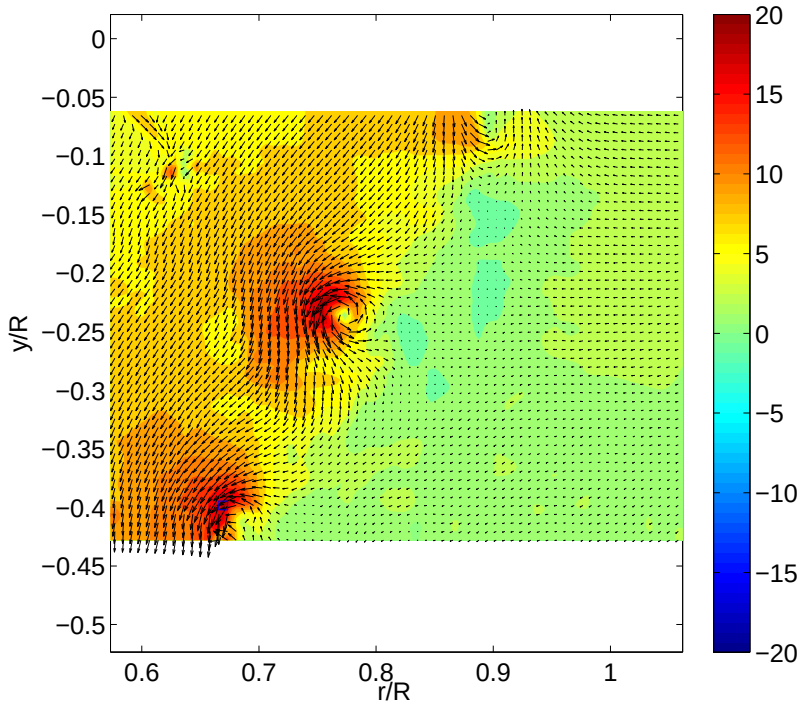

FIGURE 5.3: Instantaneous velocity field under the Large Rotor operated at a normalised advance ratio of $\mu^* = 0.51$. The rotor was quasi-trimmed and operating with a disk collective of $\theta_0 = 12.8^o$. The rotor ground distance was 1.0R and the rolling road was stationary ($V_g/V_\infty = 0$). The contour levels signify the physical velocity magnitudes observed across the imaged field-of-view.

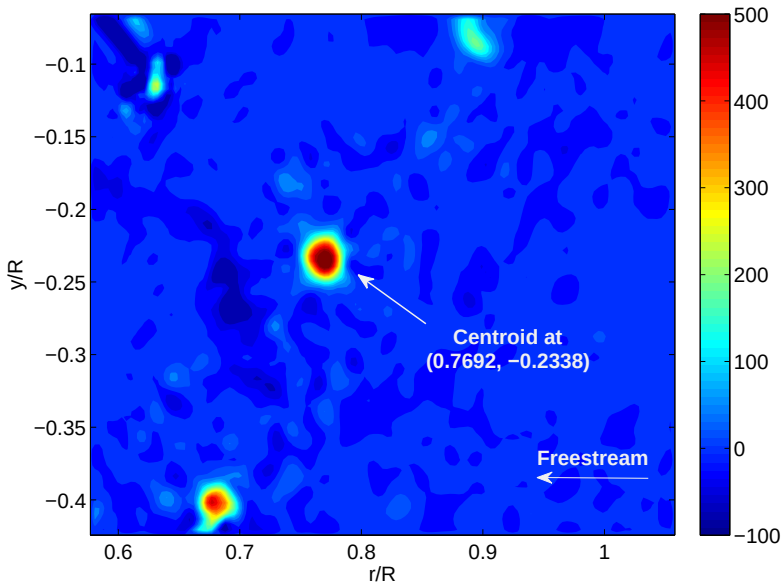

FIGURE 5.4: Instantaneous vorticity plot under the Large Rotor operated at a normalised advance ratio of $\mu^* = 0.51$. The rotor was quasi-trimmed and operating with a disk collective of $\theta_0 = 12.8^o$. The rotor ground distance was 1.0R and the rolling road was stationary ($V_g/V_\infty = 0$). The contour levels signify the vorticity scaled with $V_h = 4.35ms^{-1}$.

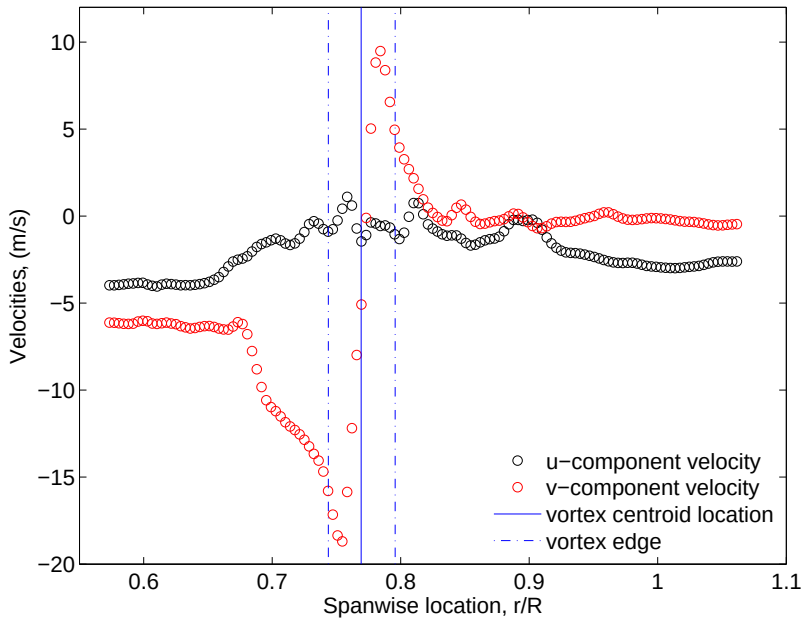

FIGURE 5.5: Velocity distribution across the PIV field-of-view at y/R=-0.2338. (u, v) velocity across the vortex with centroid at $(r/R, y/R) = (0.7692, -0.2338)$ is shown, with the vortex edges marked by the blue boundary lines in the plot. 14 PIV measurement points were recorded across the measured tip vortex.

5.2 Effect of rotor trim and moving ground conditions

Figure 5.6 presents the mean vorticity plots for the different rotor trim and ground boundary configuration tests, where the Large Rotor was operated at a normalised advance ratio of around $\mu^* \approx 0.66$. The corresponding mean flow pathline plots are presented in Figure 5.7. A different field-of-view (Figure 5.2 (b), View 2) was used for the moving ground configuration ($V_g/V_\infty = 1$) results presented in frames (b) and (d) of these figures, to capture the full extent of the ground effect flow features in these cases. In this field-of-view (View 2), artefacts caused by poor beam quality at the far edge of the light sheet, were seen to cause strong negative vorticity at the extreme top left edge of the vorticity plots (above the disk) and are ignored during the analyses of the data. The mean vorticity plots shown in Figure 5.6 present the relative locations of the mean recirculation region of positive vorticity induced by the ground at the various experimental configurations.

For the untrimmed rotor and stationary ground ($V_g/V_\infty = 0$) configuration, the mean recirculation zone was observed to form furthest upstream ahead of the rotor disk leading edge, as shown in Figure 5.6 (a). In this plot, the recirculation zone is seen to exist at around $1.4 < \frac{r}{R} < 2.1$, with the edge of the zone extending to $\frac{r}{R} \approx 2.3$. To identify the effects of the ground boundary conditions and rotor trim on the ground effect wake, each of these parameters were varied individually and the flow recorded at the same normalised advance ratio. Results of these tests are presented in Figures 5.6 (b) and (c) respectively. As shown in Figure 5.6 (b), the moving ground boundary condition ($V_g/V_\infty = 1$) is seen to move the recirculation zone closer to the rotor disk, with the vorticity zone extending to reach around $\frac{r}{R} \approx 1.7$ upstream. With the location of the mean recirculation zone influenced by the flow separation position, the change in the location of the mean flow topological separation point caused by the moving ground boundary condition was calculated. At this normalised advance ratio, the moving ground configuration was seen to cause a $0.5R$ shift in the flow separation point closer to the rotor disk, compared to the stationary ground configuration case.

Rotor trim configuration changes were seen to cause a smaller shift in the mean recirculation zone, as shown in Figure 5.6 (c); in this plot, the mean recirculation region was seen to form around $1.4 < \frac{r}{R} < 2.0$. The change in the rotor trim configuration was seen to cause a $0.1R$ shift in the topological flow separation point location, as seen through a comparison of Figures 5.6 (a) and (c) . With both the rotor trim and ground configurations seen to cause shifts in the flow separation location, the quasi-trimmed rotor and moving ground configuration ($V_g/V_\infty = 1$) case, shown in Figure 5.6 (d), was seen to cause the greatest shift in the location of the ground effect wake features. A comparison of this plot with Figure 5.6 (a), showed the mean recirculation zone to form much closer to the rotor disk, with the vorticity zone edge extending to only $\frac{r}{R} \approx 1.4$. Figure 5.7, showing the mean flow pathline plots of the respective cases, further illustrates the changes in the locations of the flow separation point and the mean recirculation zone brought about by the rotor trim and ground boundary conditions.

5.2.1 Influence of rotor trim conditions

Decisions made during the rotor design process to incorporate cyclic pitch adjustment capabilities in the Large Rotor model were based on the necessity to compare the wake produced by different rotor and experimental test configurations. With the location of the ground effect wake features known to affect the performance of the rotor [27] and its trim [23], the cyclic pitch actuation systems on the Large Rotor allowed for similar rotor trim configurations to be maintained during the tests. This ensured that wake comparisons made from the PIV tests conducted at different experimental configurations were for the ground effect wake formed at similar rotor trim configurations. Two rotor trim configurations were tested with the Large Rotor during this PIV analysis; a quasi-trimmed rotor configuration was tested to identify the influence of trim on the ground effect wake features and to allow for comparisons of the wake at a known and constant rotor configuration. An untrimmed rotor configuration with zero cyclic blade pitch angles was considered to allow for comparisons with ground effect data obtained from fixed pitch rotor models (*Small Rotor, used to verify these PIV tests and Rotor A, used in the preliminary PIV investigations*).

(a) Rotor untrimmed at $\mu^* = 0.66$, with $V_g/V_\infty = 0$

(b) Rotor untrimmed at $\mu^* = 0.66$, with $V_g/V_\infty = 1$

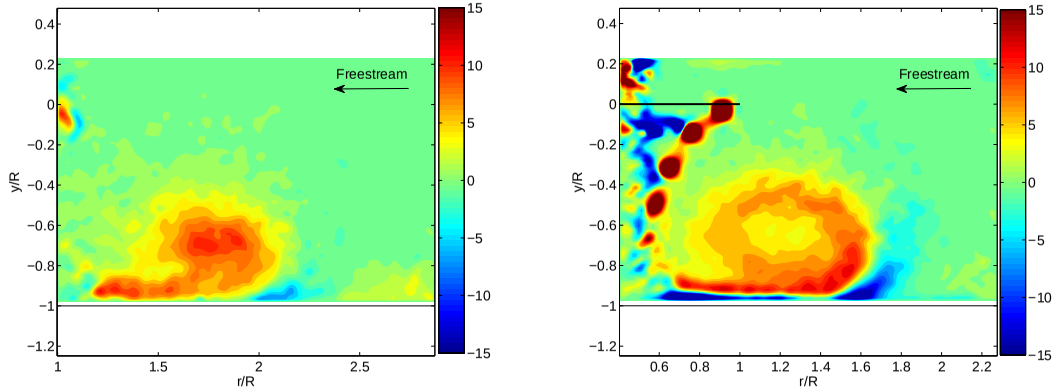

(c) Rotor quasi-trimmed at $\mu^* = 0.67$, with $V_g/V_\infty = 0$

(d) Rotor quasi-trimmed at $\mu^* = 0.66$, with $V_g/V_\infty = 1$

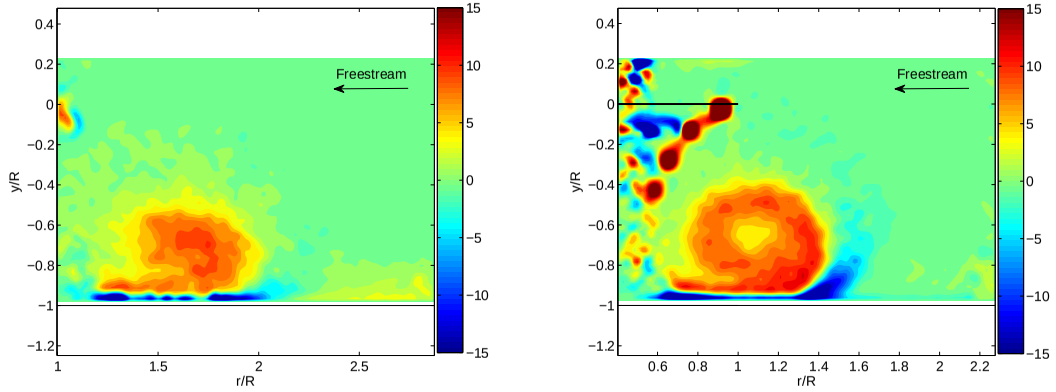

FIGURE 5.6: Mean vorticity plots at a normalised around $\mu^* = 0.66$, comparing the locations and spread of the mean recirculation regions for the Large Rotor at a ground distance of 1.0R at different rotor trim and ground boundary conditions.

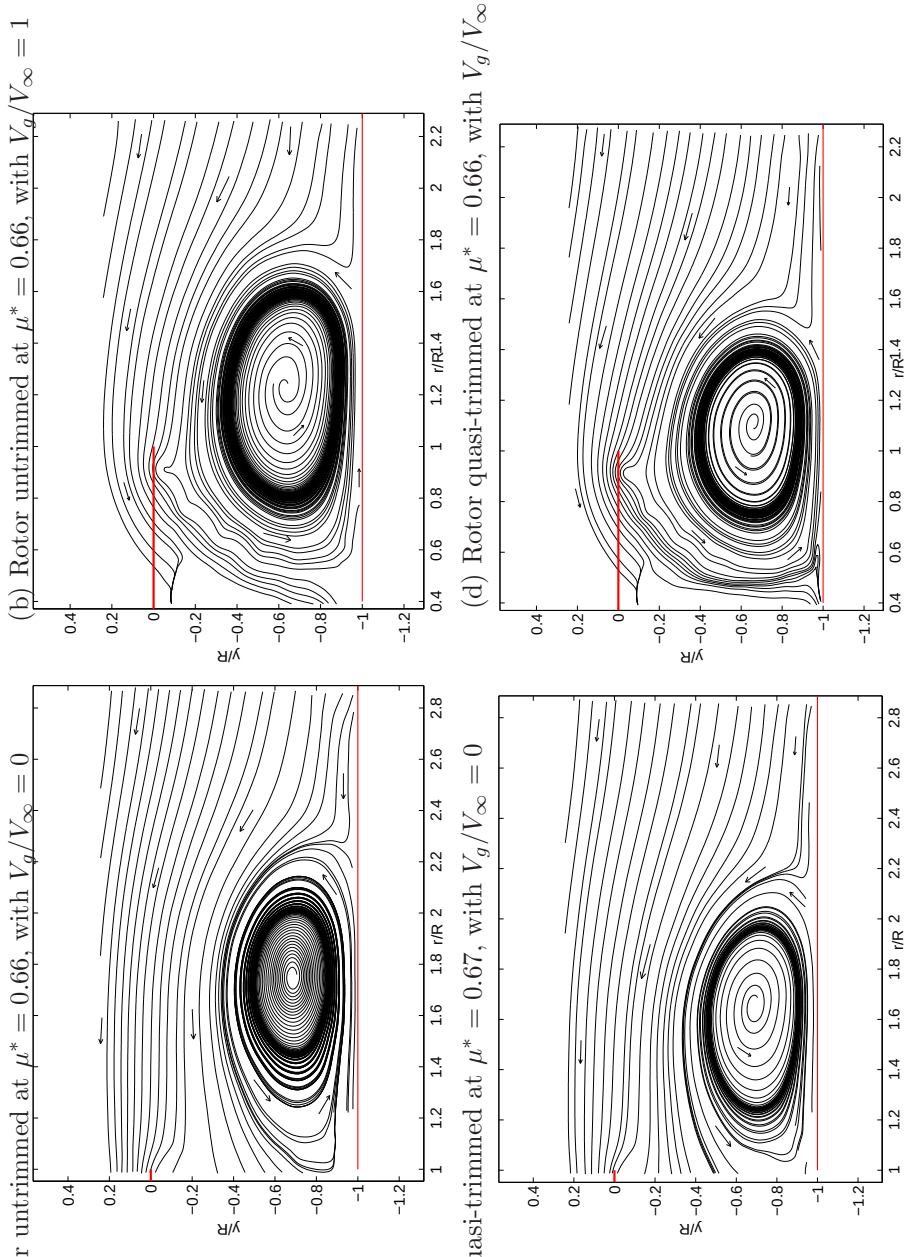

FIGURE 5.7: Mean flow pathline plots at a normalised advance ratio around $\mu^* = 0.66$, comparing the locations and spread of the mean recirculation regions for the Large Rotor at a ground distance of 1.0R at different rotor trim and ground boundary conditions.

Trimming of the Large Rotor was conducted by adjusting the cyclic blade pitch angles to align the vertical force centroid with the rotor hub. This is significantly different from helicopter trim, where cyclic pitch adjustments are made to balance all forces and moments acting on the rotor and airframe [86]. In a conventional helicopter, longitudinal cyclic pitch adjustments result in a longitudinal disk tilt, and are used to balance the longitudinal forces and pitching moments, while lateral cyclic pitch adjustments, resulting in a lateral disk tilt, are used to balance side forces (especially due to the tail rotor) and rolling moments [11]. With only the vertical forces (and its associated moments) acting on the rotor system balanced and no account made for the side forces acting on the rig, trimming of the Large Rotor did not guarantee zero pitching and rolling moments acting on the rotor system. Testing of the Large Rotor using this quasi-trim state meant that the ground effect wake produced by this rotor configuration may differ from the wake that would be produced if all the forces and moments acting on the Large Rotor was accounted for. With research conducted by Curtiss *et. al* showing longitudinal disk tilt to have little effect on the formation of the ground effect wake [27], this difference would be limited to changes in the wake symmetry caused by any additional lateral disk tilt required to compensate for side forces acting on the Large Rotor (which is not accounted for by the wake produced by the quasi-trimmed Large Rotor).

Based on this trim definition, PIV tests were conducted with the Large Rotor for a quasi-trimmed and untrimmed rotor configuration. Results from both rotor trim configurations showed an insignificant difference in the ground effect flowfield, despite significant differences in the vertical rotor force centroid locations between the cases. Besides a change in the location of the ground effect wake interaction boundary, the rotor trim configuration was seen to have little effect on the detailed structures and the vorticity strengths associated with the ground effect wake. Similar results were obtained from both the stationary and moving ground configuration tests, and is clearly illustrated in Figure 5.6; a comparison between Figures 5.6 (a) and (c) and between Figures 5.6 (b) and (d) showed little differences in the formed wake features. Instead, variations in the rotor trim state were observed to only result in small changes in the locations of the mean topological flow separation points, and these were seen to cause small changes to the sizes of the mean recirculation zones.

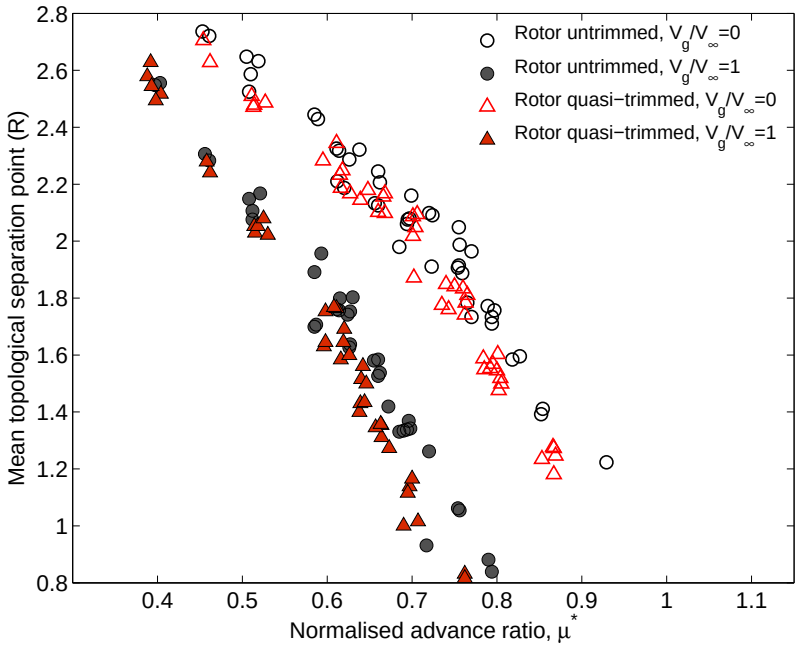

FIGURE 5.8: Mean topological separation points derived from the PIV data at varying normalised advance ratios (μ^*) for all the experimental configurations tested.

Figure 5.8 presents the variation in the mean topological separation point locations derived from the PIV, between the untrimmed and quasi-trimmed rotor configurations, for both the stationary ($V_g/V_\infty = 0$) and the moving ground ($V_g/V_\infty = 1$) configurations, for the range of normalised advance ratios tested. Flow separation along the ground was identified from the PIV velocity data by considering the u-velocity information close to the ground plane. The location where a change in sign of the u-velocity component was observed was defined as the region where flow separation occurred; a linear interpolation was done to estimate the location where $u = 0$, and this was identified as the topological separation point location of the flow. For both ground boundary configurations tested, Figure 5.8 shows the quasi-trimmed rotor configuration to result in the flow separation to occur about $0.1R$ closer to the rotor disk, with the most significant shifts of around $0.2R$ observed when $\mu^* > 0.7$. Differences observed in the mean topological flow separation locations between the rotor trim configurations can be attributed to the slight variations in the rotor thrust that was seen to result from the cyclic adjustments made during the trimming process. On average, the Large Rotor showed a 2% reduction in the C_T when the rotor was quasi-trimmed. While this reduction in C_T caused an insignificant change to the normalised advance ratio, it was seen to

cause the flow separation to occur slightly closer to the rotor disk compared to the untrimmed rotor configuration.

Analyses of the PIV results from the Large Rotor tests suggest that during wind tunnel testing of rotors in ground effect, the rotor trim conditions may not be a significant factor affecting the fluid dynamics of the ground effect wake, in terms of the general formation and structure of the ground effect flow-field. Detailed features of the ground effect flow-field, at least in a two-dimensional slice of the flow-field along the longitudinal axis of the rotor, were observed to be similar for both the quasi-trimmed and untrimmed rotor configurations. Although these observations are limited to the wake produced by a rotor system which did not take into account the side forces acting on it, the asymmetry of the wake interaction boundary which may result from the lateral disk tilt required to trim this side force is not expected to change the detailed structure of the ground effect wake features.

5.2.2 Influence of ground boundary conditions

Since little information is currently available on the validity of conducting ground effect experimental research using fixed ground planes, one of the major objectives of this research was to determine the importance of the ground boundary conditions on the formation and evolution of the ground effect wake. Accordingly, tests with the rolling road stationary ($V_g/V_\infty = 0$) were conducted to represent fixed ground plane configurations and the rolling road was moved with the freestream equivalent speed ($V_g/V_\infty = 1$) to represent moving ground conditions. This moving ground configuration was used to provide a better representation of the forward flight of a helicopter over a stationary ground, with a velocity comparable to the wind tunnel freestream velocity, V_∞. Results from these tests were compared to data obtained from experiments conducted with the non-moving ground ($V_g/V_\infty = 0$), which is analogous to a rotor hovering over a fixed ground point in a strong head-wind.

Comparison of the PIV data, presented in Figure 5.6, show the ground boundary configurations to cause significant differences in the ground effect wake. One

of the most prominent changes observed in the wake, as seen from Figure 5.7, was the change in the topological flow separation location caused by the moving ground boundary condition, which was in turn seen to alter the size and location of the mean recirculation zone. Figure 5.8 shows the moving ground configuration ($V_g/V_\infty = 1$) to cause the topological flow separation to form around $0.5R$ closer to the rotor disk, compared to the stationary ground configuration ($V_g/V_\infty = 0$). This was observed to occur for both the rotor trim configurations, throughout the range of normalised advance ratios tested. Such large shifts in the wake location imply that ground boundary conditions maintained during experimental testing of ground effect have the potential to alter the ground effect flow regimes [24, 27] at which the rotor is operating. Figure 5.8 also emphasises the changes in the ground boundary configuration to have a more prominent effect on the wake compared to changes in the rotor trim configuration.

The average vorticity plots presented in Figure 5.6 also show the presence of the wind tunnel ground boundary layer, observed particularly from the stationary ground configuration data shown in Figures 5.6 (a) and (c). In these plots, the wind tunnel boundary layer is seen to induce a region of very low magnitude positive vorticity, along the ground at $\frac{r}{R} > 2.5$, upstream of the mean recirculation zone. When the rolling road is moving, this wind tunnel ground boundary layer is less apparent, resulting in the flow near the ground plane beyond the recirculation zone to be affected by vorticity magnitudes close to zero. Flow just above the ground plane, beyond $\frac{r}{R} > 2.0$, seen in Figure 5.6 (b) and (d), show only small "spots" of weak magnitude positive vorticity present at the bottom right edge of the plots. These are artefacts resulting from the large chip size of the imaging camera, and are obtained at the corners of the images recorded for all the wide area field-of-view experiments. These artefects are also present in Figure 5.6 (a) and (c), although the weak magnitude vorticity induced by the presence of the wind tunnel boundary layers overlap the artefacts in these cases.

5.2.2.1 Effect of ground boundary conditions on rotor trim

Analyses of data from the PIV experiments conducted have also shown the ground boundary configurations to have a significant effect on the cyclic pitch angles required to trim the rotor during ground effect testing. Figure 5.9 presents the

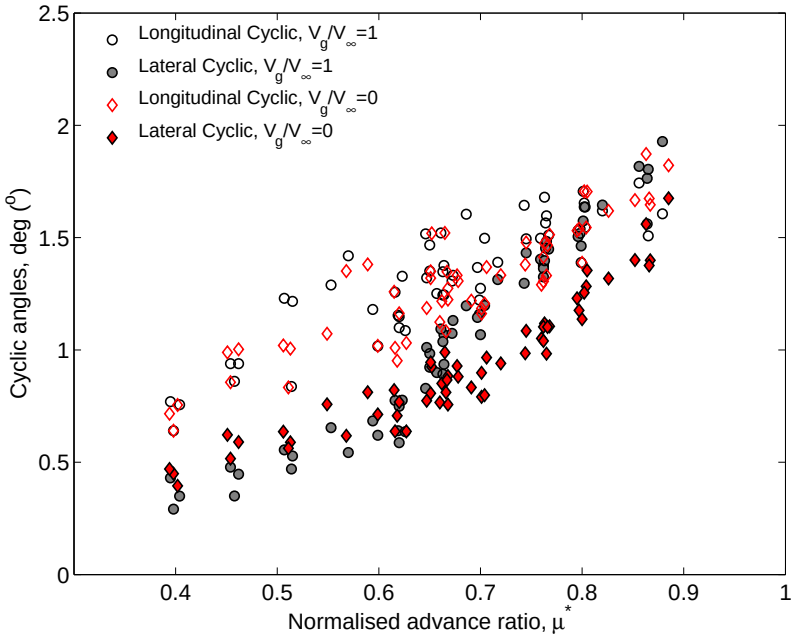

FIGURE 5.9: Lateral and longitudinal cyclic blade pitch adjustments required to reach the Large Rotor quasi-trim state, in ground effect forward flight. The rotor collective pitch setting was $\theta_0 = 8.8^o$.

longitudinal and lateral cyclic pitch inputs that were required to reach the Large Rotor quasi-trim state. Cyclic trim data when the rotor collective was $\theta_0 = 8.8^o$ are shown in the figure, for the two ground boundary configurations and range of normalised advance ratios tested. Significant differences were especially observed in the lateral cyclic adjustments required to trim the rotor between the ground configuration cases. For the moving ground boundary configuration ($V_g/V_\infty = 1$), an almost step-like change in the lateral cyclic input was observed at around $0.62 < \mu^* < 0.7$, while the increase in lateral cyclic angle for the fixed ground configuration ($V_g/V_\infty = 0$) tests were seen to be more gradual with increasing normalised advance ratio. The lateral cyclic trim data produced by the moving ground configuration was similar to those observed from helicopter flight data [36] and other ground effect experimental data [23], while trim data obtained from the stationary ground configuration case showed lesser similarities. This can be qualified through a comparison of Figure 5.9 and Figure 1.5, where test data from Sheridan and Weisner [23] show a similar step-like change in lateral cyclic input (required to overrun the ground vortex), within the range of flight speeds tested.

Trim data collected from these experiments can thus be used to conclude that the fixed ground boundary configuration is a poor representation of helicopters in

ground effect forward flight, as it does not produce the expected step-like change in lateral cyclic input observed in actual helicopter ground effect flight data. Trim data obtained from tests conducted with the moving ground condition however showed trim control inputs similar to that resulting from helicopter operations in ground effect forward flight, and suggests that this configuration can be used to obtain a good representation of the ground effect wake. Results from these experiments thus suggest that ground effect experiments can be conducted with relative ease in wind tunnels fitted with moving ground planes, instead of having to consider larger, more elaborate experimental facilities to re-create accurate ground boundary conditions necessary for ground effect testing.

5.2.2.2 Effect of ground boundary conditions on the ground effect wake features

In addition to changes in flow separation location and rotor trim characteristics, the ground boundary configuration was also seen to affect the detailed structure of the ground effect wake. The mean vorticity plots presented in Figure 5.6 clearly showing this difference. The moving ground configuration ($V_g/V_\infty = 1$) cases presented in Figure 5.6 (b) and (d) show the tip vortices, the high magnitude positive vorticity extending under the rotor disk, continuing as a trail of lower magnitude positive vorticity as they expand out along the ground. At the flow separation point, this trail is seen to leave the ground and continue in a definite track to form a loop within the mean recirculation zone. Comparisons with vorticity data from the stationary ground configuration ($V_g/V_\infty = 0$) tests presented in Figures 5.6 (a) and (c) show the track of tip vortices spreading along the ground until the flow separation point. Beyond this point, no definite track of vorticity was seen within the recirculation zone; instead, the vorticity was seen to accumulate close to the centre of the mean recirculation zone. This accumulation of vorticity within the mean recirculation zone, as shown in Figure 5.6 (a), is consistent with observations from the flow visualisation and PIV results discussed in Chapters 3 and 4, where similar experimental conditions were maintained. With Figure 5.6 showing the rotor trim configurations to cause little difference in the structure of the ground effect wake features, the differences observed in the spread of vorticity within the mean recirculation zone in the ground effect flow-field can be concluded to be an effect of only the ground boundary configuration on the resulting wake.

Another difference observed from the vorticity data in Figure 5.6 was the prominence of the negative vorticity in the flow-field. Primarily seen along the ground plane, this negative vorticity is the surface boundary layer induced by the mean rotor flow expanding along the ground plane; a detailed analysis of this will be provided in a later section (Section 5.4.3). Mean flow data presented in Figure 5.6 however show the negative vorticity to be a more prominent feature in the ground effect flow-field resulting from the moving ground configuration ($V_g/V_\infty = 1$) than in the flow-field produced by the stationary ground ($V_g/V_\infty = 0$). Referring to Figures 5.6 (b) and (d), a narrow strip of negative vorticity can be seen lying between the ground and the mean positive vorticity zone above it. This negative vorticity is seen to exist from the location where the tip vortex system reaches the ground plane right up to the flow separation zone, where the trailing vortex system was seen leaving the ground plane. Vorticity data from the stationary ground configuration ($V_g/V_\infty = 0$) tests presented in Figure 5.6 (a) and (c), captured at a more upstream field-of-view, show only part of this negative vorticity trail. It is however obvious from these plots that the trail of negative vorticity next to the ground is weaker in strength and inconsistent in appearance along the ground plane. In the case of Figure 5.6 (a), negative vorticity is only noticed around the flow separation zone. This observation suggests that the ground boundary configuration significantly affects the fluid dynamics of the ground effect wake, especially near the ground plane, and has to be carefully considered to obtain an accurate representation of the ground effect wake.

5.2.2.3 Dispersion Radius

To quantify the differences in the vorticity distribution caused by the different ground configurations in the mean ground effect flow-field, the enstrophy dispersion radius, r_{EN} was defined. This parameter essentially represents the dispersion of vorticity in a selected region of the flow-field. Calculation of the enstrophy dispersion radius involves the calculation of the total enstrophy, $EN = \int \omega^2 dA$ (derived from the vorticity in the flow-field), and the position of the enstrophy centroid, $\mathbf{x}_{EN} = \frac{1}{EN} \int \mathbf{x}\omega^2 dA$, within a specific region. Enstrophy was chosen instead of vorticity to avoid difficulties that can be encountered whilst working with changing vorticity signs in the chosen region of interest [87]. Using the calculated enstrophy parameters, the enstrophy dispersion radius, r_{EN}, is defined as [88],

$$r^2{}_{EN} = \frac{1}{EN} \int |\mathbf{x} - \mathbf{x}_{EN}|^2 \omega^2 dA \tag{5.1}$$

As an example, for a circular vortex of radius r_{vor}, and uniform vorticity (i.e. solid body rotation), the enstrophy dispersion radius, r_{EN}, can be calculated to be $\frac{r_{vor}}{\sqrt{2}}$. Equation 5.1 was used in this study to calculate the mean enstrophy dispersion radius, $\bar{r}_{EN}$ in the wake produced by the different rotor trim and ground boundary configurations, at each normalised advance ratio tested.

Figure 5.10 presents the results of the calculated mean enstrophy dispersion radius, $\bar{r}_{EN}$, scaled with respect to the rotor radius, R, for the range of normalised advance ratios tested. As seen from the plot, $\bar{r}_{EN}$ was seen to be greater for the stationary ground boundary configuration ($V_g/V_\infty = 0$) cases than the moving ground configuration ($V_g/V_\infty = 1$) cases at similar normalised advance ratios. With the different ground boundary configurations causing flow separation to occur at different locations, for the same normalised advance ratios, data presented in this figure represents the dispersion radius at different flow separation positions. To have a clearer indication of the effect of the ground boundary configuration on the distribution of vorticity, comparisons of the data at similar flow separation point locations have to be considered. Figure 5.11 presents this data, and it is obvious from the plot that at similar flow separation point locations, the dispersion of vorticity in the flow-field, produced by the stationary ground ($V_g/V_\infty = 0$) configuration, was smaller than that produced by the moving ground ($V_g/V_\infty = 1$) configuration. A smaller radius of dispersion meant that most of the vorticity was confined to smaller regions of the flow-field in the case of the stationary ground ($V_g/V_\infty = 0$) configuration. Mean vorticity plots in Figure 5.6, showed this to occur within the mean recirculation region, where the vorticity was observed to accumulate. In the case of the moving ground configuration ($V_g/V_\infty = 1$), the dispersion of vorticity within the flow-field was calculated to be about 18% larger (on average), thus signifying greater proportions of the flow-field to contain vorticity transported from the ground.

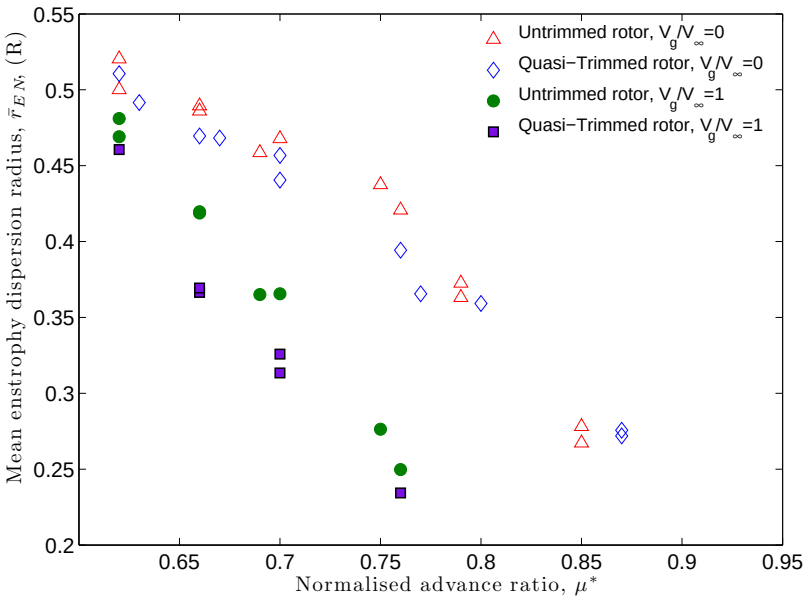

FIGURE 5.10: Mean enstrophy dispersion radius for a range of normalised advance ratios, for the different experimental configurations tested.

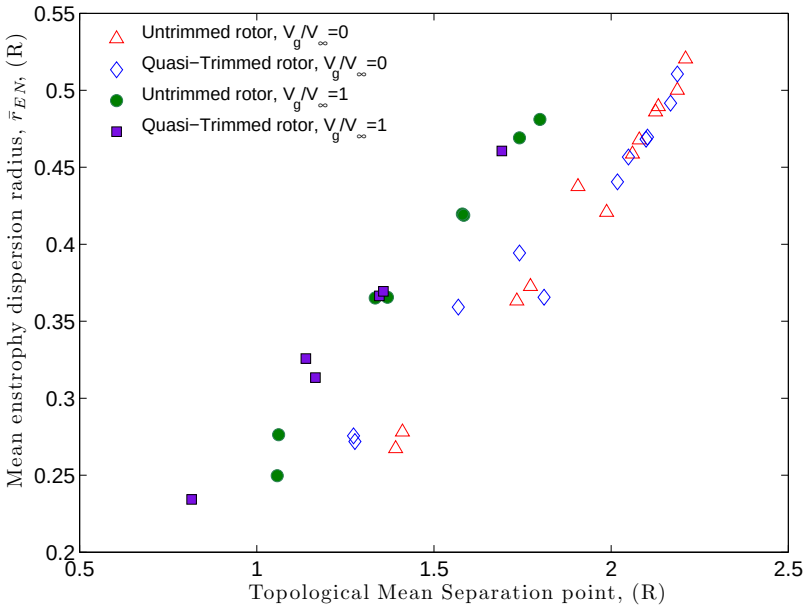

FIGURE 5.11: Mean enstrophy dispersion radius for a range of mean flow topological separation points. Differences in the vorticity dispersion in the flow-field brought about by the different rotor and ground boundary configurations are shown.

5.2.3 Summary of the importance of ground boundary conditions

With the ground boundary configurations seen to have significant effects on the location and detailed structure of the ground effect flow features, and seen to affect the control characteristics of the rotor, it can be concluded that that fluid mechanics of the ground effect wake is significantly affected by the ground boundary configurations maintained during experimental testing. This thus implies that significant consideration has to be given to re-creating appropriate ground boundary conditions during experimental testing and numerical simulation of ground effect to ensure that the fluid mechanics of the resulting ground effect wake produced accurately represents the wake produced by a helicopter operating in ground effect forward flight. Experiments conducted during this research also showed the rotor trim characteristics to play a minor role in influencing the formation of the ground effect wake features, although it can affect the location of the ground interaction boundary and the three-dimensional structure of the overall wake.

Based on these conclusions, the remaining sections of this dissertation will focus on the fluid mechanics of the ground effect wake produced by a quasi-trimmed rotor operated with a moving ground configuration ($V_g/V_\infty = 1$), as this experimental configuration best represents a helicopter operating in ground effect forward flight. The interested reader is referred to Appendix C, where PIV results from the other experimental configurations tested are presented to further highlight the differences in the flow-field caused by the varying experimental configurations.

5.3 PIV Results: Mean Flow Data

5.3.1 Effects of advance ratio

Influences of advance ratio on the mean ground effect flow-field are illustrated through a comparison of the mean vorticity plots at a range of normalised advance ratios, as shown in Figure 5.12. To capture the full extent of the ground effect flow features, a different field-of-view (Figure 5.2 (b), View 2) was used for the higher normalised advance ratio ($\mu^* > 0.62$) test results presented in this

figure. In this field-of-view (View 2), artefacts caused by poor beam quality at the far edge of the light sheet, were seen to cause strong negative vorticity at the extreme top left edge (above the disk) of the vorticity plots and are ignored during analyses of the data. Similar mean flow data, from corresponding tests done using the other experimental configurations are presented in Appendix C.1.1 for reference.

In general, the normalised advance ratio of the flow was seen to influence the location of flow separation and formation of the mean recirculation (vorticity) zone. Data presented in Figure 5.8 showed the mean topological flow separation to occur closer to the rotor disk at progressively higher normalised advance ratios, and this change was seen from Figure 5.12 to cause the corresponding mean recirculation region to form closer to the rotor disk. At low normalised advance ratio, the mean recirculation zone was seen as a large region of low magnitude vorticity, an example shown in Figure 5.12 (a). As the normalised advance ratio was increased, flow separation was seen to occur nearer the rotor disk, and the resulting mean recirculation zone was seen to become a more compact region of higher magnitude vorticity.

Vorticity data from PIV tests conducted under the rotor disk for normalised advance ratios above $\mu^* = 0.62$ showed the trail of the tip vortex system leaving the rotor. Synchronisation of the laser with rotor azimuth allowed for the tip vortex trail to be reflected in the vorticity plots without being resolved during the averaging process. Figures 5.12 (e) - (h) show this tip vortex system, with the wake skew angle seen to progressively increase with normalised advance ratio. The tip vortex system in Figure 5.12 (e), is seen leaving the rotor and reaching the ground. At the ground plane, the system continues as a trail of lower magnitude positive vorticity as it spreads out along the ground. At the separation point, the trail of vorticity is seen to leave the ground and continue in a definite track to form a loop within the recirculation zone. This loop is seen to possess lower vorticity strengths compared to the tip vortices, although its vorticity strength was seen to increase with normalised advance ratio, as seen in Figure 5.12 (f). As the normalised advance ratio was further increased, this loop was replaced by the tightly concentrated vortex, shown in Figures 5.12 (g) and (h), of magnitudes comparable to the tip vortex strengths. This reduction in size of the vorticity zone with increasing normalised

advance ratio was quantified through the enstrophy dispersion radius, presented in Figure 5.10.

The vorticity plots in Figure 5.12 also show a narrow strip of negative vorticity lying between the ground and the mean positive vorticity zone above it. As is seen from Figure 5.12 (e), this negative vorticity exists from the location where the tip vortex system reached the ground right until the flow separation zone, where the trailing vortex system was seen leaving the ground plane. As the normalised advance ratio increased, the magnitude of negative vorticity in this zone was seen to increase. The presence of this trail of negative vorticity along the ground plane can be attributed to the formation of a boundary layer induced by the rotor wake trailing along the ground plane and secondary separation induced by the tip vortices in the ground plane. Evidence of secondary separation occurring along the ground plane was provided by the talcum powder flow visualisation images, presented in Chapter 3, and a more detailed discussion of this will be presented in Section 5.4.3.

Comparison between these Large Rotor PIV results and results obtained from the preliminary PIV investigations of the ground effect flow-field, presented in Chapter 4, show similarities in the evolutionary trends of the ground effect wake with changing normalised advance ratios, although the distribution of vorticity within the mean recirculation zone, and the prominence of negative vorticity in the flow-field were different between the results. These differences in the wake are attributed to the differences in the ground boundary configurations between the two tests as was discussed in Section 5.2.2. Similar qualitative differences in the wake were also observed from the other Large Rotor tests conducted with the ground kept stationary *(Refer to Appendix C.1.1)*.

5.3.2 Effect of rotor ground distance

Variations in rotor ground distance have been seen to alter the flow separation location, and thus the size of the mean flow recirculation region. As was seen from the preliminary PIV results (Section 4.3.1), higher ground distances resulted in the mean flow separation point and the mean recirculation zone to form closer to the rotor for the same normalised advance ratio settings. Experimental results

(a) Rotor at $\mu^* = 0.4$ (b) Rotor at $\mu^* = 0.46$

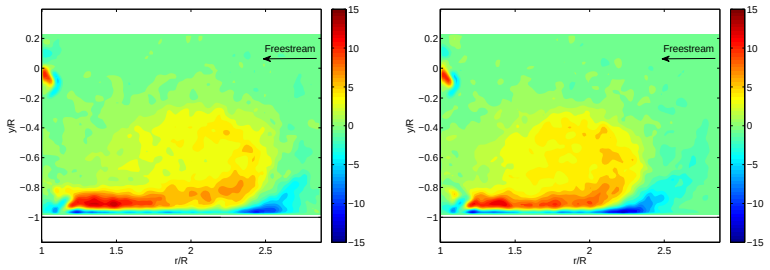

(c) Rotor at $\mu^* = 0.51$ (d) Rotor at $\mu^* = 0.55$

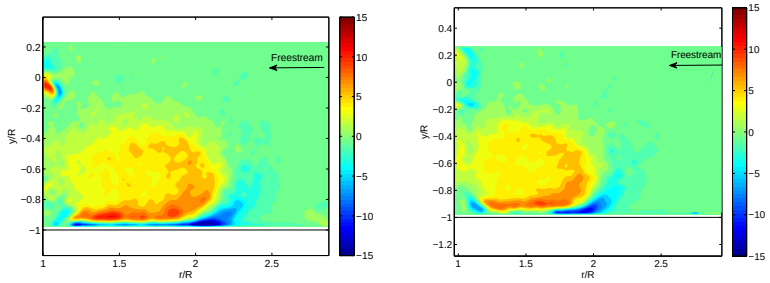

(e) Rotor at $\mu^* = 0.62$ (f) Rotor at $\mu^* = 0.66$

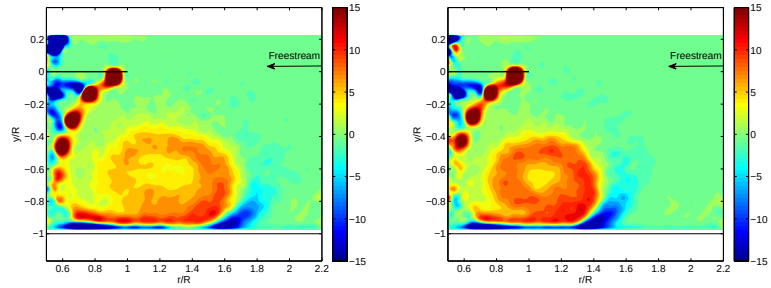

(g) Rotor at $\mu^* = 0.7$ (h) Rotor at $\mu^* = 0.76$

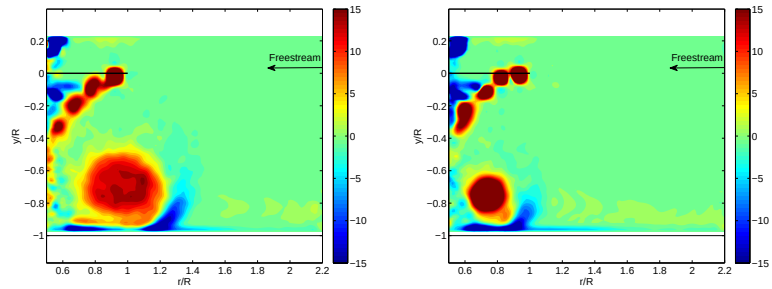

FIGURE 5.12: Mean Vorticity plots at a range of normalised advance ratio (μ^*) with the rotor quasi-trimmed and the ground moving ($V_g/V_\infty = 1$). The rotor was at a ground distance of 1.0R and the frames show the evolution of the mean recirculation zone brought about by a change in normalised advance ratio.

from the Large Rotor showed similar changes in the wake and Figure 5.13 presents the change in the mean topological separation point locations when the rotor was moved from a ground distance of $\frac{h}{R} = 1.0$ to a ground distance of $\frac{h}{R} = 2.0$. Results from the moving ground boundary configuration ($V_g/V_\infty = 1$) tests conducted are presented in this plot, and show the topological mean flow separation to occur closer to the rotor when the rotor ground distance was increased. Analysis of the PIV data showed differences in the mean separation point locations between the different ground distances at comparable normalised advance ratios to be caused by significant differences in the velocities of the rotor wake expanding along the ground.

Larger distances between the rotor and the ground, brought about by a greater rotor height above the ground plane, meant that the trailing wake undergoes more diffusion before reaching the ground [89]. The rotorwash expanding along the ground would thus contain lesser velocities. With the rotor parameters (i.e rotational speed and C_T) and the freestream velocity (advance ratio) held constant, this will allow the freestream to overcome the expanding wake nearer the rotor.

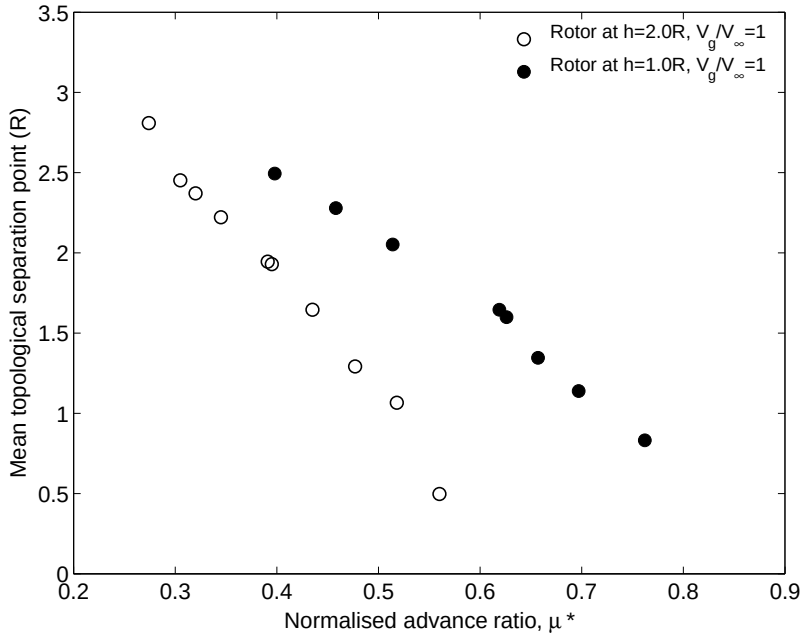

FIGURE 5.13: Mean topological flow separation point locations of the ground effect wake at a range of normalised advance ratios for the moving ground boundary configuration ($V_g/V_\infty = 1$) tested. Results from the rotor at two ground distances, $h/R = 1.0$ and $h/R = 2.0$ are presented.

Separation subsequently occurs closer to the rotor disk and the resulting recirculation zone is smaller in size. Differences in the ground effect wake brought about by changes in the rotor ground distance are illustrated through a comparison of the mean vorticity and velocity plots from the PIV. Figure 5.14 (a) presents the mean vorticity plot associated with the quasi-trimmed rotor at a ground distance of $\frac{h}{R} = 1.0$ and at a normalised advance ratio of $\mu^* = 0.52$. A comparison of this with the data obtained for the same test conditions, with the rotor at a ground distance of $\frac{h}{R} = 2.0$ is shown in Figure 5.14 (c). Relative differences between the locations, sizes and vorticity strengths of the mean recirculation zone are obvious from the plots. Mean velocities associated with the flow-field at these rotor ground distances are presented in Figures 5.14 (b) and (d) respectively, and show that at the lower ground distance ($\frac{h}{R} = 1.0$), the expanding rotorwash along the ground contained higher mean velocities compared to the higher ground distance ($\frac{h}{R} = 2.0$) case. With the rotor operated at a constant rotational speed, lesser diffusion undergone by the wake produced by the rotor at the lower ground distance, allowed the higher velocity rotorwash to trail along the ground plane over longer distances before it was overcome by the oncoming freestream.

An analysis of the flow-field produced by the rotor at different ground distances, with mean flow separation occurring at the same ground location, also showed a variation in size of the mean recirculation zone produced at the different ground heights. This can also be attributed to the difference in the rotorwash velocities experienced in the flow-field. Figures 5.14 (e) and (f) show the mean vorticity and velocity data obtained from PIV tests conducted with the rotor at a ground distance of $\frac{h}{R} = 1.0$, and operated at a normalised advance ratio of $\mu^* = 0.7$. The mean topological flow separation point at this normalised advance ratio setting was observed to occur at a similar location to the case presented in Figures 5.14 (c) and (d), where the rotor was at a ground distance of $\frac{h}{R} = 2.0$. Mean vorticity data from the two cases show slight variations in the sizes of the mean recirculation zones. Higher wake velocities associated with the rotor closer to the ground, as shown in Figure 5.14 (f), allowed for the vortices to be transported higher into the flow-field, and resulted in the vorticity distribution within the zone to be wider compared to the higher rotor ground distance case. With the ground effect flow features known to affect the inflow through the leading edge of the rotor disk [23], smaller mean recirculation zones observed in the ground effect flow-field when the rotor is at a

higher ground distance suggests that the recirculation from the ground effect wake has a lesser influence on the inflow into the rotor and thus a smaller impact on the performance of the rotor, when the rotor is at a higher ground distance. The impact of ground effect on rotor performance is therefore less obvious as the rotor ground distance is increased. This has been reflected in performance data obtained from past ground effect research, which show the benefical effects of ground effect operations to reduce with increasing ground distance [7, 9, 10]. Results from these experiments also show the size of the mean recirculation region in the ground effect flow-field to be a function of the rotor ground distance, brought about by the variations in velocity of the rotorwash expanding along the ground.

5.3.3 Effect of rotor collective angles

To identify the effect of collective angles on the ground effect wake features, PIV tests with the Large Rotor was conducted at two collective angle settings, $\theta_0 = 8.8^o$ and $\theta_0 = 12.8^o$. Results from tests conducted at a physical advance ratio of $\mu = 0.047$ are presented in Figure 5.15, to illustrate the changes caused in the ground effect wake features by variations in the rotor collective angles. The equivalent normalised advance ratio of the flow is $\mu^* = 0.66$ at the collective setting of $\theta_0 = 8.8^o$, and $\mu^* = 0.54$ for the collective setting of $\theta_0 = 12.8^o$. In this figure, both the mean vorticity and velocity plots present the actual physical vorticity strengths and velocity magnitudes experienced in the flow-field.

Increments in the rotor collective angles have an effect of increasing the thrust generated by the rotor blades through a change in overall rotor disk angle of attack. This will be reflected in the ground effect wake as a shift in the mean flow separation point further upstream away from the rotor disk, as the expanding rotor wake will contain greater velocities. Accordingly, the resulting recirculation zone and vorticity levels experienced within the wake would be altered. Figure 5.15 (a) and (b), presenting the mean velocity plots obtained from the quasi-trimmed rotor tested at a ground distance of $1.0R$ with the stationary ground configuration ($V_g/V_\infty = 1$), show that the wake trailing from the rotor at the higher collective angle ($\theta_0 = 12.8^o$) has higher velocity levels compared to the wake produced by the rotor at the lower collective angle ($\theta_0 = 8.8^o$). This results in the trailing wake

Ground Distance = 1.0R, $\mu^* = 0.52$, Mean separation point at $r/R = 2.03$
(a) Mean Vorticity (b) Mean Velocity magnitude

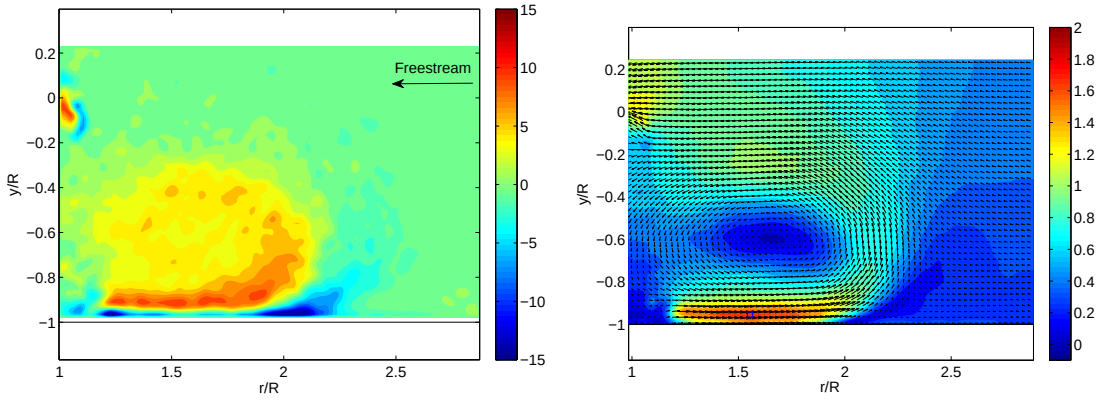

Ground Distance = 2.0R, $\mu^* = 0.52$, Mean separation point at $r/R = 1.07$
(c) Mean Vorticity (d) Mean Velocity magnitude

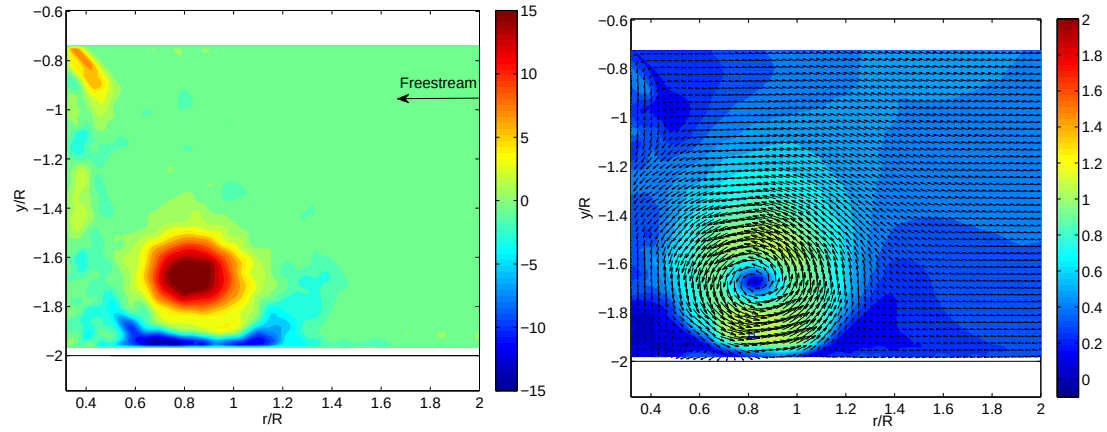

Ground Distance =1.0R, $\mu^* = 0.7$, Mean separation point at $r/R = 1.13$
(e) Mean Vorticity (f) Mean Velocity magnitude

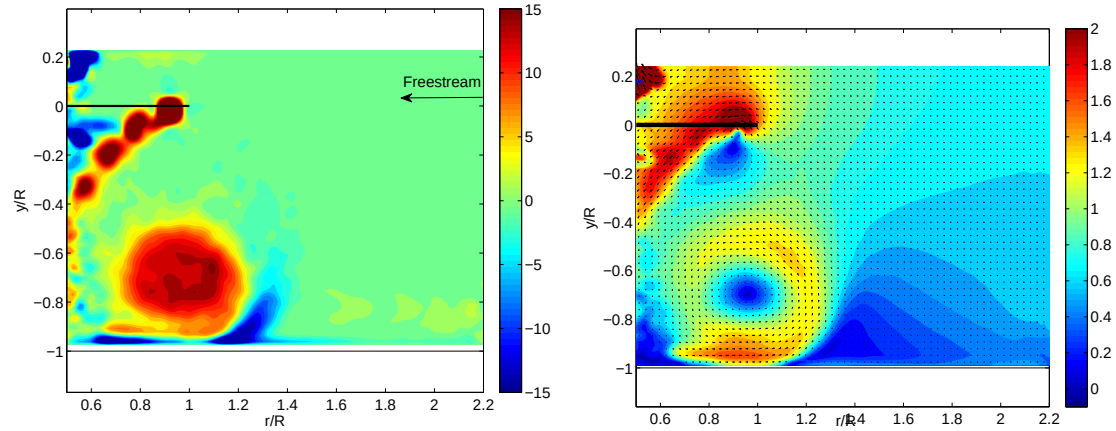

FIGURE 5.14: Average vorticity and velocity plots for a quasi-trimmed rotor configuration with the ground moving ($V_g/V_\infty = 1$). Frames (a), (b) and (c), (d) compare the effects of rotor ground distance on the wake at a normalised advance ratio of $\mu^* = 0.52$, while frames (c), (d) and (e), (f), compare this effect at a similar mean separation point location.

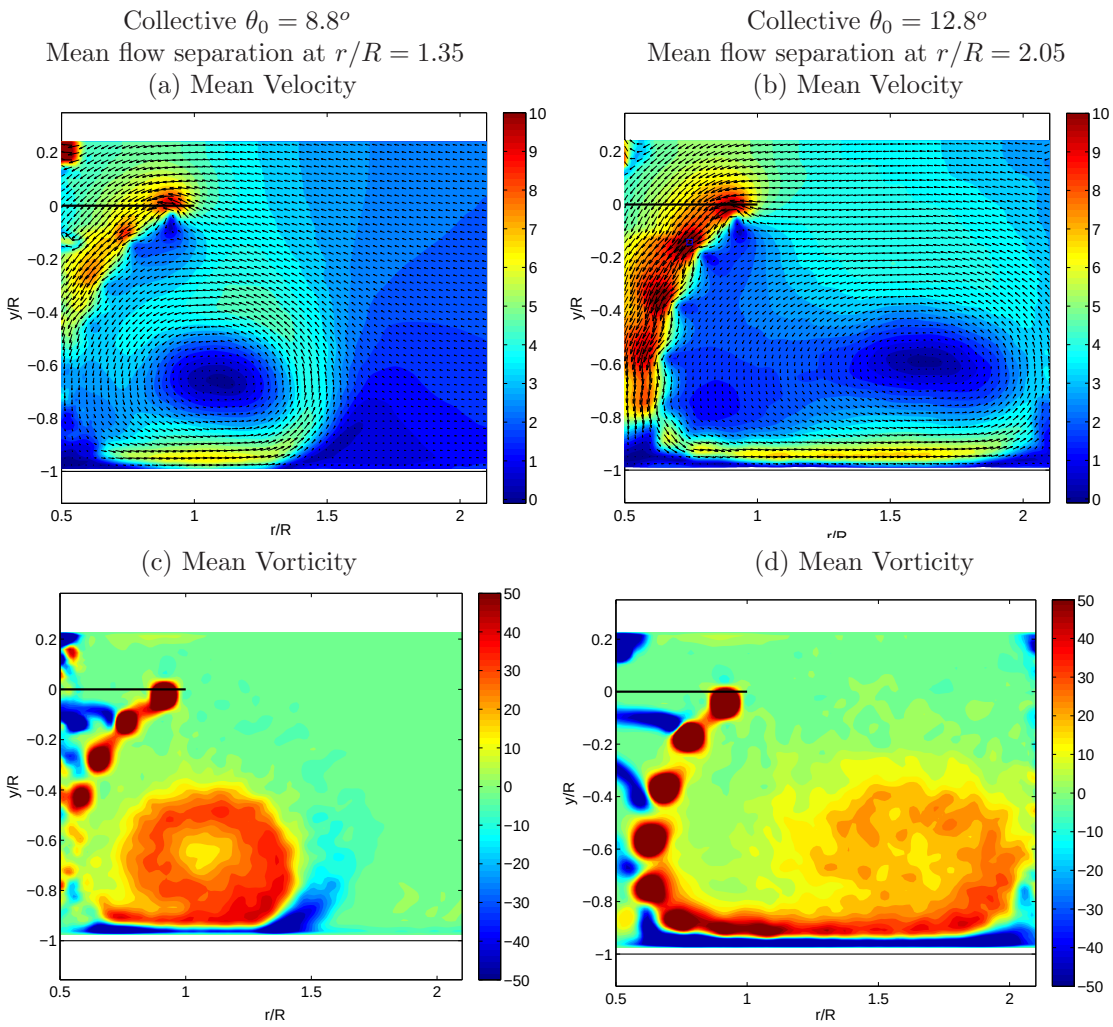

FIGURE 5.15: Mean Vorticity plots at $\mu = 0.047$ for a quasi-trimmed rotor configuration at a ground distance on 1.0R and the ground moving at $V_g/V_\infty = 1$. Results from two different rotor blade collective angles are presented. Contour levels shown represent the physical velocity magnitudes and vorticity strengths experienced in the flow-field.

to expand further upstream from the rotor before flow separation occurs. The resulting mean recirculation region is thus seen to be bigger in size compared to the lower collective angle ($\theta_0 = 8.8^o$) case, as shown in the vorticity plots presented in Figures 5.15 (c) and (d).

The vorticity plots also show the tip vortices to possess greater vorticity strength for the higher collective angle ($\theta_0 = 12.8^o$) case, with Figure 5.15 (d) showing the tip vortices just under the rotor disk to possess higher vorticity strength compared to the lower collective angle ($\theta_0 = 8.8^o$) plot presented in Figure 5.15 (c). With the vortices undergoing diffusion as they trail along the ground, the mean vorticity

within the recirculation zone will be comparably lesser than the vorticity levels observed close to the rotor disk. The differences in the vorticity levels within the mean recirculation region between the two collective angle cases shown in Figures 5.15 (c) and (d) are however subtle, despite the differences observed in the vorticity strengths of the tip vortices close to the rotor disk. This is due to the different levels of diffusion undergone by the vortices before reaching the recirculation zone. The closer flow separation location to the rotor disk at the low collective angle ($\theta_0 = 8.8^o$), meant that the vorticity levels seen within the recirculation region is as high as that observed within the recirculation zone for the higher collective angle ($\theta_0 = 12.8^o$) case, even though the initial vorticity strengths of the tip vortices between the two cases were different. This thus makes comparisons of the wake fluid dynamics between different collective angle settings difficult to perform.

Differences in the collective angle settings were also seen from the plots presented in Figure 5.15 to result is different wake skew angles below the rotor disk, although the rotor rotational speed and freestream velocity was constant for both test cases. This in turn, will affect the resultant location of the ground effect wake features. With changes in the collective angle resulting in a thrust effect, which is seen to affect the wake velocities, wake skew angles and the vorticity strengths experienced in the flow-field, a direct comparison of the flow-field between the difference collective angles is not possible without normalising the effect of thrust. This is especially important when comparative studies with other ground effect research, or different rotor models are to be conducted. Also, the changing location of the wake brought about by changing collective angles will result in the classification of the wake into the various ground effect flow regimes to be different for the different collective settings, if this thrust effect is not normalised.

Based on this, the thrust normalised advance ratio is considered during ground effect studies. This would neutralise the variations in the wake skew (deflection) angles between different thrust settings, allowing a direct comparison between the wakes, at the different collective settings, to be possible. Additionally, normalisation of the velocity and vorticity strengths with a suitable parameter, such as the hover induced velocity, V_h, would further facilitate for a direct comparison between the wakes at different thrust configurations. Consideration of the thrust normalised advance ratio would mean that a similar flow-field would be obtained

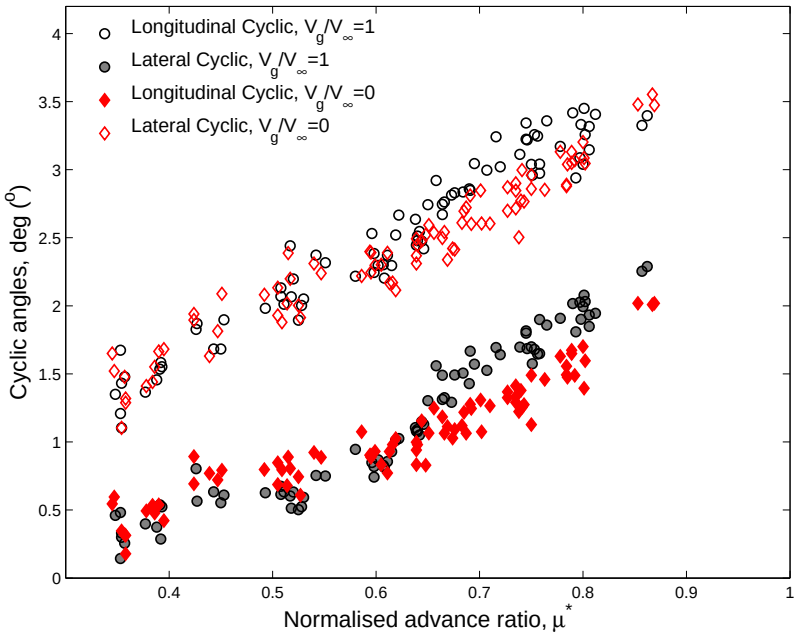

FIGURE 5.16: Lateral and longitudinal cyclic blade pitch adjustments required to reach the Large Rotor quasi-trim state, in ground effect forward flight. The rotor collective pitch setting was $\theta_0 = 12.8^o$.

for different collective angle settings (or thrust setting). Evidence for this can be seen from the cyclic trim data recorded for the Large Rotor for the collective angle of $\theta_0 = 12.8^o$, shown in Figure 5.16. A comparison of this with Figure 5.9, obtained for the collective angle of $\theta_0 = 8.8^o$, shows the step-like change in the lateral cyclic pitch angle to occur between the same normalised advance ratio range of $0.62 < \mu^* < 0.7$, despite differences in the collective angle (thrust) settings. These figures suggest that the wake is identical for both the collective angle settings, although higher cyclic inputs were required for the $\theta_0 = 12.8^o$ case to account for the differences in thrust brought about by the higher rotor collective angle.

5.4 Instantaneous flow data

Instantaneous flow data obtained from PIV are useful for providing information of the flow-field at specific instances in time. Details such as non-steady flow structures lost in the averaging process of the mean PIV data, velocity fluctuations and time-resolved data such as frequencies (only for time-resolved PIV) can be identified from these snap-shots and provide comprehensive insights into the flow-field under investigation. The PIV experiments carried out in this research were not

time resolved, and hence could not be used to determine time-dependent characteristics of the investigated flow-field. They however, could be used to provide insights into the state of the wake at arbitrary time instances and could be used to indicate the relative steadiness of the flow [90].

5.4.1 General Observations

Investigations of the instantaneous PIV vorticity data showed two prominent structures to exist in the instantaneous ground effect flow-field. Figure 5.17 presents samples of instantaneous vorticity plots obtained from the test conducted at a normalised advance ratio of $\mu^* = 0.61$, with a quasi-trimmed rotor at a ground distance of $1.0R$ and a moving ground configuration ($V_g/V_\infty = 1$). Artefacts due to poor data quality are present along the extreme left edges of these plots and are ignored during the analyses. Results from tests conducted at a similar normalised advance ratio, using the other rotor trim and ground boundary configurations, are presented in Appendix C.2 for reference.

(a) Flow separation at $r/R = 1.56$ (b) Flow separation at $r/R = 1.48$

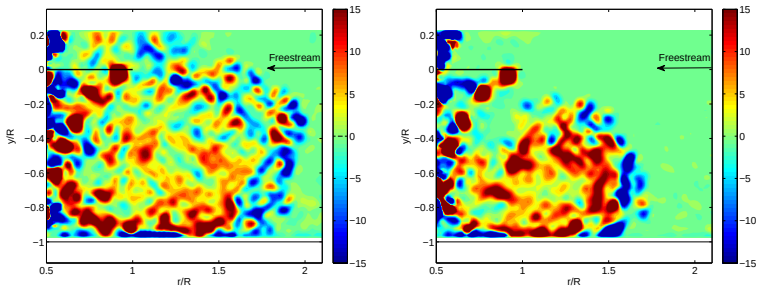

(c) Flow separation at $r/R = 1.52$ (d) Flow separation at $r/R = 1.40$

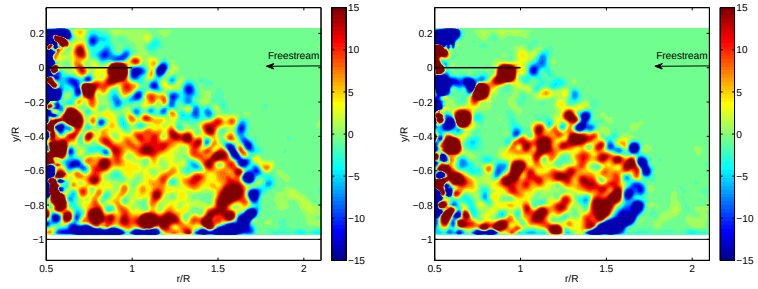

FIGURE 5.17: Instantaneous vorticity plots at $\mu^* = 0.61$ with the rotor quasi-trimmed and the rolling road moving ($V_g/V_\infty = 1$). The rotor was at a ground distance of 1.0R and the mean topological flow separation point was at $\frac{r}{R} = 1.60$.

Analyses of the plots in Figure 5.17 indicate that the instantaneous ground effect flow-field was characterised by clumps of positive and negative vorticity. Positive vorticity clumps were seen to possess varying vorticity strengths, with most of the high magnitude positive vorticity clumps observed to form closer to the ground, and those higher up in the flow-field seen to possess lower magnitudes. This distribution of positive vorticity within the flow-field can be attributed to the trailing tip vortex system leaving the rotor disk; as the tip vortices trail with the rotor wake along the ground plane, they undergo diffusion [89] resulting in vortex clumps reminiscent of these tip vortices to be observed in the track along the ground. The time taken for the tip vortices to reach higher up in the flow-field after leaving the ground at the flow separation point allows further dissipation to occur, resulting in the clumps higher above the ground to be seen with lesser vorticity strength than those nearer the ground. Figure 5.17 (a) clearly illustrates this, where the positive vorticity clumps closest to the ground, at $-1.0 < \frac{y}{R} < -0.8$, are observed to possess higher magnitudes that those further up in the flow-field, at $\frac{y}{R} > -0.6$. Accordingly, the mean vorticity data for this case (presented in Figure 5.12 (e)) shows high magnitude mean positive vorticity closer to the ground plane while the vorticity higher up in the flow-field were seen with lower mean magnitudes. Similar observations were made from the other normalised advance ratios tested, with the mean vorticity data presented in Figure 5.12 showing such distributions of positive vorticity in the ground effect wake to be more obvious in the cases where the mean topological flow separation point occurred far ahead ($\frac{r}{R} > 1.5R$) of the rotor disk.

5.4.2 Positive Vorticity

Postive vorticity associated with the tip vortices were also observed from the instantaneous flow-field to form a loop within the recirculation zone, after leaving the ground at the flow separation point. Figure 5.17 (b) provides a good representation of this process, and shows discrete high magnitude positive vorticity clumps to exist in the flow-field after the flow separation point. When compared with the mean vorticity plot presented in Figure 5.12 (e), it can be seen that these high magnitude positive vorticity clumps exist around a loop which is seen to border the mean recirculation zone. Comparison of the plots presented in Figure 5.17 show that while the instantaneous flow-field appeared to be constantly varying, as

indicated by the changing separation point locations in the plots, the tip vortices leaving the ground follow this definite loop-like path into the recirculation region. Formation of a loop of tip vortices within the mean recirculation region thus appeared to be a consistent feature of the wake, and traces of it is seen in all the plots presented in Figure 5.17. The presence of this loop of positive vorticity in the flow-field appears to be similar to the flow visualisation observations made by Ganesh *et. al* [30, 32] of a loop of tip vortices present in the flow-field during the recirculation regime. Preliminary PIV test results presented in Chapters 3 and 4, and the Large Rotor test results obtained from the stationary ground configuration ($V_g/V_\infty = 0$) tests (presented in Appendix C.2), however did not show the presence of this loop of tip vortices in the ground effect flow-field, and provide further evidence of the effect of the ground boundary configuration on the formation of the detailed ground effect flow features (as was described in Section 5.2.2.2).

Some of the instantaneous vorticity plots presented in Figure 5.17 also show significant vorticity regions near/above the rotor disk, implying that re-ingestion of the wake, identified by Curtiss *et. al* [24, 27] to occur in the recirculation regime, may occur at this normalised advance ratio. Figures 5.17 (a) and (c) clearly show significant vorticity magnitudes in regions above the rotor disk; with the rotor inducing a downwash on the airflow around it, it can be inferred that this vorticity present above the disk will be ingested through the rotor. In some cases, as shown in Figure 5.17 (a), the loop of vorticity was seen to reach the flow vicinty close to the rotor disk, transporting some of the tip vortices to this region. Presence of vorticity in flow regions near/above the rotor disk was however seen to be an inconsistent process, with Figures 5.17 (b) and (d) showing little vorticity present above the rotor disk, and imply that re-ingestion of the wake did not always occur in the flow-field at this normalised advance ratio. A more detailed analyses of the re-ingestion process will be provided in a later section (Chapter 6). At present, these instantaneous plots are sufficient to conclude that the ground effect flow-field consists of a loop of high magnitude positive vorticity, which is seen to vary in location and size due to the unsteadiness of the wake. As the normalised advance ratio is increased and the mean flow separation occurs closer to the rotor disk, the loop of positive vorticity was seen to reduce in size. Eventually, it evolves into a compact ground vortex when flow separation occurs just under the leading edge of the rotor disk, as illustrated in the mean vorticity plots presented in Figure 5.12.

5.4.3 Negative Vorticity

Another feature seen from the instantaneous vorticity plots to be prominent in the ground effect flow-field is the negative vorticity clumps. Much like the positive vorticity, these were also seen to possess varying magnitudes. Generally, the further the flow separation point from the rotor, the lesser the strength of these negative vorticity clumps. Evidence for this is provided in Figure 5.18 (a), where the negative vorticity clumps in the flow field was seen to be weaker than those seen in the plots in Figure 5.17. As in the case of the positive vorticity clumps, the negative vorticity clumps located higher up in the flow-field also appeared to be weaker compared to those nearer the ground, and a comparison of the negative vorticity in the flow-field shown in Figure 5.18 (b) proves this.

Detailed analyses of the instantaneous vorticity plots presented in Figure 5.17 show the negative vorticity clumps to mainly border the positive vorticity clumps and the ground plane, beginning from the junction where the rotor tip vortex system reached the ground and extending along the ground plane until the flow separation point. As the positive vorticity clumps form a loop in the recirculation region after leaving the flow separation point, the negative vorticity clumps were seen to continue to border the positive vorticity clumps around the outer edge of the mean recirculation region, with Figure 5.17 (d) providing a good example of this. Similar observations were made at the other normalised advance ratios tested, with a reduction in mean vorticity strength observed at the lower normalised advance ratio cases (see Figure 5.12). As in the case of the positive vorticity, the PIV data also showed instances where negative vorticity was present in the flow regions near/above the rotor disk. Figures 5.17 (a) and (c) reflect this and imply a re-ingestion of the negative vorticity through the rotor disk.

The presence of negative vorticity in the ground effect flow-field, is associated with a ground boundary layer induced by the rotor wake expanding along the ground. This wake induced boundary layer will form between the ground plane and the trailing rotor wake, and will be of opposite vorticity to the tip vortex system in the wake. While the root vortex system trailed by the rotor blades may be a source of this negative vorticity in the flow-field, this is unlikely as the PIV data shows the root vortex system to be skewed back by the oncoming freestream. Detailed

(a) Flow separation at $r/R = 2.27$ (b) Flow separation at $r/R = 2.54$

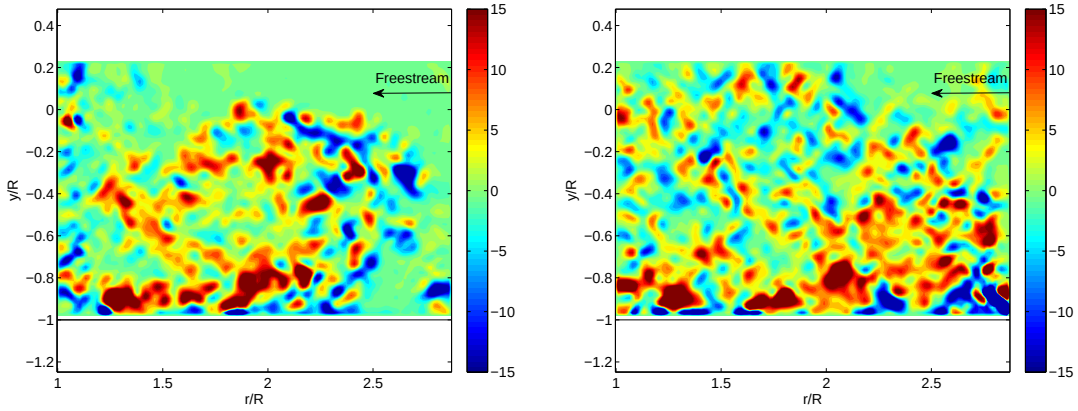

FIGURE 5.18: Instantaneous vorticity plots at a normalised advance ratio of $\mu^* = 0.4$, when the rotor was quasi-trimmed and the ground moving ($V_g/V_\infty = 1$). The rotor was at a ground distance of 1.0R and the mean topological flow separation location was at $\frac{r}{R} = 2.49$.

analyses of the experimental results show the high magnitude negative vorticity to be present especially around the regions of high magnitude positive vorticity, trailing along the ground plane. Examples of this can be seen from the intantaneous plots in Figure 5.17 and suggests that the passage of the high-magnitude tip vortices close to the ground plane induces secondary separation of the flow. Evidence for this secondary separation was also provided by the flow visualisation videos, where the talcum powder particles uplifted near the ground were seen to swirl in an opposite sense to the rotational sense of the tip vortices (see Figure 3.5). Occurrence of secondary separation along the ground plane has been suggested by Sun through numerical simulations of the ground vortex regime [33]. Through analyses of the PIV results, the formation of the secondary separation in the flow-field is attributed to vortex-induced separation caused by the passage of high vorticity-strength tip vortices close to the ground plane. The resulting velocity gradients in the flow, especially in the case of the moving ground configuration, results in the flow to separate from the ground, forming oppositely signed vorticity.

With most of the tip vortices reaching the separation point before leaving the ground plane, most of the secondary flow separation will occur in this region. Evidence for this is provided by the instantaneous vorticity data presented in Figure 5.17, where high magnitude negative vorticity are observed near the flow separation point in each plot. As in the case of the tip vortices, these negative vorticity

clumps leave the ground plane at the flow separation location; they border the tip vortices as they trail into the recirculation region in the flow-field, and like the positive vorticity, dissipate as they age. This explains the lower magnitudes of the negative vorticity located higher up in the instantaneous flow-field, away from the ground plane. Wide-spread distribution of vorticity in the flow-field have also been observed from the instantaneous flow data; an example of such an instance is shown in Figure 5.18 (b), where vorticity is seen to be distributed throughout the imaged field-of-view. A probable explanation for this may be the mutual induction effects (similar to interactions between counter-rotating vortices which causes an acceleration of the vorticies in the flow direction) caused by the close proximities of positive and negative vorticies in the flow-field, which can cause vorticity to reach flow regions far above the ground plane.

While PIV results from the moving ground configuration tests show the presence of the negative vorticity clearly in the ground effect wake, past quantitative experimental investigations conducted by other researchers have not revealed the presence of this negative vorticity in the flow-field. PIV experiments conducted by Ganesh *et. al* [36] and Boer *et. al* [35] of the ground vortex regime do not show this secondary separation or the presence of negative vorticity within the flow-field. One similarity between these experiments, was the use of a static ground plane during the tests. With the experimental results from this research showing the negative vorticity in the mean flow-field produced by the stationary ground configuration to be less prominent than that produced by the moving ground configuration (Section 5.2.2.2), the difference in the ground boundary configurations will be a contributing factor to the secondary separation and negative vorticity not being observed in the flow-field of past ground effect experiments. Other factors such as the lower resolution of the PIV system used during those tests may have also contributed to the accuracy of the results obtained from those tests.

5.5 Flow Unsteadiness

Instantaneous PIV data have also provided an indication of the unsteadiness associated with the ground effect wake. Most obvious from the instantaneous vorticity data were the fluctuations of the flow separation positions along the ground plane

at each normalised advance ratio tested. Examples presented in Figure 5.17 show flow separation in each individual plot to occur at a slightly different location compared to the mean separation point location, derived from the mean velocity data. Analyses of the instantaneous PIV data at all normalised advance ratios showed similar fluctuations of the separation point and conclusively prove the unsteady nature of the ground effect wake. The degree of the separation point fluctuations was however seen to vary with normalised advance ratios and was seen to result in changes in the distribution of vorticity in the instantaneous ground effect flow-field.

An attempt was made to quantify the flow separation point fluctuations observed in the ground effect wake at the different normalised advance ratios. Figure 5.19 presents histograms showing the positions of the instantaneous topological flow separation points and the corresponding mean topological flow separation point location derived from the mean PIV velocity data, for selected normalised advance ratio cases where the rotor was quasi-trimmed and operated at a ground distance of $1.0R$ with the moving ground configuration ($V_g/V_\infty = 1$). The histograms represent the individual flow separation locations, measured from the 120 PIV images recorded at each normalised advance ratio. As in the previous analyses, the flow separation location was topological and identified from the PIV velocity data at the point where the u-velocity component close to the ground plane was zero.

Analyses of the histograms presented in Figure 5.19 show varying trends in the spread of the separation point fluctuations at the different normalised advance ratios. Comparisons between the different frames in Figure 5.19 indicate a greater fluctuation amplitude at the lower advance ratios compared to the higher advance ratios, where a compact vortex was observed under the rotor disk. Figure 5.19 (a) presenting the data from $\mu^* = 0.4$, shows most fluctuations of the sample separation points to be within 0.05R of the mean separation location, although instances where large amplitude deviations from the mean separation point location were also seen to occur in the flow-field, as indicated by the histogram bin present at $\frac{r}{R} \approx 2$. At the higher normalised advance ratio of $\mu^* = 0.52$, indicated by Figure 5.19 (b), no large scale deviations from the mean appeared in the flow. Instead, the fluctuations were observed to be more moderate about the mean and ranging from $1.6 < \frac{r}{R} < 2.3$. At $\mu^* = 0.66$, the separation point fluctuations, presented in Figure 5.19 (c), appeared to be least, ranging from $1.0 < \frac{r}{R} < 1.5$, with more than

(a) Rotor at $\mu^* = 0.4$

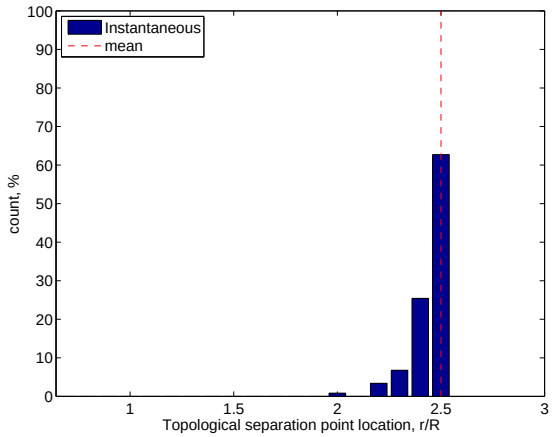

(b) Rotor at $\mu^* = 0.52$

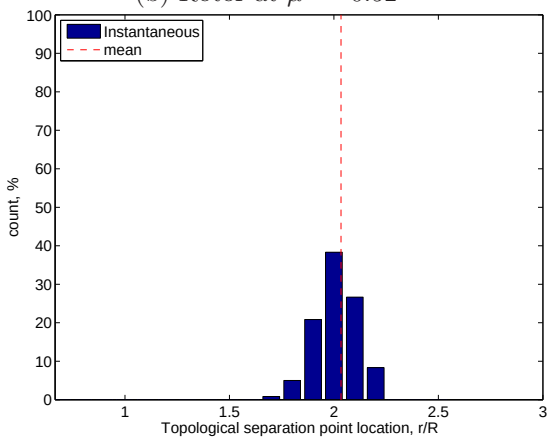

(c) Rotor at $\mu^* = 0.66$

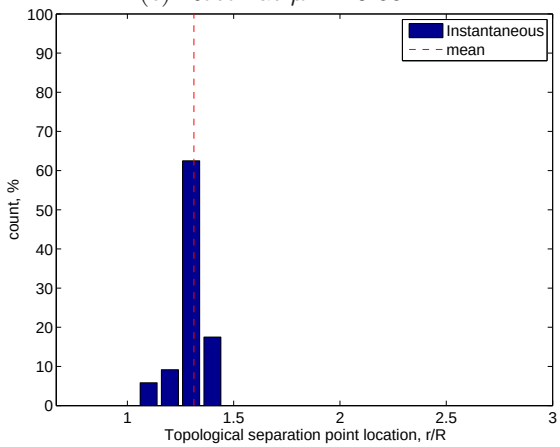

FIGURE 5.19: Spread of the instantaneous flow separation point locations in the recorded PIV sample, for a range of normalised advance ratios (μ^*), with the rotor quasi-trimmed and at a ground distance of $1.0R$ and the ground moving ($V_g/V_\infty = 1$). Frames also present the mean flow separation position derived from the average PIV data.

60% of the sample separation points within 0.05R of the mean separation location. In this case, the separation point location of the flow seemed to be steadier, and the instantaneous vorticity plots showed the resulting ground vortex to form in an almost similar location for all the recorded instances. Similar trends were also observed for the stationary ground configuration and the interested reader is referred to Appendix C.3 for further information.

This statistical analyses of the flow separation point locations, although inadequete to conclude on the overall distribution of the separation positions for the sample set (due to the small sample size), indicates the relative steadiness of the ground effect wake at different normalised advance ratios. Greatest wake fluctuations were observed at the lower normalised advance ratios, where the flow-field showed large amplitude deviations of the separation points. The fluctuations appeared more moderate around the mean as the normalised advance ratio was increased, with the wake appearing to be the most steady when the flow separation occurred close to the leading edge of the rotor disk. Variations in the separation point locations, especially at the lower normalised advance ratios where the mean recirculation region occurred ahead of the rotor disk, may contribute to the differences in the location of the loop of positive vorticity within the recirculation region; evidence for this was seen from the instantaneous flow data discussed in the previous section. This in turn can affect the location of the tip vortices and their eventual trajectories within the flow-field and influence the velocity fluctuations experienced within the wake.

5.5.1 Root-mean-square Velocity Fluctuations

Insights into the velocity fluctuations experienced in the ground effect flow-field can be obtained by considering the root-mean-square (RMS) velocity fluctuations. Figure 5.20 shows the contour plots of the RMS fluctuations of the local velocity about the local mean, non-dimensionalised with respect to the hover induced velocity, V_h. RMS data obtained from tests conducted with the quasi-trimmed rotor at a ground distance of 1.0R and a moving ground configuration ($V_g/V_\infty = 1$) are presented in this figure for a range of normalised advance ratios, and have been derived from the u and v velocity components measured from the PIV. Where present, the rotor disk location on the plots is represented by a white line; the

plots provide useful insights into the magnitude and extent of velocity fluctuations experienced in the flow-field.

The RMS plots presented in Figure 5.20 show the velocity fluctuations experienced in the ground effect wake to increase and become confined within smaller areas of the flow-field as the normalised advance ratio was increased. Comparisons of the RMS velocity plots with mean vorticity plots presented in Figure 5.12 showed the locations of the velocity fluctuations to coincide with the location of the mean recirculation zone. At the lower normalised advance ratios, where the mean flow separation occurred far upstream from the rotor and the resulting mean recirculation region encompassed a large proportion of the flow-field upstream of the rotor, the RMS fluctuations appeared to affect a greater proportion of the imaged flow-field. Figure 5.20 (a) provides a good example of this, and shows the flow-field ahead of the rotor disk, in the region of the mean recirculation, affected by high magnitude fluctuations. Regions of the flow-field higher than the rotor distance from the ground, were also seen to possess low magnitude velocity fluctuations of around $0.2V_h$, indicating that flow regions beyond the recirculation zone were affected by weak velocity fluctuations. Similar results were observed from other low normalised advance ratio tests where the mean recirculation zone was seen to form upstream of the rotor disk. As the normalised advance ratio was increased, higher magnitude velocity fluctuations were seen to occur in the wake, although these were confined to within smaller regions of the flow-field. Figure 5.20 (d) shows the velocity fluctuations to be confined to the region where the ground vortex was located, with no significant velocity fluctuations observed elsewhere in the flow-field.

Both the Large Rotor test results presented here and those obtained from the Preliminary PIV investigations presented in Chapter 4, show similarities in the confinement of the velocity fluctuations to smaller areas of the flow-field at higher advance ratios, although differences in the distribution of the velocity fluctuations within these regions were observed between the results. This can be attributed to the differences in the experimental ground boundary configurations between the two tests. (Similar differences were also observed for the stationary ground configuration tests conducted with the Large Rotor and this is presented in Appendix C.3.1.) Plots presented in Figure 5.20 show the peak RMS fluctuations to occur within the mean recirculation zone, broadly coinciding with the location of the loop

(a) $\mu^* = 0.4$ (b) $\mu^* = 0.51$

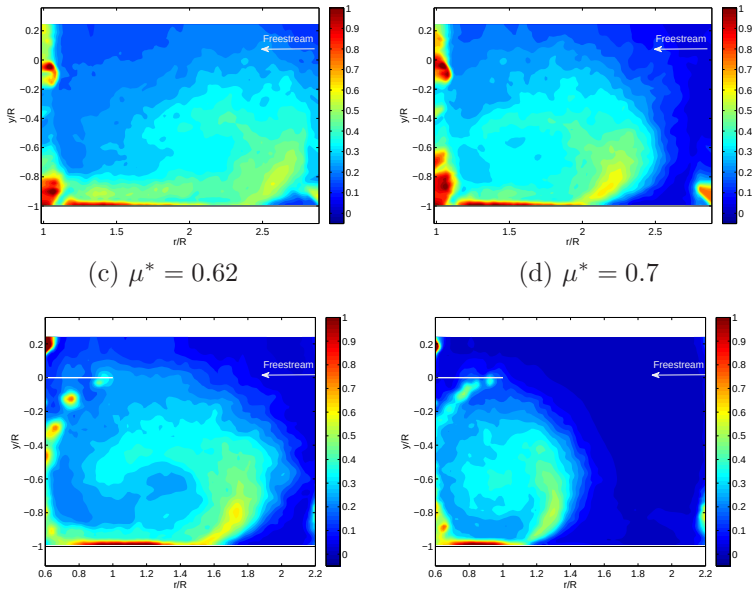

(c) $\mu^* = 0.62$ (d) $\mu^* = 0.7$

FIGURE 5.20: RMS velocity fluctuations at a range of normalised advance ratios with the rotor quasi-trimmed and the rolling road moving ($V_g/V_\infty = 1$). The rotor was at a ground height of 1.0R and the RMS velocity fluctuations are normalised with V_h.

of high magnitude positive vorticity, observed in the mean vorticity plots. This can be seen clearly from Figure 5.20 (c), where the highest velocity fluctuations were seen under the rotor disk, along the ground plane and in a loop-like trajectory within the mean recirculation zone. With the highest magnitude positive vorticity present in these regions, these RMS plots can thus be used to conclude that the velocity fluctuations observed in the flow-field are associated with the presence of vorticity in the flow-field. High magnitudes of the fluctuations in these regions provide further evidence that the likely cause of these RMS velocity fluctuations were the large scale fluctuations of the flow structures, rather than small scale fluctuations associated with turbluence in the flow-field. Instantaneous vorticity plots presented in Figure 5.17 show continuous variations in the locations of the high magnitude positive vortices along the ground plane and within the loop-like structure in the mean recirculation region, and imply this to be the most likely source of the RMS velocity fluctuations observed in the flow-field.

Based on these observations, the presence of velocity fluctuations beyond the mean recirculation regions observed from Figures 5.20 (a) - (c), imply vorticity distribution beyond the mean recirculation region to occur in the ground effect wake

at the lower normalised advance ratios, where the flow separation results in the mean recirculation region to form upstream of the rotor disk leading edge. The low magnitudes of these fluctuations imply that vorticity is not consistently present in these flow regions and reflect the unsteady nature of the ground effect flow-field. With the RMS velocity data from the flow-field containing a compact ground vortex under the rotor disk showing little velocity fluctuations above the rotor disk (Figures 5.20 (d)), this data can be used to conclude that the unsteadiness in the ground effect wake was more significant at the lower normalised advance ratios, where flow separation occurred far upstream of the rotor disk leading edge.

5.6 Investigations of cross-flow velocity components in the ground effect wake

Observations of the dust particles in the preliminary flow visualisation experiments, implied a highly three-dimensional and unsteady wake. While both the separation point and RMS velocity fluctuations presented in the previous section provide an indication of the unsteadiness of the wake along the longitudinal plane through the rotor hub, they do not account for the cross-flow velocity components affecting the flow-field. To measure the cross-flow velocities within this plane, Stereoscopic (stereo) PIV tests were conducted with the Large Rotor, in the same wake regions as the 2D2C PIV tests and for the same experimental configurations. Two cameras, arranged in the angular displacement Stereoscopic PIV set-up, were used to obtain three-component velocity (u, v, w) information from the (r, y) plane of the wake. Figure 5.21 illustrates the experimental set-up in the wind tunnel and shows the coordinate system adopted for this analysis. As was the case in the 2D2C PIV tests, the (r, y, z) coordinate system, with its origin at the rotor hub and the rotor leading edge blade tip at the position $(\frac{r}{R}, \frac{y}{R}) = (1, 0)$ was used.

The cross-flow velocity component, w, re-constructed from the stereoscopic PIV data is presented in this dissertation as contour diagrams, to allow for a distinction in the direction and magnitudes associated with the cross-flow. Negative contour levels signify a flow away from the reader (into the page) and positive contour levels represent a flow towards the reader (out of the page). The rotational sense of the rotor mean that in these contour plots, the rotor blade tip moves into the

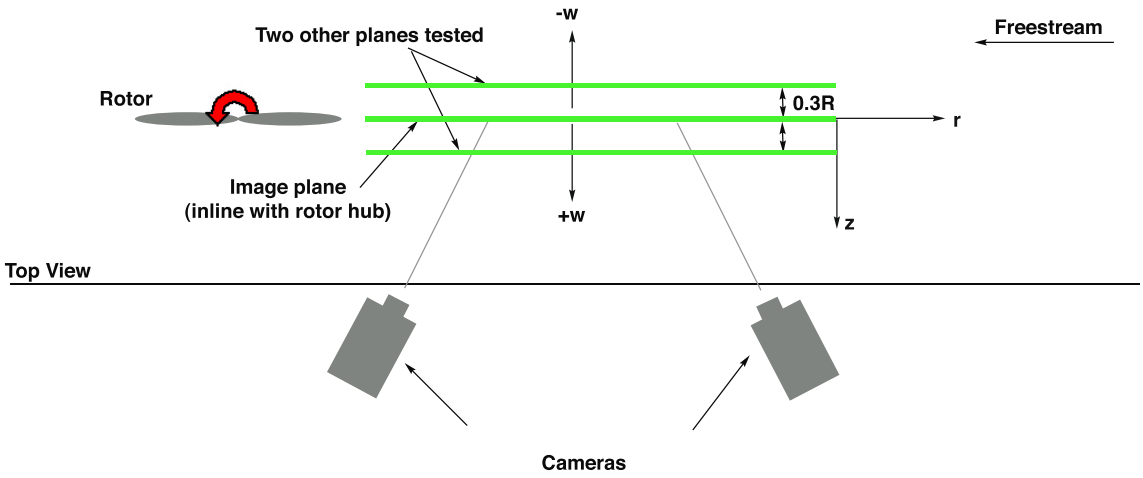

FIGURE 5.21: Illustration showing the direction sense of the cross-flow velocity component, w, derived from the stereoscopic PIV experiments. The sense of the (r, z) coordinate system is shown, with the y coordinate out of the page. The origin of the coordinate system is at the rotor hub.

page. In addition to the longitudinal plane of symmetry through the centre of the rotor hub, other planes were considered, to investigate the three-dimensional properties of the ground effect wake. Two other longitudinal planes, $0.3R$, either side of the longitudinal plane of symmetry, were investigated and the locations of these planes are also shown in Figure 5.21. Optical access difficulties meant that the transverse plane, across the width of the wind tunnel working section, could not be investigated with the stereo PIV set-up.

5.6.1 Stereo PIV Data Validity

Verification of the stereo PIV data was conducted during the PIV set-up process. A range of uniform freestream tests were conducted with the stereo PIV and these were used to benchmark the accuracy of the stereo PIV set-up. Through these experiments, it was established that there were no velocity gradients present in the cross-flow measurements across the imaged field-of-view.

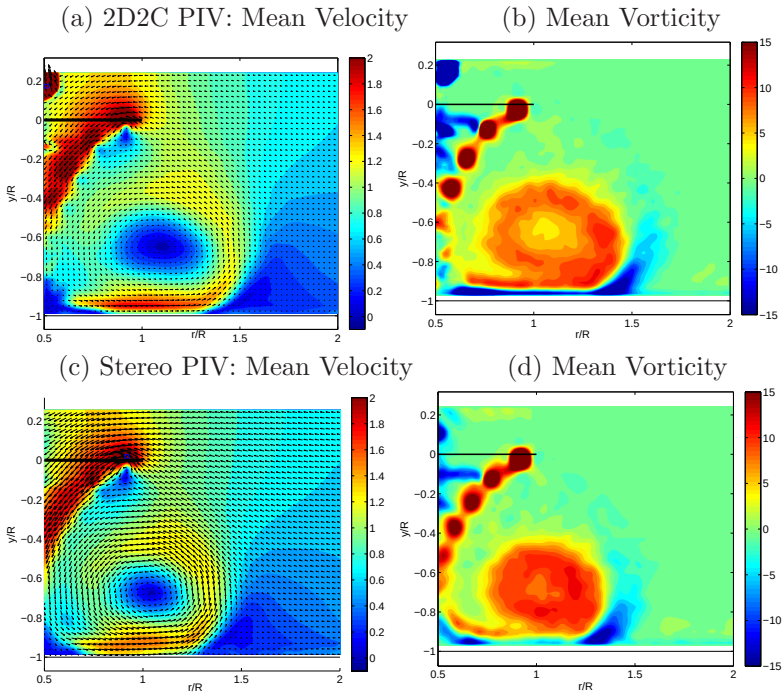

FIGURE 5.22: Mean velocity and vorticity plots obtained from the 2D2C PIV and Stereo PIV tests, for a normalised advance ratio of $\mu^* = 0.66$. In these cases, the rotor was quasi-trimmed and at a ground distance of 1.0R and was operated with the ground moving ($V_g/V_\infty = 1$).

Further verification of the stereo PIV results were conducted by comparing the stereo PIV data to results obtained from the 2D2C PIV tests. An example of this is provided in Figure 5.22, taken from tests done at a normalised advance ratio of $\mu^* = 0.66$. Comparisons of the data from both sets of experiments show similarities in terms of the mean velocity magnitudes, vorticity strengths and locations of the main ground effect flow features, and these validate the Stereo PIV results.

5.6.2 Mean cross-flow velocity in the ground effect wake

Stereo PIV tests conducted with the Large Rotor allowed for three-component velocity measurements from wide areas of the ground effect flow-field. Figure 5.23 presents contour plots showing the mean velocity magnitudes derived from the three-component velocity measurements and the corresponding mean w, the cross-flow velocity component in the ground effect flow-field, for a range of normalised advance ratios, with the quasi-trimmed rotor at a ground distance of $1.0R$ and the ground moving ($V_g/V_\infty = 1$). All the velocity plots are scaled with respect to the hover induced velocity ($V_h = 3.6ms^{-1}$). Where possible, tests at normalised

advance ratios, similar to those presented in Figure 5.12 were chosen, to allow for direct comparisons between the velocity and vorticity data from the flow-field. Artefacts, resulting from the overlapping of the camera systems' large chip sizes and the scheimpflug adaptors, are noticeable at the extreme left and right edges of the Stereo PIV data, and are particularly visible in the w-component velocity plots; these are ignored during the analysis of the data.

Figure 5.23 shows the mean velocity magnitudes in the ground effect wake to progressively increase with normalised advance ratio. With the exception of the velocities associated with the trailing tip vortices under the rotor disk, an example shown in Figure 5.23 (e), the surrounding flow-field was seen to contain relatively low magnitude mean velocity. The highest velocity magnitudes associated with the ground effect wake were seen just above the ground plane and a comparison with corresponding vorticity data show this to coincide with the trailing rotor wake expanding along the ground plane. With the tip vortices becoming more dissipated as they trailed along the ground, the mean velocity magnitudes were seen to become progressively lower. This explains the weaker velocity magnitudes observed along the ground plane at the lower normalised advance ratios, as is seen from Figure 5.23. With flow separation occurring closer to the rotor disk at higher normalised advance ratios, the vortices reaching the recirculation region remain relatively younger, thus resulting in greater velocity magnitudes to be experienced within the flow-field. Similar observations were made from the other experimental configurations tested (presented in Appendix C.4.1), although significantly higher velocity magnitudes were observed in the wake with the moving ground boundary configuration ($V_g/V_\infty = 1$) cases presented here.

Differences in the velocity magnitudes in the wake brought about by the different ground boundary configurations imply that during experimental testing of the brownout phenomenon, the ground boundary configuration will have an implication on the quantity of dust picked up from the ground. With the PIV data showing velocities along the ground plane to be higher, the moving ground configuration ($V_g/V_\infty = 1$) is expected to cause more dust particles to be uplifted from the ground plane, resulting in bigger dust cloud sizes. These results further re-iterate the importance of re-creating accurate ground boundary conditions during ground effect testing, as they are seen to have a direct effect on the velocity

magnitudes experienced in the flow-field.

Mean cross-flow (w) velocities, associated with the ground effect wake at the different normalised advance ratios are also presented in Figure 5.23. Negative cross-flow velocities visible beneath the rotor disk, as shown in Figures 5.23 (f) and (h), correspond to the locations of the trailing rotor tip vortex system and represent the axial velocities associated with the tip vortices. With the rotor blade tip at $(\frac{r}{R}, \frac{y}{R}) = (1, 0)$ moving into the page (anti-clockwise rotating rotor system), the cross-flow (axial) velocity within the tip vortices follows the rotational sense of the rotor [91], and is negative. Synchronisation of the laser with the rotor azimuth allowed for measurements of the axial velocity in the mean PIV data, although its accuracy may be affected by smearing effects caused by vortex wandering [92, 93]. The mean flow information however indicate the cross-flow velocities associated with the axial velocities of the tip vortices (under the rotor disk) to be the highest observed in the ground effect flow-field, with the mean cross-flow velocities significantly lower everywhere else in the flow-field.

Analysis of the stereo PIV data showed the mean cross-flow velocities associated with the ground effect flow features at all the normalised advance ratios tested to be of small magnitudes, with the highest mean cross-flow velocity magnitudes of around $w = 0.2V_h$, recorded at the highest normalised advance ratios tested. (Slightly higher cross-flow velocity magnitudes were observed for the stationary ground configuration tests and the interested reader is referred to Appendix C.4.1 for further information.) For the moving ground configuration ($V_g/V_\infty = 1$), most of the flow-field was seen to contain very little cross-flow, with Figures 5.23 (b) and (d) providing good examples of this. In these cases, a region of low negative cross-flow velocity was noticed along the ground plane, up to the mean flow separation point location. These regions of negative cross-flow velocity consistently appeared in the flow-field at all the normalised advance ratios, and are associated with the axial velocities of the tip vortices tracking along the ground plane. Besides this, the data showed the appearance of a region of very low magnitude cross-flow ($w \approx -0.1V_h$) in the flow-field, as the normalised advance ratio was increased. Figure 5.23 (d) shows traces of this region of negative cross-flow in the flow-field, around $(\frac{r}{R}, \frac{y}{R}) = (1.7, -0.5)$, and a comparison with the mean vorticity plot for this case (Figure 5.12 (c)) showed this region to be broadly coincident with the

mean recirculation region observed in the flow-field. As the normalised advance ratio was increased, this region of mean negative cross-flow in the flow-field was seen to become more prominent, as shown in Figures 5.23 (f) and (h).

In addition to the appearence of a region of mean negative cross-flow, the flow-field at the higher normalised advance ratios, presented in Figures 5.23 (f) and (h), also showed the appearence of regions of weak positive cross-flow velocity. Figure 5.23 (f) shows the region of mean negative cross-flow around $(\frac{r}{R}, \frac{y}{R}) = (1.1, -0.7)$, and a patch of positive cross-flow upwards and to its right at around $(\frac{r}{R}, \frac{y}{R}) = (1.4, -0.5)$, and a smaller patch of positive cross-flow to its lower left. Figure 5.23 (h) shows similar regions of positive cross-flow velocities, although in this case, the patch of positive cross-flow to the lower left of the region of negative cross-flow appears close to the artefact in the image and hence is affected by erroneous data. The appearence of these regions of positive cross-flow in the flow-field was seen to coincide with the appearence of the ground vortex under the rotor disk and was not visibile at the lower normalised advance ratios, where larger mean recirculation zones were present in the flow-field upstream of the rotor disk leading edge. Similar observations were made from the flow-field produced by the stationary ground configuration (presented in Appendix C.4.1), with the cross-flow magnitudes seen to be significantly higher due to the smaller dispersion of vorticity within the flow-field (discussed in section 5.2.2.3).

The presence of these regions of positive cross-flow when a ground vortex forms under the rotor disk may be associated with the jet velocity caused by the tip vortices as they roll up to form the ground vortex. With the locations of these regions of positive cross-flow however not coinciding with the location of the ground vortex, and the flow-field showing the presence of a region of negative cross-flow nearby, further investigations possibly at several other longitudinal planes need to be conducted before the presence of a jet flow in the flow-field can be established. With the mean flow data generally indicating very low magnitude cross-flows in the ground effect flow-field, especially at the lower normalised advance ratios, instantaneous PIV data was consulted to identify any significant features in the instantaneous cross-flow velocity maps.

(a) $\mu^* = 0.4$: Velocity Magnitude (b) w-velocity component

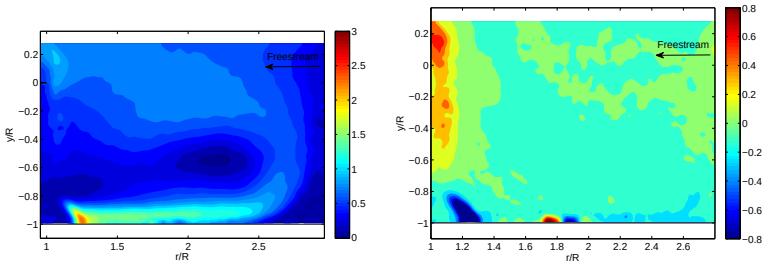

(c) $\mu^* = 0.51$: Velocity Magnitude (d) w-velocity component

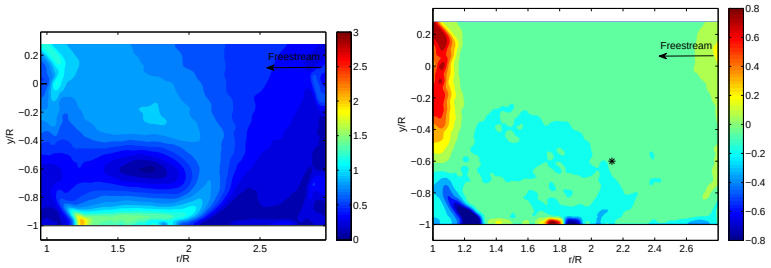

(e) $\mu^* = 0.67$: Velocity Magnitude (f) w-velocity component

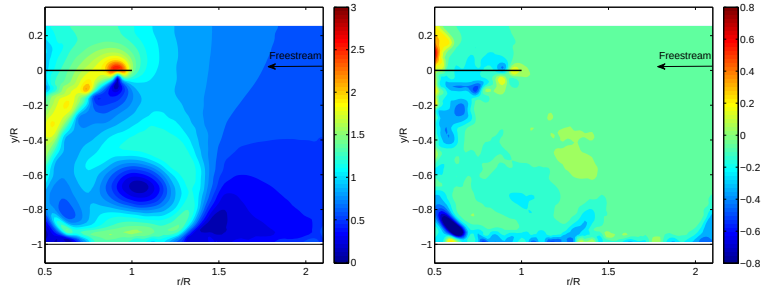

(g) $\mu^* = 0.75$: Velocity Magnitude (h) w-velocity component

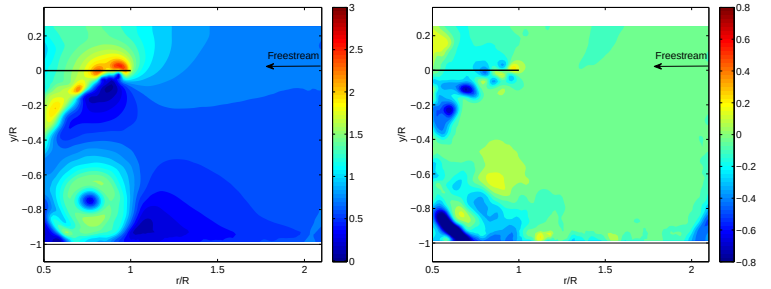

FIGURE 5.23: Mean velocity plots showing the velocity magnitudes and mean cross-flow (w) velocity in the flow-field, for a range of normalised advance ratios. In these cases, the rotor was quasi-trimmed and at a ground distance of 1.0R and was operated with the ground moving ($V_g/V_\infty = 1$).

5.6.3 Instantaneous cross-flow velocity in the ground effect flow-field

While the mean cross-flow velocity maps of the ground effect flow-field suggested very little cross-flow present in the wake, analysis of the instantaneous plots showed more significant cross-flow velocity magnitudes to exist in the flow-field. Significant variations in these cross-flow velocity magnitudes, observed to occur at each time instant, were seen to result in the low magnitude averages observed in the mean cross-flow velocity plots. With Figure 5.23 showing the mean cross-flow velocity to be broadly coincident with the mean vorticity regions seen in Figure 5.12, a comparison between the instantaneous cross-flow velocity and vorticity data obtained from the flow-field was performed to identify any correlation between the vorticity and cross-flow velocity locations in the flow-field. These comparisons however, showed little correlation between the vorticity and cross-flow velocity seen in the flow-field.

As an example, instantaneous cross-flow velocity contour plots for a normalised advance ratio of $\mu^* = 0.51$ and their corresponding instantaneous vorticity plots are presented in Figure 5.24. Figures 5.24 (b) and (d), presenting two instances of the flow-field, show significant differences in the cross-flow velocity components measured in the flow-field, and provide evidence of the constantly varying cross-flow velocity in the instantaneous flow-field. A comparison between corresponding vorticity and cross-flow velocity plots also showed little correlation. As an example, the track of negative vorticity seen in Figure 5.24 (a), extending from the ground plane at the separation point location at $\frac{r}{R} \approx 2.0$, is seen to correspond closely to the location of negative cross-flow velocity seen on the cross-flow (w) velocity plot shown in Figure 5.24 (b). The plot also shows a wide region of high magnitude negative cross-flow velocity present around $(\frac{r}{R}, \frac{y}{R}) = (1.6, -0.5)$, and this is seen to be broadly coincident with the positive vorticity observed within the same region, seen in Figure 5.24 (a). Similar observations were made through a comparison of Figures 5.24 (b) and (d) and highlight the difficulty in correlating the vorticity and cross-flow velocity locations from the instantaneous ground effect flow-field. Stereo PIV results from the other experimental configurations tested showed similar results and a summary of this is provided in Appendix C.4.2.

Information gathered from the investigations of the instantaneous cross-flow velocity component in the ground effect wake imply a constantly changing flow-field. Close proximities of the oppositely signed vorticity regions, which result in very complex flow patterns with very tightly woven vortex lines, and the re-orientation of the vortices as they enter the flow-field make the relationship between the vorticity and cross-flow velocities difficult to quantify. With the positive vorticity populating the instantaneous flow-field sourced mainly from the rotor tip vortex system, it is reasonable to expect the cross-flows to follow the rotational sense of the rotor. Positive vortex remnants of the tip vortices seen in the flow-field would however be thousands of revolutions old. With research and experiments showing the axial velocities associated with rotor tip vortices to fall by over 50% within half a rotor revolution [94–96], the cross-flow velocities associated with the tip vortices seen in the flow-field will be low. With inter-woven regions of positive and negative cross-flow velocities observed throughout the flow-field, regardless of the positive (and negative) vorticity locations, these instantaneous velocity plots suggest significant lateral flow present within the ground effect wake, providing an indication of its unsteadiness. Although no correlation between the positive and negative vorticity and the positive and negative cross-flow velocity components

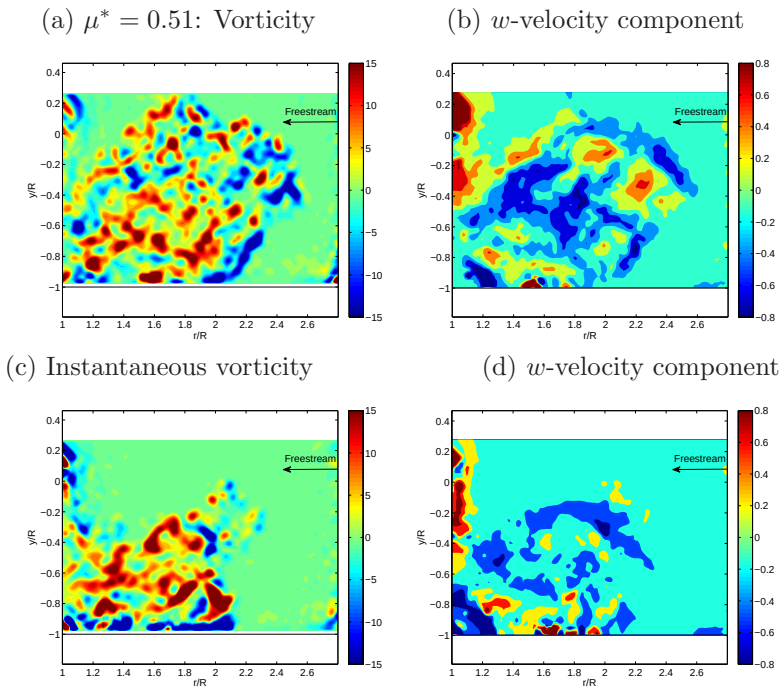

FIGURE 5.24: Instantaneous vorticity and cross-flow (w) velocity component plots, with the rotor at the ground distance of 1.0R. In these cases, the rotor was quasi-trimmed and was operated with the ground moving ($V_g/V_\infty = 1$), at a normalised advance ratio of $\mu^* = 0.51$.

could be established, the instantaneous flow data suggest the cross-flow velocity locations to broadly coincide with the regions of vorticity as is reflected in the mean vorticity and cross-flow velocity data. .

5.6.4 Cross-flow Velocity Fluctuations

Unsteadiness associated with the ground effect wake is better represented by considering the root-mean-square (RMS) velocity fluctuations. Plots associated with a range of normalised advance ratios tested with the quasi-trimmed rotor at a ground distance of $1.0R$ and the moving ground configuration ($V_g/V_\infty = 1$) are presented in Figure 5.25. In addition to the cross-flow (w) RMS fluctuations, the total RMS velocity fluctuations, derived from three-component velocity measurements of the wake, are also presented to quantify the unsteadiness in the flow-field. Similar figures for the other experimental configurations tests are presented in Appendix C.4.3 for reference.

Comparisons between the total RMS velocity fluctuations and the cross-flow RMS fluctuations in the flow-field revealed the peak cross-flow fluctuations to occur in the regions of the wake where the overall peak velocity fluctuations were observed. This was seen from Figure 5.25 to occur within the mean recirculation region, at all the normalised advance ratios tested. As was the case with the two-dimensional RMS velocity fluctuation data, presented in Figure 5.20, the total RMS velocity fluctuations were seen to affect large proportions of the ground effect flow-field, owing to the bigger mean recirculation regions forming upstream of the rotor disk, at low normalised advance ratios. Accordingly, the cross-flow velocity fluctuations were also seen from Figure 5.25 to affect wider areas of the flow-field, with regions as high as the rotor distance from the ground affected by low magnitude cross-flow velocity fluctuations. At higher normalised advance ratios, where the flow separation occurred under the rotor disk, the cross-flow velocity fluctuations were seen to be confined within smaller regions of the flow-field, coinciding with the location of the ground vortex formed under the rotor disk. Similarities in the locations of the peak cross-flow velocity flucuations and the high magnitude vorticity associated with the tip vortices present in the flow-field imply that the cross-flow velocity fluctuations are associated with the vorticity present in the ground effect wake.

(a) $\mu^* = 0.4$: RMS Velocity Magnitude (b) RMS w-component

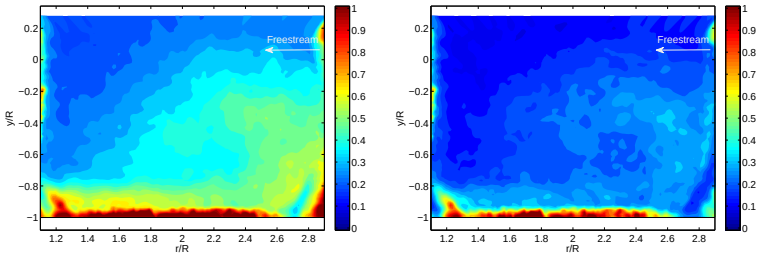

(c) $\mu^* = 0.51$: RMS Velocity Magnitude (d) RMS w-component

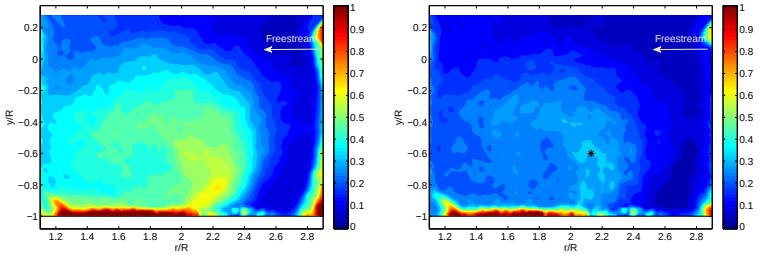

(e) $\mu^* = 0.67$: RMS Velocity Magnitude (f) RMS w-component

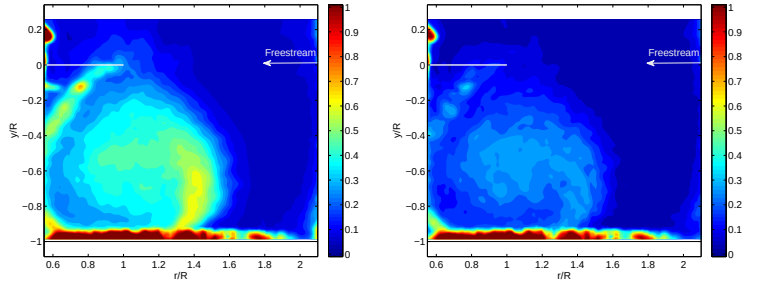

(g) $\mu^* = 0.75$: RMS Velocity Magnitude (h) RMS w-component

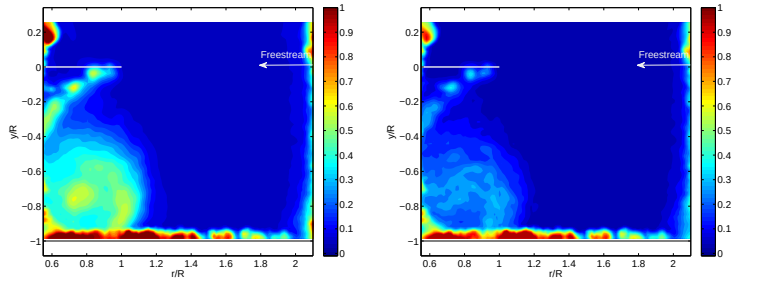

FIGURE 5.25: RMS velocity fluctuations showing the total velocity fluctuations and the cross-flow (w) velocity fluctuations experienced in the flow-field. In these cases, the rotor was quasi-trimmed and at a ground distance of 1.0R and was operated with the ground moving ($V_g/V_\infty = 1$).

Instantaneous cross-flow velocity vector maps, presented in Figure 5.24 showed flow regions coinciding within the mean recirculation region to be affected by significantly different cross-flow velocities at each instant. These observations support the cross-flow (w) RMS velocity fluctuation plots presented in Figure 5.25, which show the peak fluctuations to occur within the mean recirculation region of the ground effect flow-field. With the mean cross-flow velocity maps revealing low mean cross-flow velocities in the flow-field, at most of the normalised advance ratios tested, high cross-flow fluctuations within the wake suggested large cross-flow velocity deviations from the mean. To investigate this, the instantaneous cross-flow velocity, at a selected location in the flow-field was measured from the PIV at a particular normalised advance ratio.

Figure 5.26 presents the cross-flow velocity component measured from 120 PIV image samples, with the rotor operated at a normalised advance ratio of $\mu^* = 0.51$. Instantaneous cross-flow velocity data from the point $(\frac{r}{R}, \frac{y}{R}) = (2.13, -0.6)$, was plotted, together with the mean cross-flow velocity calculated from the flow-field, to indicate the magnitudes of the velocity deviations. The chosen location in the flow-field is indicated in the respective mean cross-flow velocity (Figure 5.23(d)) and w-component RMS velocity (Figure 5.25(d)) plots, and was seen to possess a high cross-flow velocity fluctuation magnitude, with a mean value close to zero. Figure 5.26 shows the data sample to contain high velocity deviations from the mean, with peak-to-peak fluctuations calculated to be around $1.6V_h$; in physical terms, this corresponds to around $5.6ms^{-1}$, and demonstrates the large cross-flow velocity fluctuations experienced in the wake. Significant variations in cross-flow velocities observed in the wake substantiates the appearence (and disappearence) of clusters of talcum powder particles observed from the talcum powder flow visualisation experiments. Furthermore, observations of low magnitude cross-flow fluctuations in flow regions above the rotor further imply the occassional presence of vorticity in these regions, substantiating the intermittent expansion of the dust cloud observed in the flow visualisation of the brownout dust cloud and provide evidence for a three-dimensional, highly unsteady wake.

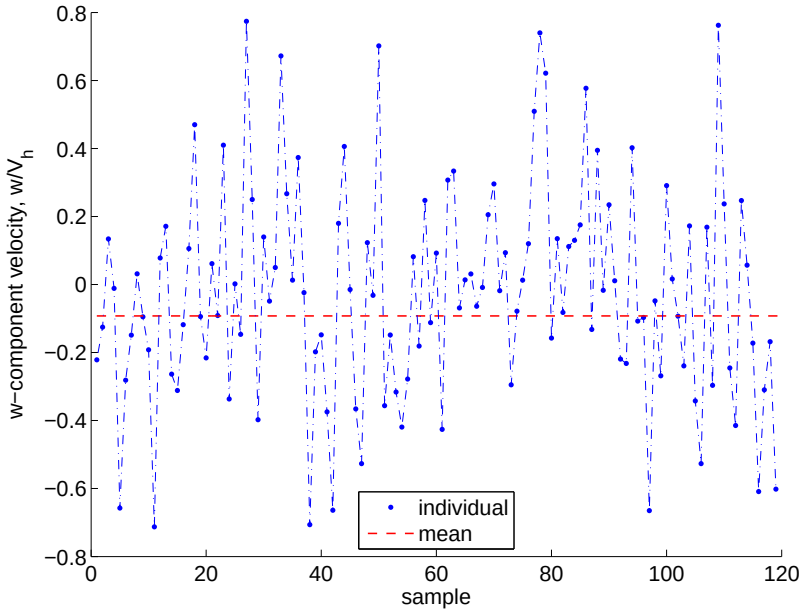

FIGURE 5.26: Deviations of the cross-flow velocity component from the mean cross-flow at the point $(\frac{\mathrm{r}}{\mathrm{R}}, \frac{\mathrm{y}}{\mathrm{R}}) = (2.13, -0.6)$ in the flow-field. The rotor was quasi-trimmed and at a ground distance of 1.0R and operated at a normalised advance ratio of $\mu^* = 0.51$ and the ground was moving $(V_g/V_\infty = 1)$.

5.6.5 Ground effect wake symmetry

To investigate the symmetry of the ground effect wake, stereoscopic PIV tests were conducted at two different longitudinal planes, approximately 0.3R either side of the rotor longitudinal plane of symmetry. Figures 5.27 and 5.28 present the mean vorticity and mean cross-flow velocity data at the different longitudinal planes, for a case where the quasi-trimmed rotor was operated at the normalised advance ratio of $\mu^* = 0.51$, at a ground distance of $1.0R$, and the ground moving $(V_g/V_\infty = 1)$. Frame (a) in both figures show the mean vorticity and mean cross-flow velocity components measured in the longitudinal plane of symmetry along the rotor hub. Frame (b) represents the flow-field in the plane 0.3R behind the rotor hub, while frame (c) corresponds to the flow-field in the plane 0.3R ahead of the rotor hub. All the plots were sized with respect to the plane along the rotor longitudinal plane of symmetry, to allow for easy comparisons between the tests.

Analysis of the mean vorticity plots shown in Figure 5.27 show the mean recirculation region to be of similar size and contain similar vorticity magnitudes to the central plane shown in frame (a). Comparisons of the location of the mean topological flow separation point locations showed a $0.1R$ shift in the separation

(a) Plane along the rotor hub

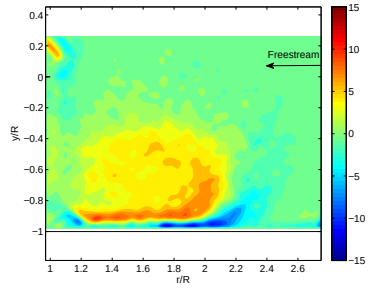

(b) 0.3R behind

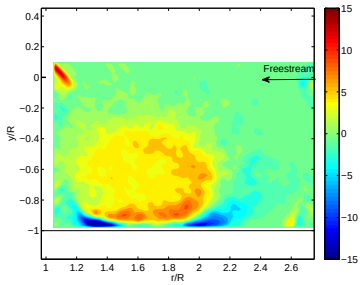

(c) 0.3R forward

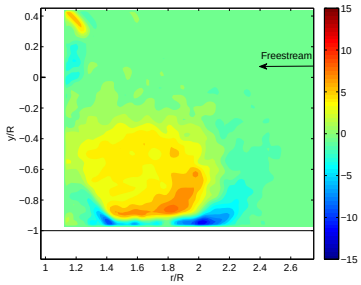

FIGURE 5.27: Mean vorticity plots at the three different longitudinal planes investigated. In these cases, the rotor was quasi-trimmed and at a ground distance of $1.0R$ and was operated with the ground moving ($V_g/V_\infty = 1$) at a normalised advance ratio of $\mu^* = 0.51$. Frame (a) corresponds to the longitudinal plane of symmetry along the rotor hub, frame (b) corresponds to the plane 0.3R aft of the rotor hub and frame (c) corresponds to the plane 0.3R infront of the rotor hub.

point location closer to the rotor disk, compared to the central plane. Both off-axis planes showed shifts of comparable magnitudes, implying the formation of a parabolic ground interaction boundary around the front end of the rotor disk, similar to observations made by Boyd and Kusmarwanto [28, 29].

While the mean vorticity regions were not observed to vary significantly between the different longitudinal planes, some detailed changes in the relative positions and magnitudes of the cross-flow velocity components were observed. Compared with the central longitudinal plane of symmetry shown in Figure 5.28 (a), Figure 5.28 (b) shows the longitudinal plane behind the rotor hub to contain intensified regions of negative mean cross-flow velocity close to the ground, with a significant portion of the flow-field affected by low magnitude negative cross-flow. Figure 5.28 (c) shows the flow near the ground plane to contain positive cross-flow velocities, while significant proportions of the flow-field (except the mean recirculation zone) were seen to contain weak positive cross-flow. Analyses of the cross-flow velocity

(a) Plane along the rotor hub

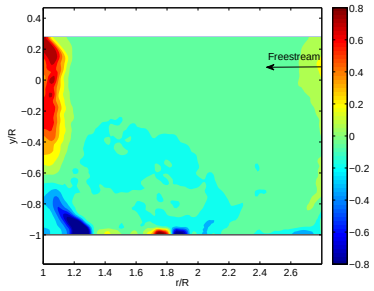

(b) 0.3R behind

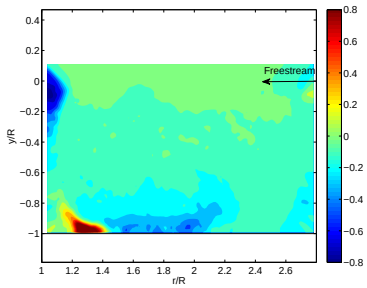

(c) 0.3R forward

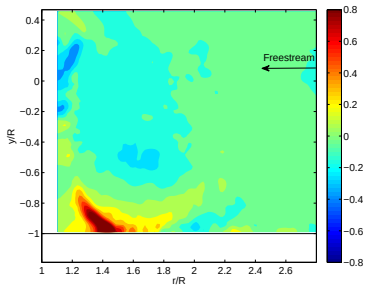

FIGURE 5.28: Mean cross-flow (w) velocity plots at the three different longitudinal planes investigated. In these cases, the rotor was quasi-trimmed and at a ground distance of $1.0R$ and was operated with the ground moving ($V_g/V_\infty = 1$) at a normalised advance ratio of $\mu^* = 0.51$. Frame (a) corresponds to the longitudinal plane of symmetry along the rotor hub, frame (b) corresponds to the plane 0.3R aft of the rotor hub and frame (c) corresponds to the plane 0.3R infront of the rotor hub.

data imply the presence of a horse-shoe vortex in the ground effect wake, although more tests at other longitudinal planes need to be conducted to characterise this horse-shoe vortex. PIV experiments conducted along the transverse plane across the wind tunnel width would have provided further information about the symmetry of the ground effect wake and the horse-shoe vortex, but optical access difficulties meant that these experiments could not be conducted in this research.

5.7 Summary

PIV investigations of wide regions of the ground effect flow-field were conducted using the Large Rotor model. Three-component velocity information was measured from a two-dimensional slice of the flow-field, along the longitudinal plane of symmetry of the rotor disk, to quantify the ground effect flow-field. The design of the Large Rotor model and the use of a rolling road in the wind tunnel allowed for a range of rotor trim and ground boundary configurations to be tested, and

their influences on the fluid mechanics of the wake characterised.

Variations in rotor trim settings were seen to only cause small changes in the mean flow separation locations, with the quasi-trimmed rotor seen to cause a $0.1R$ shift in the mean flow separation point closer to the rotor disk plane, compared to results from the untrimmed rotor configuration. Investigations of the detailed flow features and the velocity fluctuations associated with the flow-field showed no significant changes caused by this shift in mean flow separation location. The quasi-trim state of the rotor defined for these experiments was attained by considering only the vertical forces and associated moments acting on the rotor rig. While trimming of the side force acting on the rig may result in a further shift in the flow separation location, it is not expected to cause changes to the detailed structures of the ground effect flow-field.

Changes in ground boundary configurations were seen to significantly affect the ground effect wake, with prominent changes in flow separation locations, performance and detailed flow features. The moving ground boundary configuration ($V_g/V_\infty = 1$) was seen to cause mean flow separation to occur $0.5R$ closer to the rotor disk compared to the stationary ground configuration ($V_g/V_\infty = 0$) cases. Lateral cyclic pitch adjustments required to trim the rotor also showed differences, with only the moving ground configuration cases resulting in cyclic inputs similar to that observed from helicopter flight data in ground effect. Additionally, the moving ground configuration was also seen to cause vorticity associated with the trailing tip vortex system to follow a loop like tajectory into the recirculation region. This was unlike the stationary ground configuration cases, where the high magnitude vorticity was seen to accumulate near the centre of the mean recirculation zone. With the varying ground boundary configurations having an effect on the trajectories of the tip vortices entering the flow-field, this has significant implications on the vorticity distribution and the velocity fluctuations observed in the flow-field. Observations from the PIV data showed the moving ground configuration to result in larger mean recirculation regions in the flow-field and the formation of larger ground vortices, compared to the stationary ground configuration. Significant differences caused by the ground boundary configurations in both the fluid mechanics of the ground effect wake and the performance of the

rotor conclusively showed this to be an important parameter that has to be considered during experimental and numerical investigations of rotors in ground effect.

With the quasi-trimmed rotor and moving ground configuration providing the best representation of a helicopter in ground effect forward flight, this experimental configuration was used to further investigate the fluid mechanics of the ground effect wake. Effects of advance ratio, rotor ground distances and collective angles were considered, and showed these to primarily result in a change in the location of flow separation. This in turn was seen to affect the location and size of the mean recirculation zone and the velocity fluctuations experienced in the wake. Unsteady measurements of the flow-field also showed the the velocity fluctuations to be associated with large scale fluctuations in the flow-field, related to the variations in the trajectories of the tip vortices in the instantaneous flow-field.

Investigation of the cross-flow velocity components in the longitudinal plane of symmetry about the rotor hub showed low mean cross-flows, while instantaneous snap-shots of the flow-field showed higher cross-flow velocities present in the flow-field. These were seen to be constantly varying and broadly coincident with the mean recirculation region observed in the wake. High cross-flow velocity fluctuations measured from the flow-field reflected the large velocity deviations from the mean, and show the cross-flow velocity fluctuations to occur in regions where vorticity is present. Results from these analyses can be used to explain the three-dimensional and unsteady nature of the ground effect wake observed from the flow visualisations experiments. Limited investigations along off-axis longitudinal planes of the ground effect wake, either side of the rotor symmetry plane implied the formation of a parabolic interaction boundary upstream of the rotor disk. While mean vorticity data showed little difference in the wake, cross-flow velocity measurements showed more detailed variations, with the location and magnitudes of the cross-flow velocities suggesting the presence of a horse-shoe vortex in the ground effect wake.

Chapter 6

Discussion and Analysis

6.1 Introduction

PIV experiments conducted with the Large Rotor in ground effect allowed for quantitative measurements from wide areas of the ground effect flow-field. Investigations conducted using the rolling road allowed for the importance of re-creating accurate ground boundary configurations during ground effect testing to be established. A range of experiments conducted using different rotor configurations also allowed for the effects of rotor trim, collective angles, rotor ground distance and the effects of varying advance ratios on the ground effect wake features to be detailed. Results from PIV tests conducted for a range of rotor and ground configurations using the Large Rotor were presented in Chapter 5. This chapter focuses on the fluid dynamics of the ground effect wake, obtained from the experiments conducted with the quasi-trimmed Large Rotor and the moving ground configuration ($V_g/V_\infty = 1$).

6.2 Large Rotor Data Verification

The model-span-to-tunnel-width-ratio of the Large Rotor was 0.37, well within the limits of 0.3-0.5 recommended for fixed wing model experiments in wind tunnels [59]. With very limited guidelines available for conducting accurate ground effect experiments in wind tunnel environments, the ground effect experiments conducted in this research were based on this design guideline established for wind

tunnel model testing in free flight conditions. Since little research has been conducted to test the applicability of this guideline to ground effect experiments, it was important to establish the effects of the wind tunnel interference on the ground effect wake obtained from the Large Rotor, as this would have a direct influence on the fluid dynamics associated with the resulting wake. Preliminary ground effect flow visualisation experiments conducted in this research have shown the ground effect wake produced by a rotor model to spread over wide distances. The rotor model (Rotor A) used for those experiments had a model-span-to-tunnel-width ratio of 0.15, and at the lowest normalised advance ratio ($\mu^* = 0.37$) tested, the resulting ground effect wake was seen to extend radially to about 2-diameters ahead of the rotor hub, and to about 4-diameters across the width of the wind tunnel. The radial expansion of the wake in these cases was estimated by measuring the spread of the talcum powder boundary along the wind tunnel floor. With the PIV results obtained from the Large Rotor showing similar longitudinal spreads of the wake upstream of the rotor at comparable normalised advance ratios, the radially expanding wake ahead of the rotor disk could spread across the width of the tunnel and reach the boundaries of the wind tunnel side walls. Obstructions caused by the side walls on the wake can set up recirculatory systems within the tunnel environment, which can alter the dynamics of the wake being investigated, thus causing inaccuracies in the experimental results.

To verify the results obtained from the Large Rotor, a smaller rotor model, which would result in a considerably smaller wake, was tested in the same wind tunnel for a range of normalised advance ratios. Details of the rotor and experimental set-up were provided in Section 2.5.2.7. The Small Rotor used for these tests was a fixed pitch ($\theta_0 = 10^o$), two-bladed model, and tests for an untrimmed rotor configuration, for both the stationary ($V_g/V_\infty = 0$) and moving ground ($V_g/V_\infty = 1$) configurations were conducted. The decision of using the Small Rotor for these validation tests lay in its small model-span-to-tunnel-width-ratio. Calculated to be 0.10, this was similar to the model-span-to-tunnel-width-ratio for Rotor A used for the preliminary flow visualisation experiments, and meant that at comparable normalised advance ratio settings, the radial spread of the ground effect wake would be similar for both the rotors models. This thus meant that at the lowest test speed (corresponding to the normalised advance ratio of $\mu^* \approx 0.3$), the radial expansion of the ground effect wake produced by the Small Rotor (expected

to be around 4 diameters across the width of the Argyll wind tunnel) would not reach the boundaries of the wind tunnel, hence avoiding most of the interference effects that the wind tunnel walls may induce on the flow. Based on this, 2D2C PIV experiments, with the Small Rotor operated at $3600RPM$ $(60Hz)$ and at a measured out of ground effect thrust coefficient of $C_T = 0.010$, were conducted for a normalised advance ratio range of $0.3 < \mu^* < 1.0$. Differences in thrust between the Large and Small Rotors were accounted for through the consideration of μ^*, the thrust normalised advance ratio. Comparison of data obtained from the two rotor models would help to reveal any wind tunnel constraint effects on the ground effect wake produced by the Large Rotor model.

Figures 6.1 and 6.2 present a comparison of the mean vorticity and flow pathline plots associated with the ground effect wake produced by the Small Rotor and the Large Rotor at a variety of normalised advance ratios, for the moving ground boundary configuration ($V_g/V_\infty = 1$), with the rotor disk at a ground distance of half a diameter ($\frac{h}{R} = 1.0$). Both sets of results present data from an untrimmed rotor configuration, due to the fixed collective pitch limitations of the Small Rotor. As was the case with all the other PIV data, the (u, v) velocity components presented in the plots represent the longitudinal and vertical velocity components along the (r, y) plane. All the plots derived from the Small Rotor results were scaled with the rotor radius, R ($R = 0.15m$ for the Small Rotor), with the origin of the coordinate system situated at the rotor hub, and the leading edge blade tip at the ordinate $(\frac{r}{R}, \frac{y}{R}) = (1, 0)$. In these plots, the ground is represented by a black line along $\frac{y}{r} = -1$. All vorticity data were normalised with $\frac{V_h}{R}$, where V_h is the rotor hover induced velocity ($V_h = 4.0ms^{-1}$ for the Small Rotor). A representative chord based Reynolds number for these Small Rotor experiments was calculated to be around $Re_c = 124,000$ at the rotor blade tip and the circulation based Reynolds number, derived from the PIV conducted near the rotor disk plane was around $Re_\Gamma = 23,000$. Results from the Large Rotor were presented in a similar manner, and details of this was presented in Section 5.1.3.

Data presented in Figures 6.1 and 6.2 show the ground effect wake formed by the Small Rotor to comprise of wake structures similar to that observed in the wake produced by the Large Rotor. A mean flow separation point and a resulting mean recirculation zone were seen in the flow-field and appeared to form closer to the

(a) Large Rotor at $\mu^* = 0.4$

(b) Small Rotor at $\mu^* = 0.39$

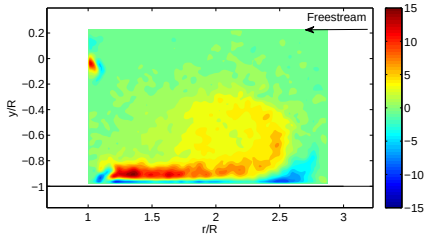

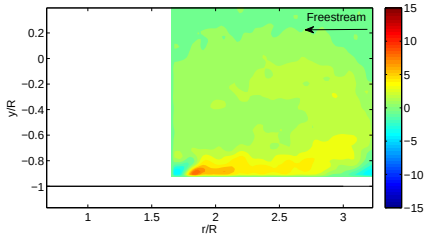

(c) Large Rotor at $\mu^* = 0.46$

(d) Small Rotor at $\mu^* = 0.46$

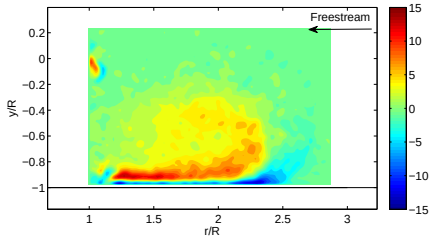

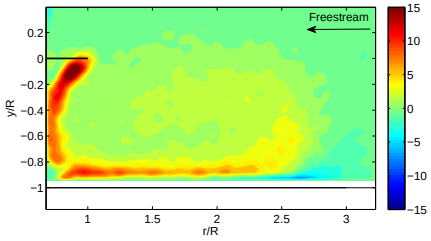

(e) Large Rotor at $\mu^* = 0.62$

(f) Small Rotor at $\mu^* = 0.62$

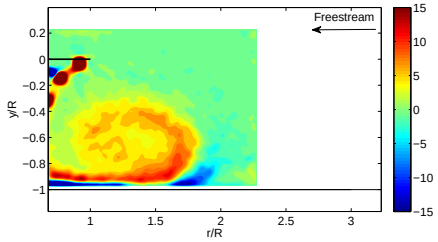

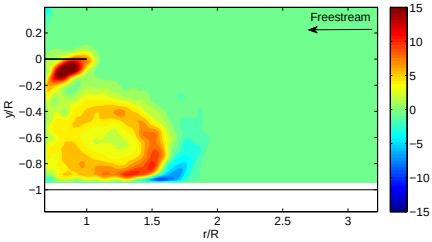

(g) Large Rotor at $\mu^* = 0.7$

(h) Small Rotor at $\mu^* = 0.7$

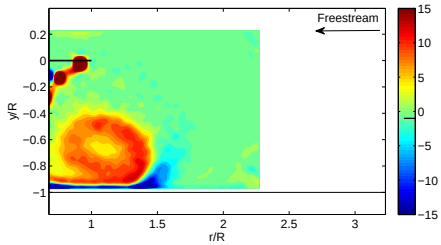

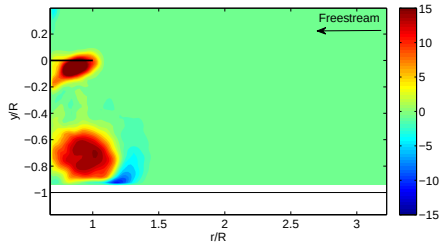

FIGURE 6.1: Mean vorticity plots at a range of normalised advance ratio with an untrimmed rotor with the moving ground ($V_g/V_\infty = 1$) boundary condition. Results were obtained from the Large and Small Rotors operated at a ground distance of 1.0R. Frames (a),(c),(e) and (g) were obtained from PIV results using the Large Rotor and frames (b),(d),(f) and (h) were obtained from PIV results using the Small Rotor. Plots have been scaled to allow for easy comparison between the data.

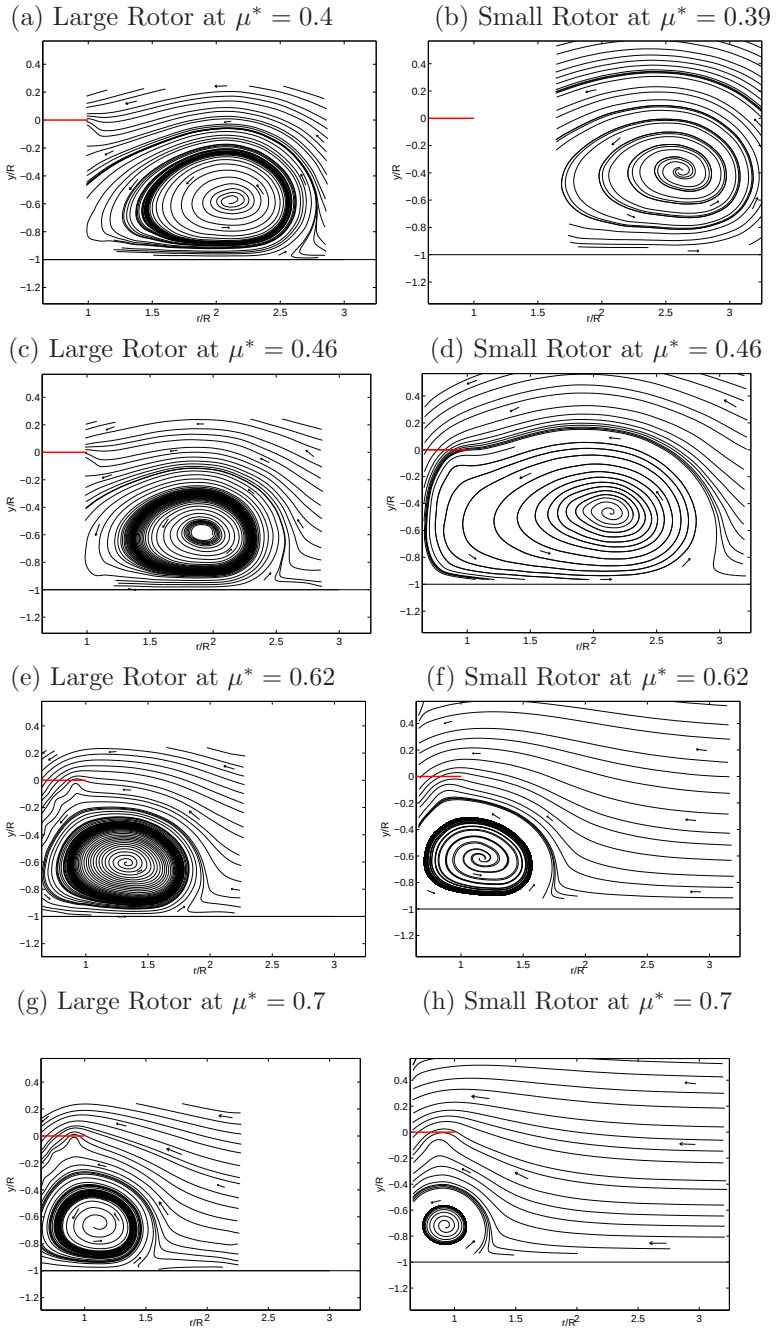

FIGURE 6.2: Mean flow pathline plots at a range of normalised advance ratio with an untrimmed rotor with the moving ground ($V_g/V_\infty = 1$) boundary condition. Results were obtained from the Large and Small Rotors operated at a ground distance of 1.0R. Frames (a),(c),(e) and (g) were obtained from PIV results using the Large Rotor and frames (b),(d),(f) and (h) were obtained from PIV results using the Small Rotor. Plots have been scaled to allow for easy comparison between the data.

rotor with higher normalised advance ratios. As in the case of the wake produced by the Large Rotor, the tip vortices trailing from the rotor disk and expanding upstream along the ground were seen to follow a loop-like trajectory into the mean recirculation zone. This loop was seen to contain higher vorticity strengths and become more compact as the normalised advance ratio increased, and was observed to be replaced by a ground vortex at higher normalised advance ratios when the flow separation was seen to occur under the rotor disk leading edge. Mean flow pathline plots, presented in Figure 6.2, further highlight similarities in the flow separation point locations between the wakes produced by the Large and Small Rotors, for comparable normalised advance ratios.

The presence of identical wake features observed from the PIV data obtained from both the rotors suggests that the ground effect flow-fields were qualitatively similar despite differences in the mounting arrangements used for both models. With the Large Rotor mounted on the sting support system such that most of the rig components were situated under the rotor disk, and the Small Rotor mounted vice versa, this difference in mounting arrangement can cause varying degrees of obstruction to the inflow through the rotor, hence affecting the resulting wake. This was especially the case with the Small Rotor, which was mounted in the wind tunnel such that all the other rig components (the motor driving the rotor and the load-cell) were above the rotor disk. Care was however taken during the design and wind tunnel installation phases to ensure that the Small Rotor rig components present above the rotor disk plane were appropriately shrouded. Additionally, both the Large and Small Rotors were installed on the sting support system in the wind tunnel such that the majority of the additional rig components were situated aft of the rotor hub, such that the wake through the front portion of the rotor disk was unaffected by interference effects from the rig components. Accordingly, data derived from the PIV showed insignificant effects caused by the rotor mounting arrangements on the wake, with Figures 6.1 and 6.2 showing small differences between the flow-fields.

More detailed analyses of the topological mean flow separation location at comparable normalised advance ratios provided further evidence for quantitative similarities between the wake formed by both rotors. Table 6.1 presents the mean topological flow separation location for both the rotors at a normalised advance

Untrimmed Rotor Configuration	**Large Rotor Topological Mean Separation Point (R)**	**Small Rotor Topological Mean Separation Point (R)**
$\mu^* = 0.62$ and $(V_g/V_\infty = 1)$	1.74	1.64
$\mu^* = 0.62$ and $(V_g/V_\infty = 0)$	2.31	2.46

TABLE 6.1: Comparison of the mean flow separation points calculated from the Large Rotor and Small Rotor tested at a normalised advance ratio of $\mu^* = 0.62$. The rotors were untrimmed and at a ground distance of 1.0R. Results from both the ground configurations are presented.

ratio of $\mu^* = 0.62$. The corresponding mean vorticity plots are presented in Figure 6.1 (e) (mean pathline plots in Figure 6.2 (e)) for the Large Rotor test and Figure 6.1 (f) (mean pathline plot in Figure 6.2 (f)) for the Small Rotor test. At comparable normalised advance ratios, results from both the rotors showed the mean topological flow separation to occur at similar ground positions, for the moving ground configuration ($V_g/V_\infty = 1$). Similar displacements in the topological mean flow separation locations were also observed to occur in the flow-field produced by both rotor models when the ground was stationary ($V_g/V_\infty = 0$).

Similar comparisons of the mean topological flow separation point locations for the range of normalised advance ratios tested during the PIV, are presented in Figure 6.3. Flow separation locations, derived from results produced by the two rotors in the untrimmed configuration, for both the moving ground ($V_g/V_\infty = 1$) and stationary ground ($V_g/V_\infty = 0$) configurations are presented in the plot and show comparable shifts in the mean separation point locations caused by the moving ground configuration. For normalised advance ratios greater than $\mu^* = 0.5$, experimental results from both the rotors showed the mean flow separation to occur at similar locations. Greater deviations between the flow separation point locations were observed at the lowest normalised advance ratios tested at $\mu^* < 0.5$. Test results from the Large Rotor at these speeds show a shift in the flow separation location closer to the rotor disk compared to the Small Rotor, for comparable normalised advance ratios. These deviations in the mean flow separation positions were noticed for both the ground boundary configurations tested, and can be an effect of the wind tunnel constraints on the rotor wake. PIV data showed the ground effect wake associated with the Large Rotor to extend to distances beyond 1-diameter upstream of the rotor at these normalised advance ratios. These will correspond to radial expansions of the wake close to the wind tunnel side walls,

resulting in wind tunnel interference effects to affect the dynamics of the wake. While differences in the flow separation location were observed, comparisons of the detailed wake structures between the two rotors (Figures 6.1 and 6.2) showed small differences. Based on these observations, it was concluded that for the majority of the normalised advance ratios tested, the ground effect wake produced by the Large Rotor was insignificantly affected by wind tunnel constraint effects. At the lower normalised advance ratios, below $\mu^* = 0.5$, constraint effects caused by the wind tunnel walls were seen to affect the wake more significantly, causing a change in the location of the mean flow separation position, although little changes to the detailed wake structures were observed. These results imply that for ground effect testing in a wind tunnel environment, considerably smaller rotor models, with model-span-to-tunnel-width ratios smaller than 0.3, should be used. This is especially the case where accurate representations of the wake at very low normalised advance ratios are sought.

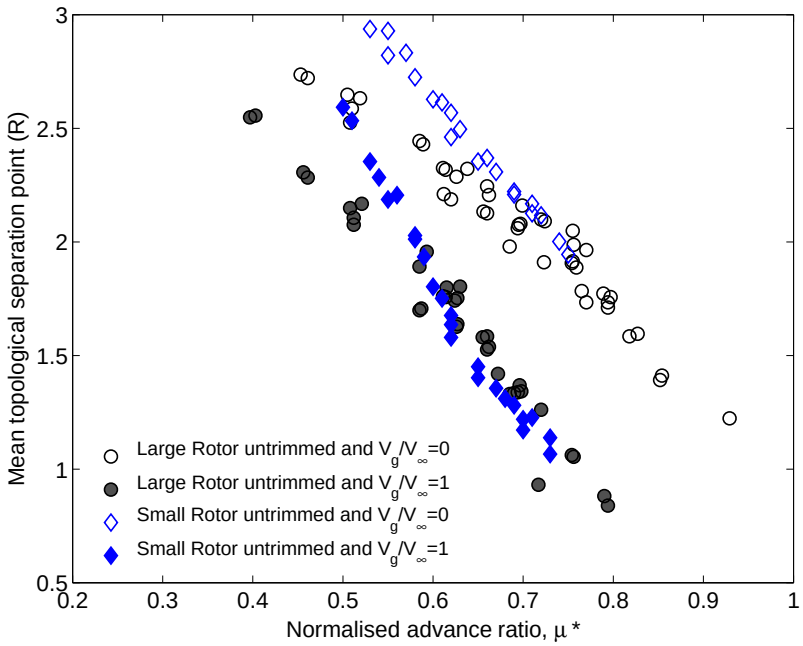

FIGURE 6.3: Mean topological flow separation point locations in the ground effect flow-field at varying normalised advance ratios for different ground boundary configurations. Results from the Large and Small Rotors in an untrimmed rotor configuration are presented, with the rotor at a ground distance of 1.0R.

6.3 Fluid Mechanics of the Ground Effect Wake

Ground effect experimentation conducted in the past have provided some insights into the fluid dynamics of the ground effect wake. Most of these research have been based on flow visualisation methods so that large areas of the wide-spreading wake can be observed. One of the primary ground effect features identified from these tests has been a flow separation boundary. Surface visualisations experiments have shown the presence of this flow separation boundary [28, 29], which appears as a separation point in a two-dimensional longitudinal slice of the wake. Hot-wire anemometry tests conducted along the longitudinal plane of symmetry of the rotor have shown oscillations of this ground separation point [32].

In wind tunnel ground effect experiments, the position of this flow separation point is influenced by the relative velocities of the oncoming airflow and that of the rotor wake expanding along the ground. Observations from the dust flow visualisation experiments conducted in this research suggested the presence of a flow separation zone in the flow-field along the rotor longitudinal plane of symmetry; the flow visualisation videos showed talcum powder seeding particles accumulating at the ground location where interactions between the expanding rotor wake and the freestream flow occurred. Fluctuations of the separation zone were also observed from the flow visualisation tests, and these seemed to be more pronounced at the low normalised advance ratio tests, where the separation zone was located upstream of the rotor disk. Analyses of the PIV test data from the Large Rotor tested with the moving ground configuration also showed similar distinctions in the separation point fluctuations at varying normalised advance ratios.

6.3.1 Evolution of the ground effect wake

While smoke flow visualisation experiments (conducted in previous ground effect research) have led to qualitative observations of the ground effect wake, a more quantitative description of the wake has been obtained from the current research. Most of the past ground effect research speak of the flow separation occurring in the flow-field to cause a wake roll up, resulting in the formation of a ground induced vortex far upstream of the rotor disk at low normalised advance ratios. As was illustrated in the schematics of Figure 1.4, these research document the

ground vortex developing from a weak vortex far upstream of the rotor disk to a well-defined, high strength ground vortex under the rotor disk at higher advance ratios. Quantitative measurements of the wake have also shown this vortex to influence the performance of the rotor, by affecting the inflow through the rotor disk [23, 24, 31, 34]. Investigations of the ground effect wake conducted in this research however, have shown significant differences in the wake evolutionary pattern compared to those described in previous ground effect research.

Unlike results from flow visualisation experiments (Figure 1.4) presented by Sheridan and Weisner [23], the PIV results obtained from this research showed no ground vortex to exist far upstream of the rotor at low normalised advance ratios. Instead, the ground effect wake was seen to contain a wide region of mean recirculation, reaching heights comparable to the rotor distance from the ground. This was seen to reduce in size and evolve into a concentrated vortex under the rotor disk at higher normalised advance ratios; further increments in advance ratio were seen to cause further reductions in the ground vortex size as it forms further aft of the rotor disk leading edge, until it eventually disappears from the flow-field. Schematics of the evolving ground effect wake at increasing normalised advance ratios, as was observed from the PIV data obtained from this research, are presented in Figure 6.4, with each schematic accompanied by an example from the instantaneous ground effect flow-field.

Analyses of the PIV data have shown the evolution of the ground effect wake to be influenced by the trajectories of the tip vortices trailing from the rotor disk. Interactions between the oncoming freestream and the rotor wake determine the location of flow separation and affect the size of the mean recirculation occurring in the flow-field. At low normalised advance ratios, the rotor wake expands far upstream of the rotor before it is overcome by the low velocity freestream. The rotor wake dissipates as it expands along the ground, and flow separation occurs at the point where the freestream has adequete momentum to overcome the expanding rotor wake. At this point, tip vortices carried by the expanding rotor wake leave the ground and encounter the freestream, which then re-directs them back towards the rotor. As the freestream convects the tip vortices towards the rotor, the vortices continue to age, reducing in vorticity strength. The trajectory of the tip vortices at these low freestream speeds are shown in Figure 6.4 (a) and

an instantaneous vorticity plot, showing the path taken by the tip vortices as they leave the flow separation point is presented in Figure 6.4 (b). Unsteadiness of the ground effect wake results in the freestream to convect the tip vortices along different trajectories, at different time instances. This results in the formation of a wide region of low magnitude mean recirculation in the flow-field ahead of the rotor disk, as was seen in Figures 5.12 (a) - (c).

At higher normalised advance ratios, flow separation occurs closer to the rotor disk and the tip vortices entering the flow-field are younger, having undergone lesser dissipation. The higher freestream velocity (associated with the higher advance ratio) causes the tip vortices to be convected across the flow-field towards the rotor at a faster rate. Near the rotor disk, the downflow through the rotor results in the vortices to be convected back towards the ground, where they are once again influenced by the expanding rotorwash and are transported along with the younger tip vortices back towards the separation point. This convection of the vortices by the freestream results in a distinct loop-like trajectory to be observed in the flow-field, and a schematic of this is shown in Figure 6.4 (c). Smaller distances between the flow separation region and the rotor disk and the higher freestream speed, result in the formation of a smaller mean recirculation zone. Lesser dissipation undergone by the wake also causes the vorticity levels within the mean recirculation zone to be higher. Mean vorticity plots presented in Figures 5.12 (d) - (f) show this loop-like trajectory and higher vorticity levels occurring within the flow-field.

Unsteadiness observed in the ground effect wake was seen to result in the tip vortex trajectories to vary instantaneously in the wake. In some cases, these trajectory changes were seen to transport the tip vortices to flow regions above the rotor disk, causing the vorticity to be ingested through the rotor. An example of this is shown in Figure 6.4 (d), where the presence of high magnitude vorticity above the rotor disk, implies a re-ingestion. Variations in the trajectories taken by the tip vortices were also seen in the talcum powder flow visualisation, which showed some vortices accumulating close to the ground plane within the mean recirculation region, while some were seen to be transported back towards the rotor disk and re-ingested through it. The presence of tip vortices within close vicinity of each other were also seen to induce variations in their trajectories. Flow visualisation videos showed the presence of vortices higher up in the flow-field to cause the

younger vortices along the ground plane to be accelerated towards the separation zone (Figure 3.8), causing them to leave the ground plane with higher velocities and reach flow regions high above the mean recirculation region. Occurrences of vortex mergers were also observed from the flow visualisations images (Figure 3.7), and these highlight the complex nature of the instantaneous ground effect flow-field.

Further increments in the normalised advance ratio were seen to cause flow separation to occur under the rotor disk leading edge. In these cases, the freestream speed is high enough to interact with the trailing rotor wake as soon as it reaches the ground. Consequently, tip vortices with high vorticity strength are ejected into the flow-field, and the high speed freestream transports these vortices rapidly towards the vicinity of the downflow from the rotor disk. This results in the formation of a tightly concentrated, compact vortex. A schematic of this is shown in Figure 6.4 (e), and an instantaneous vorticity plot from the wake at high normalised advance ratio is presented in Figure 6.4 (f). The wake at these high normalised advance ratios were seen to be more steady compared to the lower normalised advance ratios, resulting in high magnitude vorticity levels to be experienced in the mean flow-field. Examples of these were seen from the mean vorticity plots presented in Figures 5.12 (g) - (h).

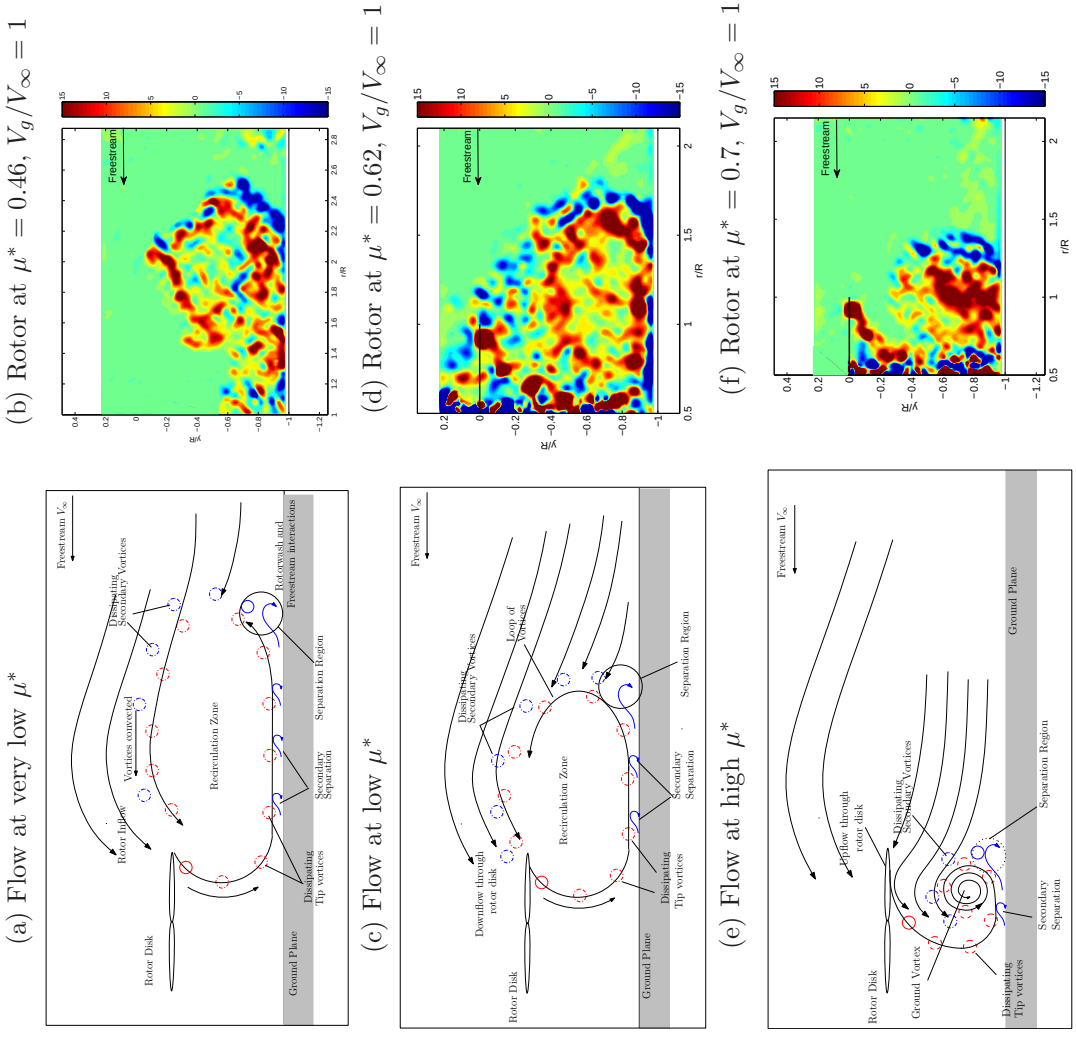

FIGURE 6.4: Schematics showing the evolution of the ground effect wake at increasing normalised advance ratios. Instantaneous PIV vorticity plots representing the flow-field accompany each schematic.

6.3.1.1 Secondary Separation

In addition to the presence of positive vorticity in the flow-field, the PIV results also showed the ground effect wake to contain negative vorticity clumps. With the root vortex system trailing from the rotor blades skewed backwards by the oncoming freestream, the boundary layer induced by the mean recirculating flow along the ground plane is the likely source of this negative vorticity. Observations from the PIV and flow visualisation have also shown secondary separation to occur in the boundary layer, as the high-vorticity strength tip vortices trail close to the ground plane.

Figure 6.5 presents data from higher magnification PIV tests conducted in flow regions near the ground plane, with the rotor at a ground distance of $1.0R$ and operating at a normalised advance ratio of $\mu^* = 0.66$. The mean vorticity plot for the flow-field was presented in Figure 5.12 (f), and a magnification of the flow around the separation region is represented in Figure 6.5 (a). The presence of the ground boundary layer induced by the mean flow-field is reflected in this plot, and the instantaneous plot presented in Figure 6.5 (b) shows this to extend from under the trailing rotor wake until the flow separation region. It was observed from the velocity plots that the rotational sense of some of the flow regions near the ground plane was opposite to that of the tip vortices trailed in the rotorwash, and this was particularly observed near the flow separation zone. Figure 6.5 (c), presenting an instantaneous pathline plot of the flow-field shows the flow around the separation zone to circulate in a sense opposite to the mean recirculation region (and tip vortices) in the flow-field, indicating secondary separation occurring close to the ground. Flow visualisation videos also showed dust particles rotating in a sense opposite to the tip vortices near the ground plane, implying secondary vortices to be induced under the tip vortex track along the ground plane and near the flow separation zone (Figure 3.5).

Based on these observations, the wake schematics presented in Figure 6.4 include the occurrence of this secondary separation in the flow-field and the formation of the negative secondary vortices along the ground plane. Analyses of the PIV data at varying normalised advance ratios suggested that secondary separation occurred at all the normalised advance ratios tested and that the resulting negative vortices

(a) Mean Vorticity plot

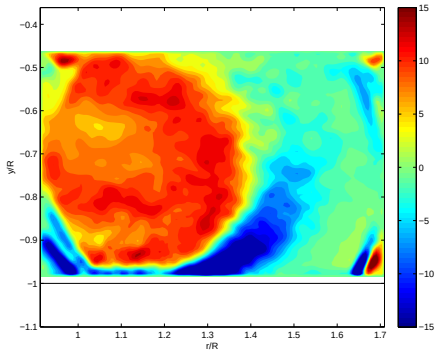

(b) Instantaneous Vorticity plot

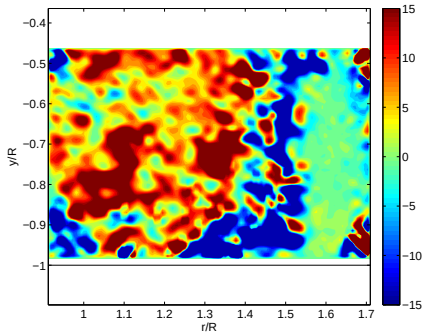

(c)Instantaneous Pathline plot

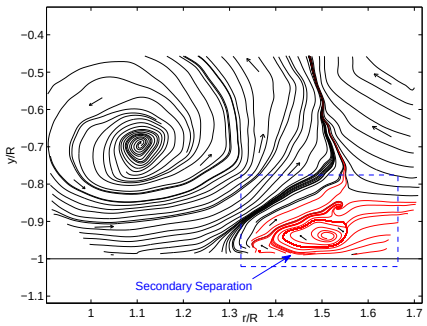

FIGURE 6.5: PIV data showing secondary separation occurring in the ground effect flow-field. Data obtained with the quasi-trimmed Large Rotor at a ground distance of 1.0R, operated at a normalised advance ratio of $\mu^* = 0.66$, with the ground moving ($V_g/V_\infty = 1$). Frame (a) presents the mean vorticity plot, while frame (b) and (c) present an instantaneous snap-shot of the vorticity and flow pathlines in the flow-field.

were seen to increase in vorticity strengths as the separation occurred closer to the rotor disk. The schematic diagrams presented in Figure 6.4 also show the trajectory taken by these negative vortices as they leave the separation zone and reflect observations from instantaneous PIV data that show the negative vorticity to border the loop of positive vorticity, and to be directed towards the rotor disk by the freestream. As in the case of the positive vorticity, the trajectories of the negative vorticity clumps in the flow-field were influenced by the unsteadiness of the wake, and instances where the presence of negative vorticity above the rotor disk plane were also observed from the PIV data. The presence of negative vorticity in the flow-field further adds to the complex trajectories of the vortices; close proximities of counter-rotating vortices have been known to cause an acceleration of the vortices, and this can be a contributing factor to the occassional dispersion of vorticity to flow regions far above the rotor disk (discussed in Section 5.4).

6.3.2 Three-dimensional nature of the ground effect wake

Together with the two-dimensional data, PIV experiments conducted either side of the longitudinal plane of symmetry provided some insights into the three dimensional nature of the ground effect wake. Locations of the mean cross-flow velocity components in the off-axis longitudinal planes (refer to section 5.6.5) implied the presence of a horse-shoe vortex in the ground effect wake. A three-dimensional representation of the ground effect wake is provided in Figure 6.6 and the colour convention adopted for the PIV is maintained in this schematic. Flow separation occurring upstream of the rotor disk results in the formation of a parabolic separation boundary, and a horse-shoe vortex tube just aft of it. This horse-shoe vortex tube is made up of inter-twined tip vortex systems trailed by the rotor blades, and this is represented in the schematic by the red vortex lines wrapped around the vortex tube. In some instances, streamlines of the freestream flowing towards the rotor disk can be entrained into this horse-shoe vortex tube, and this is represented in the schematic by the black streamlines inter-woven around the vortex tube.

The size of this vortex tube is influenced by the mean recirculation region observed along the longitudinal planes. At low normalised advance ratios, this horse-shoe vortex tube was seen to occupy a large region of the wake ahead of the rotor disk and was seen to reach heights as high as the rotor distance off the ground. This is represented in Figure 6.6, which shows a large horse-shoe vortex tube ahead of the rotor disk. The rotor wake system, trailing from the rotor blades, expands along the ground upstream of the rotor and extends under the mean recirculation region up to the flow separation boundary, where it is then ejected into the flow-field and picked up by the freestream. This rotor tip vortex system is then wrapped around the mean vortex tube and together with it, vorticity associated with the rotor tip vortices (represented in red), wrap around the mean flow recirculation and are transported towards the disk, where some are re-ingested through the rotor, while others are recirculated within the mean recirculation zone.

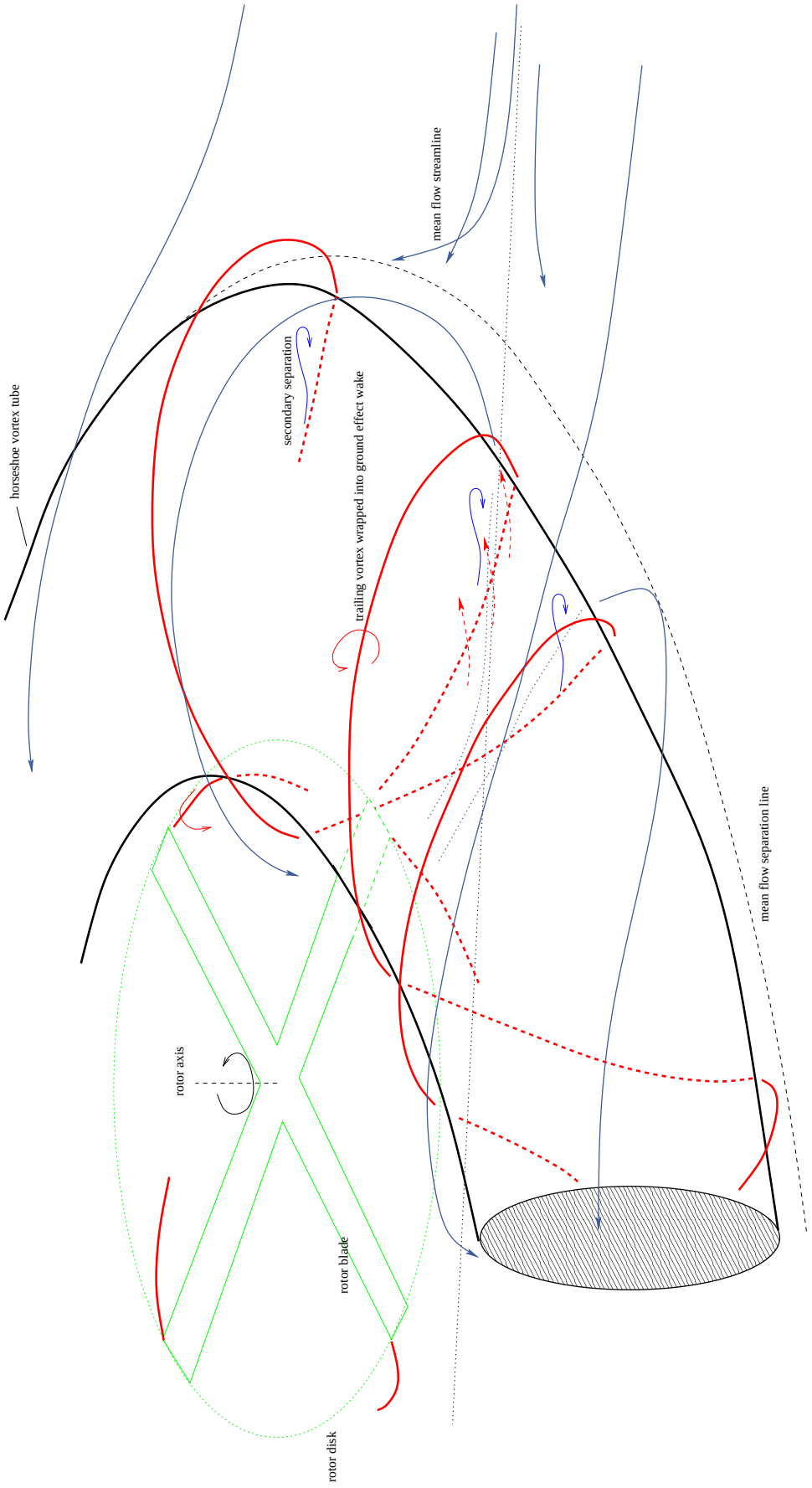

FIGURE 6.6: Schematic diagram showing the three-dimensional view of the ground effect wake. The diagrams shows a horse-shoe vortex formed in the wake, and the various flow structures observed around this vortex.

Additional negative vorticity induced by the passage of tip vortices along the ground are also introduced into the flow-field and contribute to the complex nature of the mean flow (horse-shoe vortex). This is represented in Figure 6.6 by the blue vortices, which are seen under the horse-shoe vortex tube and around the separation line. These vortices border the tip vortices as they are ejected into the flow-field at the separation line, and are transported by the mean flow towards to rotor disk. The highly unsteady nature of the flow-field, together with the cross-flow identified by the stereo PIV tests, further add to the complexity of the wake, where the flow within the horse-shoe stream-tube was seen to consist of complex re-oriented vortex lines with highly fluctuating cross-flow velocity components. At higher normalised advance ratios, this horse-shoe vortex tube becomes more compact in size as it forms under the rotor disk leading edge. In these cases, the trailing rotor wake is entrained into the horse-shoe vortex as it is ejected into the flow-field at the separation boundary, and this results in the formation of a horse-shoe ground vortex under the rotor disk.

6.4 Ground Effect Flow Regimes

Curtiss *et. al* [24, 27] made use of flow visualisation observations to categorise the ground effect wake into two regimes, based on the structures observed within the ground effect flow-field (Refer to Section 1.4.2). At low normalised advance ratios, a recirculation flow regime was defined, where the main wake feature was the trailing rotor wake separating from the ground plane and recirculating through the rotor disk. Further flow visualisation experiments conducted by Ganesh *et. al* using high energy lasers have detailed the flow in the recirculation regime to consist of a loop of tip vortices within the wake; part of this loop was seen to reach the flow near/above the rotor, causing a re-ingestion of the tip vortices through the rotor disk [30–32].

Curtiss *et. al* also classified the ground effect wake to be in the ground vortex flow regime when the horse-shoe vortex formed under the rotor disk leading edge [24, 27]. Significant lateral movement of the smoke filaments used for the visualisation experiments were additionally seen to accompany the formation of the ground vortex. Later flow visulisation experiments conducted by Ganesh *et. al*

established similar observations, and traced the tip vortices as the source feeding the ground vortex [26, 36]. Formation of the ground vortex close to the vicinity of the rotor has also been seen from previous research to affect the performance characteristics of helicopters by influencing the inflow at the rotor disk. Data presented by Sheridan and Weisner [23] showed a change in the rotor inflow angle from a downflow through the disk to an upflow, when the ground vortex was formed under the rotor leading edge (Refer to Figure 1.4). These changes in inflow through the disk were related to variations in the lateral cyclic control inputs (Figure 1.5) required to over-run the ground vortex formed under the rotor disk [23].

PIV experiments conducted during this research showed the ground effect wake to consist of the loop of vortices and ground vortex identified by Curtiss *et. al* [24, 27] and Ganesh *et. al* [30–32], and these were seen to occur at different normalised advance ratios as shown in Figure 5.12. Experiments conducted with the Large Rotor have also shown the cyclic trim angles to vary significantly with normalised advance ratio. The step-like increase in lateral cyclic trim inputs observed in Figure 5.9, implies variations in the wake features to be significant enough to cause changes in the flow near the rotor disk. Based on these observations, the mean vorticity magnitude and the mean flow angle in a region of the flow-field above the rotor disk was calculated from the PIV data, in an attempt to classify the flow into the different ground effect flow regimes. Figure 6.7 shows the rectangular region, K, of the flow-field above the rotor disk used for this analysis. Extending from $(\frac{r}{R}, \frac{y}{R}) = (1.2, 0) - (1.6, 0.2)$, this region was chosen so that re-ingestion of vorticity through the rotor disk could be identified from the PIV data. With the recirculation regime defined based on the presence of recirculation of the wake (re-ingestion of the tip vortices), a region close to and above the rotor disk leading edge was required for this analysis. Additionally, to avoid complications working with changing vorticity signs in the chosen region of interest, the enstrophy level in Region K was considered. The enstrophy measured in this analysis is non-dimensional, and scaled with the hover induced velocity, V_h, and rotor radius, R.

Figure 6.8 presents the data obtained from analyses of the mean enstrophy and mean flow angle in the region K above the rotor disk, and this is compared to the lateral cyclic trim variations at different normalised advance ratios. Both the mean enstrophy shown in Figure 6.8 (b) and the mean flow angle, presented in Figure

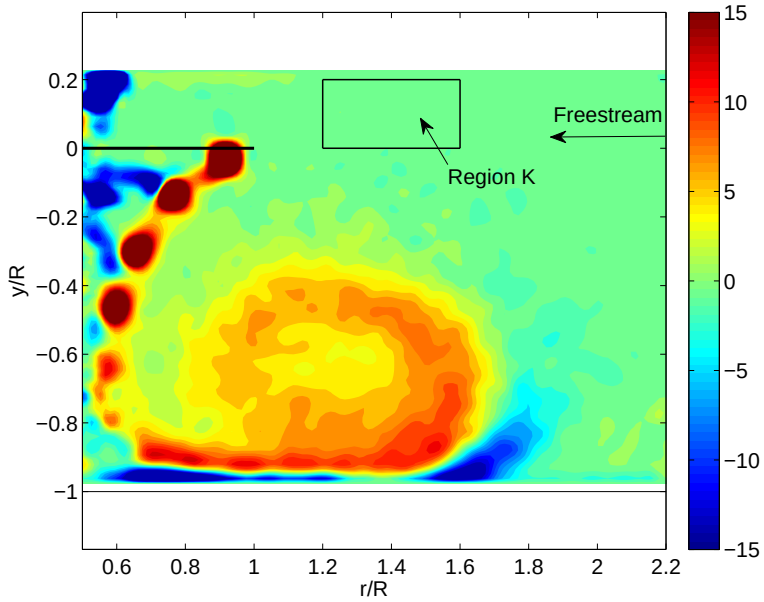

FIGURE 6.7: The rectangular Region K selected for the analysis of the mean flow angle and the mean enstrophy above the rotor disk. Vertices of this region extend from $(\frac{r}{R}, \frac{y}{R}) = (1.2, 0) - (1.6, 0.2)$.

6.8 (c) show a step-like change at around the same normalised advance ratio of $0.62 < \mu^* < 0.7$, and this correlated well to the step-like change in lateral cyclic inputs observed from the trim plot presented in Figure 6.8 (a). Mean enstropy levels in the region K, presented in Figure 6.8 (b), were seen to be significantly higher at normalised advance ratios below $\mu^* \approx 0.62$ compared to the values at normalised advance ratios above $\mu^* \approx 0.7$. Additionally, Figure 6.8 (c) shows the mean flow angle in the region K to change from a negative value, signifying a downward flow in the region at $\mu^* < 0.62$, to a positive value, signifying an upward flow.

Distinct changes in the mean flow angle measured, seen to occur at normalised advance ratios coinciding with where the step-like change in lateral cyclic inputs were observed, were similar to the observations made by Sheridan and Weisner [23]. An analysis of the mean vorticity information, presented in Figure 5.12, showed the wake formed at normalised advance ratios above $\mu^* = 0.7$ to consist of a ground vortex under the rotor disk leading edge, and this was seen from Figure 6.8 to correspond with a positive mean flow angle in Region K and a mean enstrophy level close to zero. Below $\mu^* = 0.62$, the PIV data showed the ground effect wake to consist of a wide region of mean recirculation ahead of the rotor disk, with traces of a loop-like structure of high vorticity present within it; Figure

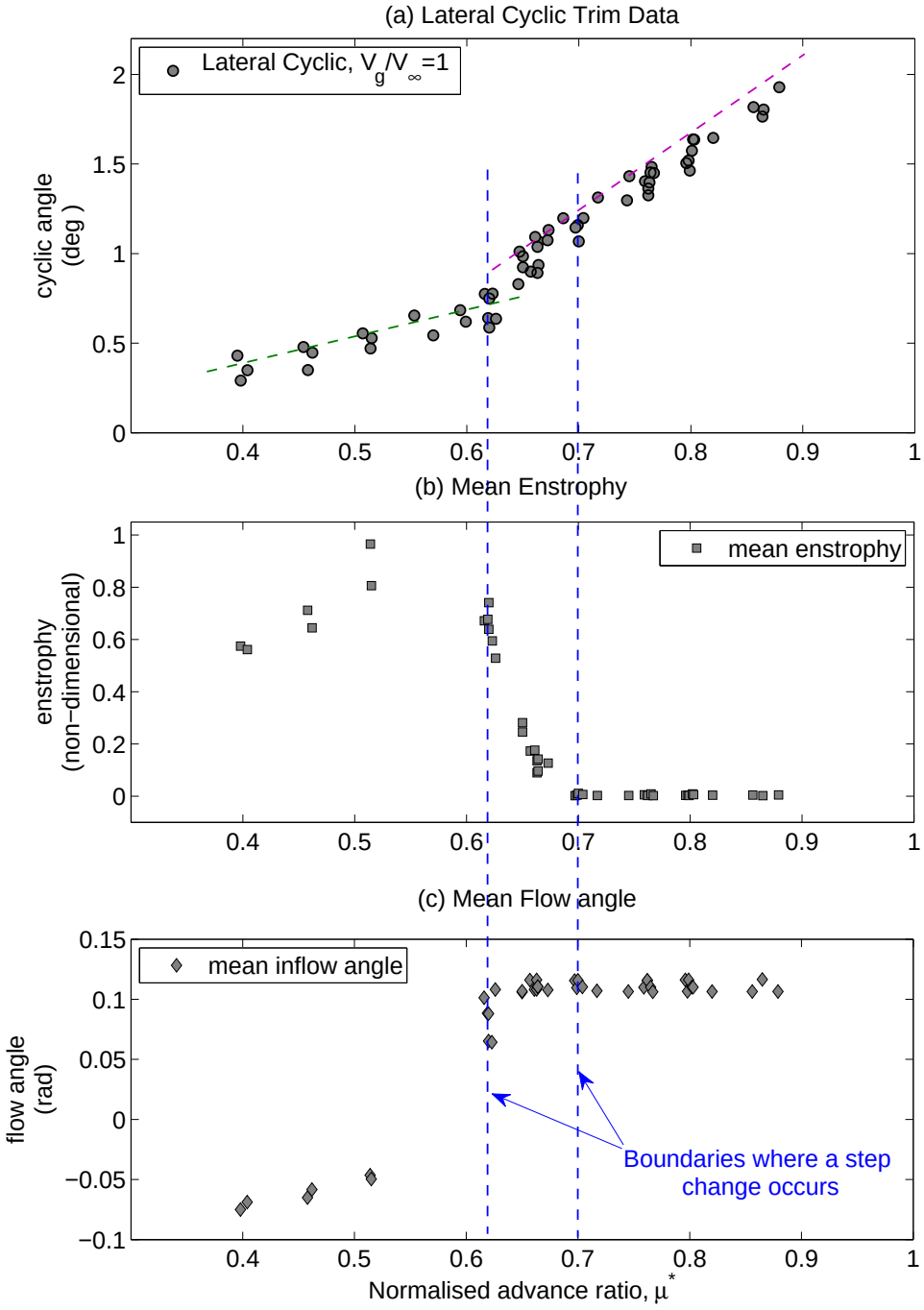

FIGURE 6.8: Mean enstrophy and mean flow angle in the Region K above the rotor disk for the range of normalised advance ratios tested. Frame (a) presents the lateral cyclic trim inputs required to attain the quasi-trim state of the Large Rotor. Frame (b) presents the mean enstrophy measured within Region K, and frame (c) presents the mean flow angle measured within Region K.

6.8 showed this to coincide with high mean enstrophy levels and negative mean flow angles in the Region K. In addition to this, Figure 6.8 showed the ground effect wake produced between $0.62 < \mu^* < 0.7$ to be characterised by moderately high mean enstrophy levels and positive mean flow angles. Analysis of the mean vorticity information presented in Figure 5.12 showed the wake in this normalised advance ratio range to consist of a loop-like region of high vorticity within a wider region of mean recirculation ahead of the rotor disk.

While analyses of the mean enstrophy and mean flow angle in Region K showed the flow-field above $\mu^* = 0.7$ to closely resemble the ground vortex regime, it was established that these parameters alone could not be used to distinguish the ground effect flow regimes. This was particularly the case at the lower normalised advance ratios, where the flow-field consisted of the mean recirculation region ahead of the rotor disk leading edge; Figure 5.12 showed this to occur at $\mu^* < 0.7$. While the PIV vorticity data show the presence of a loop-like structure of vorticity in the flow-field, closely resembling the recirculation loop described by Ganesh *et. al* [30–32], consideration of the instantaneous vorticity data showed significantly varying flow-fields at different time instances. In some instances, the loop of vortices were seen to reach flow regions above the rotor disk, implying a re-ingestion of the wake, while in other instances, this loop was seen to form close to the ground plane, resulting in little (or zero) vorticity to be observed above the rotor disk; examples of these were shown in Figure 5.17. Similar observations of varying tip vortex trajectories were also made from the flow visualisation experiments (presented in Chapter 3 and the preliminary PIV experiments conducted with the stationary ground configuration (discussed in Chapter 4)).

These unsteady characteristics of the wake imply that the recirculation regime cannot be defined solely based on observations of wake re-ingestion [24], or by the appearence of the recirculation loop and the re-ingestion of the vortices [30–32], or through consideration of the mean enstrophy (vorticity) above the rotor disk. Instead, a re-ingestion criterion, taking into account the degree of re-ingestion observed in the wake needs to be considered.

6.4.1 Re-ingestion Criterion

The re-ingestion criterion used for this research was based on calculating the proportion of samples showing the presence of vorticity in the Region K above the rotor disk. In this analysis, the enstrophy level in Region K was measured for each instantaneous PIV snap-shot of the flow-field at each normalised advance ratio tested. Based on a chosen threshold enstrophy level, EN_t, the proportion of the sample with enstrophy level greater than the threshold was calculated. For this analysis, the enstrophy threshold was chosen to be $EN_t = 0.05$, five times the minimum mean enstrophy measured in Region K (seen from Figure 6.8 to occur when $\mu^* > 0.7$). Instantaneous data which showed the enstrophy level in Region K to be lesser than $EN_t = 0.05$ was considered to have no vorticity (enstrophy) above the rotor disk. Snap-shots which showed enstrophy levels in Region K to be greater than $EN_t = 0.05$ was considered to have vorticity present above the rotor disk; this will eventually be ingested through the rotor disk, thus implying a re-ingestion of the wake.

Figure 6.9 presents the proportion of the flow-field showing the enstrophy in Region K to be greater than $EN_t = 0.05$, for the range of normalised advance ratio tested. The figure shows the proportion of the samples containing significant enstrophy (vorticity) levels in Region K to reduce as the normalised advance ratio was increased. Analyses of the data obtained showed that the presence of vorticity above the rotor disk and hence re-ingestion of the wake was not consistently observed in all the PIV samples at any of the normalised advance ratio tested, as previously implied by Curtiss *et. al* [24, 27] and Ganesh *et. al* [26, 36]. Instead a re-ingestion criterion based on a proportion of the sample showing re-ingestion had to be defined to classify the flow into the recirculation flow regime. For this research, it was decided that normalised advance ratios which showed more than 75% of the sample to contain enstrophy (vorticity) values in the Region K above the threshold enstrophy $EN_t = 0.05$ would be classified into the recirculation flow regime. With the ground vortex flow regime identified to only contain a ground vortex under the rotor disk [24, 26, 27, 36], normalised advance ratios which showed none (0%) to the instantaneous images to contain enstrophy (vorticity) values in the Region K above the threshold enstrophy $EN_t = 0.05$ was classified into the ground vortex flow regime.

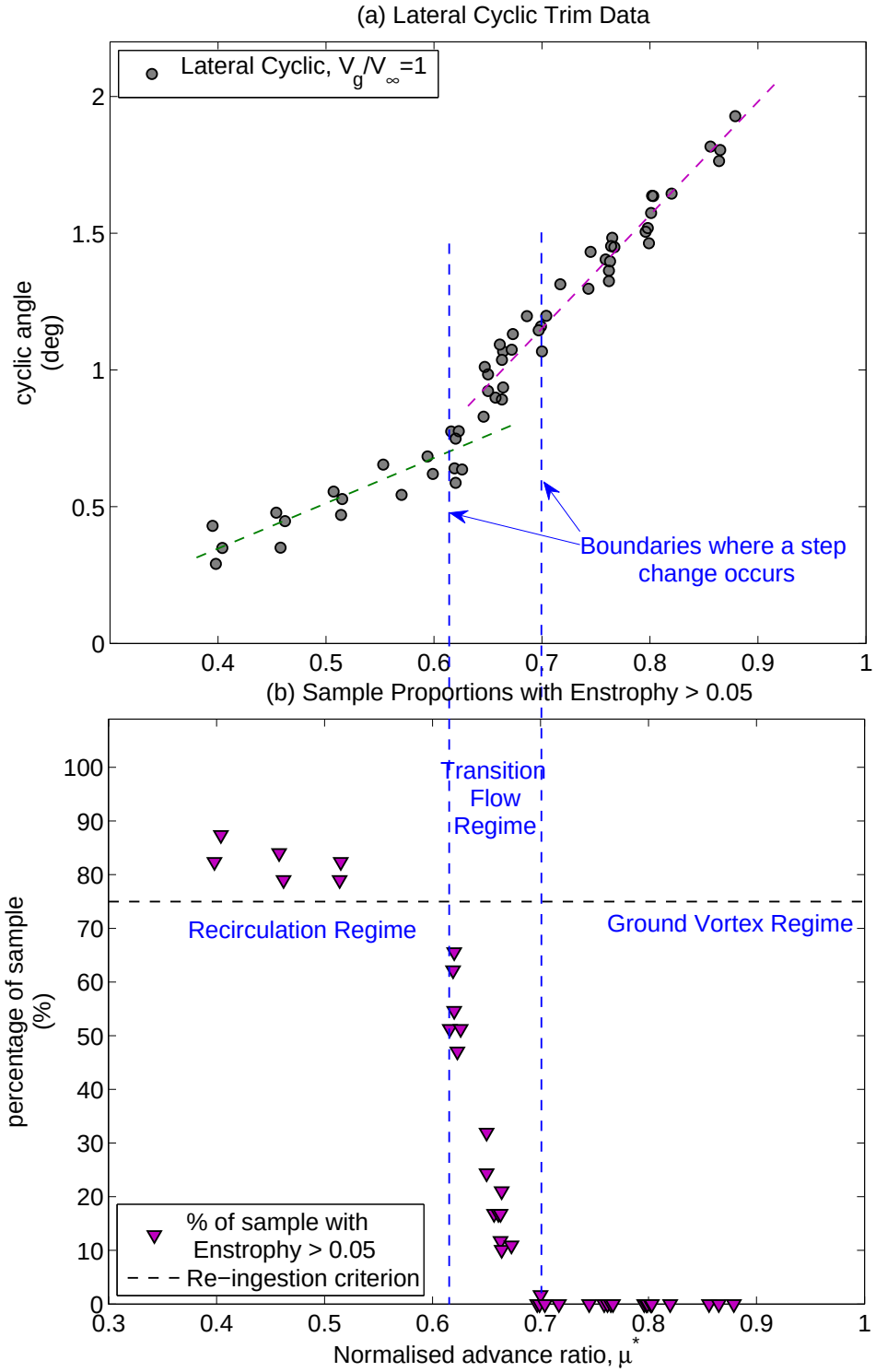

FIGURE 6.9: Proportion of the sample showing enstrophy level within Region K to be above the enstrophy threshold, $EN_t = 0.05$. Frame (a) presents the lateral cyclic trim inputs required to attain the quasi-trim state of the Large Rotor. Frame (b) presents the sample proportions for the range of normalised advance ratios tested, and the re-ingestion criterion (of 75%) used for this analysis. It also shows the classification of the flow into the different ground effect flow regimes.

(a) Instantaneous Enstrophy (b) Image 9

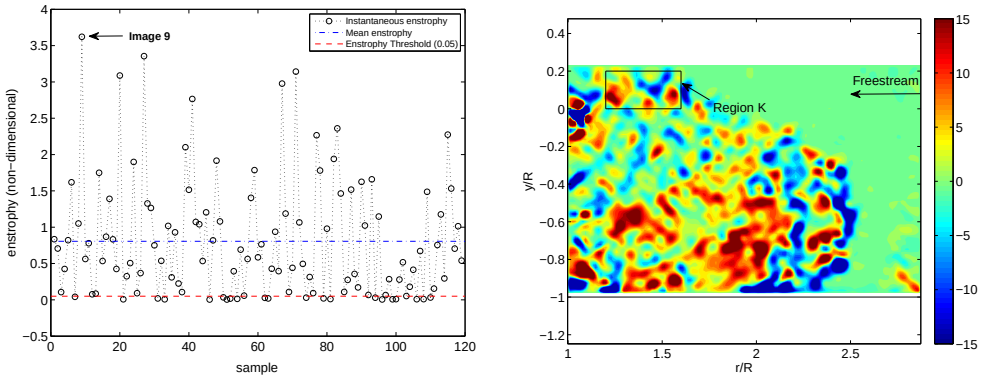

FIGURE 6.10: Example of the flow-field in the recirculation flow regime. Enstrophy levels measured from the Region K when the rotor is operated at a normalised advance ratio of $\mu^* = 0.52$ is presented in Frame (a). Frame (b) presents a typical instantaneous vorticity plot from the recirculation flow regime.

6.4.2 Recirculation Flow Regime

Based on this definition of the re-ingestion criterion, it was identified that the ground effect wake produced by the Large Rotor can be classified into the recirculation flow regime between the normalised advance ratio range of $0.4 < \mu^* < 0.62$. In this range, the PIV data showed more than 75% of the instantaneous snap-shots of the wake to contain significant vorticity levels in the Region K above the rotor disk, hence implying a re-ingestion of the wake. As an example, Figure 6.10 (a) shows the mean and instantaneous enstrophy levels measured in the wake produced at a normalised advance ratio of $\mu^* = 0.52$, when the rotor was $1.0R$ above the ground. The threshold enstrophy level is also shown in the plot, and it can be seen that most of the instantaneous data have enstrophy levels in Region K significantly higher than $EN_t = 0.05$. A typical example of the flow-field observed in the recirculation regime is presented in Figure 6.10 (b), and shows the presence of high positive and negative vorticity levels near/above the rotor disk signifying a re-ingestion of the wake.

The lower limit defined for the recirculation flow regime is based on the lowest normalised advance ratio that was tested during this research. This boundary may extend to lower values if further tests, at $\mu^* < 0.4$, were conducted, although this could not be done during this research due to experimental limitations. Consideration of the mean enstrophy level at the low normalised advance ratios of

$\mu^* = 0.45$ and $\mu^* = 0.4$ in Figure 6.8, however shows this to begin to fall from the peak mean enstrophy level observed around $0.5 < \mu^* < 0.62$. Together with the locations of the mean recirculation regions identified from the PIV vorticity plots, this observation suggests that the wake at normalised advance ratios lesser than $\mu^* = 0.4$ will occur much further upstream ahead of the rotor disk, thus having lesser influence on the flow area above the rotor disk. Re-ingestion of the wake would thus be less likely to occur, and this implies that at these very low normalised advance ratios, the wake may not satistfy the re-ingestion criterion used to identify the recirculation flow regime; instead the wake may resemble one that is produced when the rotor is in ground effect hover [41]. Further experimentation at very low normalised advance ratios below $\mu^* < 0.4$ are however required before this can be validated.

6.4.3 Ground Vortex Regime

Classification of the ground effect flow into the ground vortex regime was performed by considering the appearance of a ground vortex in the flow-field under the rotor disk. Analyses of the PIV data from the Large Rotor showed this to occur at normalised advance ratios between $0.7 < \mu^* < 0.85$. Measurements from the flow-field showed the appearance of the ground vortex to be accompanied by positive mean flow angle, as shown in Figure 6.8. Corresponding mean enstrophy levels in the Region K above the rotor disk also showed a distinct drop from high magnitude mean enstrophy to a value close to zero. Both the changes in the mean flow angle and mean enstrophy where seen to occur after the step increase in lateral cyclic input required to attain the quasi-trim state of the Large Rotor as shown in Figure 6.8 (a).

Consideration of the instantaneous enstrophy levels in the flow-field, show 0% the flow samples to possess enstrophy levels in Region K above the threshold enstrophy, $EN_t = 0.05$. An example of the flow from the ground vortex regime is shown in Figure 6.11. In this case, the rotor is operated at a normalised advance ratio of $\mu^* = 0.7$, and it can be seen from Figure 6.11 (a) that all the individual images have enstrophy levels significantly lower than the threshold enstrophy chosen for the analyses. With the flow above the rotor disk showing almost zero vorticity, a typical example of the flow-field from the ground vortex regime is shown in Figure

(a) Instantaneous Enstrophy (b) Image 72

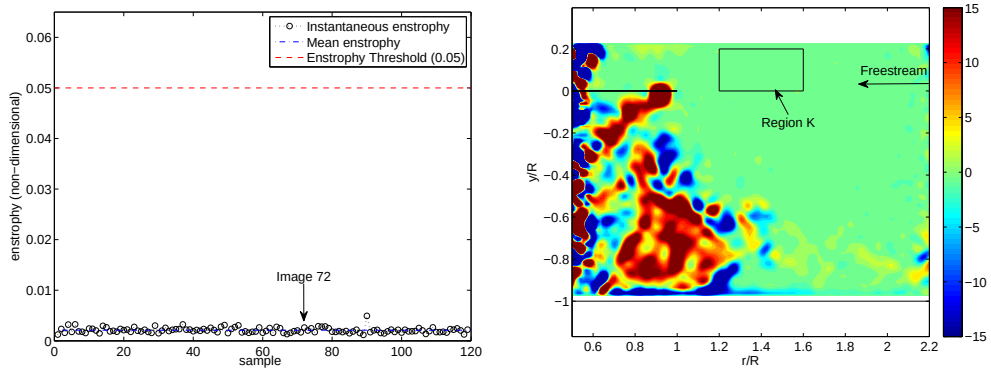

FIGURE 6.11: Example of the flow-field in the ground vortex flow regime. Enstrophy levels measured from the Region K when the rotor is operated at a normalised advance ratio of $\mu^* = 0.7$ is presented in Frame (a). Frame (b) presents a typical instantaneous vorticity plot from the ground vortex flow regime.

6.11 (b). As in the case of the recirculation flow regime, the upper boundary of the ground vortex flow regime was defined by the disappearance of the ground vortex from the imaged field-of-view. Experimental constraints limited the normalised advance ratio range that could be tested during this research, and further testing at a wider range of normalised advance ratios will provide a more accurate definition of the upper boundary for the ground vortex regime.

6.4.4 Transition Flow Regime

While the re-ingestion criterion and the enstrophy threshold defined in this analyses allowed for the identification of the recirculation and ground vortex flow regimes, the PIV data showed results from a range of normalised advance ratios where the ground effect flow could neither be classified into the ground vortex or recirculation regime. Analysis of the wake produced by the Large Rotor, presented in Figure 6.9, showed the wake produced between $0.62 < \mu^* < 0.7$ to exhibit characteristics of both the defined flow regimes. Within this normalised advance ratio range, the PIV data showed less than 75% of the sample to imply re-ingestion. While this meant that the flow could not be classified in the recirculation regime, it was observed that significant proportions of the sample showed enstrophy values in Region K to be above the threshold, $EN_t = 0.05$. This thus meant that the flow could not be classified into the ground vortex flow regime, where 0% of the sample show enstrophy values greater than the threshold. This

(a) Instantaneous Enstrophy

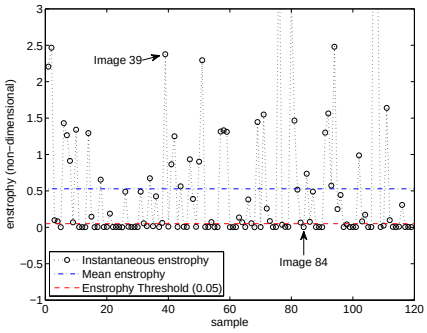

(b) Image 39 (c) Image 84

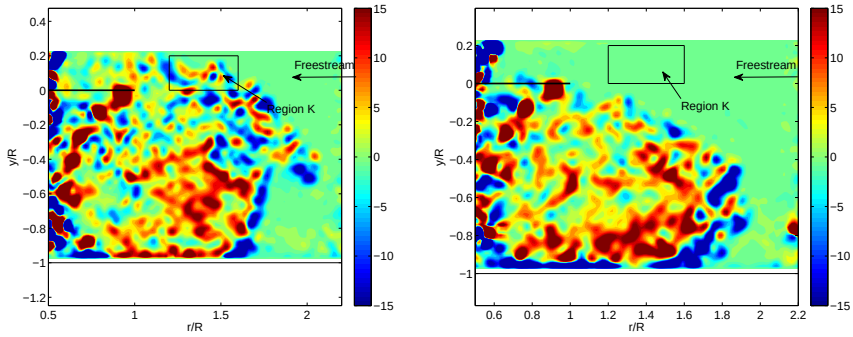

FIGURE 6.12: Example of the flow-field in the transition flow regime. Enstrophy levels measured from the Region K when the rotor is operated at a normalised advance ratio of $\mu^* = 0.64$ is presented in Frame (a). 51% of the sample was calculated to have enstrophy levels higher than $EN_t = 0.05$. Frame (b) presents an instantaneous vorticity plot where the Region K contains high enstrophy levels, similar to flow in the recirculation regime. Frame (c) presents an instantaneous vorticity plot where the Region K contains low enstrophy levels, similar to flow in the ground vortex regime.

variation in enstrophy levels measured in Region K was reflected in the mean enstrophy measurements shown in Figure 6.8. Mean flow angle measurements also showed the wake to contain positive flow angles in Region K, although this was seen to approach negative values at the lower end of the normalised advance ratio range, around $\mu^* \approx 0.62$. While the positive flow angles imply the flow to be similar to the flow-field in the ground vortex flow regime, the high enstrophy levels measured in the wake show similarities to the wake in the recirculation flow regime. Additionally, the wake in this normalised advance ratio range was seen to occur in the range where the step change in lateral cyclic inputs was seen to occur.

Based on these observations, a transition flow regime, at the normalised advance ratio range of $0.62 < \mu^* < 0.7$ is defined, where the wake is seen to exhibit

characteristics of the flow from both the ground vortex and recirculation flow regimes. An example of this transition flow regime is presented in Figure 6.12, where the wake produced by the rotor operating at the normalised advance ratio of $\mu^* = 0.64$ is presented. Enstrophy measurements from the Region K is provided in Figure 6.12 (a), where it was calculated that 51% of the sample had enstrophy levels higher than the threshold. Snap-shots from the flow-field, showing a high and low enstrophy value in Region K, is presented in Figures 6.12 (b) and (c), and shows significant variations in the spread of vorticity in the flow-field. The presence of this transition flow regime in the ground effect wake implies a complex flow-field and suggests that simple flow visualisation techniques such as those used by Curtiss *et. al* [24, 27] and Ganesh *et. al* [26, 36] cannot be used to accurately define the ground effect flow regimes, especially at the low normalised advance ratios, where the mean recirculation and flow separation occur upstream of the rotor disk leading edge.

6.5 Implications of rotor parameters and ground boundary configurations on the fluid dynamics the ground effect wake

Rotor parameters such as rotor ground distance, trim configurations, collective angles and blade root cut-out ratios (presented in Chapter 4), were seen to cause insignificant changes in the detailed structure of the ground effect wake. Changes in these rotor parameters were however seen to affect the trailing wake velocities, hence influencing the location where flow separation occurred. This in turn had an effect on the location and size of the mean recirculation region in the flow-field.

Increasing blade root cut-out ratio was seen to cause the flow separation location to shift by small magnitudes further upstream for comparable normalised advance ratios (refer to Section 4.3.2), with an example presented in Figure 4.6. Shifts in the flow separation location imply that the different ground effect flow regimes would occur at higher normalised advance ratios for rotors with higher blade root cut-out ratios. Similar observations were made when rotor collective angles were increased, as was shown in Figure 5.15, although the thrust normalised advance

ratios are usually considered during ground effect analyses to ensure comparisons between similar wake states.

6.5.1 Influence of rotor ground distance

Increasing rotor ground distance was seen to result in flow separation to occur closer to the rotor disk due to a change in the rotorwash velocities along the ground plane. An analysis of the change in flow separation locations between two rotor ground distances was provided in Figure 5.13. At higher ground distances, the dissipation of the wake, resulting from greater distances between the rotor disk and the ground plane, causes the trailing wake velocities at the ground to be significantly lower than that measured at lower rotor ground distances. Velocity plots presented in Figure 5.14 illustrated the variation in rotorwash velocities caused by changing rotor ground distances, and showed that at comparable normalised advance ratios, the higher rotor ground distance was seen to result in flow separation to occur closer to the rotor disk, causing the mean recirculation region to be more compact in size and located closer to the rotor. Lower rotorwash velocities also mean that vorticity in the flow-field was seen to be confined to flow regions closer to the ground plane, thus having a lesser effect on the flow-field above/around the rotor disk, and hence having lesser influence on the performance of the rotor. With the recirculation regime identified based on the observation of vorticity re-ingestion through the rotor, the smaller vorticity dispersion radius resulting from higher rotor ground distances thus mean that the classification of the wake into the different ground effect flow regimes cannot be conducted at high rotor ground distances. This was the case with the PIV results obtained from the $\frac{h}{R} = 2.0$ tests conducted in this research.

6.5.2 Influence of rotor trim

Varying rotor trim configurations were also seen to cause insignificant changes in the detailed structures of the ground effect wake features, although small changes in the flow separation location were identified. For similar normalised advance ratios, Figure 5.8 showed an untrimmed rotor configuration to cause a $0.1R$ shift in flow separation location further upstream compared to the quasi-trimmed rotor configuration cases. Changes to the rotor thrust coefficients, brought about by the

	Large Rotor Quasi-Trimmed	**Large Rotor Untrimmed**
Recirculation Regime	$0.4 < \mu^* < 0.62$	$0.4 < \mu^* < 0.65$
Transition Flow Regime	$0.62 < \mu^* < 0.7$	$0.65 < \mu^* < 0.72$
Ground Vortex Regime	$0.7 < \mu^* < 0.85$	$0.72 < \mu^* < 0.87$

TABLE 6.2: Comparison of the ground effect flow regimes for the quasi-trimmed and untrimmed Large Rotor configurations tested with the ground moving at $V_g/V_\infty = 1$.

changing trim configurations, were seen to result in small differences in the trailing wake velocities, which in turn caused this shift in flow separation location. This shift was seen to marginally affect the classification of the wake into the different ground effect flow regimes. Table 6.2 shows the results from the quasi-trimmed and untrimmed data obtained from the PIV tests conducted using the Large Rotor.

While the quasi-trimmed rotor configuration considered in this research accounted for the vertical forces (and associated moments) acting on the Large Rotor, no measurements were made of the side forces acting on the model. As such, this quasi-trimmed rotor configuration considered in this research was not the true trimmed state of the rotor. Accounting for all the forces and moments acting on the Large Rotor may cause a bigger change in the location of the wake features and result in further differences in the classification of the ground effect flow regimes. Results from these tests suggest that, while ground effect experimental testing with an untrimmed or fixed pitch rotor model may not affect the fluid mechanics of the ground effect wake, it will have an implication on the rotor performance characteristics and the classification of the ground effect flow regimes.

6.5.3 Influence of ground boundary configurations

Ground boundary conditions were seen to have the most influence on the fluid mechanics of the ground effect wake, causing prominent changes to both the location of flow separation and detailed structures of the wake features. Figure 5.8 showed the moving ground boundary configuration to cause a $0.5R$ shift in the flow separation location closer to the rotor disk compared to the stationary ground configuration, for comparable normalised advance ratios. This was seen to cause

significant changes to the size and location of the mean recirculation zone and the vorticity distribution within the ground effect flow-field.

Variations in the location and structure of the wake caused by the moving ground boundary configuration can be attributed to the changes in the relative velocity of the flow close to the ground plane. For the stationary ground configuration, a wind tunnel ground boundary layer, extending from the wind tunnel contraction along the fixed ground plane, reduces the freestream flow velocity very close to the ground plane. With the ground moving at $V_g/V_\infty = 1$, this wind tunnel boundary layer is considerably reduced; literature suggests the boundary layer displacement thickness to be approximately 20% of that experienced with the ground stationary [97]. The freestream flow velocity close to the ground plane is thus higher for the moving ground configuration, causing interactions between the freestream and trailing rotor wake and hence flow separation to occur closer to the rotor disk.

Changes in the freestream velocity close to the ground plane, caused by the moving ground configuration is illustrated in Figure 6.13. Mean vorticity data, with flow separation occurring at similar ground locations for the two ground boundary configurations are presented in this figure. With the rotor operated at a constant rotational speed, it can be seen that the moving ground configuration ($V_g/V_\infty = 1$) causes flow separation to occur at a similar position to the stationary ground configuration ($V_g/V_\infty = 0$), at a lower normalised advance ratio ($\mu^* = 0.62$). The moving ground configuration was also seen to cause an 18% increase in the vorticity dispersion radius (as described in Section 5.2.2.3) in the flow-field compared to the stationary ground case.

Smaller dispersion of vorticity in the flow-field caused by the stationary ground configuration (Figure 5.11) meant that classification of the wake into the various ground effect flow regimes was difficult to perform for this case, especially at the low normalised advance ratios, where the mean recirculation region formed ahead of the rotor disk. Figure 6.14 shows the differences in the lateral cyclic trim inputs, mean enstrophy and mean flow angle measured from Region K above the Large Rotor, for both the ground boundary configurations. Sample proportions showing enstrophy values above the threshold enstrophy, $EN_t = 0.05$, measured from both

(a) Quasi-trimmed rotor at $\mu^* = 0.76$, $V_g/V_\infty = 0$

(b) Quasi-trimmed rotor at $\mu^* = 0.62$, $V_g/V_\infty = 1$

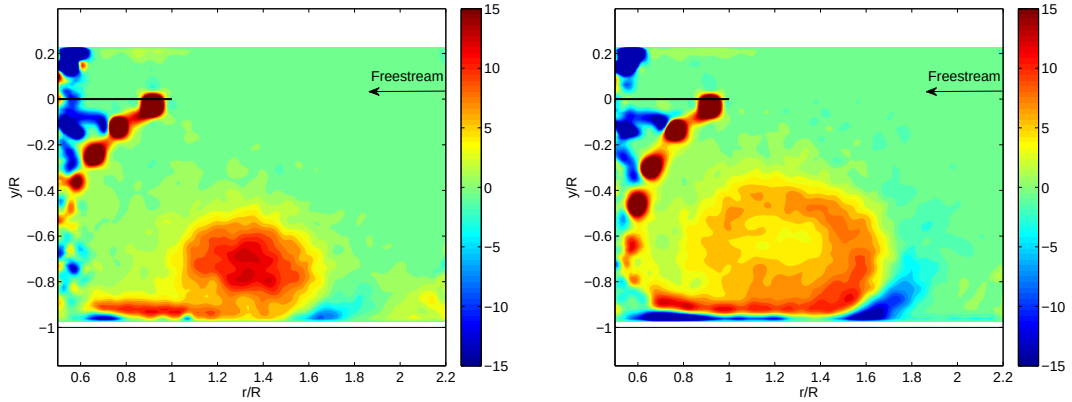

FIGURE 6.13: Mean vorticity plots from the different ground boundary configurations, where the mean topological flow separation point was located at $\frac{r}{R} \approx 1.7$. The Large Rotor was at a ground distance of 1.0R, and the moving ground boundary configuration was seen to cause an 18% increase in vorticity dispersion radius.

ground boundary configuration cases are also presented in Figure 6.14 (d).

In addition to the absence of the step-like change in lateral cyclic inputs corresponding to over-running the ground vortex (see Figure 6.14 (a)), the stationary ground configuration was seen to result in a lower mean enstrophy in Region K, compared to the moving ground configuration, although a similar change in mean flow angle in Region K was observed for the range of normalised advance ratios tested. The mean enstrophy and mean flow angle plots in Figures 6.14 (b) and (c) also show a step-like change between $0.66 < \mu^* < 0.8$ for the stationary ground configuration ($V_g/V_\infty = 0$) cases, although this was less well-defined compared to the moving ground boundary configuration ($V_g/V_\infty = 1$) case. Consideration of the enstrophy threshold and re-ingestion criterion defined in Section 6.4.1, did not allow for the recirculation flow regimes to be defined from the stationary ground configuration case, with Figure 6.14 (d) showing less than 50% of the sample to contain enstrophy values greater than the defined threshold. An analyses of the data however allowed for the ground vortex regime to be distinguished and this was seen to occur at normalised advance ratios between $0.8 < \mu^* < 0.87$.

The absence of a distinct recirculation flow regime for the stationary ground configuration tests can be attributed to the influence of the freestream velocity on

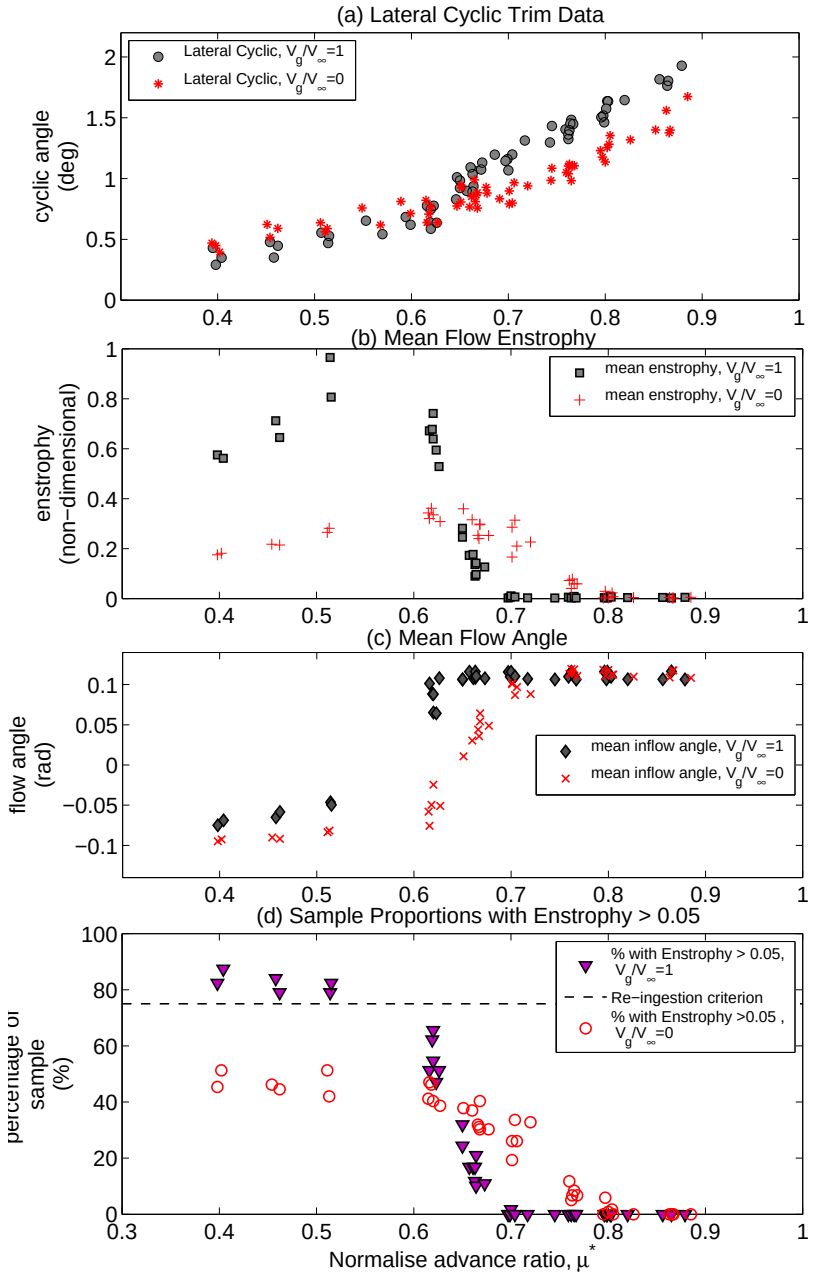

FIGURE 6.14: Mean topological separation points derived from the PIV data for the ground effect wake at varying μ^* for all the experimental configurations tested. From the top, frame (a) shows the lateral cyclic inputs required to trim the Large Rotor, frame (b) shows the mean enstrophy levels measured in Region K, frame (c) shows the mean flow angle measured in Region K and frame (d) shows the proportion of the samples containing enstrophy values higher than $EN_t = 0.05$.

the tip vortices entering the flow-field. At comparable separation point locations, the higher freestream velocity associated with the stationary ground configuration ($V_g/V_\infty = 0$) case forces the tip vortices, entering the flow-field at the separation point, back towards the rotor at a higher rate. The vorticity thus remains closer to the ground, consequently resulting in smaller vorticity dispersion radii. In the case of the moving ground configuration ($V_g/V_\infty = 1$), the lower freestream velocity allows for the tip vortices to be ejected further into the flow-field, before they are transported back towards the rotor, resulting in a wider dispersion of vorticity in the wake. Furthermore, more severe velocity gradients induced by the moving ground configuration along the ground plane would facilitate secondary separation in the wake induced boundary layer, thus increasing the amount of negative vorticity in the flow-field, as shown in Figure 6.13. Mutual interactions between the close-lying counter-rotating positive and negative vortices as they leave the ground plane, will induce further accelerations in the flow, and may result in a wider dispersion of vorticity in the flow-field. This effect will be less pronounced in the stationary ground configuration cases, where the PIV data show the negative vorticity in the flow-field to contain lesser magnitudes. Additionally, the smaller vorticity dispersion radius caused by the stationary ground configuration can result in (co-rotating) tip vortices to be present within close vicinity of each other, facilitating interactions between the vortices. This can result in the co-rotating vortices to orbit each other, and may be a factor contributing to the accumulation of vorticity close to the ground plane observed from the stationary ground configuration results and the preliminary dust flow visualisation and PIV experiments.

6.6 Wind tunnel experimentation of the rotor in ground effect

Results from the ground effect experiments conducted with the moving ground plane have shown some similarities with experimental data obtained from past ground effect experiments. Table 6.3 presents a comparison of the ground effect flow regimes identified from flow visualisation experiments conducted by Curtiss *et. al* [24, 27] and those obtained from the Large Rotor PIV tests. Flow regime boundaries presented for the Large Rotor results are based on the normalised advance ratios tested in this research, and do not accurately represent the flow regime

boundaries. A wider range of normalised advance ratios is required to be tested if more accurate definition of the ground effect flow regime boundaries are sought. Table 6.3 shows the results obtained from the Large Rotor tests to broadly coincide with the classification of the ground effect flow regimes defined by benchmark experiments conducted by Curtiss *et. al* [24, 27].

While the general definition used by Curtiss *et. al* [24, 27] to classify the ground effect wake was maintained for this research, the availability of instantaneous flow data showed the ground effect flow-field to be highly unsteady, particularly at the lower normalised advance ratios ($\mu^* < 0.66$). While the recirculation flow regime was defined through the identification of wake re-ingestion, it was observed from the PIV data that the flow-field at these low normalised advance ratios were highly unsteady, significantly affecting the vorticity locations in the flow-field and hence the re-ingestion of the wake. Analyses of the PIV sample hence did not show a consistent re-ingestion of the wake at any normalised advance ratio in the flow-field as has been implied by Curtiss *et. al* [24, 27] and Ganesh *et. al* [26, 36]. A quantitative re-ingestion criterion, based on a pre-defined threshold enstrophy, was hence defined to identify normalised advance ratios where the PIV showed a significant proportion of the sample to show re-ingestion; this was used to classify the wake into the recirculation flow regime. Based on this enstrophy threshold level, the ground vortex regime and a transition flow regime, showing characteristics of both the ground vortex and recirculation flow regimes, were also identified. Consideration of this enstrophy threshold and re-ingestion criterion allowed for

	Curtiss *et. al* [24] μ^*	**Large Rotor PIV Data** μ^*
Ground distance	0.45D	0.5D
Rotor status	Trimmed	Quasi-Trimmed, $V_g/V_\infty = 1$
Recirculation Regime	$0.4 < \mu^* < 0.64$	$0.4 < \mu^* < 0.62$
Transition Flow Regime		$0.62 < \mu^* < 0.7$
Ground Vortex Regime	$0.64 < \mu^* < 0.83$	$0.7 < \mu^* < 0.85$

TABLE 6.3: Comparison of the ground effect flow regimes identified from the PIV analysis with results published by Curtiss *et. al* [24, 27]. Results from the quasi-trimmed rotor configuration tested with the ground moving at $V_g/V_\infty = 1$ are presented.

the unsteady and complex nature of the ground effect wake to be accounted for in the ground effect flow regime classification process and provides for a better representation of the flow-field.

Although a slightly different definition of the ground effect flow regimes was adopted for this research, the general wake features identified in the ground effect flow-field showed similarities to those identified by Curtiss *et. al* [24, 27]. This was despite significant differences in the experimental set-ups between the two research. While Curtiss *et. al* used a model rotor towed along a vast stretch of ground to closely simulate the motion of a helicopter in forward flight operations near a stationary ground [24, 27], experiments conducted in this research were performed with a stationary rotor model, with both the air and ground moving at the same velocity around the model. Data obtained from both experiments showed the ground vortex flow regime to consist of a compact ground vortex under the rotor disk. Measurements of significant cross-flow velocities observed from the stereo PIV measurements at these normalised advance ratios coincide well with observations of significant lateral movement of smoke filaments made by Curtiss *et. al* [24, 27]. In the recirculation flow regime, Curtiss *et. al* observed recirculation of the wake [24, 27], while the Large Rotor PIV results showed a significant proportion of the PIV sample to show re-ingestion of vorticity present in the flow-field. Similarities in the wake features between the two sets of results suggest that ground effect experiments can be conducted in a wind tunnel facility, although an accurate representation of the ground boundary configuration is vital in the formation of wake features. Tests conducted with a stationary ground plane showed the fluid mechanics of the wake to be significantly affected by the ground boundary configurations, and this was seen to have significant implications on the definition of the ground effect flow regimes.

While it has been suggested that the complete removal of the ground boundary layer is essential in obtaining accurate ground effect data in wind tunnels [98, 99], the PIV experiments conducted with the moving ground configuration in this research showed good compatibility with results from other more accurate representations of the ground effect wake, despite the presence of a wind tunnel ground boundary layer. Although the incorporation of the moving ground configuration allowed for a better wind tunnel simulation of the actual flow kinematics of the

rotor in ground effect problem, the boundary layer associated with the wind tunnel was not completely removed during these experiments. In these tests, the ground boundary layer was allowed to develop over the floor of the wind tunnel, until the beginning of the rolling road, where the moving ground condition was implemented. While this prevented the wind tunnel boundary layer to develop further, the flow along the moving ground would still be affected by a wind tunnel boundary layer, modified because of the implementation of the moving ground boundary condition. Removal of this wind tunnel boundary layer required a suction slot, ideally placed just ahead of the moving ground to remove any wind tunnel boundary layer formed by the freestream up to that point on the ground [100]. While such a suction slot was available in the Argyll wind tunnel, it was not designed to remove the thick boundary layer formed at low wind tunnel speeds. Ground effect tests conducted with the suction slot operational, showed air from different directions around the tunnel working section to be drawn by it during the experiments, thus interfering with the ground effect wake formed by the rotor. PIV experiments of ground effect, conducted using the moving ground in this research, were thus partially affected by a boundary layer along the rolling road, although this would have been significantly less than that present along a fixed, stationary ground plane.

Despite the presence of a ground boundary layer, comparison of the PIV data with flow visualisation results obtained by Curtiss *et. al* [24, 27] showed good qualitative compatibility, in terms of the detailed structure of the wake features in the different ground effect flow regimes. Results obtained from these PIV tests thus show that ground effect experimentation in wind tunnels can re-create the ground effect wake of a helicopter moving along the ground, so long as the ground boundary conditions are simulated in some way. These experiments have demonstrated the important effect of the moving ground on the formation of the wake and have shown this to be vital in obtaining accurate representations of the ground effect wake. These results suggest that the representation of the ground in both experimental analyses as well as simulation studies of ground effect are vital in capturing the fluid mechanics of the wake formation and the evolution of the resulting flow-field.

Chapter 7

Conclusions and Future Work

7.1 Conclusions

This research was based on the experimental investigation of the ground effect wake of rotors in a wind tunnel environment. Qualitative and quantitative experimental investigations of the ground effect wake produced by isolated rotor models were conducted for a variety of flight speeds, rotor parameters and ground boundary configurations using flow visualisation and Particle Image Velocimetry (PIV). Wide regions of the ground effect flow-field were investigated to track the evolution of the ground effect wake structures and their influence on the flow-field surrounding the rotor. A review of the available literature has shown little quantitative experimental research on the ground effect wake of rotors, and limited information on the fluid dynamics associated with this flow, and served as the motivation for this research. Experimental ground effect wake research has been limited due to the difficulties in conducting ground effect experiments in wind tunnel environments. Issues associated with re-creating realistic ground boundary conditions for ground effect forward flight experiments and wind tunnel wall interference effects on the developing ground effect wake have mainly discouraged experimental research on the ground effect wake. Additional issues in accurately obtaining quantitative measurements from wide areas of the ground effect flow-field using probe based techniques have contributed to the unavailability of accurate ground effect wake data. These issues have meant that validation of computational and numerical models of ground effect have been based on mostly qualitative experimental information of the flow-field, and have also resulted in poor understanding

of ground effect wake related problems, such as the brownout phenomenon and helicopter control and handling issues experienced during ground effect operations.

Based on these, the objective of this research was to quantitatively investigate wide areas of the ground effect flow-field of a rotor in a wind tunnel facility. Insights into the fluid mechanics of the ground effect wake and influences of the wake structures on the surrounding flow-field were sought. Additionally, the effects of rotor parameters such as rotor trim and blade root cut-out ratios on the wake were also to be investigated. Particular attention was also placed on the investigations of the effects of ground boundary conditions on the formation of the ground effect wake, as these have not been experimentally quantified. Based on these research objectives, the following contributions have been made by this research:

1. Wide areas of the ground effect wake produced by an isolated rotor in a wind tunnel environment were investigated using Stereoscopic Particle Image Velocimetry (PIV). Three-component velocity measurements from the flow-field were used to characterise the ground effect wake features and their influence on the flow-field surrounding the rotor and was used in the definition and classification of the ground effect flow regimes.

2. Rotor related parameters were seen to cause minor changes in the location of the flow separation point of the ground effect wake with insignificant effect of the fluid mechanics of the wake. Rotor trim, defined for this research, was seen to cause small changes in the wake location and the classification of the ground effect flow regimes.

3. Wind tunnel interference effects were seen to only affect the flow separation location, and these were most prominently observed at the lowest flight speeds tested, where the spread of the ground effect wake was observed to be the greatest.

4. Ground boundary conditions were seen to affect the fluid mechanics of the ground effect wake most significantly, causing changes in both the location and the detailed structures of the wake features. Ground boundary condition is thus the most influential factor on the formation of the ground effect wake and the most important to consider during wind tunnel testing.

5. The brownout phenomenon was re-created in a wind tunnel facility with the use of talcum powder to simulate the ground debris. Flow visualisation of the wake revealed the ground effect wake structures and dust transport mechanisms that lead to the formation of the dust clouds that may cause the so called brownout phenomenon.

Quantitative investigations of the ground effect flow-field conducted using stereoscopic (stereo) PIV allowed for velocity measurements of wide regions of the ground effect wake produced by an isolated rotor model designed especially for these experiments. A range of normalised advance ratios, rotor ground distances, rotor trim, collective angles, blade root cut-out ratios and ground boundary conditions were investigated during these tests. Experiments conducted with a quasi-trimmed rotor operated in moving ground configurations were seen to provide the most accurate representation of a helicopter operating in ground effect forward flight, and this was used to investigate the fluid mechanics associated with the ground effect wake. The main features of the ground effect flow-field identified from these investigations were a track of tip vortices trailing from the rotor disk along the ground upstream of the rotor disk, a flow separation point along the ground plane and a resulting region of recirculation. Interactions of the rotor wake expanding along the ground and the oncoming freestream was seen to cause a flow separation point. Tip vortices associated with the rotor wake were seen to move away from the ground at the separation point and re-directed back towards the rotor by the freestream, forming a mean recirculation zone between the rotor and the flow separation zone.

Unlike observations made from past ground effect research, the mean recirculation in the ground effect wake was seen to evolve from a wide region of low magnitude vorticity, encompassing large portions of the flow-field ahead of the rotor disk, at low normalised advance ratios, to a compact ground vortex under the rotor disk at higher normalised advance ratios. The rotor wake trailing along the ground plane was also observed to induce a ground boundary layer and the passage of the high strength rotor tip vortices along the ground plane was seen to cause secondary separation in this ground boundary layer. Negative vorticity, resulting from this separation were carried by the freestream together with the tip vortices such that the instantaneous ground effect flow-field consisted of interwoven clumps

of positive and negative vorticity. Three-component velocity measurements from the stereo PIV showed significant fluctuations of the cross-flow velocity, and these were seen to coincide with the locations of vorticity in the flow-field. Measurements of the mean cross-flow velocity components from several planes parallel to the rotor longitudinal plane of symmetry implied the presence of a horse-shoe vortex in the ground effect wake, behind a parabolic flow separation line. At low normalised advance ratios, this horse-shoe vortex was seen to occupy wide regions of the flow-field encompassing the mean recirculation regions observed from the PIV data. The trailing rotor tip vortex system was seen to extend under this mean recirculation region and wrap round the horse-shoe vortex tube as it leaves the flow separation point. Unsteadiness associated with the flow-field was seen to cause fluctuations of the flow separation boundary, causing the freestream to transport vorticity picked up at the flow separation point along different trajectories. This was seen to cause a constantly evolving flow-field, identified through the instantaneous PIV results. At higher normalised advance ratios, flow separation occurring under the rotor disk was seen to result in a horse-shoe shaped ground vortex under the rotor leading edge. Vorticity from the expanding rotor wake was seen to feed this ground vortex, and significant cross-flow velocity components were observed near the location of this ground vortex.

PIV data from tests conducted at a range of normalised advance ratios allowed for the ground effect wake to be classified into different flow regimes. Although previous research have defined the ground effect wake into a recirculation and ground vortex regime, it was seen that these definitions could not be used to categorise the PIV data. This was particularly the case in the recirculation flow regime, where past research have implied a well-defined recirculation of the rotor wake to be observed in the flow-field. PIV data obtained from this research did not show this to be observed at any normalised advance ratio, with the flow-field instantaneously varying, causing significant differences in vorticity distribution. A re-ingestion criterion based on a threshold enstrophy level was hence used to define the recirculation flow regime. This criterion identified the wake to be in the recirculation flow regime when more than 75% of the recorded sample showed vorticity levels in a particular region of the flow-field above the rotor disk to be higher than the threshold enstrophy level, $EN_t = 0.05$. The ground vortex flow regime was identified by the appearance of a ground vortex under the rotor disk,

and this was accompanied by an upflow near the rotor disk, and the appearance of a step-like change in lateral cyclic inputs required to trim the rotor. Enstrophy measurements above the rotor disk also showed none of the instantaneous PIV data to contain high vorticity levels above the rotor disk, signifying no wake re-ingestion through the rotor. Analyses of the PIV data also showed a range of normalised advance ratios where the flow-field exhibited the characteristics of the wake in both ground vortex and recirculation regimes. The wake in this range was classified to be in the transition flow regime, with significant proportions of the sample showing re-ingestion of the wake. Mean flow angle near the rotor disk was also measured to be positive, signifying an upflow near the rotor which is characteristic of the flow in the ground vortex regime. Consideration of this enstrophy threshold and re-ingestion criterion ensured that the unsteady nature of the ground effect wake was incorporated in the wake flow regime classification process.

Rotor parameters were seen to have an insignificant effect on the fluid mechanics of the ground effect wake. Parameters such as the rotor ground distance, collective angles and blade root cut-out ratios were seen to cause a change in the velocities of the rotorwash trailing along the ground, which in turn, was seen to affect the flow separation location. The resulting size and mean vorticity strength of the recirculation zone were also seen to be altered by this shift in the flow separation location, and these in turn will affect the classification of the wake into the different flow regimes. Variations in rotor trim configuration was seen to cause a $0.1R$ change in the flow separation locations, with no significant changes in the wake fluid mechanics identified. Results from these tests imply that ground effect testing with fixed pitch (untrimmed) rotor models will not affect the fluid mechanics of the ground effect wake, although they will alter the ground effect flow regimes; classifications of the ground effect wake obtained from the untrimmed Large Rotor tests showed small variations compared to the quasi-trimmed configuration tested. With only a quasi-trim state of the Large Rotor considered in this research, it is expected that the fully trimmed Large Rotor will cause further differences in the wake classification, although no alterations to the detailed wake features are expected.

Wind tunnel ground boundary configurations were seen to have the most significant influence on the fluid mechanics of the ground effect wake, causing significant

changes to both the location and detailed wake structures. A stationary and a moving ground condition was considered in this research through the use of a rolling road, with the ground moved with a freestream equivalent velocity to provide a more realistic simulation of a helicopter in ground effect forward flight. The moving ground configuration was seen to alter the freestream velocity close to the ground, hence affecting the flow separation location; at comparable advance ratios, the moving ground caused flow separation to occur $0.5R$ closer to the rotor disk, compared to the results from the stationary ground configuration. At comparable separation point locations, the flow-field produced by the moving ground configuration was seen to contain a loop of tip vortices while the stationary ground configuration was seen to cause vorticity to accumulate closer to the ground; this difference is caused by the lower freestream speed required by the moving ground configuration to cause flow separation to occur at comparable ground locations. Differences in velocity gradients in the wake induced boundary layer, brought about by the varying ground boundary conditions, also meant that lesser secondary separation occurred in the flow-field for the stationary ground cases. Lower velocities of the freestream and interactions between the close-lying positive and negative vortices will result in a greater dispersion of vorticity in the flow-field produced by the moving ground configuration compared to the stationary ground configuration; this was quantified through the enstrophy dispersion radius parameter. The accumulation of vorticity close to the ground, caused by the stationary ground condition, meant that classification of the wake into the different ground effect flow regimes could not be performed, especially for the recirculation flow regime which is based on the observation of wake re-ingestion.

Verification of the Large Rotor PIV results with data from a smaller rotor model, showed wind tunnel interference effects on the ground effect wake to be insignificant, mainly causing small shifts in the flow separation locations at the lowest flight speeds tested. Results from this research imply that experiments representative of helicopter flights in ground effect can be accurately conducted in wind tunnels so long as suitably sized rotor models and ground boundary conditions, representative of actual flight conditions, are modelled. Through these experiments, it was seen that this could be achieved by employing a moving ground plane to re-create the ground boundary conditions necessary for the formation of

the ground effect wake and by employing rotor models with model-span-to-tunnel-width ratios lesser than 0.3.

Talcum powder flow visualisation experiments conducted during this research with a stationary ground plane, enabled the visualisation of the main ground effect flow features, and allowed for a simulation of the dust clouds associated with the brownout phenomenon. Observations near the ground showed the rotor wake expanding along the ground plane to cause particles to be uplifted from the ground, and dust transport mechanisms such as saltation, traction and suspension to occur in the wake. It was seen that the high velocities associated with the rotor wake expanding along the ground, resulted in the entrainment and uplift of the dust particles. These particles were seen to be convected by the freestream, together with the tip vortices leaving the ground, into the recirculation region, resulting in the formation of the dust clouds. Passage of the tip vortices close to the ground plane was also seen to induce secondary separation in the flow-field, and these were seen to be ejected into the flow-field along different trajectories together with the tip vortices. Visualisation of dust clusters appearing and disappearing from the plane of observation provided further evidence for the three-dimensional nature of the wake. Quantitative PIV data from experiments conducted with an identical rotor set-up showed most of the dust particles to exist within the mean recirculation region, where most of the vorticity associated with the tip vortices was observed. Velocity fluctuations measured from the PIV data showed instances where vorticity was transported close to the rotor disk, and this was associated with the occasions where the flow visualisation sequences showed dust particles to reach regions of the flow far above the rotor. Results from these experiments suggest that these complex transport mechanisms need to be accurately implemented within simulation codes if accurate brownout dust cloud prediction models are to be created.

7.2 Recommendations for Future Work

Work presented in this dissertation has provided some quantitative measurements from the ground effect wakes of rotors. Effects of some rotor parameters, wind tunnel wall interference effects and ground boundary conditions on the resulting

ground effect wake of the rotors were considered during these investigations. While some progress in quantitatively measuring wide regions of the ground effect flow-field has been made, further research can be conducted to investigate the ground effect wake.

In the case of the brownout dust cloud flow visualisations, the experiments were conducted using talcum powder as the dust particles. These were introduced into the flow-field by simply allowing the rotor wake trailing along the stationary ground plane to pick up the dust. While these allowed for a good understanding of the dust transport mechanism, these experiments were conducted over a static ground plane. With the PIV investigations showing significant effects of ground boundary conditions on the formation of the ground effect wake features, more realistic representations of the ground boundary conditions are required to study the interactions of the debris and the ground effect flow features. These may have implications on the overall distribution and the size of the resulting dust cloud. One approach that can be considered in this case would be to employ a moving rotor model in the wind tunnel to recreate the boundary conditions necessary in forward flight. This can also be modified to investigate transient manoeuvres such as landing or take-off routines.

Furthermore, a variety of particle sizes could be considered to track the changes to the dust cloud distribution during brownout operations. Simultaneous qualitative and quantitative measurements of the flow-field can also be attempted to allow for the dust, velocity and vorticity associated with the tip vortices to be tracked. Recent experiments conducted by Leishman *et. al* employ high speed flow visualisation and PIV to track the particle pick-up mechanisms occurring at the ground during hover in brownout conditions [101]. A similar approach can be employed for the forward flight condition tests.

Three-dimensional measurements of the flow-field using stereo PIV allowed for velocity measurements along a single longitudinal plane of the flow-field. While wide regions of the flow-field were covered and revealed significant cross-flow fluctuations, the causes for these fluctuations are still unknown. Further PIV investigations conducted along planes parallel to the lateral axis of the rotor disk will

allow for further insights into the three-dimensional nature of the wake. Moreover, these experiments could be used to gain insights into the characteristics of the horse-shoe vortex in the flow-field.

While the PIV experiments provided adequate spatial resolution of the ground effect wake, no temporal information from the flow-field was recorded. Laser Doppler Velocimetry or other probe bases techniques could be used to investigate the variations in flow separation point fluctuations observed to occur between the different ground boundary cases. Additionally, measurements of the dust cloud fluctuations could also be performed to determine frequency components associated with the dust cloud formation. These tests could also be used to investigate the secondary separation in the flow-field, caused by the tip vortices passing over the ground plane. Variations to the inflow through the rotor disk at different flight speeds could also be considered through the use of probe-based techniques.

While the ground boundary configurations were varied during the PIV experiments, a ground boundary layer was still affecting the formation of the ground effect wake in the experiments conducted. Although the experimental results from the conducted experiments showed good correlation to results from more realistic ground effect experiments, the ground boundary layer would still have an effect on the wake and could alter important flow structures. This could include effects on the negative vorticity observed in the flow-field as well as the location of the separation points on the ground. Effects of this ground boundary layer on the ground effect wake could be investigated by employing suitable techniques to remove the boundary layer. This will also allow for the experiments to be conducted with a more realistic representation of the ground boundary conditions associated with ground effect. Additionally, the Large Rotor can be completely trimmed to investigate any effect of trim on the ground effect wake symmetry and flow regime classifications of the ground effect wake.

Appendix A

Particle Image Velocimetry

Early fluid flow measurements were conventionally conducted using probe based techniques such as hot-wire anemometry and pressure transducers. The necessity to insert probes into the flow-field to be measured makes these techniques spatially limited to specific points. Experimental measurements using probe-based techniques are considered intrusive; in some cases, the insertion of probes into the flow-field can alter the flow structures and make measurements of vortical or highly three-dimensional flows difficult to perform accurately. Flow measurements using these techniques are also influenced by ambient effects such as temperature, pressure and humidity, and non-linearity effects which require calibration. Such issues compound the difficulties of using these techniques in measuring highly unsteady or three-dimensional flows [102]. The advent of laser technology, in the late 1960s, led to the development of tracer based optical flow measurement techniques such as Laser Doppler Velocimetry (LDV) and Particle Image Velocimetry (PIV). These techniques involve visualisations of tracer seeded flows and hold an advantage over probe based techniques because of their non-invasive measurements of the flow. While LDV is spatially limited to specific points in the flow, PIV holds further advantage over the other experimental techniques because of its capabilities of measuring wide areas of flow. In this research, this ability was one of the defining factors in the choice of PIV as the main experimental technique.

One of the added beneficial features of PIV is its ability to produce instantaneous flow information over large flow regions. While this provides the spatial resolution

that can be unrivalled by most other experimental techniques, it lacks in temporal resolution capabilities that probe based techniques possess. This limitation however, has been rectified by the development of high frequency lasers and high camera frame rates, which now allow for time-resolved PIV to be possible [102]. With PIV being a mature and well-developed experimental technique, many variations of the PIV technique exist, ranging from holographic PIV, to dual-plane PIV [103] and even micron-resolution PIV [104]. In the context of this research, the PIV method that would be employed to measure the ground effect flow-field is based on gathering three-dimensional flow information from a two dimensional slice of the flow-field. Known as Stereoscopic Particle Image Velocimetry, this is derived from two-dimensional, two-component PIV. The basics of the PIV technique and a summary of concepts used in Stereoscopic PIV in acquiring three-dimensional velocity information from a two-dimensional slice of the flow-field are provided in the upcoming sections.

A.1 Principles of Particle Image Velocimetry

PIV is a well developed experimental technique, brought to prominence in the early 1990s. It involves the tracking of a flow through the use of particles seeding the flow-field. Velocity of the fluid flow is derived from measuring the displacements of the tracer particles seeding the flow, within a specified time frame [105]. With the assumption that the particles faithfully follow the flow-field, the velocity of the particles correspond to the velocity of the flow-field at that instant of time [106]. A conventional PIV system is made up for four primary components. Firstly, a suitable particle medium is required to seed the flow-field under investigation. A light source is required to illuminate the region of the flow-field of interest. Scattering of the light source by the tracer particles seeding the flow-field is recorded by an imaging system which captures two exposures of the illuminated flow. Image and signal processing algorithms are used to process the recorded images to extract the particle displacement information necessary in reconstructing the velocity information of the flow [107].

While a range of imaging systems can be used to record the flow-field, the PIV technique commonly employed today makes use of digitally recorded images of

the flow-field. This was introduced as a replacement to PIV conducted using photographic material, and was quickly adopted as a favourite among researchers as it removed the need for long photograph processing times and allowed for easier reconstruction of flow velocities [108]. Known as digital PIV (DPIV), modern adaptations of the PIV concept are based on this. Figure A.1 provides a schematic of the different components of the DPIV system. The arrangement shown in this figure is typical of a PIV arrangement used to measure two-dimensional velocity information from a two-dimensional slice of the flow-field. This is commonly referred to as two-dimensional two-component (2D2C) PIV.

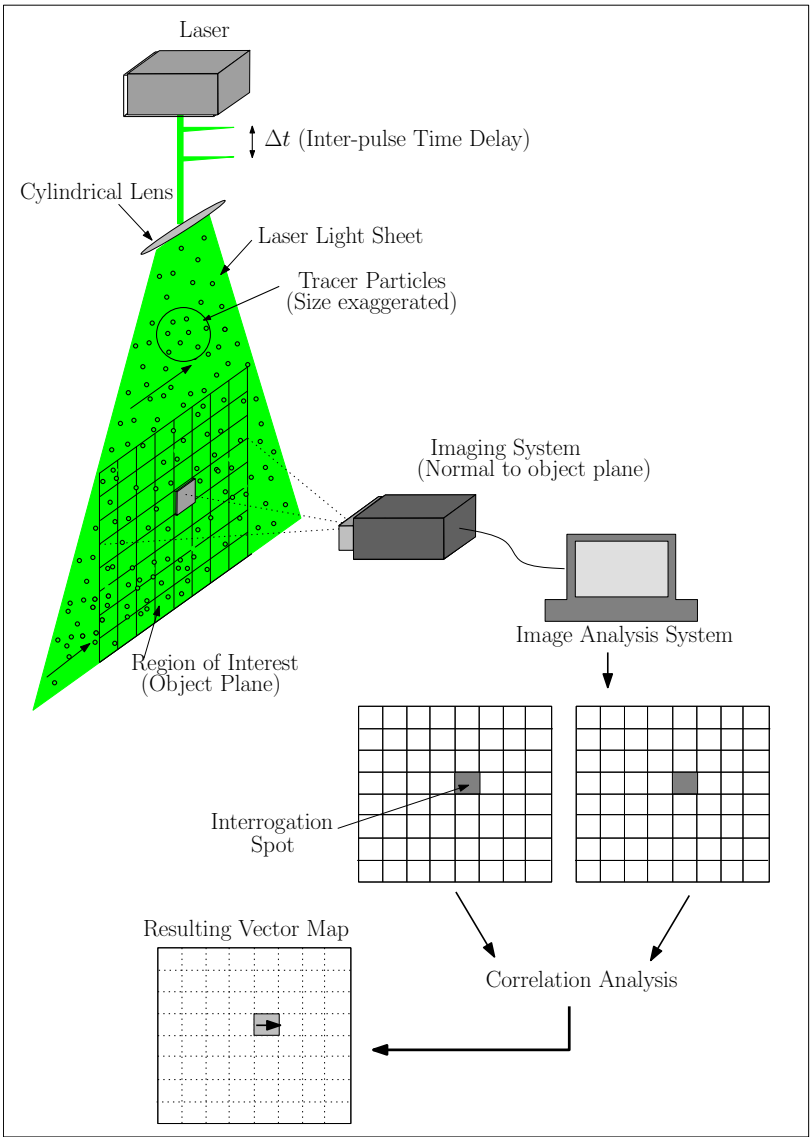

FIGURE A.1: Components of a digital PIV system [102].

The concept of PIV is based on the tracing of fluid flow through the light scattering properties of particles seeding the fluid. Velocities of the fluid flow are inferred from the velocity of the tracer particles suspended in the fluid flow, making the accuracy of the PIV measurements strongly dependent upon the ability of the particles in faithfully following the flow [109]. Choosing suitable tracer particles to seed the fluid flow is thus essential in PIV, as this can result in errors even before the PIV experiment is commenced. Theories related to particle dynamics have proven that neutrally buoyant particles exhibit excellent flow tracing properties in highly turbulent, accelerating or vortical flow-fields. In general, identifying neutrally buoyant particles for PIV experiments conducted in liquid flows is not difficult, as the size of liquid molecules generally tend to be large. In gaseous flows such as air, where the molecules sizes are smaller, this tends to be a more difficult procedure. In this case, the general principle is to use particles which are generally small in size, as these are usually seen to have good responses in accelerating flow-fields [103, 109]. For flow investigations conducted in air, it is common practice to employ oil-based particles as seeding. These generally are produced through smoke/mist generators, which vapourise oils to produce a mist of particles with nominal particle diameters between 1-2μm [109].

Besides the mechanical properties of the tracer particles, their associated optical properties are also important in PIV, as the light scattering properties of the particles are used to measure their relative displacements and hence the fluid velocity. For small particles, typical of those used in PIV, the Lorentz-Mie theory can be used to describe the intensity of scattered light caused by the particles encountering light beams at different angles [78]. A typical Mie scattering intensity diagram, as shown in Figure A.2, for a small spherical particle, would show lobes of intensity at different angles, with the lobes at the front (at 0^o scattering angle) and at the back (at 180^o scattering angle) the longest, indicating the highest scattering intensity [110]. Consideration of the scattering intensity of light is important for PIV, which relies on this scattering property. With reference to Figure A.1, the set-up for the 2D2C PIV constitutes of the image recording system arranged normal (90^o) to the object plane, which contains the tracer particles. This arrangement means that 2D2C PIV operates at 90^o (side) scatter, where the tracer particles do not scatter light with maximum intensity [111]. This means that a powerful illumination source is required in PIV to illuminate the tracer particles

in the fluid so that adequate scattered light can be captured by the imaging system. Frequently, in PIV applications, the fluid flow is illuminated by a frequency doubled Nd:YAG laser with an optical wavelength of $532nm$. Suitable cylindrical lenses are used to expand the laser beam into a thin lightsheet which usually has a Gaussian profile [78]. Usually a light sheet thickness of around $1-2mm$ is sought, to minimise measurement errors caused by out-of-plane movement of the particles [107]. The laser system used is normally pulsed to emit short bursts of intense high energy light to illuminate the tracer particles in the required plane of the flow-field.

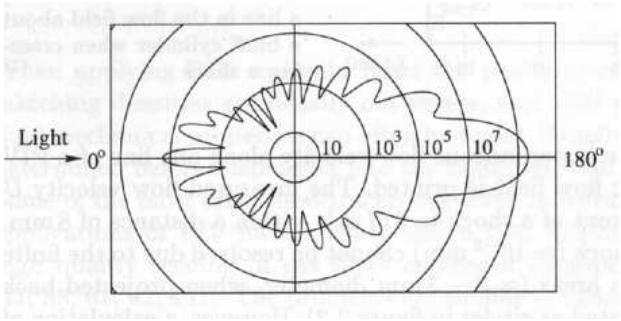

FIGURE A.2: Scatter intensity diagram for a $1\mu m$ oil particle in air. Lobes at 0^o and 180^o show greatest scatter intensity at these angles [110].

In digital PIV, two successive images of the illuminated plane are required to determine the displacement of the particles. Pulses of the laser illuminating a plane in the flow-field are usually separated by a short time period, usually referred to as the inter-pulse time delay, Δt [78]. With Δt between the two exposures known, the particle velocity, $\mathbf{u(x,t)}$, in the plane of contention can be determined using the equation,

$$\mathbf{u(x,t)} = \lim_{\Delta t \to 0} \frac{\Delta\ \mathbf{x(x,t)}}{\Delta t} \tag{A.1}$$

where $\mathbf{\Delta x(x,t)}$ represents the displacement of the particles within the laser light sheet. The two pulses of the laser light sheet are usually recorded on some form of recording medium. This depends on the imaging system used. In the case of digital PIV, a CCD (charged coupled device) chip camera is usually used [78, 107]. Both pulses of the laser can be recorded on a single frame or multiple frames, and this affects how the PIV analysis is carried out. Single frame images are recorded with

both the laser pulses recorded within one frame [78]. This usually means that the displacement and speed of the particles can be determined without any knowledge of the velocity. Referred to as directional ambiguity, this was a common problem in early PIV, conducted using photographic medium [108]. Numerous methods have been developed to overcome this issue, and some include introducing time-coded exposures [112], varying the pulse intensities of the laser [103], or employing image shifting techniques [113]. Usage of video CCD cameras can remove this directional ambiguity as the cameras are capable of recording multiple images in succession. This is typically applied in current digital PIV techniques and is referred to as multi frame PIV [78]. In this case, each laser exposure is captured on a single image, and with the recording sequence known, the directional ambiguity is resolved. While this method allows for a simpler image analysis process to resolve the fluid velocity, it comes with a disadvantage of having lower image resolution compared to PIV carried out using photographic film [108].

Image pairs recorded by the imaging system are then analysed by image analysis algorithms to derive particle displacement information, which are then used to measure the velocities in the flow-field. Numerous image analysis techniques exist, and the choice usually depends on the type of image recorded. Particle density within the recorded images play an important part in determining whether particle tracking techniques or correlation algorithms are applied to the PIV images. A sparsely populated PIV image could easily be analysed using particle tracking methods, as the relatively small amount of particles within the images mean that particle motion patterns can easily be detected [103, 106]. While this analysis can be employed with relative ease, the sparsity of the images mean that finer details of the flow can be lost [110]. More conventional PIV employs densely populated images, where correlation schemes are better suited to derive particle displacement information. In this case, each PIV image is split into smaller tiles known as interrogation spots or windows. These square tiles are usually between 32×32 pixels and 128×128 pixels in size [107]. It is thus essential for correlation based PIV to be conducted with adequate seeding to allow for sufficient particles to appear within each interrogation tile [114]. With the assumption that all the particles within a tile follow a general displacement pattern in the same direction according to the motion of the fluid, a correlation analysis is performed on the image to detect the magnitude of the displacement [110]. For single frame, multiple exposure

images, auto-correlation is used, whereby each interrogation tile is correlated with itself [106, 107]. In the case of multi-frame exposures, interrogation tiles from the same region of the image from each frame are cross-correlated [108, 114]. To reduced computational demands, cross-correlation analyses in DPIV are usually performed via fast fourier transform (FFT) in the frequency domain. This is then transformed back to the spatial domain to acquire the particle displacement information. Correlation analysis *(whether auto or cross correlation)* of the PIV images usually result in a displacement peak, which is offset from the centre of the interrogation window by the displacement magnitude of the particles. Usually a Gaussian surface fit or a centroid detection algorithm is implemented to improve the accuracy of the measurements of the correlation peak location [78]. This will give better accuracy in the displacement information derived from the flow-field and the corresponding velocity information of the flow-field. Additional techniques to reduce errors associated with the detection of correlation peaks have also been introduced to minimise measurement errors in DPIV [115, 116].

A.1.1 Calibration process for 2D2C PIV

While image analysis of the raw PIV data provides the pixel displacement information, this needs to be converted to the physical displacements of the particles in the flow-field, before velocity information of the flow can be derived. This conversion is carried out using a calibration process, which is used to account for any distortion or magnification effects between the image and object plane. Usually a calibration grid containing markers (such as dots, crosses or squares) is placed within the laser light sheet in the region of interest [78]. With the camera fixed in the same position as during the PIV image recording process, transfer functions are used to define the differences between the locations of the markers in the image plane and in the object plane on the calibration grid [110]. These functions are then employed to convert the pixel displacements derived from the PIV images, into physical particle displacements. Equation A.1 is then used to derive the velocities associated with the particle displacements measured.

A.1.2 Consistency of PIV data

De-correlation effects during image processing, can lead to erroneous vectors to be defined within the PIV vector map. Usually referred to as wild vectors, these spurious vectors are identified by their deviations from the general flow direction, identified through comparisons with neighbouring vectors [107]. Common causes of these inconsistencies in the flow-field include poor signal to noise ratio between the correlating images (caused by the lack of illumination on one image), low seeding density, poor focusing of the imaging system and large out-of-plane velocity components [78, 107]. PIV parameters, such as the user defined interrogation tile size and inter-pulse time delay, Δt, can also cause de-correlation between the images [110]. To minimise user-determined de-correlation effects, useful guidelines have been provided regarding the choice of inter-pulse time delays [110], seeding densities and tile sizes [117].

Wild vectors present in PIV vector maps can usually be corrected during post interrogation processes to ensure valid interpretations of the flow-field. These processes essentially condition the interrogated images, and reliance on these techniques to produce acceptable velocity maps suggest a fundamental problem in the PIV experiment. Post-interrogation processes in PIV essentially consist of two stages, vector detection and correction. Vector detection processes are used to identify the spurious vectors in a velocity map. The most commonly used method is a Coherence method, based on comparing vectors within a 3×3 pixels filter map of the vector field [107]. Each vector within the filtered map has an assigned coherence value and a comparison with a spurious vector would result in a value excessive of a user-defined tolerance limit [118]. The identified erroneous vector is then passed through a vector correction scheme, which replaces the spurious vector identified by a vector derived from the velocity of its neighbouring vectors. Bi-linear interpolation schemes are used during this correction process [110]. This Coherence method is commonly used in PIV post-processing despite its proven limitations [119]. Other more recent, sophisticated wild vector detection and replacement schemes have also been implemented with good success. Some of these include the forward/reverse tile test method employed by Green *et. al* [64] and a method of increasing signal to noise ratio in the correlation process to aid in the removal of wild vectors [117].

A.1.3 Errors in PIV

Velocity information derived from PIV have been known to be affected by two forms of errors, bias errors and random errors [78]. Random errors are caused by experimental uncertainty and are difficult to predict. These can be difficult to eliminate from the system, with care taken in the experimental setup a way to minimise this [110]. Bias errors are usually associated with the PIV systems, and can be rectified through the implementation of post-processing algorithms, in some cases, or by following guidelines from other similar experiments [78]. Some of the bias errors affecting PIV data include digitisation effects, image bit depth and image density effects and velocity bias errors [110].

Digitisation effects in PIV occur when the imaged flow seeding particles are too small in size to be adequately defined as a distinctive image. This is an effect of the limited spatial resolution of the CCD sensors used in digital cameras and most prominently affect digital PIV experiments. The limited pixel size of these cameras result in reduced fine detail resolution, at a given magnification. The small tracer particles in the flow-field are thus imaged without an accurate profile [110]. This results in a phenomenon known as "peak-locking", which occurs when the particle images cannot provide enough information to accurately predict the particle displacement [107]. While the particles provide an image allowing for cross-correlation, the sub-pixel image of the particles, mean that the finer velocity details cannot be derived from the images. The displacements derived from the correlation processes thus tend to be biased to integer-values resulting in clusters of vectors in the derived velocity maps to have angular, block-like changes in velocity. Histograms relating to the velocities will show peaks at integer values [78]. Peak-locking effect is commonly seen in digital PIV data, and numerous algorithms are available to resolve peak-locked PIV data [78].

Image density effects relate to situations where the interrogation tiles are sparsely populated. This results in the signal to noise ratio between the images to be poor, resulting in wild vectors to be developed in the flow-field. Errors related to this can be easily rectified by the introduction of more tracer particles into the flow-field, although too much of this can also result in image saturation and poor

measurements [117].

Interrogation window sizes can also result in biasing errors and these are usually referred to as velocity bias errors. When a flow contains high velocity variations within small regions of the flow, consideration of small interrogation windows can cause errors. High velocities of the particles in this case can cause the second exposure of the PIV image to not feature the particles, thus resulting in poor correlation [103]. Employing larger interrogation window sizes can reduce this error, although too large interrogation window sizes can result in velocity maps with low vector resolution. This can cause important details in the flow-field to be lost. Appropriate tile sizes can be chosen by careful considerations of the maximum velocities experienced within the local flow-field, and these can be used to set appropriate inter-pulse time delays [110].

A.2 Principles of Stereoscopic Particle Image Velocimetry

Concepts of particle image velocimetry presented in Section A.1 can be employed to derive the out-of-plane velocity information from a two-dimensional slice of the flow-field. This branch of obtaining three-dimensional velocity measurements from a two-dimensional slice of the flow-field is referred to as Stereoscopic Particle Image Velocimetry. Simultaneous images of the flow-field region of interest are recorded by two cameras, placed off-axis to the same region of interest. This is unlike conventional two-dimensional two-component (2D2C) PIV, which makes use of a single camera placed normal to the object plane to be recorded. One shortcoming of 2D2C PIV pertains to inaccuracies in the measurements of the two dimensional velocities in the plane due to perspective errors. This is particularly the case in highly three dimensional flows with significant out-of-plane velocity components. Out-of-plane motion of the tracer particles are projected onto the imaging plane, causing an over-estimation (or under-estimation) of the in-plane velocity components [120]. The utilisation of two cameras, placed off axis to the object plane being recorded, ensures two different views of the same region of interest in the flow. The respective in-plane displacements combined with the

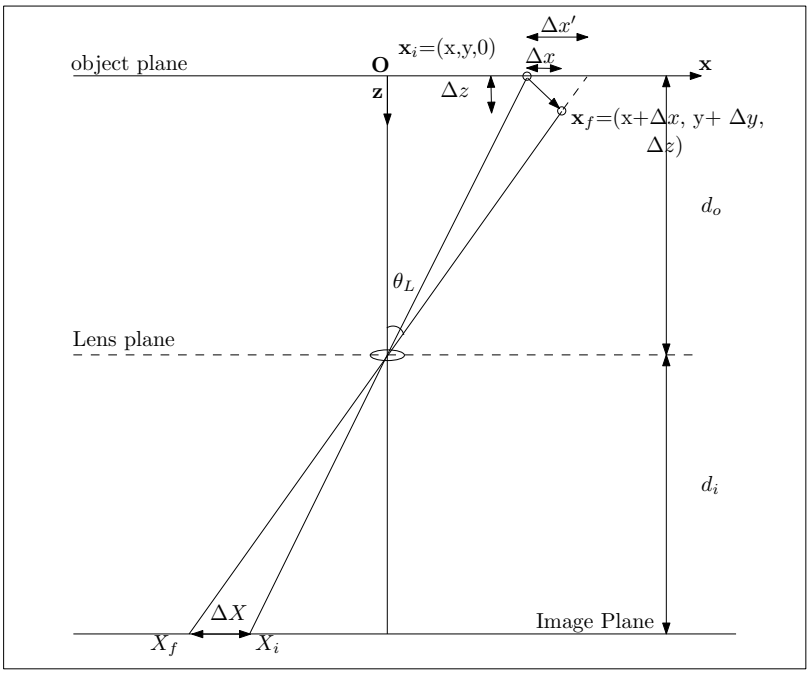

FIGURE A.3: Perspective Error due to the projection of the out-of-plane velocity on a 2D image plane [121]

representative camera off-axis angles are then used to derive accurate in-plane displacement information and the out-of-plane displacements [121].

Figure A.3 illustrates the error arising in the 2D2C PIV measurements of in-plane displacements. As can be seen from the figure, the viewing angle of the imaging system to the location of the particle results in the out-of-plane velocity component to be projected onto the two-dimensional image plane. The resulting error, ε_x, is referred to as the perspective error and is given by the equation [121]:

$$\Delta x' - \Delta x = \varepsilon_x \tag{A.2}$$

The perspective error, can be expressed in terms of the perspective angle θ (i.e the angle between the camera lens axis and the normal of the object plane) as [65]:

$$\varepsilon_x = \Delta z \tan\theta \tag{A.3}$$

Errors in the measured in-plane velocities are removed when two cameras offset from one another, by known perspective angles, are used to record images of the same region of interest (ROI) [122]. Referring back to Figure A.3, and considering the image to show the left camera, the measured displacement from the cameras can be represented by [65]:

$$\Delta x'_L = \Delta x + \Delta z \tan\theta_L \tag{A.4}$$

$$\Delta x'_R = \Delta x + \Delta z \tan\theta_R \tag{A.5}$$

With the perspective angles θ_L and θ_R measured during the experiment, the two equations can be used to re-construct the out-of plane velocity component, as well as obtain accurate two-dimensional in-plane velocity information [65]:

$$\Delta x = \frac{\Delta x'_L \tan\theta_R - \Delta x'_R \tan\theta_L}{\tan\theta_R - \tan\theta_L} \tag{A.6}$$

$$\Delta z = \frac{\Delta x'_R - \Delta x'_L}{\tan\theta_R - \tan\theta_L} \tag{A.7}$$

Through literature, it is apparent that two different stereoscopic PIV arrangements exist; namely, the translation (linear displacement) system and the rotational (angular displacement) system. The distinction between the two systems lie in the orientation of the imaging plane [111, 120, 122–124], and a schematic of the two systems are presented in Figure A.4. In the translation system, both the cameras are aligned such that the object plane, image plane and lens plane are all parallel to each other [120]. This is illustrated in Figure A.4 (a), and although the translation system represented in this image appears to be symmetric about the system axis, this condition is not necessary for its implementation [124]. In the rotational configuration represented by Figure A.4 (b), the camera lens plane is not parallel with the object plane; it is rotated such that the lens axes intersects the object plane at the system axis [124].

Simplicity in the arrangement of the cameras in the translation system with respect to the object plane result in good focusing and uniform magnifications across the

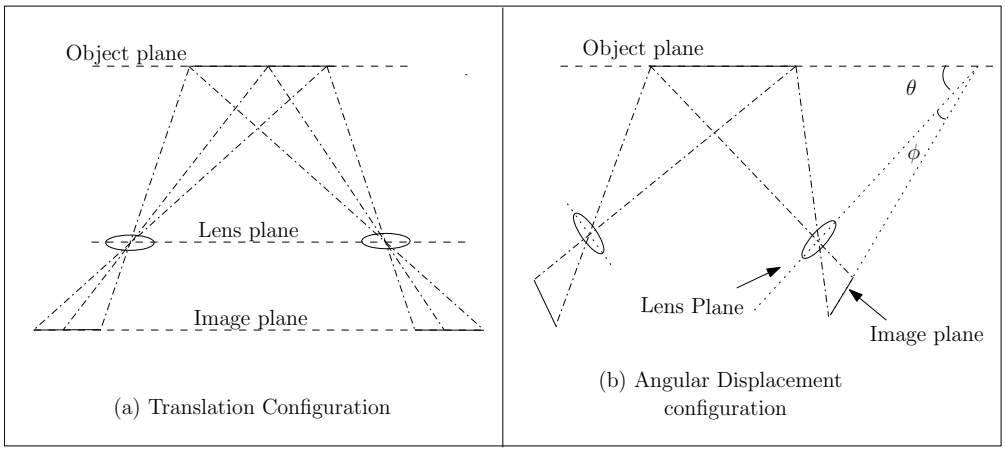

FIGURE A.4: Difference between the translational and angular displacement stereoscopic PIV configurations [123]

imaged region of interest [124]. With both cameras arranged such that the object plane, image plane and lens plane are parallel, both the cameras will record identical fields-of-view. Combination of these fields-of-view to re-construct the velocity information would therefore be a straight-forward process, without additional post-processing that would be required for non-uniform magnification images [120]. These factors contribute to the advantage held by the translation system to the rotational stereoscopic PIV system. However, a major disadvantage of this system is the small combined field-of-view obtained from this system in comparison to the rotational system [111, 124]. This is a result of a maximum perspective angle, θ, that can be established between the centre of the object plane and then centre of the lens axis [123]. Limitations in the perspective angles are based on the camera lens performance limitations, which significantly degrade when it is forced to operate outside its performance limit, which will occur when the set perspective angle is too large. The main inaccuracies of the translation system occurs in the out-of-plane velocities, with research suggesting a 40% degradation in the out-of-plane accuracy compared to the rotational system [125].

The rotational system has been deemed to be more difficult to implement in experimental conditions [78]. This configuration further complicates the process of obtaining velocity information from the raw images, as extensive image-processing of the raw images have to be conducted to re-construct the velocity information. However, if successfully implemented, this configuration allows higher accuracy to be obtained for the out-of-plane velocity, and hence allows more accurate in-plane

velocity information to be extracted. In the rotational system, the camera lens plane is rotated with respect to the object plane so that higher perspective angles can be achieved. This allows for wider regions of the flow-field to be imaged [124]. This arrangement of the camera lens plane introduces non-uniform magnification across the image plane. To ensure that all regions of the imaged field-of-view are in good focus, the image plane has to be further rotated, such that the object plane, image plane and lens plane are all collinear [111]. Known as the Sheimpflug condition, this is achieved by the usage of special Scheimpflug adaptors mounted in between the camera and lens, which allows for the camera image plane to be rotated independently of the lens plane. Compliance with the Scheimpflug condition, however means that the rotational systems leads to further non-uniformity in the magnification [124]. Furthermore, the oppositely rotated lens planes mean that the resulting images are oppositely stretched. This therefore requires the images to first be independently interpolated into a common grid and then the non-uniform magnification effects to be tackled [124].

Based on the rotational system, the PIV cameras could also be arranged on opposing sides of the laser light sheet, to exploit the light scattering intensity of the tracer particles in the forward/back scatter position. First proposed by Willert, this system makes use of the higher light scattering efficiency possessed by particles in forward scatter to achieve higher signal-to-noise ratio [123], allowing for better correlation between the images. A schematic of this rotational PIV set-up is presented in Figure A.5. Like the conventional rotational stereoscopic PIV systems, an interpolation is still required to combine the flow information from the separate cameras onto a common grid, although in this case, both the images will be stretched in the same direction [123].

A.2.1 Calibration Procedure

As in the case of the 2D2C PIV, the physical displacement of the tracer particles need to be derived from the PIV images, before the velocity information of the flow-field can be re-constructed. This requires a calibration process, done to map the pixel locations of the image and the physical location of the object plane. The calibration also ensures that the presence of any image distortion effects are accounted for during the transformation of the displacement information from

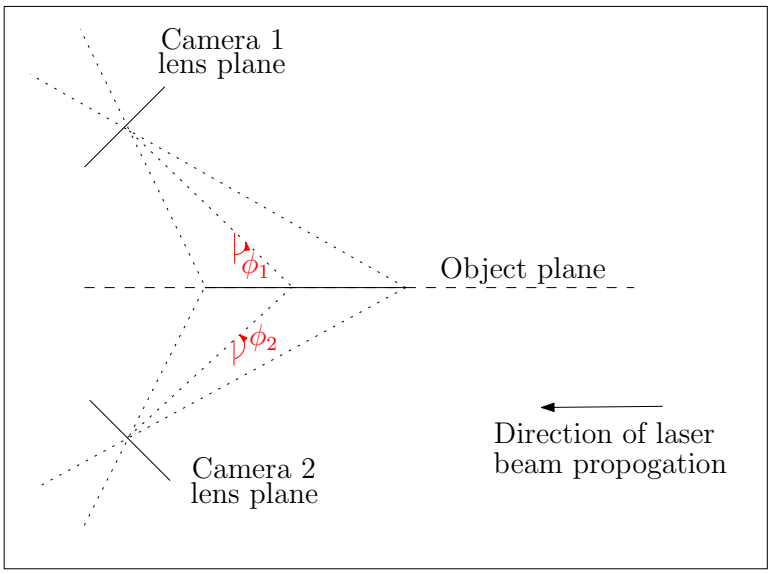

FIGURE A.5: Angular displacement stereoscopic PIV set-up with the cameras operating in forward scatter [123].

the image plane to the object plane. It is common to use a non-linear mapping function to represent image distortion effects and for stereo PIV calibration, this is also employed [126]. Usually a Taylor series expansion can be used to derive the non-linear function that maps the image plane to the object plane. If the acquired images suffer from more severe distortion effects, higher order Taylor series terms can be considered. This will provide the function F, that maps, the physical particle displacement, d_p to the image pixel displacement, D_p, according to the equation [126],

$$D_p = \mathbf{F}(d_p) \tag{A.8}$$

As in the case of the 2D2C PIV, a calibration grid of markers is placed within the field-of-view of the cameras, and images of the calibration grid are recorded to derive the mapping functions. In Stereoscopic PIV, the need to determine the perspective distortions in the flow-field require multiple images of the plane parallel to the object plane to be recorded. This can be conducted using a stepped calibration grid, which contains two distinct levels [78]. A mapping function for each camera is obtained, which are then used to combine the individual camera images into a single image containing three-dimensional displacement information.

The inverse of the mapping function is then applied to the combined image to convert the pixel displacements into physical displacements.

Appendix B

Large Rotor Blade Pitch Calibration Curves

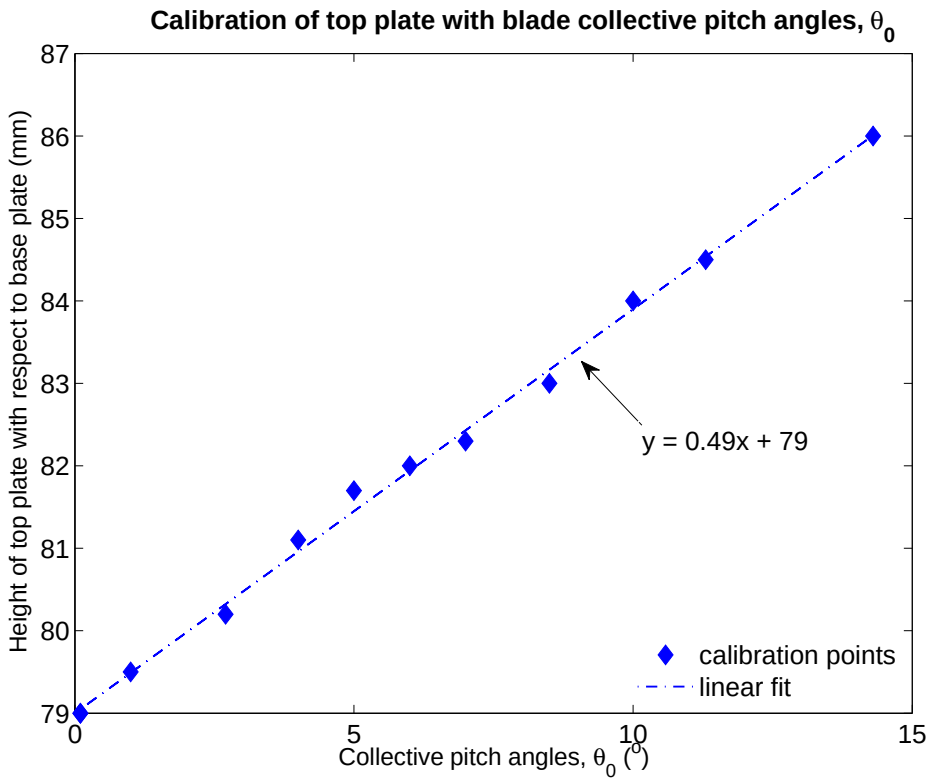

FIGURE B.1: Calibration Curve for the collective blade pitch angles for the Large Rotor. The plot shows the calibration of the top plate of the rotor system with respect to its base plate for a range of blade collective angles, θ_0.

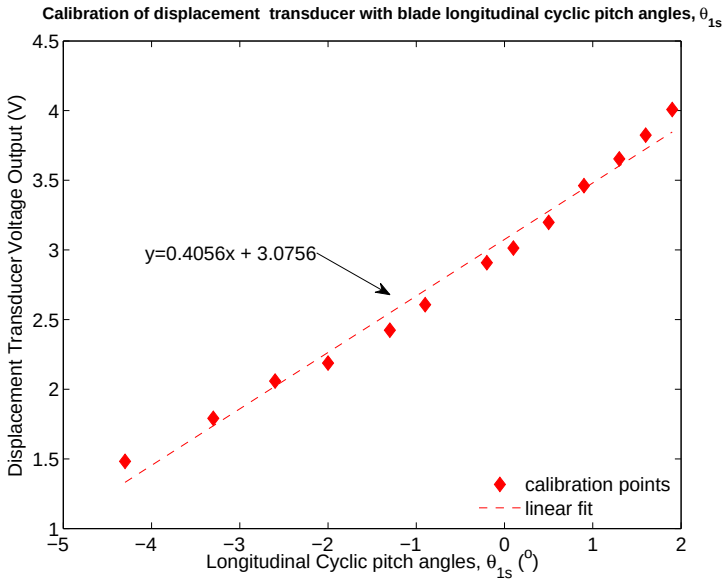

FIGURE B.2: Calibration Curve for the longitudinal cyclic blade pitch angles for the Large Rotor. The plot shows the calibration of the voltage measured by the longitudinal displacement transducer for a range of longitudinal cyclic angles, θ_{1s}.

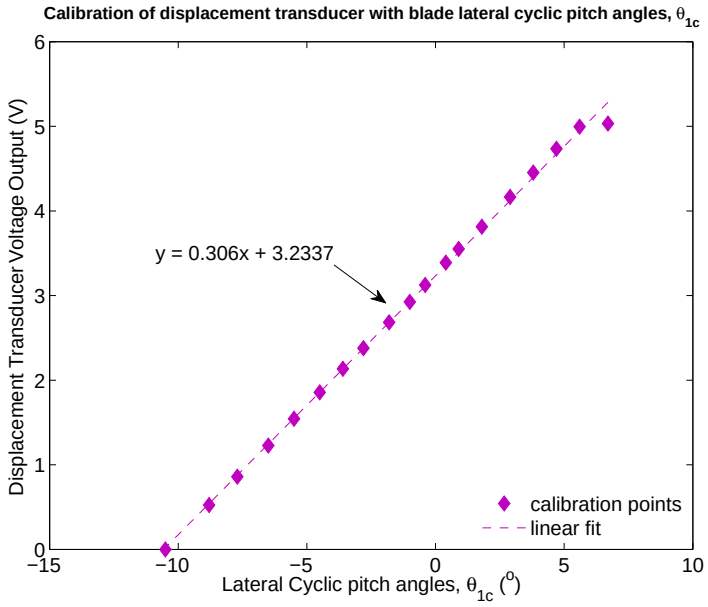

FIGURE B.3: Calibration Curve for the lateral cyclic blade pitch angles for the Large Rotor. The plot shows the calibration of the voltage measured by the lateral displacement transducer for a range of lateral cyclic angles, θ_{1c}.

Appendix C

Large Rotor PIV Experimental Results

C.1 Mean PIV Data

C.1.1 Effect of advance ratio

Influences of advance ratio on the mean ground effect flow-field, produced by the other experimental configurations tested with the Large Rotor are illustrated through a comparison of the mean vorticity plots at a range of normalised advance ratios, as shown in Figures C.1 to C.3. A different field-of-view (Figure 5.2 (b), View 2) was used for the higher normalised advance ratio ($\mu^* > 0.62$) tests presented in these figures, to capture the full extent of the ground effect flow features in these cases. In this field-of-view (View 2), artefacts caused by poor beam quality at the far edge of the light sheet, were seen to cause strong negative vorticity at the extreme top left edge (above the disk) of the vorticity plots and are ignored during analyses of the data. Influences of rotor trim and ground boundary conditions on the ground effect wake can also be identified through a comparison of these figures with Figure 5.12, presented in Chapter 5 .

Variations in normalised advance ratio was seen to influence the location of flow separation and formation of the mean recirculation (vorticity) zone. Figures C.1 to

C.3 show the mean recirculation region forming closer to the rotor disk at progressively higher normalised advance ratio settings, for all the configurations tested. This is brought about by a shift in the mean flow separation location, caused by changes in the relative freestream velocity, V_∞. At low normalised advance ratio, the mean recirculation zone was seen as a large region of low magnitude vorticity, an example shown in Figure C.3 (a). As the normalised advance ratio was increased, flow separation occurred nearer the rotor disk, and the resulting mean recirculation zone was seen to become a more compact region of higher magnitude vorticity. At a particular normalised advance ratio, this mean recirculation region evolved into a concentrated vortex which was formed under the rotor disk leading edge, an example of which is shown in Figure C.3 (h). This ground vortex was seen to possess vorticity magnitudes comparable to the vorticity strength of the tip vortex system under the rotor disk, featured in this plot.

Variations in the rotor trim configurations, as shown through a comparison of Figures C.1 and C.2, was seen to have little impact on the ground effect flow features, except causing a slight shift in the mean flow separation locations. Through analyses of the topological flow separation location from the PIV data, rotor trim was seen to cause a $0.1R$ shift in the flow separation location. This in turn was seen to result in small changes in the size of the mean recirculation regions.

Variations in ground boundary conditions however, as shown through a comparison of Figures C.1 and C.3, was seen to result in more significant differences in the structure of the ground effect features, as well as cause a greater shift in the mean recirculation regions. PIV data showed the moving ground configuration ($V_g/V_\infty = 1$) to cause flow separation to occur around $0.5R$ closer to the rotor disk, a change significantly greater than that caused by variations in rotor trim configurations. Additionally, the moving ground boundary configuration was seen to result in a change in the distribution of vorticity within the mean recirculation zone. Through the mean vorticity plots presented in Figure C.3, it can be seen that the tip vortex system trailing along the ground plane followed a more defined loop-like path into the mean recirculation zone for the tests conducted with the moving ground boundary configuration. A direct comparison with the stationary ground configuration ($V_g/V_\infty = 0$) cases, as shown in Figure C.1 showed the vorticity to accumulate close to the centre of the mean recirculation zone, for the range of

normalised advance ratios tested. This difference in the vorticity dispersion was quantified by the mean enstrophy dispersion radius of the flow, calculated from the PIV data *(Refer to Section 5.2.2.3)*. The moving ground boundary configuration was also seen to result in greater prominence of the negative vorticity in the flow-field.

(a) Rotor at $\mu^* = 0.45$ (b) Rotor at $\mu^* = 0.51$

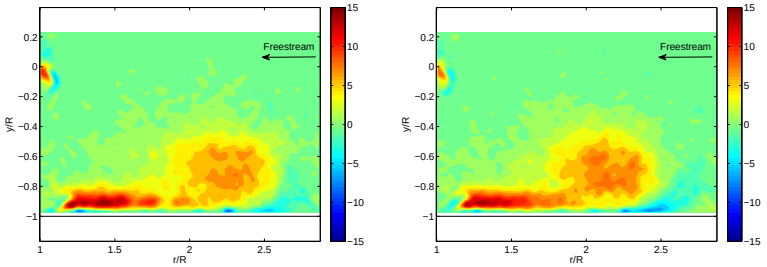

(c) Rotor at $\mu^* = 0.62$ (d) Rotor at $\mu^* = 0.66$

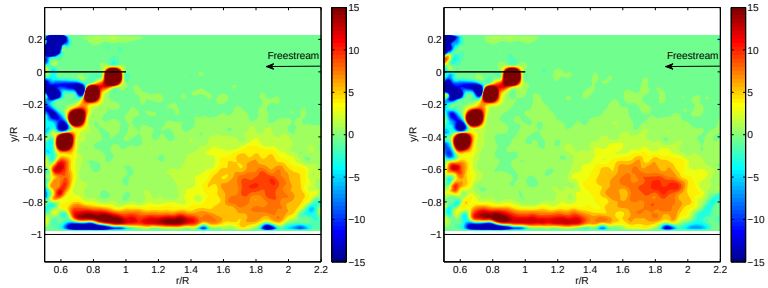

(e) Rotor at $\mu^* = 0.7$ (f) Rotor at $\mu^* = 0.74$

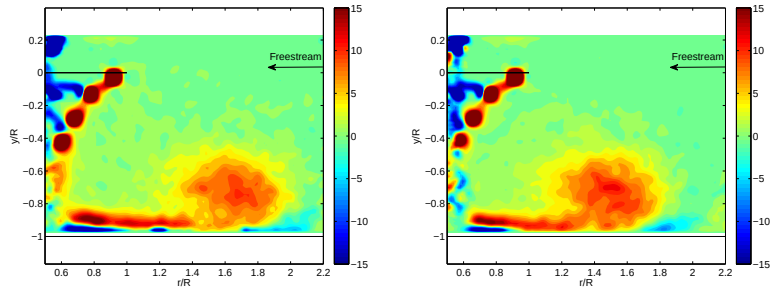

(g) Rotor at $\mu^* = 0.79$ (h) Rotor at $\mu^* = 0.85$

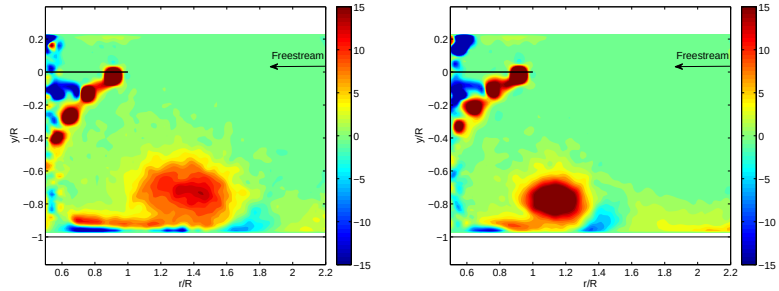

FIGURE C.1: Mean Vorticity plots at a range of normalised advance ratios (μ^*) with the rotor untrimmed and the ground stationary ($V_g/V_\infty = 0$). The rotor was at a ground distance of 1.0R and the frames show the evolution of the mean recirculation zone brought about by a change in the normalised advance ratio.

(a) Rotor at $\mu^* = 0.45$

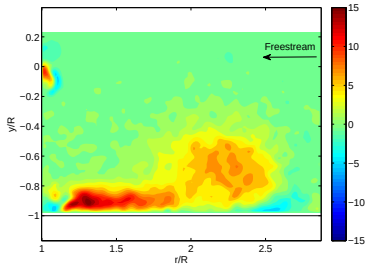

(b) Rotor at $\mu^* = 0.51$

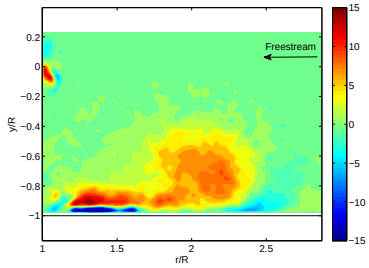

(c) Rotor at $\mu^* = 0.62$

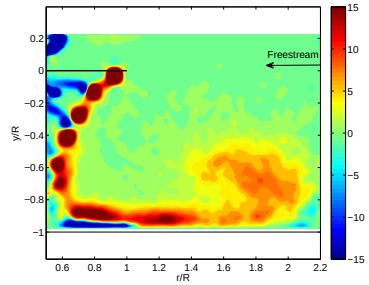

(d) Rotor at $\mu^* = 0.66$

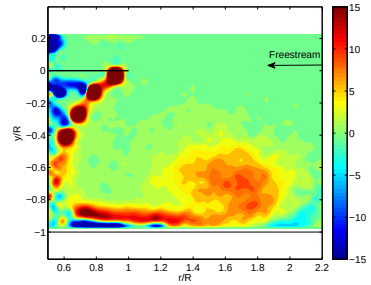

(e) Rotor at $\mu^* = 0.7$

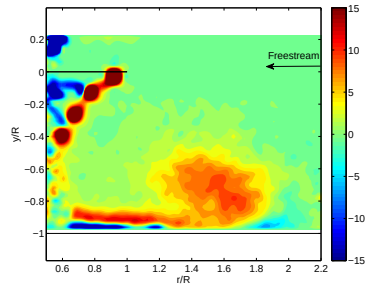

(f) Rotor at $\mu^* = 0.76$

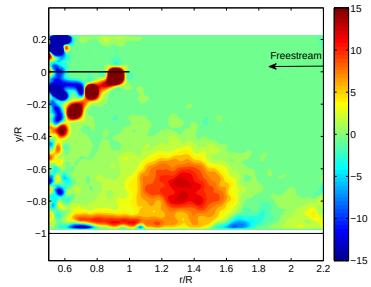

(g) Rotor at $\mu^* = 0.8$

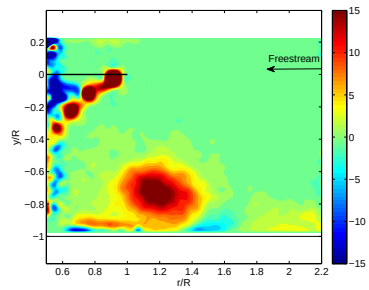

(h) Rotor at $\mu^* = 0.87$

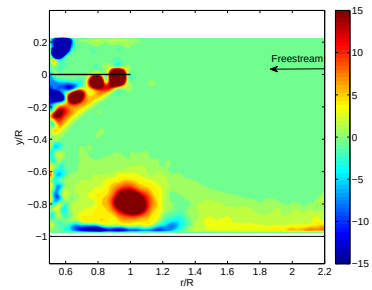

FIGURE C.2: Mean Vorticity plots at a range of normalised advance ratio (μ^*) with the rotor quasi-trimmed and the ground stationary ($V_g/V_\infty = 0$). The rotor was at a ground distance of 1.0R and the frames show the evolution of the mean recirculation zone brought about by a change in the normalised advance ratio.

(a) Rotor at $\mu^* = 0.4$

(b) Rotor at $\mu^* = 0.46$

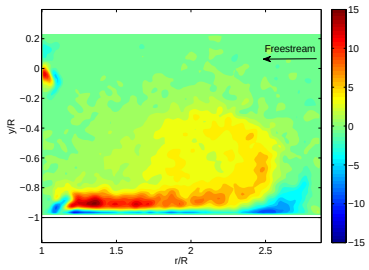

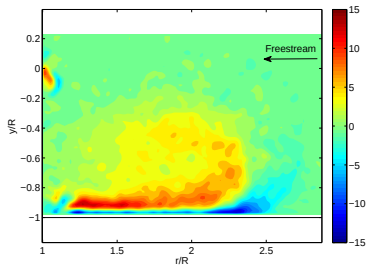

(c) Rotor at $\mu^* = 0.51$

(d) Rotor at $\mu^* = 0.62$

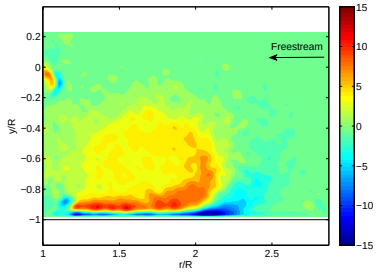

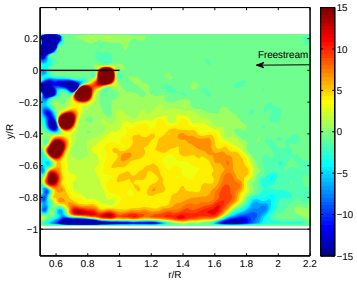

(e) Rotor at $\mu^* = 0.66$

(f) Rotor at $\mu^* = 0.70$

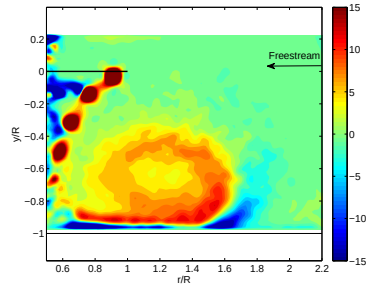

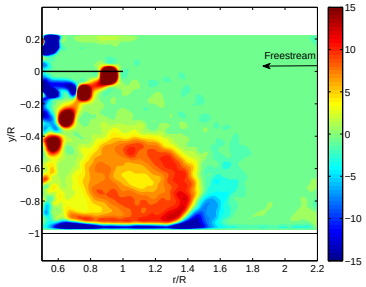

(g) Rotor at $\mu^* = 0.76$

(h) Rotor at $\mu^* = 0.79$

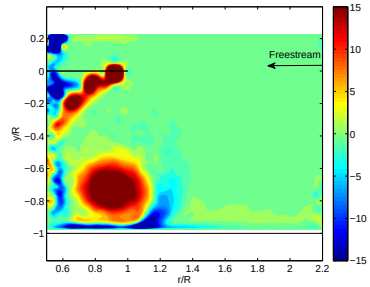

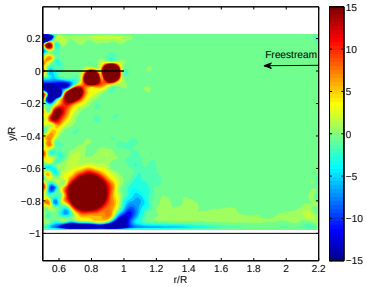

FIGURE C.3: Mean Vorticity plots at a range of normalised advance ratio (μ^*) with the rotor untrimmed and the ground moving ($V_g/V_\infty = 1$). The rotor was at a ground distance of 1.0R and the frames show the evolution of the mean recirculation zone brought about by a change in the normalised advance ratio.

C.2 Instantaneous PIV Data

Figures C.4 - C.6 present samples of instantaneous flow-field produced with different rotor trim and ground configuration tests conducted at a normalised advance ratio of $\mu^* \approx 0.60$. Comparisons of these figures with Figure 5.17 (Section 5.4.1) illustrate the effect of rotor trim and ground boundary configurations on the instantaneous ground effect flow-field. From the figures, it is immediately obvious that the ground effect flow-field was characterised by clumps of positive and negative vorticity. Positive vorticity clumps were seen to possess varying vorticity strengths, with most of the high magnitude positive vorticity clumps observed closer to the ground, and those higher up in the flow-field seen to possess lower magnitudes. This was especially noticeable for the stationary ground ($V_g/V_\infty = 0$) cases, as can be seen from Figures C.4 and C.5.

The instantaneous ground effect flow-fields produced by varying rotor trim configurations showed little differences, in terms of the detailed wake structures. Differences between the instantaneous vorticity plots presented in Figures C.4 and C.5 are unnoticeable, although the mean PIV data indicated rotor trim to result in a small shift in the mean flow separation location, for similar normalised advance ratio settings. Similar observations can also be made between Figure C.6 and Figure 5.17 for the moving ground ($V_g/V_\infty = 1$) configuration.

Comparisons of the flow-field produced by the different ground boundary configurations, however, showed more significant differences. For the stationary ground ($V_g/V_\infty = 0$) cases, the oppositely signed vorticity clumps appeared to be interwoven throughout the imaged wake regions. In these cases, most of the vorticity in the wake was seen to concentrate within a particular region of the flow-field. Figures C.4 (b) and (c) and Figures C.5 (b) and (c) show high magnitude positive vorticity to be present near the ground plane, and a comparison with corresponding mean vorticity data for these cases showed this to occur near the centre of the mean flow recirculation zones. Preliminary ground effect tests, described in Chapters 3 and 4, showed similar results, and this can be attributed to similarities between the experimental ground boundary configurations maintained during the tests. Additionally, instances of wide-spread vorticity distribution throughout the imaged flow regions were also observed from the results and examples of this are

shown in Figures C.4 (b) and (c). In these plots, vorticity clumps, with significant strengths were seen close to the rotor disk plane, implying that ingestion of vorticity, as described by Curtiss *et. al* [24, 27], can take place. Instances of implied vorticity re-ingestion through the rotor disk were seen to occur in the flow-field until the normalised advance ratio which resulted in the formation of a compact vortex under the rotor disk.

In the case of the flow-field produced by the moving ground ($V_g/V_\infty = 1$) configuration, vorticity associated with the tip vortices leaving the ground at the separation point, was seen to exist around a loop within the mean recirculation zone. Figure C.6 (a) provides a good representation of this process. Through a comparison with mean vorticity data from the flow-field, it was seen that this loop of positive vorticity clumps border the mean recirculation zone. This is unlike observations from the stationary ground configuration ($V_g/V_\infty = 0$) results presented in Figures C.4 and C.5, where most of the vorticity was seen to be accumulated around the centre of the mean recirculation zone. As the normalised advance ratio was increased and the mean flow separation point location occurred closer to the rotor disk, the positive vorticity clumps were seen to maintain their loop-like trajectory around the perimeter of the mean recirculation zone, which was seen to be more compact in size. This was observed to result in the formation of larger ground vortices under the rotor leading edge (as seen in Figure C.3 (g)), compared to the stationary ground configuration case (Figure C.2 (h)).

Instantaneous vorticity plots presented in these figures also show the prominence of the clumps of negative vorticity in the ground effect flow-field. Much like the positive vorticity, the negative vorticity clumps were also seen to possess varying magnitudes. Generally, the further the flow separation point from the rotor, the lesser the strength of these negative vorticity clumps. Figure C.4 and Figure C.5, showing examples from the stationary ground configuration ($V_g/V_\infty = 0$) tests, reveal no obvious pattern in the location of these negative vorticity clumps, which appear to be interwoven with the positive vorticity clumps in the flow-field. This was unlike observations from the moving ground configuration ($V_g/V_\infty = 1$), shown in Figure C.6, where the majority of the negative vorticity clumps were seen to border the tip vortices as they trailed along the ground plane and formed a loop within the mean recirculation zone. In the stationary ground configuration cases,

(a) Flow separation at $r/R = 2.16$ (b) Flow separation at $r/R = 2.44$

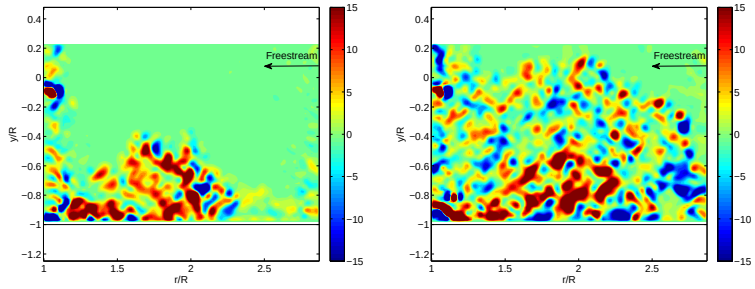

(c) Flow separation at $r/R = 2.12$ (d) Flow separation at $r/R = 2.32$

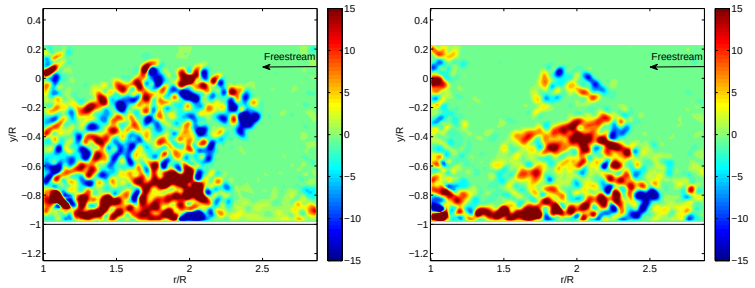

FIGURE C.4: Instantaneous vorticity plots at $\mu^* = 0.61$ with the rotor untrimmed and the rolling road stationary ($V_g/V_\infty = 0$). The rotor was at a ground distance of 1.0R and the mean topological flow separation point was at $\frac{r}{R} = 2.31$.

(a) Flow separation at $r/R = 2.38$ (b) Flow separation at $r/R = 2.01$

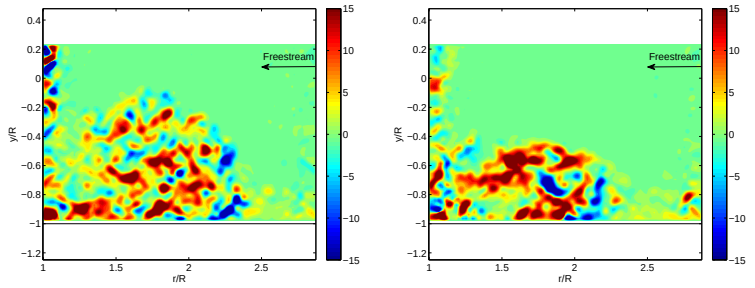

(c) Flow separation at $r/R = 2.28$ (d) Flow separation at $r/R = 2.41$

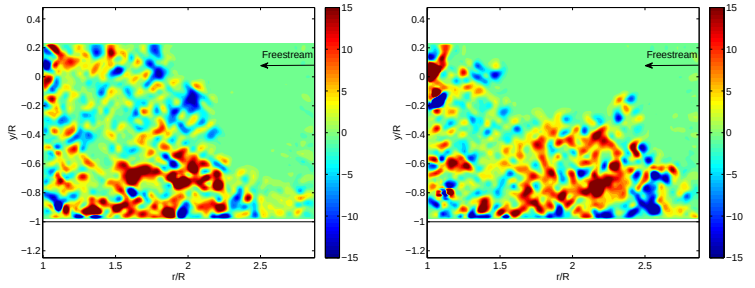

FIGURE C.5: Instantaneous vorticity plots at $\mu^* = 0.62$ with the rotor quasi-trimmed and the rolling road stationary ($V_g/V_\infty = 0$). The rotor was at a ground distance of 1.0R and the mean topological flow separation point was at $\frac{r}{R} = 2.23$.

(a) Flow separation at $r/R = 1.66$ (b) Flow separation at $r/R = 1.71$

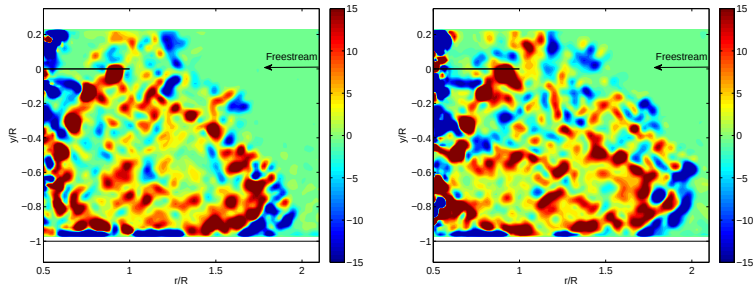

(c) Flow separation at $r/R = 1.76$ (d) Flow separation at $r/R = 1.82$

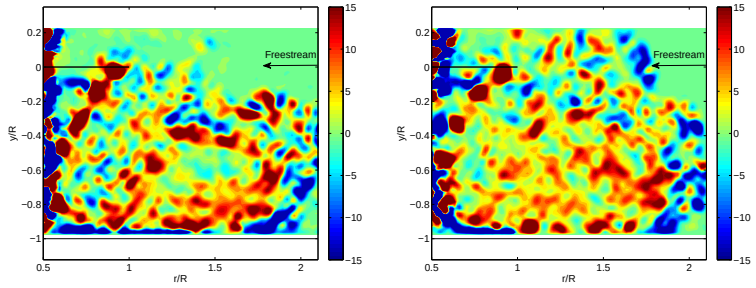

FIGURE C.6: Instantaneous vorticity plots at $\mu^* = 0.61$ with the rotor untrimmed and the rolling road moving ($V_g/V_\infty = 1$). The rotor was at a ground distance of 1.0R and the mean topological flow separation point was at $\frac{r}{R} = 1.74$.

most of the high magnitude negative vorticity appeared to be located around the flow separation region, close to the vicinity of the high magnitude positive vorticity clumps accumulating near the ground plane. Examples of this are seen from Figure C.4 (a) and Figure C.5 (b). In instances where the positive vorticity was more distributed throughout the flow-field, as seen in Figure C.4 (b) and Figure C.5 (c), the negative vorticity was seen to follow the same trend of being more distributed, with those higher up in the flow-field possessing lesser strength than those observed nearer the ground.

C.3 Flow Unsteadiness

Figure C.7 presents histograms of the positions of the instantaneous flow separation points and the representative mean topological flow separation point location for a range of normalised advance ratios, for the stationary ground ($V_g/V_\infty = 0$) configuration. Results from a quasi-trimmed rotor configuration, tested at normalised advance ratios resulting in comparable mean flow separation point locations are presented in this figure to facilitate a direct comparison between this

figure and Figure 5.19 presented in Chapter 5, for the moving ground ($V_g/V_\infty = 1$) boundary configuration. Figure C.7 shows the fluctuations of the separation points to be more pronounced across the normalised advance ratio range for the stationary ground ($V_g/V_\infty = 0$) case than when compared to the moving ground ($V_g/V_\infty = 1$) configuration cases presented in Figure 5.19. This is inferred from the spread of the separation point locations about the mean, with Figure C.7 showing the stationary ground cases to have more histogram bins at all the normalised advance ratios, compared to the moving ground configuration cases. Results from this analysis suggests that the fluctuations of the separation point locations in the wake was less severe in the moving ground cases than in the stationary ground cases.

As in the moving ground configuration cases, results from the stationary ground configuration tests also showed the degree of the separation point fluctuations to vary with normalised advance ratio. Figure C.7 (a) presenting the data from $\mu^* = 0.51$, shows most of the sample separation points to be located around the mean, exhibiting small scale fluctuations. The plot also reveals instances of large separation point deviations in the flow-field; these can be seen from the histogram bins located around $\frac{r}{R} < 1.6$, where all of these large deviations in instantaneous flow separation locations tended to occur ahead of the calculated mean. At the higher normalised advance ratio of $\mu^* = 0.67$ shown in Figure C.7 (b), the high amplitude deviations disappear and the flow-field is seen to be characterised by more moderate fluctuations about the mean. This was also the case at $\mu^* = 0.81$, presented in Figure C.7 (c), where most of the deviations from the mean were observed to occur beyond the mean separation point location.

These statistical analyses of the flow separation point locations indicate the ground effect wake to experience greater wake fluctuations at the lower normalised advance ratios, with the flow-field showing more large amplitude deviations. At higher normalised advance ratio, the fluctuations appeared more moderate around the mean. These trends were observed for both the ground boundary configurations tested and were also seen in the flow-field produced by the untrimmed rotor. While both the ground configuration cases show similar trends, the separation point fluctuations experienced with the moving ground ($V_g/V_\infty = 1$) cases were smaller in amplitude compared to that observed from the flow-field produced by the stationary ground ($V_g/V_\infty = 0$) cases, implying a steadier wake, at least in terms of the

(a) Rotor at $\mu^* = 0.51$

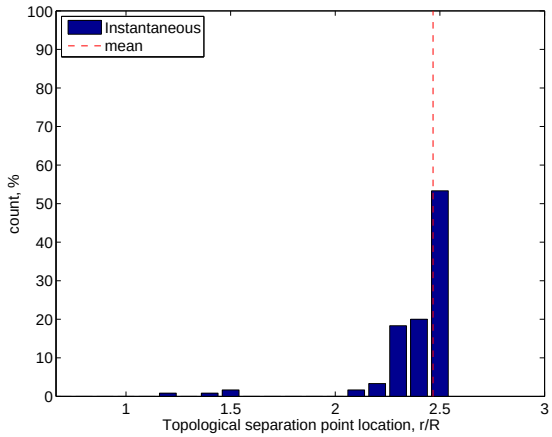

(b) Rotor at $\mu^* = 0.67$

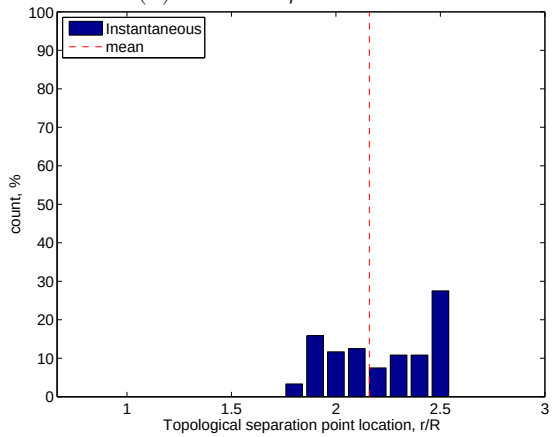

(c) Rotor at $\mu^* = 0.81$

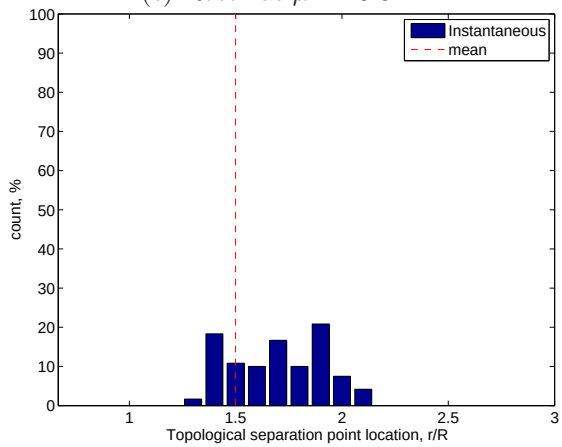

FIGURE C.7: Spread of the instantaneous flow separation point locations in the recorded PIV sample, for a range of normalised advance ratios (μ^*), with the rotor quasi-trimmed and at a ground distance of $1.0R$ and the ground stationary ($V_g/V_\infty = 0$). Frames also present the mean flow separation position derived from the average PIV data.

separation point locations. These results coincide well with previous experimental results which suggest greater separation point fluctuations along stationary ground planes with thick boundary layers [127]. Since these ground effect tests were conducted at relatively low speeds in the Argyll wind tunnel, experiments conducted with the stationary ground would result in a thick boundary layer along the ground plane, compared to the moving ground configuration tests. Variations in the separation point locations may contribute to the differences in the tip vortex trajectories observed in the ground effect flow-field, and evidence for this was seen from the instantaneous vorticity plots presented in Figure C.5. Changes in the vorticity distribution in the flow-field can in turn result in velocity fluctuations to be experienced in the flow-field, contributing to the overall unsteadiness of the wake.

C.3.1 Root-mean-square Velocity Fluctuations

Figures C.8 - C.10 show the contour plots of the RMS fluctuations of the local velocity about the local mean, non-dimensionalised with respect to the hover induced velocity, V_h, for the other experimental configurations tested with the Large Rotor. This can be compared to Figure 5.20 presented in Section 5.5.1 to highlight the variations in the flow-field brought about by the different rotor trim and ground boundary configurations.

All the experimental configurations presented here show the RMS velocity fluctuations to become confined within smaller regions of the wake as the normalised advance ratio was increased. Confinement of the fluctuations within smaller wake regions coincided with the changes in the mean recirculation zone sizes observed from the mean vorticity plots presented in Figures C.1 - C.3, with the peak RMS velocity fluctuations seen to occur within the mean recirculation zones. At the lower normalised advance ratios, where the mean flow separation occurred far upstream from the rotor disk, the RMS fluctuations appeared to affect parts of the flow-field beyond the mean recirculation zone. At higher normalised advance ratios, most of the velocity fluctuations were seen to occur within smaller regions of the flow-field, and these fluctuations were seen to possess higher magnitudes.

Rotor trim effects on the RMS velocity fluctuations experienced in the ground effect flow-field were insignificant, although major differences could be spotted in the wake produced by the different ground boundary configurations. In both the untrimmed and quasi-trimmed rotor configurations, the stationary ground configuration ($V_g/V_\infty = 0$) tests, presented in Figures C.8 and C.9, show the highest magnitude fluctuations to occur around the centre of the recirculation region, just above the ground plane. When compared to this, the RMS velocity fluctuation data for the moving ground configuration ($V_g/V_\infty = 1$) cases, presented in Figure C.10 and Figure 5.20, show the highest magnitude fluctuations to occur around a loop within the mean recirculation zone, and these were seen to possess lower magnitudes compared to the results from the stationary ground configuration tests.

High magnitudes of the RMS velocity data suggest large scale fluctuations of the ground effect flow structures to be a likely source of these velocity fluctuations. Analyses of the instantaneous PIV data and the RMS data showed the peak RMS fluctuations to occur in regions where the highest magnitude vorticity were located. This was especially noticeable along the trailing tip vortex system and within the mean recirculation region, and suggests that the variations in the location of the high magnitude vortices was the cause of the velocity fluctuations in the flow-field. For the stationary ground ($V_g/V_\infty = 0$) cases, where most of the vorticity was seen to accumulate close to the centre of the mean recirculation zone, the highest magnitude RMS velocity fluctuations were seen to occur in these areas. A comparison between Figure C.4 and the RMS velocity fluctuation plot, shown in Figure C.8 (a) provide evidence for this. For the moving ground ($V_g/V_\infty = 1$) cases, the RMS plots show the highest magnitude velocity fluctuations around a loop bordering the recirculation zone. In this case, the high magnitude vorticity were seen in similar locations, and a comparison between Figure C.6 and the RMS plot in Figure C.10 (c) illustrates this. Analyses of the RMS velocity fluctuation data suggest the ground boundary configuration to have a significant effect on the distribution of vorticity and hence the extent of velocity fluctuations experienced in the ground effect flow-field. Comparisons of Figures C.8 and C.10, show wider regions of the flow-field affected by velocity fluctuations for the moving ground ($V_g/V_\infty = 1$) configuration, although the fluctuations were seen to occur with greater magnitudes within smaller regions for the stationary ground ($V_g/V_\infty = 0$) cases.

(a) $\mu^* = 0.61$ (b) $\mu^* = 0.7$

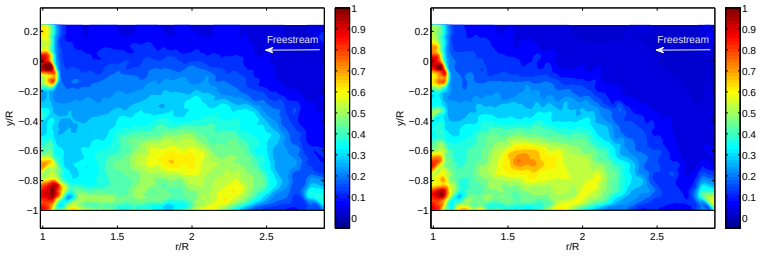

(c) $\mu^* = 0.79$ (d) $\mu^* = 0.85$

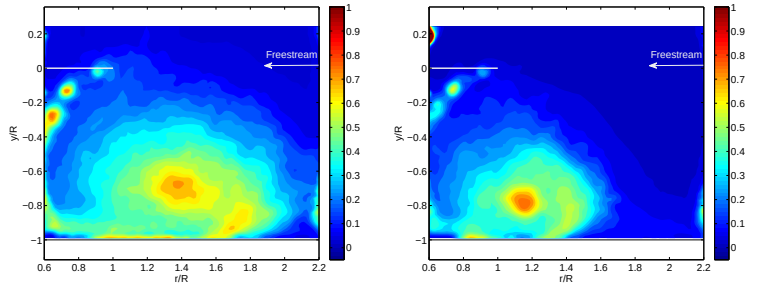

FIGURE C.8: RMS velocity fluctuations at a range of normalised advance ratios with the rotor untrimmed and the rolling road stationary ($V_g/V_\infty = 0$). The rotor was at a ground height of 1.0R and the RMS velocity fluctuations are normalised with V_h.

(a) $\mu^* = 0.51$ (b) $\mu^* = 0.62$

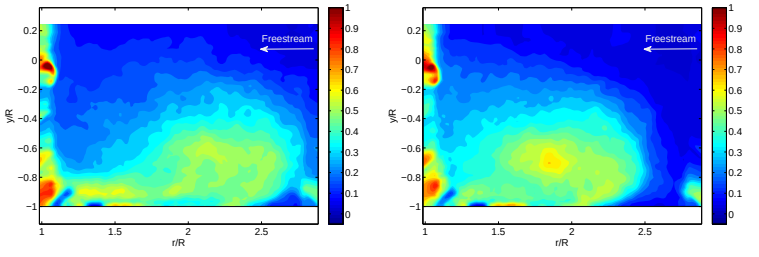

(c) $\mu^* = 0.7$ (d) $\mu^* = 0.87$

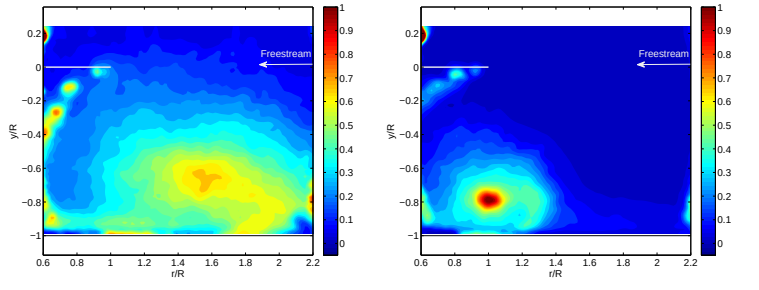

FIGURE C.9: RMS velocity fluctuations at a range of normalised advance ratios with the rotor quasi-trimmed and the rolling road stationary ($V_g/V_\infty = 0$). The rotor was at a ground height of 1.0R and the RMS velocity fluctuations are normalised with V_h.

(a) $\mu^* = 0.46$ (b) $\mu^* = 0.51$

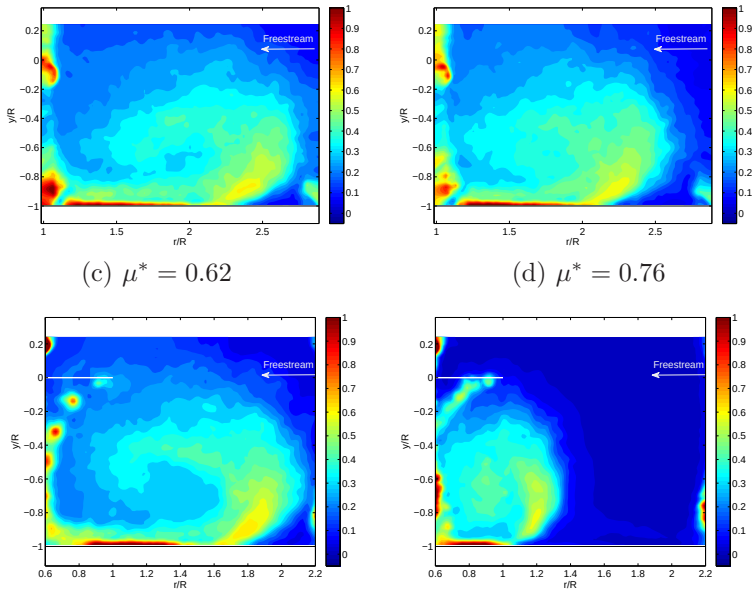

(c) $\mu^* = 0.62$ (d) $\mu^* = 0.76$

FIGURE C.10: RMS velocity fluctuations at a range of normalised advance ratios with the rotor untrimmed and the rolling road moving ($V_g/V_\infty = 1$). The rotor was at a ground height of 1.0R and the RMS velocity fluctuations are normalised with V_h.

C.4 Cross-flow velocity in the ground effect wake

C.4.1 Mean cross-flow velocity

Stereoscopic (stereo) PIV tests conducted with the Large Rotor are presented in Figures C.11 - C.13 and can be compared to Figure 5.23, presented in Section 5.6.2, to differentiate between the wake produced by the different rotor trim and ground boundary configurations. These figures present contour plots showing the mean velocity magnitudes in the ground effect wake, derived from the three-component velocity measurements, and the corresponding mean cross-flow (w) velocity in the flow-field, for a range of normalised advance ratios.

Comparisons between the varying rotor trim configuration cases showed little differences in the flow-field, although significantly higher velocity magnitudes were observed in the wake when the ground boundary configurations were altered. This can be seen through a comparison of Figure C.11 and C.13, where the trailing rotor wake along the ground plane was seen to contain higher velocity magnitudes in the

moving ground ($V_g/V_\infty = 1$) cases than the stationary ground ($V_g/V_\infty = 0$) cases. This is a direct consequence of the ground boundary condition on the wake. For comparable normalised advance ratios, the shift of the flow separation point closer to the rotor disk, brought about by the moving ground configuration, results in the rotor wake trailing along the ground plane to be less dissipated compared to the stationary ground cases, thus resulting in the flow-field produced by the moving ground boundary configuration to contain higher magnitude velocities. Similar results can be seen between the quasi-trimmed rotor cases presented in Figure C.12 and Figure 5.23, and these will have an implication on the quantity of dust picked up from the ground, if the rotor is operated close to an erodible ground surface. With the velocities along the ground plane higher, the moving ground ($V_g/V_\infty = 1$) configuration is expected to cause more dust particles to be uplifted from the ground plane, and result in bigger dust cloud sizes.

Differences in magnitudes of the mean cross-flow velocity, w, experienced in the ground effect wake were also seen to be caused by the varying ground boundary configurations. As in the case of the moving ground boundary configuration, results from the stationary ground configuration tests show the mean cross-flow velocity in the wake at all the normalised advance ratios tested to generally be of low magnitudes, although these were seen to be comparatively higher than those experienced with the moving ground. For comparable flow separation locations, Figures C.11 (h) and C.12 (h) show the highest cross-flow velocity magnitudes recorded in the flow-field to be around $w = 0.4V_h$, compared to the moving ground configuration cases shown in Figure C.13 (h) and Figure 5.23 (h), where the highest cross-flow velocity magnitudes experienced in the flow-field was around $w = 0.2V_h$.

Results from the stationary ground configuration ($V_g/V_\infty = 0$) cases showed very low cross-flow velocity in the majority of the flow-field at the lowest normalised advance ratios tested, besides the presence of a region of negative cross-flow velocity coinciding with the trailing rotor wake expanding along the ground plane. As the mean recirculation region formed closer to the rotor disk at higher normalised advance ratios, a region of weak negative cross-flow was seen to form in the flow-field and this was seen to broadly coincide with the location of the mean recirculation region. Further increments in normalised advance ratios were seen

to result in the formation of regions of weak positive cross-flow. These were especially noticeable when a compact ground vortex was formed under the rotor disk, as shown in Figures C.11 (h) and C.12 (h) and may be associated with the jet velocities induced by the tip vortices as they merge to form the ground vortex.

(a) $\mu^* = 0.64$: Velocity Magnitude (b) w-velocity component

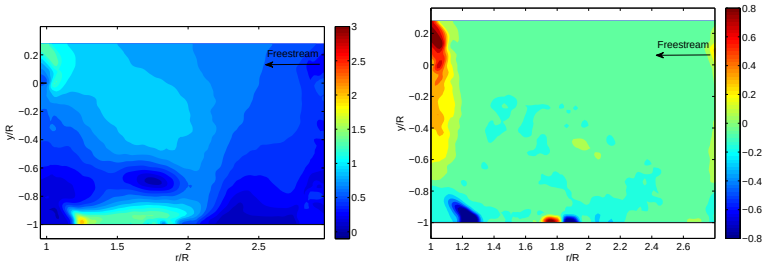

(c) $\mu^* = 0.72$: Velocity Magnitude (d) w-velocity component

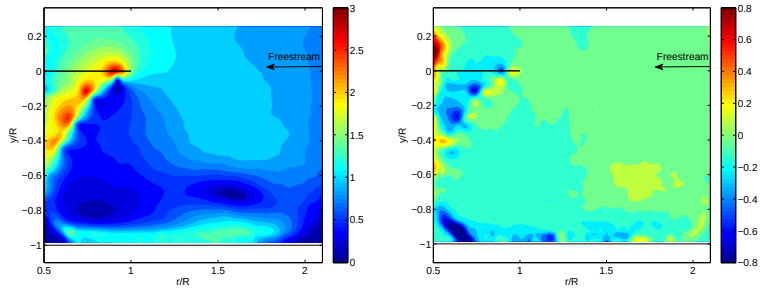

(e) $\mu^* = 0.79$: Velocity Magnitude (f) w-velocity component

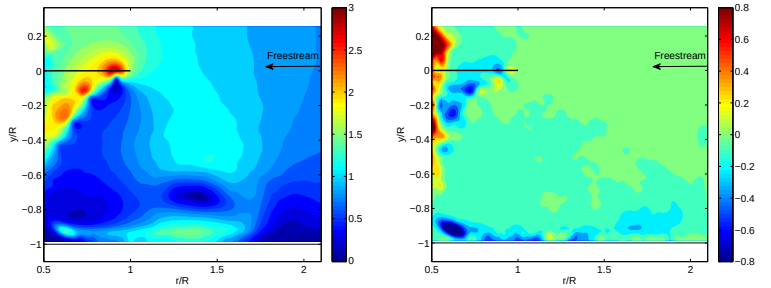

(g) $\mu^* = 0.87$: Velocity Magnitude (h) w-velocity component

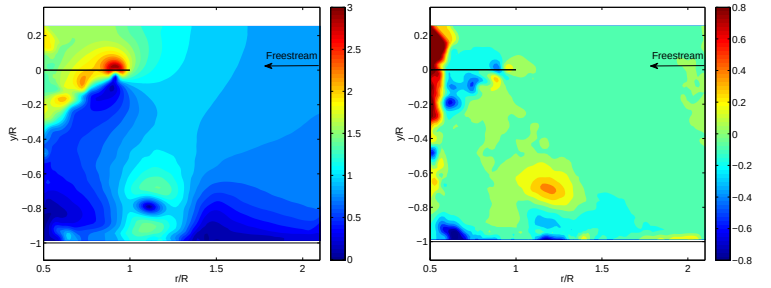

FIGURE C.11: Mean velocity plots showing the velocity magnitudes and mean cross-flow (w) velocity in the flow-field. In these cases, the rotor was untrimmed and at a ground distance of 1.0R and was operated with the ground stationary ($V_g/V_\infty = 0$).

(a) $\mu^* = 0.51$: Velocity Magnitude (b) w-velocity component

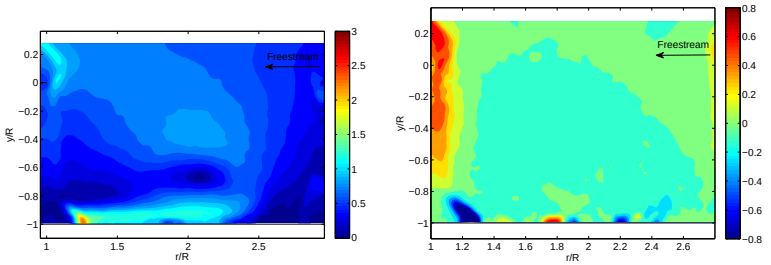

(c) $\mu^* = 0.65$: Velocity Magnitude (d) w-velocity component

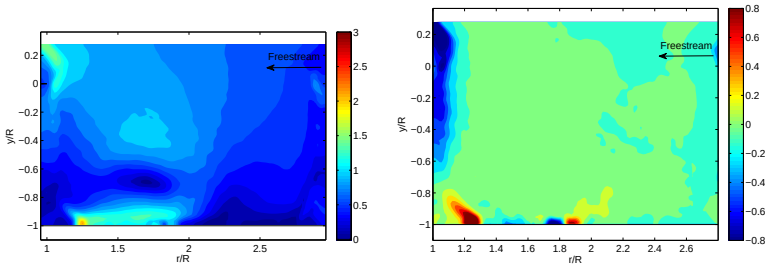

(e) $\mu^* = 0.72$: Velocity Magnitude (f) w-velocity component

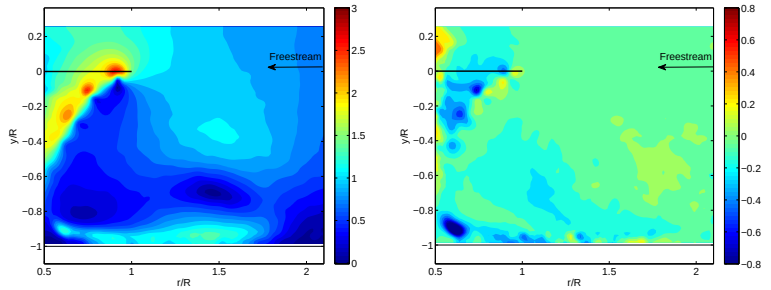

(g) $\mu^* = 0.86$: Velocity Magnitude (h) w-velocity component

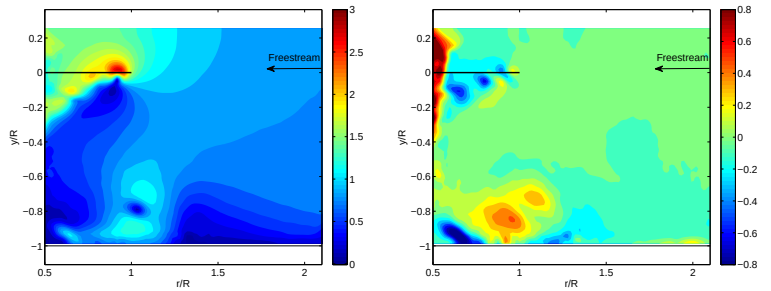

FIGURE C.12: Mean velocity plots showing the velocity magnitudes and mean cross-flow (w) velocity in the flow-field. In these cases, the rotor was quasi-trimmed and at a ground distance of 1.0R and was operated with the ground stationary ($V_g/V_\infty = 0$).

(a) $\mu^* = 0.45$: Velocity Magnitude (b) w-velocity component

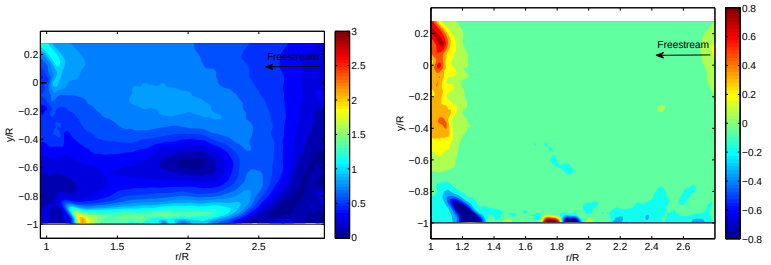

(c) $\mu^* = 0.56$: Velocity Magnitude (d) w-velocity component

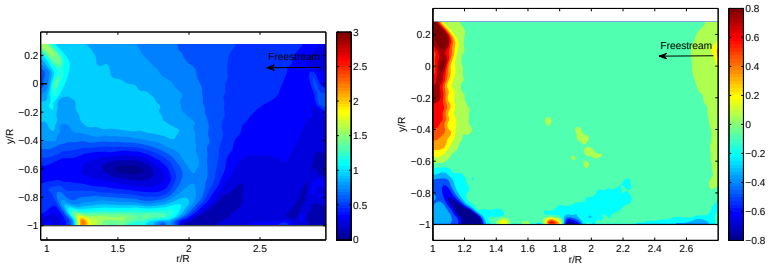

(e) $\mu^* = 0.67$: Velocity Magnitude (f) w-velocity component

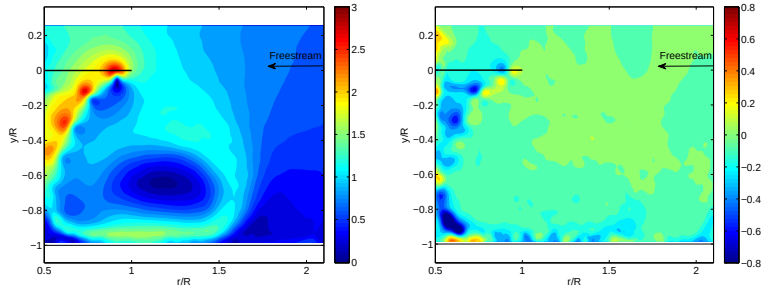

(g) $\mu^* = 0.76$: Velocity Magnitude (h) w-velocity component

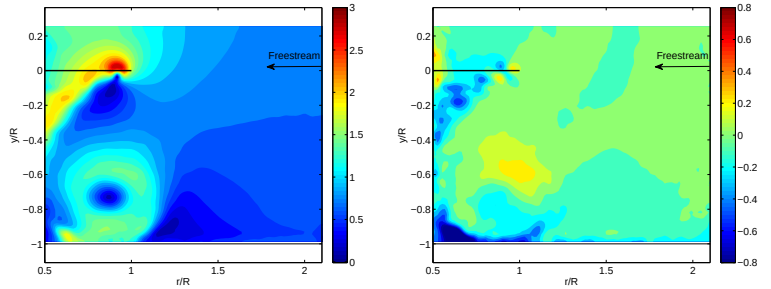

FIGURE C.13: Mean velocity plots showing the velocity magnitudes and mean cross-flow (w) velocity in the flow-field. In these cases, the rotor was untrimmed and at a ground distance of 1.0R and was operated with the ground moving ($V_g/V_\infty = 1$).

C.4.2 Instantaneous cross-flow velocity in the ground effect flow-field

Instantaneous cross-flow velocity maps, obtained from the stationary ground boundary configuration, also showed significant cross-flow velocity magnitudes to exist in the instantaneous flow-field. An example of this is provided in Figure C.14, which shows the instantaneous cross-flow (w) velocity contour plots and the corresponding instantaneous vorticity plots, for a normalised advance ratio of $\mu^* = 0.51$. As in the case of the moving ground configuration test results presented in Figure 5.24 in Chapter 5, little correlation between the vorticity and cross-flow velocity locations could be established from the instantaneous data.

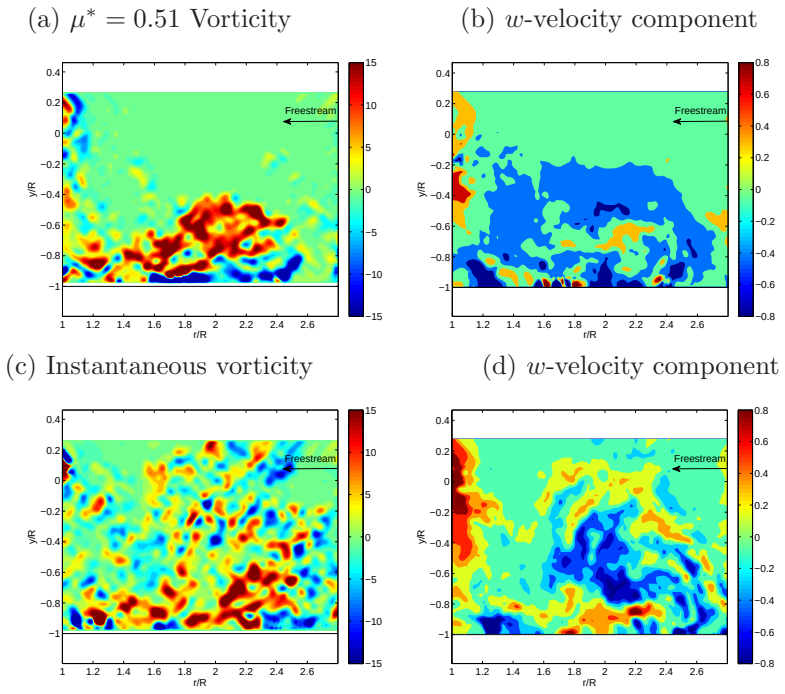

FIGURE C.14: Instantaneous vorticity and w-velocity component plots. In these cases, the rotor was quasi-trimmed and at a ground distance of 1.0R and was operated with the ground stationary ($V_g/V_\infty = 0$), at a normalised advance ratio of $\mu^* = 0.51$.

C.4.3 Cross-flow Velocity Fluctuations

Unsteadiness associated with the cross-flow velocity component in the ground effect wake is analysed by considering the root-mean-square (RMS) velocity fluctuations. Cross-flow RMS velocity fluctuation plots for the different experimental configurations are presented in Figures C.15 - C.17. In addition to the w-component RMS fluctuations, the total RMS velocity fluctuations, derived from the three-component velocity measurements of the wake are also presented in these plots for a range of normalised advance ratios. As in the case of the moving ground configuration ($V_g/V_\infty = 1$) results presented in Figure 5.25 in Chapter 5, comparisons between the RMS velocity magnitude fluctuations and the cross-flow RMS fluctuations in these figures, revealed the peak cross-flow fluctuations to occur in the regions of the wake where the overall peak velocity fluctuations were observed.

Comparison of the RMS velocity fluctuation data from different rotor trim configuration cases, as shown in Figures C.15 and C.16 showed little differences in terms of the fluctuation magnitudes observed in the wake. Changes in the ground boundary configurations, were however seen to cause more significant variations in the velocity fluctuations, with the moving ground boundary configuration seen to cause wider regions of the wake to be affected by low magnitude velocity fluctuations.

Figure C.15 presenting the velocity fluctuations in the flow-field produced by the untrimmed rotor with a stationary ground boundary configuration ($V_g/V_\infty = 0$), shows the total RMS velocity fluctuations as well as the cross-flow velocity fluctuations experienced in the flow-field to be higher than those seen to affect the flow-field resulting from the moving ground configuration ($V_g/V_\infty = 1$), shown in Figure C.17. Additionally the spread of the velocity fluctuations within the wake also appeared to be different for both the ground boundary configuration cases. Figure C.15 shows the highest magnitude RMS velocity fluctuations to occur around the centre of the mean recirculation zone, with the corresponding peak cross-flow velocity fluctuations, although lower in magnitudes, seen to occur within similar regions. In the case of the moving ground configuration, shown in Figure C.17, both the peak RMS velocity fluctuations and the cross-flow velocity fluctuations were seen to occur in regions corresponding to the location of the loop

of high magnitude positive vorticity within the recirculation zone. With the dispersion of vorticity within the flow-field caused by the moving ground boundary configuration greater than the stationary ground configuration, this explains the differences in location and magnitudes of the peak velocity fluctuations.

(a) $\mu^* = 0.64$: RMS Velocity Magnitude (b) RMS w-component

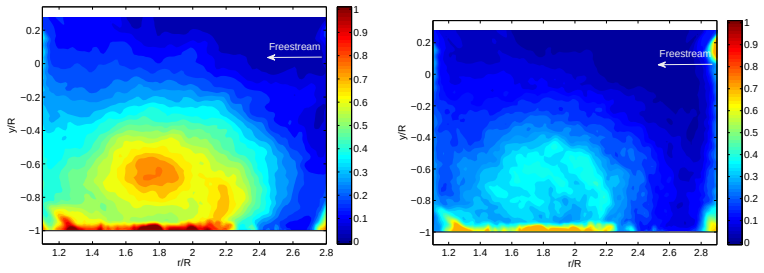

(c) $\mu^* = 0.72$: RMS Velocity Magnitude (d) RMS w-component

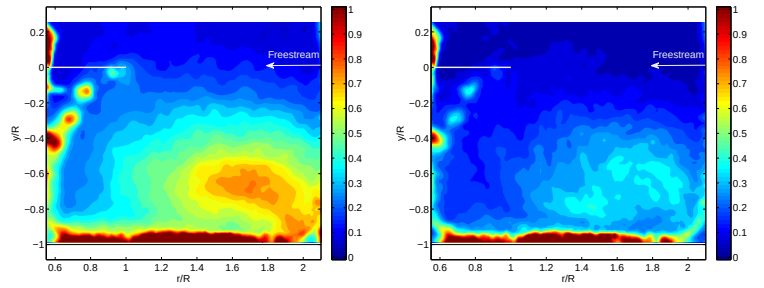

(e) $\mu^* = 0.79$: RMS Velocity Magnitude (f) RMS w-component

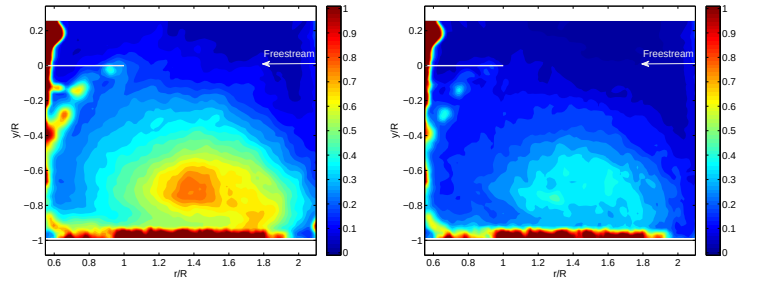

(g) $\mu^* = 0.87$: RMS Velocity Magnitude (h) RMS w-component

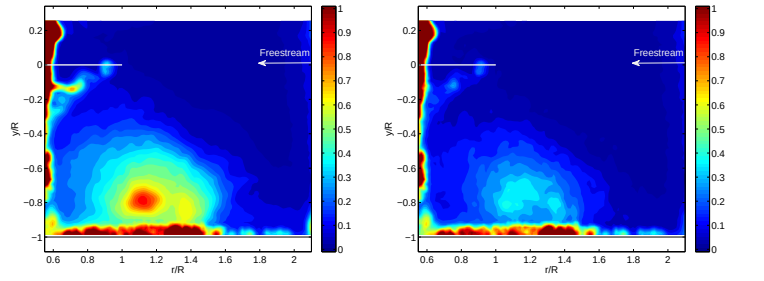

FIGURE C.15: RMS velocity fluctuations showing the total velocity fluctuations and the cross-flow (w) velocity fluctuations experienced in the flow-field. In these cases, the rotor was untrimmed and at a ground distance of 1.0R and was operated with the ground stationary ($V_g/V_\infty = 0$).

(a) $\mu^* = 0.51$: RMS Velocity Magnitude (b) RMS w-component

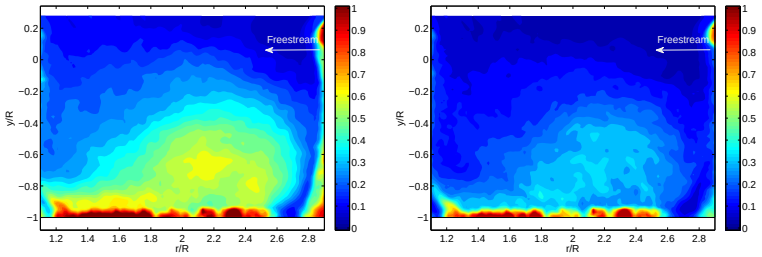

(c) $\mu^* = 0.62$: RMS Velocity Magnitude (d) RMS w-component

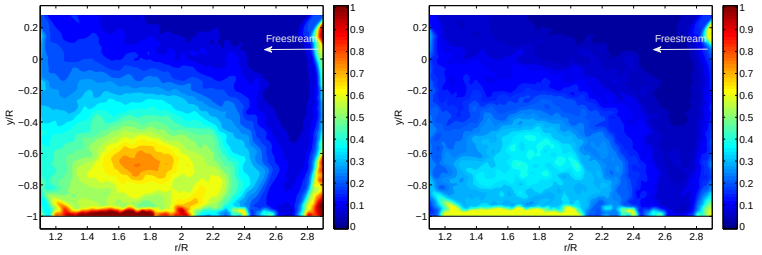

(e) $\mu^* = 0.72$: RMS Velocity Magnitude (f) RMS w-component

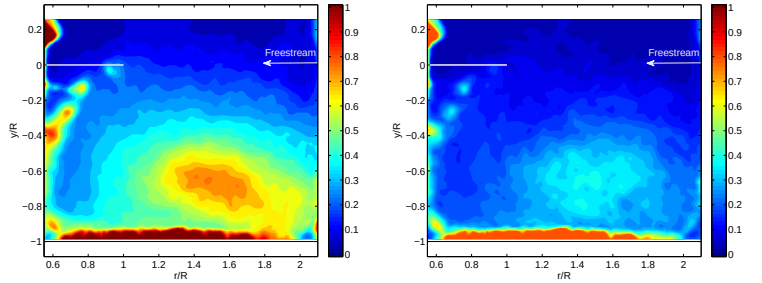

(g) $\mu^* = 0.86$: RMS Velocity Magnitude (h) RMS w-component

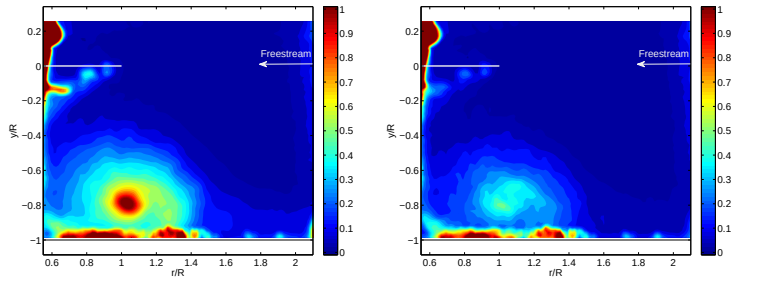

FIGURE C.16: RMS velocity fluctuations showing the total velocity fluctuations and the cross-flow (w) velocity fluctuations experienced in the flow-field. In these cases, the rotor was quasi-trimmed and at a ground distance of 1.0R and was operated with the ground stationary ($V_g/V_\infty = 0$).

(a) $\mu^* = 0.45$: RMS Velocity Magnitude (b) RMS w-component

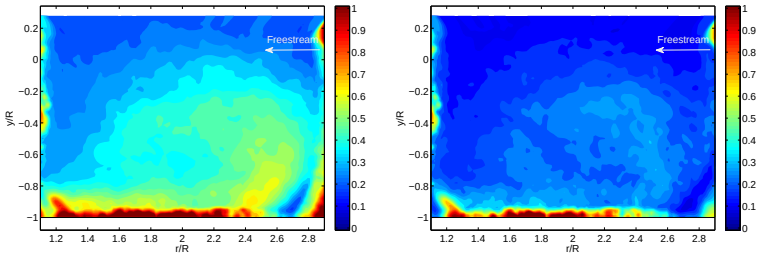

(c) $\mu^* = 0.56$: RMS Velocity Magnitude (d) RMS w-component

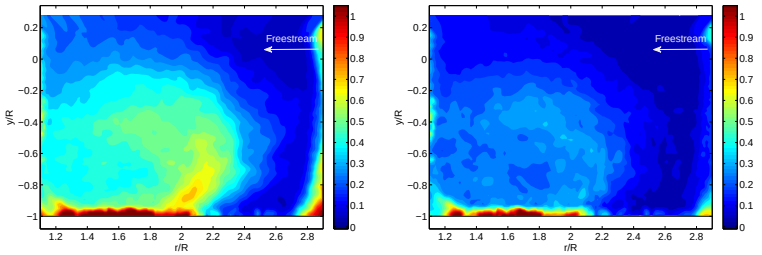

(e) $\mu^* = 0.67$: RMS Velocity Magnitude (f) RMS w-component

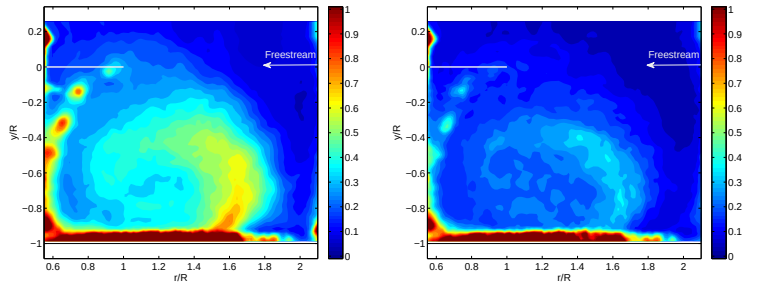

(g) $\mu^* = 0.76$: RMS Velocity Magnitude (h) RMS w-component

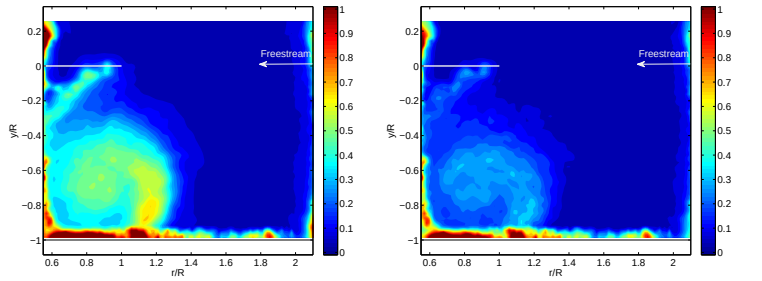

FIGURE C.17: RMS velocity fluctuations showing the total velocity fluctuations and the cross-flow (w) velocity fluctuations experienced in the flow-field. In these cases, the rotor was untrimmed and at a ground distance of 1.0R and was operated with the ground moving ($V_g/V_\infty = 1$).

References

[1] D.L. Key. Analysis of Army Helicopter Pilot Error Mishap Data and the Implications for Handling Qualities. In 25^{th} *European Rotorcraft Forum*, Rome, Italy, 14-16 September 1999.

[2] D. Learmount. Uk cuts light helicopter accidents. Flight International magazine, February 2003. URL `http://www.flightglobal.com/articles/2003/02/11/161551/uk-cuts-light-helicopter-accidents.html`.

[3] N.J. Mourtos, S. Couillaud, D. Carter, C. Hange, D. Wardwell, and R.J. Margason. Flow Visualization Studies of VTOL Aircraft Models During Hover In Ground Effect. In *NASA Technical Memorandum No. 108860*, NASA Ames Research Center, Moffett Field, California, USA, January 1995.

[4] G. Jennings. Down in the dirt: helicopter brownouts. Jane's Defence: Air Force, February 2008. URL `http://www.janes.com/news/defence/air/jdw/jdw080213_1_n.shtml`.

[5] E. A. Fradenburgh. The helicopter and the ground effect machine. *Journal of the American Helicopter Society*, 5(4):24, October 1960.

[6] H.G. Küssner. Helicopter Problems. In *NACA Technical Memorandums No. 827*, Washington, USA, May 1937.

[7] A. Betz. The Ground Effect on Lifting Propellers. In *NACA Technical Memorandums No. 836*, Washington, USA, August 1937.

[8] M. Knight and R.A. Hefner. Static Thrust Analysis of the Lifting Airscrew. In *NACA Technical Notes No. 626*, Washington, USA, December 1937.

[9] J. Zbrozek. Ground Effect on the Lifting Rotor. *British ARC*, R & M No. 2347, July 1947.

[10] J.S. Hayden. The effect of the ground on helicopter hovering power required. *32nd Annual Forum of the American Helicopter Society*, May 1976.

[11] J.G. Leishman. *Principles of Helicopter Aerodynamics, Second Edition.* Cambridge Aerospace Series. Cambridge University Press, Cambridge, UK, 2006.

[12] I.C. Cheeseman and W.E. Bennett. The Effect of the Ground on a Helicopter Rotor in Forward Flight. In *ARC Reports and Memorandums No. 3021*, Washington, USA, September 1955.

[13] H.A. Saberi and M.D. Maisel. A Free Wake Rotor Analysis Including Ground Effect. In 43rd *Annual Forum of the American Helicopter Society*, St. Louis, Missouri, USA, 18-20 May 1987.

[14] T.R. Quackenbush and D.A. Wachspress. Enhancements to a New Free Wake Hover Analysis. In *NASA Contractor Report No. 177523*, NASA Ames Research Center, Moffett Field, California, USA, April 1989.

[15] A. Graber, A. Rosen, and A. Seginer. An Investigation of a Hovering Rotor in Ground Effect. In 16th *European Rotorcraft Forum*, Glasgow, Scotland, UK, 18-20 September 1990.

[16] H. Xin, J.V.R. Prasad, D.A. Peters, T. Nagashima, and N. Iboshi. A Finite State Inflow Model for Simulation of Helicopter Hovering in Ground Effect. In 54th *Annual Forum of the American Helicopter Society*, Washington DC, USA, 20-22 May 1998.

[17] N. Itoga, T. Nagashima, N. Iboshi, J.V.R. Prasad, and D.A. Peters. Numerical Analysis of Ground Effect for a Lifting Rotor Hovering above Close proximity to Inclined Flat Surface. In *American Helicopter Society Specialists' Meeting on Advanced Rotorcraft Technology and Disaster Relief*, Gifu City, Japan, April 1998.

[18] D.A. Griffiths and J.G. Leishman. A Study of Dual-Rotor Interference and Ground Effect using a Free-Vortex Wake Model. In 58th *Annual Forum of the American Helicopter Society*, Montréal, Canada, 11-13 June 2002.

[19] V.J. Rossow. Effect of Ground and/or Ceiling Planes on Thrust of Rotors in Hover. In *NASA Technical Memorandums No. 86754*, NASA Ames Research Center, Moffett Field, California, USA, July 1985.

[20] J.S. Light. Tip Vortex Geometry of a Hovering Helicopter Rotor in Ground Effect. In 45^{th} *Annual Forum of the American Helicopter Society*, Boston, Massachusetts, USA, 22-24 May 1989.

[21] M. Saritas, E. Tinar, and O. Cetiner. Interaction of Rotor Blade Tip Vortices with Surface. In 11^{th} *International Symposium on Flow Visualisation*, Notre Dame, Indiana, USA, 9-12 August 2004.

[22] T.E. Lee, J.G. Leishman, and M. Ramasamy. Fluid Dynamics of Interacting Blade Tip Vortices With a Ground Plane. In *64*th *Annual Forum of the American Helicopter Society*, Montréal, Canada, April 2008.

[23] P. F. Sheridan and W. Wiesner. Aerodynamics of Helicopter Flight Near the Ground. In *33*rd *Annual Forum of the American Helicopter Society*, May 1977.

[24] H. C. Jr. Curtiss, M. Sun, W. F. Putman, and E. J. Jr. Hanker. Rotor Aerodynamics in Ground Effect At Low Advance Ratios. *Journal of the American Helicopter Society*, 29(1):48–55, 1984.

[25] R.E. Brown and G.R. Whitehouse. Modelling Rotor Wakes in Ground Effect. *Journal of the American Helicopter Society*, July 2004.

[26] B. Ganesh. *Unsteady Aerodynamics of Rotorcraft at Low Advance Ratios in Ground Effect*. PhD thesis, Georgia Institute of Technology, May 2006.

[27] H. C. Jr. Curtiss, W. Erdman, and M. Sun. Ground Effect Aerodynamics. *Vertica*, 11(1-2):29–42, 1987.

[28] E.A. Boyd and I. Kusmarwanto. Ground Effect on a Rotor Wake. In *Cranfield Institue of Technology, College of Aeronautics, Report 8323*, August 1983.

[29] I. Kusmarwanto. *Ground Effect on a Rotor Wake*. PhD thesis, Cranfield Institute of Technology, College of Aeronautics, March 1985.

[30] T. Saijo, B. Ganesh, A. Huang, and N.M. Komerath. Development of unsteadiness in a rotor wake in ground effect. In *21*st *AIAA Applied Aerodynamics Conference*, Orlando, Florida, USA, 23-26 June 2003.

[31] B. Ganesh and N.M. Komerath. Unsteady Aerodynamics of Rotorcraft in Ground Effect. In *AIAA Fluid Dynamics Meeting*, Portland, Orlando, USA, June 2004.

[32] B. Ganesh, N.M. Komerath, D. Pulla, and A.T. Conlisk. Unsteady Aerodynamics of Rotorcraft in Ground Effect. In *43rd AIAA Aerospace Sciences Meeting and Exhibit*, Reno, Nevada, USA, 10-13 January 2005.

[33] M. Sun. *A Study of Helicopter Rotor Aerodynamics in Ground-Effect at Low Speeds*. PhD thesis, Princeton University, New Jersey, USA, October 1983.

[34] E.J. Hanker Jr and R.P. Smith. Parameters Affecting Helicopter Interactional Aerodynamics in Ground Effect. *Journal of the American Helicopter Society*, 30(1):52–61, January 1985.

[35] J.F. Boer, C. Hermans, and K. Pengel. Helicopter ground vortex: Comparison of numerical predictions with wind tunnel measurements. In 27th *European Rotorcraft Forum*, Moscow, Russia, 11-14 September 2001.

[36] B. A. Ganesh and N. Komerath. Study of ground vortex structure of rotorcraft in ground effect at low advance ratios. In 24th *Applied Aerodynamics Conference*, San Francisco, California, USA, 5-8 June 2006.

[37] C.S. Lee and C.J. He. A Free Wake/Ground Vortex Model for Rotors at Low Speed In-Ground-Effect Flight. In 51st *Annual Forum of the American Helicopter Society*, Fort Worth, Texas, USA, 9-11 May 1995.

[38] H.H. Heyson. Ground Effect for Lifting Rotors in Forward Flight. In *NASA Contractor Report No. 177523*, NASA Langley Research Center, Langely Field, Virginia, USA, May 1960.

[39] H.H. Heyson. Theoretical Study of the Effect of Ground Proximity on the Induced Efficiency of Helicopter Rotors. In *NASA Contractor Report No. 177523*, NASA Langley Research Center, Langely Field, Virginia, USA, 3 May 1977.

[40] M.A. Moulton, J.A. O'Malley, and R.G. Rajagopalan. Rotorwash Prediction Using an Applied Computational Fluid Dynamics Tool. In 60th *Annual Forum of the American Helicopter Society*, Baltimore, Maryland, USA, 7-10 June 2004.

[41] G.R. Whitehouse and R.E. Brown. Helicopter Rotor Response to Wake Encounters in Ground Effect. In 59^{th} *Annual Forum of the American Helicopter Society*, Phoenix, Arizona, USA, 6-8 May 2003.

[42] S. Bhattacharyya and A.T. Conlisk. The Structure of the Rotor Wake in Ground Effect. In 41^{st} *Aerospace Science Meeting and Exhibit*, Reno, Nevada, USA, January 2003.

[43] D. Pulla and A.T. Conlisk. The Long Term Structure of the Rotor Wake in Ground Effect. In *43rd AIAA Aerospace Sciences Meeting and Exhibit*, Reno, Nevada, USA, 10-13 January 2005.

[44] J.G. Leishman. *The Helicopter - Thinking Forward, Looking Back*. College Park Press, College Park, Maryland, 2007.

[45] J.M. Brower. Preventing Brownout. *Special Operations Technology*, 2(4), July 2004.

[46] G. Warwick. Efforts to prevent helicopter accidents in brownout receiving high-level U.S. attention. *Aviation Week and Space Technology*, 168(18):34, May 2008.

[47] L. Sabbagh. Flying Blind in Iraq: U.S. Helicopter Navigate Real Desert Storms. Popular Mechanics e-magazine, October 2006. URL `http://www.popularmechanics.com/technology/military_law/4199189.html`.

[48] S.J. Rodgers. Evaluation of the Dust Cloud Generated by Helicopter Rotor Blade Downwash. In 7^{th} *Annual Conference on Environmental Effects on Aircraft and Propulsion Systems*, Princeton, New Jersey, September 1967.

[49] A.N. Modha, T.A. Blaylock, and W.Y.F. Chan. Brown-out - Flow Visualisation using FLUENT® VBM. In *International Aerospace CFD Conference*, Paris, June 2007.

[50] Ryerson C.C., R.B. Hachnel, G.G. Koenig, and M.A. Moulton. Visibility Enhancement in Rotorwash Clouds. In *43rd AIAA Aerospace Sciences Meeting and Exhibit*, Reno, Nevada, January 2005.

[51] J.D. Keller, G.R. Whitehouse, D.A. Wachpress, M.E. Teske, and Quackenbush T.R. A Physics-Based Model of Rotorcraft Brownout for Flight

Simulation Applications. In *62th Annual Forum of the American Helicopter Society*, Phoenix, Arizona, May 2006.

[52] D.A. Wachpress, G.R. Whitehouse, J.D. Keller, K. McClure, P. Gilmore, and M. Dorsett. Physics based modeling of Helicopter Brownout for Piloted Simulation Applications. In *Interservice/Industry Training, Simulation and Education Conference (I/ITSEC)*, Paper No. 8177, 2008.

[53] C. Phillips and R.E. Brown. Eulerian Simulation od the Fluid Dynamics of Helicopter Brownout. In *64th Annual Forum of the American Helicopter Society*, Montréal, Canada, April 2008.

[54] B.R. White. Soil Transport by Wind on Mars. *Journal of Geophysical Research*, 84(B9), August 1974.

[55] R.E. Brown and A.J. Line. Efficient High-Resolution Wake Modeling Using the Vorticity Transport Equation. *AIAA Journal*, 43(7):1434–1443, July 2005.

[56] R. Whittle. Combact Operations: Matting Down Brownout, Engine Wear. Aviation Today e-magazine, August 2007. URL `http://www.aviationtoday.com/rw/military/attack/14521.html`.

[57] S. Colby. Military Spin. Aviation Today e-magazine, August 2005. URL `http://www.aviationtoday.com/rw/training/specialty/1418.html`.

[58] Z.P. Szoboszlay, W.B. Albery, T.S. Turpin, and G.M. Neiswander. Brown-Out Symbology Simulation (BOSS) on the NASA Ames Vertical Motion Simulator. In *64th Annual Forum of the American Helicopter Society*, Montréal, Canada, April 2008.

[59] J.B. Barlow, W.H. Rae Jr, and A. Pope. *Low-Speed Wind Tunnel Testing*. John Wiley & Sons, 3rd edition, 1999.

[60] V.M. Ganzer and Jr. W.H. Rae. An experimental investigation of the effect of wind tunnel walls on the aerodynamic performance of a helicopter rotor. In *NASA Technical Note No. D-415*, University of Washington, Washington, USA, May 1960.

[61] A. Pope and J.J. Harper. *Low-speed Wind Tunnel Testing*. John Wiley & Sons, Inc., USA, 1966.

[62] R.B. Green, E.A. Gillies, and R.E. Brown. The flow field around a rotor in axial descent. *Journal of Fluid Mechanics*, 534:237–261, January 2005.

[63] URL `http://www.cosmeticsinfo.org/aboutus.php`.

[64] R.B. Green, C.J. Doolan, and R.M. Cannon. Measurements of the orthogonal blade-vortex interaction using a particle image velocimetry technique. *Experiments in Fluids*, 29:369–379, November 2000.

[65] R. Green and K. W. McAlister. Systematic errors in stereo piv when imaging through a glass window. *NASA/ TM-2004-212832*, October 2004.

[66] J. Wilson and J.F.B. Hawkes. *Lasers-Principles and Applications*. International Series in Optoelectronics. Prentice Hall, Great Britain, 1987.

[67] M. Saffarian and F. Fahimi. A Comprehensive Kinamatic Analysis of a Model Helicopter's Actuation Mechanism. In *46th AIAA Aerospace Sciences Meeting and Exhibit*, Reno, Nevada, January 2008.

[68] *Raptor 60 - Assembly and Maintenance Manual*. Thunder Tiger Corporation, 2001.

[69] J.C. Avila Vilchis, B. Brogliato, A. Dzui, and R. Lozano. Nonlinear modelling and control of helicopters. *Automatica*, 39(9):1583–1596, September 2003.

[70] F.N. Coton, S.B. Mat, R.A.McD. Galbraith, and R. Gilmour. Low speed wind tunnel characterization of the vfe-2 wing. In *46th AIAA Aerospace Sciences Meeting and Exhibit*, Reno, Nevada, January 2008.

[71] *DaVis 7.2 Software - Product Manual*. LaVision GmbH, Germany, May 2007.

[72] M. Ramasamy and J.G. Leishman. Reynolds number based blade tip vortex model. In *61st Annual Forum of the American Helicopter Society*, Grapevine, Texas, 2005.

[73] L. Lyles. Basic wind erosion processes. *Agriculture, Ecosystems and Environment*, 22/23:99–101, 1988.

[74] W.G. Nickling. The initiation of particle movement by wind. *Sedimentology*, 35:499–511, 1988.

[75] M. Ramasamy and J.G. Leishman. The Interdependence of Straining and Viscous Diffusion Effects on Vorticity in Rotor Flow Fields. In *59th Annual Forum of the American Helicopter Society*, Phoenix, Arizona, May 2003.

[76] C. Phillips and R.E. Brown. The Effect of Helicopter Configuration on the Fluid Dynamics of Brownout. In *34th European Rotorcraft Forum*, Liverpool, United Kingdom, September 2008.

[77] M. Ramasamy, B. Johnson, T. Huismann, and J.G. Leishman. Procedures for Measuring the Turbulence Characteristics of Rotor Blade Tip Vortices. *Journal of the American Helicopter Society*, 54(2):pp 022006–1–022006–17, April 2009.

[78] M. Raffel, C.E. Willert, and J. Kompenhans. *Particle Image Velocimetry. A Practical Guide*. Springer-Verlag Berlin Heidelberg, 1998.

[79] A.L. Chen, Jacob J.D., and Ö Savaş. Dynamics of corotating vortex pairs in the wakes of flapped airfoils. *Journal of Fluid Mechanics*, 382:155–193, 1999.

[80] J.Z. Wu, H.Y. Ma, and M.D. Zhou. *Vorticity and Vortex Dynamics*. Springer-Verlag Berlin Heidelberg, Germany, 2006.

[81] J. Watkinson. *Art of the Helicopter*. Butterworth-Heinemann, December 2003.

[82] W. Johnson. *Helicopter Theory*. Dover Publications, Inc. New York, 1980.

[83] *FlowMaster-D72, Product-Manual*. LaVision GmbH, Gerrmany, March 2007.

[84] H. Vollmers. Detection of vortices and quantitative evaluation of their main parameters from experimental velocity data. *Measurements Science and Technology*, 12:1199–1207, April 2001.

[85] M. Ramasamy and J.G. Leishman. Benchmarking PIV with LDV for Rotor Wake Vortex Flows. In *24th AIAA Applied Aerodynamics Conference*, number AIAA 2006-3479, San Francisco, California, USA, 5-8 June 2006.

[86] J. Seddon. *Basic Helicopter Aerodynamics: An account of first principles in the fluid mechanics and flight dynamics of the single rotor helicopter*. BSP Professional Books, Oxford, UK, 1990.

[87] Ö Savaş, R.B. Green, and F.X. Caradonna. Coupled thrust and vorticity dynamics during VRS. *Accepted for publication in Journal of the American Helicopter Society*, 2009.

[88] J.M. Ortega, R.L. Bristol, and Ö Savaş. Experimental study of the instability of unequal-strength counter-rotaating vortex pairs. *Journal of Fluid Mechanics*, 474:35–84, 2003.

[89] A.J. Landgrebe. The Wake Geometry of a Hovering Helicopter Rotor and Its Influence on Rotor Performance. In 28^{th} *Annual National Forum of the American Helicopter Society*, May 1972.

[90] A. Schroeder and C.E. Willert. *Particle Image Velocimetry: new developments and recent applications*. Springer, Berlin, 2008.

[91] McAlister K.W., C.A. Schuler, L. Branum, and J.C. Wu. 3d Wake Measurements Near a Hovering Rotor for Determining Profile and Induced Drag. *NASA Technical Paper*, (3577), August 1995.

[92] J.T. Heineck, G.K. Yamauchi, A.J. Wadcock, and L. Lourenco. Application of three-component PIV to a hovering rotor wake. In *56th Annual Forum of the American Helicopter Society*, Virginia Beach, Virginia, USA, 2-4 May 2000.

[93] H. Richard, J. Bosbach, A. Henning, M. Raffel, C. Willert, and B.G. van derr Wall. 2C and 3C PIV Measurements on a Rotor in Hover Condition. In *13th International Symposium on Applications of Laser Techniques to Fluid Mechanics*, Lisbon, Portugal, 26-29 June 2006.

[94] B. Johnson, M. Ramasamy, and J.G. Leishman. Turbulence Measurements in Rotor Tip Vortices Using Dual-Plane Digital Particle Image Velocimetry. In 34^{th} *European Rotorcraft Forum*, Liverpool, UK, 19-21 September 2008.

[95] O. Wong, R. Mahalingam, C. Tongchitpakdee, and N.M. Komerath. The Near Wake of a 2-Bladed Rotor in Forward Flight. In *American Helicopter Society Aeromechanics Specialists Meeting*, Atlanta, Gerogia, USA, 13-14 November 2000.

[96] R. Mahalingam and N.M. Komerath. Measurements of the near wake of a rotor in forward flight. In *AIAA Aerospace Sciences Meeting and Exhibit*, Reno, Nevada, USA, 12-15 January 1998.

[97] East. L.F. The Measurement of Ground Effect using a Fixed Ground Board in a Wind Tunnel. In *Aeronautical Research Council, Reports and Memoranda, No. 3689*, Bedford, UK, 1970.

[98] T.R. Turner. Endless Belt Technique for Ground Simulation. In *Conference on V/Stol and Stol Aircraft, NASA SP-116*, Washington D.C., USA, 1966.

[99] H. H. Heyson. Some Considerations in Wind-Tunnel Tests of V/STOL Models. In *NASA Technical Note TMX-60772*, Tullahoma, Tennesse, USA, September 1967.

[100] T.R. Turner. A Moving Belt Ground Plane for Wind Tunnel Ground Simulation and Results for Two Jet Flap Configurations. In *NASA Technical Note TN D-4228*, Hampton, Virginia, USA, November 1967.

[101] B. Johnson, J.G. Leishman, and A. Sydney. Investigation of Sediment Entrainment in Brownout Using High-Speed Particle Image Velocimetry. In 65^{th} *Annual National Forum of the American Helicopter Society*, Grapevine, Texas, USA, 27-29 May 2009.

[102] K. D. Jensen. Flow measurements. *Journal of the Brazilian Society of Mechanical Sciences and Engineering*, 26(4):pg 400–419, October - December 2004.

[103] I. Grant. Particle image velocimetry: a review. *Journal of Mechanical Engineering Science*, 211(1):55–76, 1997.

[104] J.G. Santiago, S.T. Wereley, C.D. Meinhart, D.J. Beebe, and R.J. Adrian. A particle image velocimetry system for microfluidics. *Experiments in Fluids*, 25(4):316–319, September 1998.

[105] R.J. Adrian. Twenty years of particle image velocimetry. *Experiments in Fluids*, 39:159–169, July 2005.

[106] R.J. Adrian. Particle-imaging Techniques for Experimental Fluid Mechanics. *Experiments in Fluids*, 23:261–304, January 1991.

[107] A. K. Prasad. Particle image velocimetry. *Current Science- Bangalore*, 79 (1):pg 51–60, 10 July 2000.

[108] C.E. Willert and M. Gharib. Digital particle image velocimetry. *Experiments in Fluids*, 10(4):181–193, January 1991.

[109] A. Melling. Tracer particles and seeding for particle image velocimetry. *Measurement Science and Technology*, 8:pg 1406–1416, 1997.

[110] R.B. Green. Optical methods. Experimental Aerodynamics 5 - Course Lecture Notes, 2005.

[111] K. D. Hinsch. Three-dimensional particle velocimetry. *Journal of Measurement Science Technology*, 6(6):pg 742–753, 1995.

[112] I. Grant and A. Lui. Directional ambiguity resolution in particle image velocimetry by pulse tagging. *Experiments in Fluids*, 10(2-3):pg 71–76, December 1990.

[113] R.J. Adrian. Image shifting technique to resolve directional ambiguity in double-pulsed velocimetry. *Applied Optics*, 25(21):pg 3855–3858, 1986.

[114] R. D. Keane and R. J. Adrian. Theory of cross-correlation analysis of piv images. *Flow, Turbulence and Combustion*, 49(3):pg 191–215, July 1992.

[115] H. Haung, D. Dabiri, and M. Gharib. On errors of digital particle image velocimetry. *Measurement Science and Technology*, 8:pg 1427–1440, 1997.

[116] J. Westerweel. Fundamentals of digital particle image velocimetry. *Measurement Science and Technology*, 8:pg 1379–1392, 1997.

[117] D.P. Hunt. Piv error correction. *Experiments in Fluids*, 29(1):13–22, July 2000.

[118] J. Nogueira, A. Lecuona, and P.A. Rodríguez. Data vaalidation, false vectors correction and derived magnitudes calculation on piv data. *Measurement Science and Technology*, 8:pg 1493–1501, 1997.

[119] J. Westerweel. Efficient detection of spurious vectors in particle image velocimetry. *Experiments in Fluids*, 16(3-4):236–247, February 1994.

[120] M.P. Arroyo and C.A. Greated. Stereoscopic particle image velocimetry. *Measurement Science and Technology*, 2:1181–1186, August 1991.

[121] A.K. Prasad and R.J. Adrian. Stereoscopic particle image velocimetry applied to liquid flows. *Experiments in Fluids*, 15:49–60, 1993.

[122] A.K. Prasad and K. Jensen. Scheimpflug stereocamera for particle image velocimetry in liquid flows. *Applied Optics*, 34(30), 20 October 1995.

[123] C. Willert. Stereoscopic digital particle image velocimetry for application in wind tunnel flows. *Measurement Science and Technology*, 8:1465–1479, September 1997.

[124] A.K. Prasad. Stereoscopic particle image velocimetry. *Experiments in Fluids*, 29:103–116, February 2000.

[125] N. J. Lawson and J. Wu. Three-dimensional particle image velocimetry: error analysis of stereoscopic techniques. *Measurement Science and Technology*, 8:pg 894–900, September 1997.

[126] S.M. Soloff, R. J. Adrian, and Z-C Lui. Distortion compensation for generalized stereoscopic particle image velocimetry. *Measurement Science and Technology*, 8:pg 1441–1454, September 1997.

[127] H. H. Heyson. Theoretical Study of Conditions Limiting V/STOL Testing in Wind Tunnels with Solid Floor. In *NASA Technical Note TN D-5819*, Hampton, Virginia, USA, June 1970.